STUDY OF $\mathrm{B} \to \mathrm{X}(3872)\mathrm{K}\pi$ DECAY WITH BELLE DETECTOR AT KEK B-FACTORY

A THESIS

Submitted to the

FACULTY OF SCIENCE

PANJAB UNIVERSITY, CHANDIGARH

for the degree of

DOCTOR OF PHILOSOPHY

2015

ANU BALA

DEPARTMENT OF PHYSICS

CENTRE OF ADVANCED STUDY IN PHYSICS

PANJAB UNIVERSITY, CHANDIGARH

INDIA

Acknowledgements

Finally the long awaited time has come to thank wonderful people who helped me directly or indirectly for completing this research work. Without them, it would not be possible to complete this piece of work.

First of all, I would like to express my sincere regards and gratitude to Prof. J.B.Singh for his supervision, endless patience, support, co-operation and encouragement all through my journey of research. I am thankful to him for giving me a chance to work in very interesting field of physics, to explore new physics and to understand various new phenomena. It has been a great experience for me. He always motivated me by saying beautiful words "It is perfectly fine". I could not have imagined having a better advisor and mentor than him.

I am truly indebted to K. Trabelsi and V. Bhardwaj for the incredible amount of time they spent for helping me for debugging C++ codes, for analysis and pushing me constantly to explore different ideas. I also thank them for motivating me to present my analysis work in International Conferences, Belle Analysis Meeting, Belle General Meeting, which has been a great experience. I learnt a lot from their expertise, enthusiasm and immense knowledge of high energy physics, as well as their insightful way of resolving problems, which have been my most valuable asset. And, I certainly will profit much more from it in the future. At this moment, I may only give all my gratefulness. Without their hard work, I could not go this far.

The measurements showed in this thesis also benefited from the discussion in the Belle charm group. I would like to thank everyone in this group for their assistance, helpful suggestions and constructive criticism which has kept the analysis on the right track. In particular, I would really like to thank my charm group ex-conveners: A. Zupanc and J. Brodzicka for their suggestions during analysis and for helping to keep this analysis moving along. And I would specially like to thanks the referees of my analysis Y. Iwasaki, T. Aziz, P. Krokovny for providing us many comments and suggestions.

I can't forget to thank Prof. Y. Sakai (KEK) for providing me monetary support without which doing this analysis would have been impossible. I would also like to thank

S. Eidelman, T. Browder, S.L. Olsen, Y. Watanabe-san, Miyabayashi-san, M. Nakao-san, Jim Libby, V. Bansal, M. Ziegler, G. Mohanty and L. Piilonen for their efforts to improve this analysis and paper draft. In fact, I would like to thank all the wonderful people of Belle Collaboration. Without their hard work in designing, building and running this experiment, it would have been impossible to complete this analysis.

Many thanks to Prof. M. Kaur, Prof. S. Beri, Prof. J.M. Kohli and Dr. Vipin Bhatnagar and other Department faculty for their constant motivation.

I would also like to thank the Chairman, Department of Physics at Panjab University (Chandigarh) and Vice Chancellor of P.U. for providing an environment that is open to Guru/shishya (Professor/student) interaction and provides a well rounded program.

I would like to extend my thanks to EHEP group members, V.K. Bhandari, Baljinder Singh, Sohan, Subhash, Gyan, Poonam and also to all members of the purchase section for their support.

Thanks also to all my friends outside the Belle world for the breath of fresh air when I most needed it. Thanks to Raman, Amandeep, Ankita, Ruchi, Monika, Bhanu, Kuldeep, Gurpreet, Amandeep Singh, Nitish, Archana di, Anter, Ridhi, Daisy, Kanishka, Bhawan, Manbir, Navkiran, Nidhi Sharma, Richa, Rajbir di, Navneet, Rajeev sir, Nancy, Gaurav, Priyanka, Abhimanyu, Minakshi, Deepanwita, Saurav, Nisar, Subhashree, Vipin and all the others. Sorry for those not named here, however they are not forgotten. I am also thankful to all my college colleagues who help me in one way or other. I would like to thank specially my junior Neeraj Kumar, who always supported me.

I also want to acknowledge DST (India), MEXT (Japan) and JSPS (Japan) for their financial support.

I would really like to thank my in-laws for supporting me to complete my research work and understanding me. Special thanks to my brother-in-law Gurdit Singh and my sister-in-law Harpreet Kaur for their moral support.

I also wish to specially thanks my caring parents, my brother Naveen Garg, my sister Shifali for their support throughout my (not so short) academic career, especially for giving me the opportunity to study at Belle and making all of this possible, putting me up whenever I needed a roof over my head and for encouraging me when I was down about it

all. Without them, I can never achieve this thesis, which should be dedicated to them. I would also really like to thanks my Jiju ji Raj Kumar Bansal, my sweet nephew Diapnshu Bansal and Niket Bansal for pushing me up in low times.

Finally, I am whole-heartedly thankful to my caring husband, Flying Officer Kuldeep Singh and my daughter Japleen Kaur for becoming a beautiful part of this journey and for overwhelming support right from day one. They both form the backbone and origin of my happiness. Their love and support without any complaint or regret has enabled me to complete this research work. He took every responsibility and suffered all the bitterness to take care of our daughter. He always understands me. This would not have been possible without his support. But, there is definitely too much more than that. It is difficult for me to express in words. Thanks for always being there for me. I owe my every achievement to both of them.

I would really thanks "Almighty GOD" for giving me strength to complete this wonderful task with wonderful people.

It is hard to print all the names. I would like to thank all the people whose efforts have made this thesis come to fruition. I thank them all here...

Anu Bala

Abstract

Recently, many unexpected new particles are discovered with masses around 4 GeV/c^2 which lie under the field of charmonium spectroscopy. They are collectively called XYZ mesons. Out of them, many states have properties that resembles like charmonium, but don't fit in charmonium spectrum. Those states are known as charmonium like "exotic" states. The $X(3872)$ meson is one of such exotic charmonium state found in 2003. It was the first to be discovered in exotic era. There are a number of hypotheses and theories on its unknown nature. More experimental information is required to understand the nature of this "exotic" state.

The study performed in this thesis uses whole Belle data set (711 fb^{-1}) collected with Belle detector at KEKB e^+e^- asymmetric collider having energy 8 GeV and 3.5 GeV for high energy ring (HER) and lower energy ring (LER), respectively. The experimental data used for this analysis is collected at the $\Upsilon(4S)$ resonance which immediately produce $B\bar{B}$ pairs (almost at rest) and it creates a perfect platform to perform the analysis related with B-physics. Study for the search of $B^0 \to X(3872)K^+\pi^-$, $B^+ \to X(3872)K^0_S\pi^+$ and $B^+ \to X(3872)K^+\pi^0$ decay modes along with their respective calibration decay modes $B^0 \to \psi' K^+\pi^-$, $B^+ \to \psi' K^0_S\pi^+$ and $B^+ \to \psi' K^+\pi^0$ has been performed in this investigation. The above stated decay modes (having ψ' as final state) are color-suppressed and Cabibbo-favored at tree level.

This is the first time that decay of B-meson to three body final states having $X(3872)$ has been studied in much detail. We have observed the $B^0 \to X(3872)K^+\pi^-$ decay mode with a statistical significance of 7σ (after including systematic uncertainties) and measured the product of branching fractions $\mathcal{B}(B^0 \to X(3872)K^+\pi^-) \times \mathcal{B}(X(3872) \to J/\psi\pi^+\pi^-)$ as $(7.91 \pm 1.29(\text{stat.})^{+0.43}_{-0.42}(\text{syst.})) \times 10^{-6}$. First evidence for charged B-meson decay $B^+ \to X(3872)K^0_S\pi^+$ is also found with a statistical significance of 3.7σ (after including systematic uncertainties). The product of branching fractions $\mathcal{B}(B^+ \to X(3872)K^0\pi^+) \times \mathcal{B}(X(3872) \to J/\psi\pi^+\pi^-)$ is measured as $(10.64 \pm 3.04(\text{stat.})^{+0.81}_{-0.86}(\text{syst.})) \times 10^{-6}$. We also estimated branching fractions $\mathcal{B}(B^0 \to \psi' K^+\pi^-)$ and $\mathcal{B}(B^+ \to \psi' K^0_S\pi^+)$ as $(5.79 \pm 0.14(\text{stat.}) \pm 0.31(\text{syst.})) \times 10^{-4}$

and $(6.00 \pm 0.28(\text{stat.}) \pm 0.35(\text{syst.})) \times 10^{-4}$, respectively.

A search for any resonance or new particle has also been performed with $B^0 \to X(3872)K^+\pi^-$ decay mode. We didn't observe any clear peak for background subtracted distributions of $M_{X(3872)K}$ and $M_{X(3872)\pi}$. However for background subtracted distribution of $M_{K\pi}$, we observe a clear peak. Thus further binned minimum χ^2 fit is performed to the background subtracted $M_{K\pi}$ distribution to extract different $(K\pi)$ components. From this study, it was found that for $X(3872)$ mass region, ratio of branching fractions i.e. $\frac{\mathcal{B}(B^0 \to X(3872)K^*(892)^0) \times \mathcal{B}(K^*(892)^0 \to K^+\pi^-)}{\mathcal{B}(B^0 \to X(3872)K^+\pi^-)}$ is $0.34 \pm 0.09(\text{stat.}) \pm 0.02(\text{syst.})$, which is in contrast with the same ratio for ordinary charmonium states like ψ', where this ratio is $0.68 \pm 0.01(\text{stat.}) \pm 0.01(\text{syst.})$. This property indicates that $X(3872)$ is not behaving like ordinary charmonium state. The product of branching fractions $\mathcal{B}(B^0 \to X(3872)K^*(892)^0) \times \mathcal{B}(X(3872) \to J/\psi\pi^+\pi^-)$ is measured to be $(3.99 \pm 1.48(\text{stat.}) \pm 0.28(\text{syst.})) \times 10^{-6}$, while for its calibrated decay mode, the branching fraction $\mathcal{B}(B^0 \to \psi' K^*(892)^0)$ has been found to be $(5.88 \pm 0.18(\text{stat.}) \pm 0.31(\text{syst.})) \times 10^{-4}$.

Further the very preliminary study of $B^+ \to X(3872)K^+\pi^0$ decay mode is performed. Because of much more multiple B candidates during reconstruction of events and less significance, we are able to set only the upper limit (U.L.) @90% confidence level (C.L.) on the product of branching fractions $\mathcal{B}(B^+ \to X(3872)K^+\pi^0) \times \mathcal{B}(X(3872) \to J/\psi\pi^+\pi^-) < 11.2 \times 10^{-6}$ and for its corresponding calibration decay mode branching fraction $\mathcal{B}(B^+ \to \psi' K^+\pi^0)$ is estimated to be $(3.56 \pm 0.24(\text{stat.})) \times 10^{-4}$.

Contents

1 Introduction: Phenomenological and Experimental Review of $X(3872)$ 1

1.1 Standard Model . . . 2

1.1.1 Quantum Chromodynamics . . . 3

1.1.2 Electro-Weak Theory . . . 4

1.1.3 Discrete Symmetries . . . 5

1.2 The Quark Model . . . 7

1.2.1 Baryons . . . 7

1.2.2 Mesons . . . 7

1.2.3 Quarkonium . . . 7

1.3 Charmonium . . . 8

1.3.1 Charmonium Production . . . 10

1.3.2 Charmonium Decays . . . 14

1.3.3 Charmonium Spectroscopy . . . 16

1.4 Charmonium-Like "Exotic" States . . . 18

1.4.1 Multiquark . . . 18

1.4.2 Charmonium Hybrid . . . 19

1.4.3 Near-Threshold Enhancement . . . 19

1.4.4 Glueballs . . . 20

1.5 Review of "Exotic" X(3872) State . . . 20

1.6 Feynman Diagrams for $B \to \psi' K\pi$ decay modes . . . 26

1.7 $B \to X(3872)K\pi$ decay modes and Motivation . . . 27

1.8 Chapter in Compact . . . 28

2 KEK *B*-Factory and Belle Detector 29

2.1 Introduction . . . 29

2.2 $\Upsilon(4S)$ Meson . . . 31

2.3 KEKB Accelerator . . . 32

2.4 The Belle Detector . . . 35

2.4.1 Beam Pipe . . . 37
2.4.2 Silicon Vertex Detector (SVD) . . . 39
2.4.3 Central Drift Chamber (CDC) . . . 44
2.4.4 Aerogel Čerenkov Counter (ACC) . . . 49
2.4.5 Time of Flight Counter (TOF) . . . 52
2.4.6 Electromagnetic Calorimeter (ECL) . . . 55
2.4.7 Solenoid Magnetic Field . . . 59
2.4.8 K_L/μ Detector (KLM) . . . 60
2.4.9 Extreme Forward Calorimeter (EFC) . . . 63
2.4.10 The Trigger . . . 64
2.4.11 Data Acquisition System (DAQ) . . . 67
2.5 Detection of Different Particles for the Concerned Decay Modes . . . 69
2.6 Data Samples . . . 69
2.7 Chapter in Compact . . . 70

3 Analysis Strategies and Software Tools 71
3.1 Calibration Decay Mode Sample . . . 72
3.2 Tools and Framework . . . 72
3.2.1 Event Generation . . . 73
3.2.2 Event Reconstruction and Signal Extraction . . . 74
3.3 Blind Analysis . . . 75
3.3.1 Signal Monte Carlo Samples . . . 75
3.3.2 Background MC (J/ψ Inclusive MC Sample) . . . 77
3.3.3 Data Sample Analyzed . . . 77
3.4 $B\bar{B}$ Event Selection . . . 78
3.5 Particle Identification . . . 79
3.5.1 Track Selection . . . 79
3.5.2 π/K Identification . . . 80
3.5.3 Photon Selection . . . 81
3.5.4 e, μ Identification . . . 81

3.5.5 J/ψ Reconstruction 82
3.5.6 K^0_S Reconstruction 83
3.5.7 Reconstruction of ψ' and $X(3872)$ Candidates 84
3.5.8 B-meson Reconstruction 84
3.6 Best Candidate Selection (BCS) 86
3.7 Analysis Procedure 90
3.7.1 $B^0 \to X(3872)K^+\pi^-$ and $B^+ \to X(3872)K^0_S\pi^+$ Decay Modes 93
3.8 Background Study and It's Reduction 94
3.9 Systematic Uncertainty 95
3.9.1 K/π Identification 96
3.9.2 Charged Track Finding Efficiency 96
3.9.3 Secondary Branching Fraction ($\mathcal{B}$) 96
3.9.4 Lepton Identification 96
3.9.5 Systematic Uncertainty due to K^0_S 97
3.9.6 Systematic Uncertainty due to Efficiency 97
3.9.7 Uncertainty on Number of $B\bar{B}$ Events ($N_{B\bar{B}}$) 97
3.9.8 Systematic Uncertainty due to PDF Modeling 97
3.10 Chapter in Compact 97

4 Search for $X(3872)$ in 3-body B^0 decay 99
4.1 Search for $B^0 \to X(3872)K^+\pi^-$ Decay Mode 99
4.2 Event Reconstruction Procedure 99
4.3 Branching Fractions 100
4.3.1 Efficiency Estimation from Signal MC study and PDF Parametrization 100
4.3.2 Background Study 108
4.3.3 Branching Fraction Estimation for J/ψ Inclusive MC Sample . 112
4.3.4 Fit Validation 116
4.3.5 Extraction of Signal Yield from Experimental Data and Results 119
4.3.6 Significance of Signal Yield for $B^0 \to X(3872)K^+\pi^-$ Decay Mode123

4.4 Systematic Uncertainty Study 123
4.4.1 Kaon Identification 124
4.4.2 Pion Identification 124
4.4.3 Charged Track Finding Efficiency 124
4.4.4 Lepton Identification 125
4.4.5 Systematic Uncertainty due to Efficiency 125
4.4.6 Secondary Branching Fraction 126
4.4.7 Uncertainty on Number of $B\bar{B}$ Events ($N_{B\bar{B}}$) 127
4.4.8 Systematic Uncertainty due to PDF Fitting Model 127
4.4.9 Systematic Uncertainty due to Fit Bias 129
4.4.10 Total Systematic Uncertainty 129
4.5 Chapter in Compact 130

5 Search for Resonant structures in $B^0 \to X(3872)K^+\pi^-$ 131
5.1 Search for Resonances in ($K\pi$) System 131
5.2 ($K\pi$) Components and its Background Subtracted Binned Fit Study . 132
5.2.1 Branching Fractions and Ratio of Branching Fractions 133
5.2.2 Signal MC Study - Efficiency Estimation and PDF Modeling . 134
5.2.3 J/ψ Inclusive MC Study 136
5.2.4 Fit Validation 138
5.2.5 Extraction of Signal Yield from Experimental Data and Results 140
5.3 Systematic Uncertainty Study 143
5.3.1 Systematic Uncertainty due to Efficiency 143
5.3.2 Systematic Uncertainty due to PDF Modeling 143
5.3.3 Systematic Uncertainty due to Fit Bias 145
5.3.4 Total Systematic Uncertainty 146
5.4 Search for Resonances in $X(3872)K$ and $X(3872)\pi$ Systems 146
5.5 Chapter in Compact 148

6 Search for $X(3872)$ in 3-body B^+ decay 149
6.1 Search for $B^+ \to X(3872)K^0_S\pi^+$ Decay Mode 149

6.2 Event Reconstruction Procedure 149
6.3 Branching Fractions 150
6.3.1 Efficiency Estimation from Signal MC Study and PDF Parametrization 151
6.3.2 Background Study 156
6.3.3 Branching Fractions Estimation for J/ψ Inclusive MC Sample 158
6.3.4 Fit Validation 161
6.3.5 Extraction of Signal Yield from Experimental Data and Results 163
6.3.6 Significance of Signal Yield for $B^+ \to X(3872)K_S^0\pi^+$ Decay Mode 167
6.4 Systematic Uncertainty Study 167
6.4.1 Systematic Uncertainty due to K_S^0 Reconstruction 168
6.4.2 Systematic Uncertainty due to PDF Modeling 168
6.4.3 Total Systematic Uncertainty 170
6.5 Search for $B^+ \to X(3872)K^+\pi^0$ Decay Mode 170
6.6 Event Reconstruction Procedure 171
6.6.1 Efficiency Estimation from Signal MC Study and PDF Parametrization 171
6.6.2 Background Study 173
6.6.3 Extraction of Signal Yield from Experimental Data and Results 177
6.7 Chapter in Compact 180

7 Summary of Results and Conclusions 181

7.1 Search for $B^0 \to X(3872)K^+\pi^-$ and $B^+ \to X(3872)K_S^0\pi^+$ Decay Modes 182
7.2 Preliminary Study of $B^+ \to X(3872)K^+\pi^0$ Decay Mode 184
7.3 Results for $B^0 \to X(3872)K^+\pi^-$, $B^+ \to X(3872)K_S^0\pi^+$ and $B^+ \to X(3872)K^+\pi^0$ Decay Modes 185
7.4 Search for Resonances/New Particles in Background Subtracted Mass Distributions 185
7.5 Results from Resonance Study 189
7.6 Discussions and Future Scenario 191

A Weighted Efficiency **193**

B Significance (Including Systematic) **195**

List of Figures

1.1 Charmonium production diagrams at e^+e^- colliders. (a) e^+e^- annihilation, (b) B-meson decay, (c) Photon-photon fusion, (d) Initial state radiation, (e) Double charmonium production. 12

1.2 Annihilation of $c\bar{c}$. 14

1.3 Strong decay of charmonium states. 15

1.4 Radiative decay of charmonium states. 16

1.5 Weak decay of charmonium states. 16

1.6 Charmonium spectrum for known, predicted and experimentally established charmonium and charmonium-like states. 17

1.7 Observation of $X(3872)$, in left plot with experimental data (peak around 0.78 GeV/c^2) as compared to right plot in Monte Carlo. . . . 21

1.8 Mass measurements of the X(3872) state. Vertical band shows uncertainty in world average value (3871.69±0.17 MeV/c^2). 25

1.9 Tree diagram for $B \to \psi' K^*$ decay mode. 26

1.10 Tree diagram for $B \to \psi' K\pi$ decay mode. 26

1.11 Penguin diagram for $B \to \psi' K^*$ decay mode. 27

2.1 Total e^+e^- annihilation cross-section measured by CLEO. The energy regions (a) $\Upsilon(1S)$ through $\Upsilon(4S)$ (b) $\Upsilon(4S)$ through $\Upsilon(6S)$ are shown. Widths of $\Upsilon(1S)$, $\Upsilon(2S)$ and $\Upsilon(3S)$ are dominated by the beam energy resolution. A small bump between $\Upsilon(4S)$ and $\Upsilon(5S)$ is not clarified. . 31

2.2 Configuration of the KEKB accelerator. 35

2.3 Side-view (top) and over-view (bottom) of Belle detector with the major components indicated. 36

2.4 Cross-section of the beryllium beam pipe at the interaction point. . . 39

2.5 Detector configuration of first version of silicon vertex detector (SVDI) shown in a cross-section (left) and in a side-view (right). 41

2.6 Impact parameter resolution of the SVDI. 42

2.7 Detector configuration of the second version of silicon vertex detector (SVDII) shown in a cross-section. 42

2.8 Side-view of SVDII. 43

2.9 Structure of the CDC. Lengths in figure are in the unit of mm. 45

2.10 CDC Cell structure. Cathode sector configuration is also shown in the right figure. 46

2.11 Spatial resolution as a function of the drift distance. 47

2.12 p_t dependence on p_t resolution for cosmic rays. The solid curve shows the fitted result $((0.201\pm 0.003)p_t\oplus(0.290\pm 0.006)/\beta)\%$ and the dotted curve shows the ideal expectation for $\beta = 1$ particles. 47

2.13 Scatter plot for momentum vs dE/dx taken during accelerator operations. Expected relation for π, K, p and e are shown by the solid curves. The momenta are given in units of GeV/c. 48

2.14 Transverse view of the ACC. Here n indicates the refractive index. . . 50

2.15 Schematic drawing of typical ACC module. (a) barrel and (b) endcap modules. 51

2.16 Pulse height spectrum for electrons and kaons in units of photoelectrons (p.e.) observed by the barrel ACC. Kaon candidates are obtained by dE/dx and TOF measurements. The MC expectation are superimposed. 52

2.17 Configuration of a TOF module made of two TOF counters and one TSC. 54

2.18 Scheme for the time stretcher for the TOF. 54

2.19 Mass distribution from TOF measurements for particles with momentum below 1.2 GeV/c. Points and histogram show the data and MC distributions respectively. 55

2.20 Configuration of the ECL. 58

2.21 Two photon invariant mass distribution for hadronic events: (a) $\pi^0 \to \gamma\gamma$, (b) $\eta \to \gamma\gamma$, where each of photon energy was required to be above 30 MeV in the barrel region. 59

2.22 (a) E/p and (b) E_9/E_{25} distributions for electrons (solid) and charged pions (dashed). In (a), particle momenta limited to $0.5 < p < 3.0$ GeV/c. 60

2.23 Configuration of the superconducting magnetic coil. 61

2.24 KLM detector plate diagram for a) Barrel RPC and b) Endcap RPC. 61

2.25 Cross-section of a KLM superlayer. 62

2.26 Configuration of the EFC. 63

2.27 Overview of the Level-1 trigger system for the Belle detector. 66

2.28 Overview of the Belle DAQ system. 68

3.1 dr and dz of the tracks (plots are normalized to unity), with arrows showing cuts used in the analyses. 80

3.2 $R_{\pi/K}$ distribution (plots are normalized to unity), with arrows showing cuts used in the analyses. The peak at 0.5 is caused by tracks for which no particle ID information is available, such as tracks reconstructed only in the SVD. 81

3.3 Reconstructed mass of J/ψ from e^+e^- and $\mu^+\mu^-$ decay modes (plots are normalized to unity), with arrows showing cuts used in the analyses. 82

3.4 Reconstructed mass of $\pi^+\pi^-$ being identified as K^0_S (plots are normalized to unity), with arrows showing cuts used in the analyses. 83

3.5 Reconstructed masses of ψ' and $X(3872)$ (plots are normalized to unity). Arrows shows cuts used in these analyses. 85

3.6 Schematic of the hierarchical reconstruction, starting from the lightest particles. Available particles are consecutively combined until a B-meson is reached. 86

3.7 Flowchart of the full event selection and reconstruction. 91

3.8 Flowchart for analysis procedure. 92

3.9 MC illustration of ΔE against $M_{J/\psi\pi^+\pi^-}$ distribution for signal events. 93

4.1 Correctly reconstructed (CR) and self cross feed (SCF) events plots for signal MC simulated samples in ΔE and $M_{J/\psi\pi\pi}$ dimensions (middle plots are zoomed plots for ΔE dimension) for $B^0 \to \psi' K^+\pi^-$ decay mode. Top plots are of $B^0 \to \psi' K^*(892)^0$ decay mode, middle ones are of $B^0 \to \psi'(K^+\pi^-)_{NR}$ and bottom plots are of $B^0 \to \psi' {K_2}^*(1430)^0$ decay mode. 102

4.2 Correctly reconstructed (CR) and self cross feed (SCF) events plots for signal MC simulated samples in ΔE and $M_{J/\psi\pi\pi}$ dimensions (middle plots are zoomed plots for ΔE dimension) for $B^0 \to X(3872)K^+\pi^-$ decay mode. Top plots are for $B^0 \to X(3872)(K^+\pi^-)_{NR}$ decay mode and bottom plots are for $B^0 \to X(3872)K^*(892)^0$ decay mode. 103

4.3 2D extended UML fit to signal MC simulated samples for ΔE (left) and $M_{J/\psi\pi\pi}$ (right) dimensions for $B^0 \to \psi' K^*(892)^0$ (top), $B^0 \to \psi'(K^+\pi^-)_{NR}$ (middle) and $B^0 \to \psi' {K_2}^*(1430)^0$ (bottom) decay modes. The curves show the signal [red dotted] and the background components [black dotted for the component peaking in $M_{J/\psi\pi\pi}$ but non-peaking in ΔE, green dotted for the one peaking in ΔE but non-peaking in $M_{J/\psi\pi\pi}$, and magenta dotted for combinatorial background in both dimensions] as well as the overall fit [blue solid]. 105

4.4 2D extended UML fit to signal MC simulated samples for ΔE (left) and $M_{J/\psi\pi\pi}$ (right) dimensions for $B^0 \to X(3872)(K^+\pi^-)_{NR}$ (top) and $B^0 \to X(3872)K^*(892)^0$ (bottom) decay modes. The curves show the signal [red dotted] and the background components [black dotted for the component peaking in $M_{J/\psi\pi\pi}$ but non-peaking in ΔE, green dotted for the one peaking in ΔE but non-peaking in $M_{J/\psi\pi\pi}$, and magenta dotted for combinatorial background in both dimensions] as well as the overall fit [blue solid]. 106

4.5 J/ψ mass sidebands for $B^0 \to \psi' K^+\pi^-$ decay mode. 109

4.6 J/ψ mass sidebands for $B^0 \to X(3872)K^+\pi^-$ decay mode. 109

4.7 Background estimation for $B^0 \to \psi' K^+\pi^-$ decay mode using J/ψ inclusive MC ($\sim$ 100$\times$ experimental data) for ΔE (left) and $M_{J/\psi\pi\pi}$ (right) dimensions. 110

4.8 Background estimation for $B^0 \to X(3872)K^+\pi^-$ decay mode using J/ψ inclusive MC ($\sim$ 100$\times$ experimental data) for ΔE (left) and $M_{J/\psi\pi\pi}$ (right) dimensions. 111

4.9 Comparison of experimental data and J/ψ inclusive MC sample before (left) and after (right) removing $B \to \psi' X_{sd}$ decay mode for ψ' mass region. 112

4.10 Signal region projections for only signal $B^0 \to \psi' K^*(892)^0$ from J/ψ inclusive MC sample (top) and whole J/ψ inclusive MC ($\sim 100\times$ experimental data) sample (bottom). Left plot is the projection for $M_{J/\psi\pi\pi}$ signal region $[3.675, 3.695]$ GeV/c^2 and right plot is the projection for ΔE signal region $[-11, 8]$ MeV. The curves show the signal [red dotted] and the background components [black dotted for the component peaking in $M_{J/\psi\pi\pi}$ but non-peaking in ΔE, green dotted for the one peaking in ΔE but non-peaking in $M_{J/\psi\pi\pi}$, and magenta dotted for combinatorial background in both dimensions] as well as the overall fit [blue solid]. 114

4.11 Signal region projections for whole J/ψ inclusive MC ($\sim 100\times$ experimental data) sample. Left plot is the projection for $M_{J/\psi\pi\pi}$ signal region $[3.860, 3.881]$ GeV/c^2 and right plot is the projection for ΔE signal region $[-11, 8]$ MeV. The curves show the signal [red dotted] and the background components [green dotted for the one peaking in ΔE but non-peaking in $M_{J/\psi\pi\pi}$, and magenta dotted for combinatorial background] as well as the overall fit [blue solid]. 116

4.12 Pull distribution (left), return yield distribution (middle) and error distribution (right) for 1000 toy MC study for $B^0 \to \psi' K^+\pi^-$ decay mode. 117

4.13 Pull distribution (left), return yield distribution (middle) and error distribution (right) for 1000 toy MC study for $B^0 \to X(3872)K^+\pi^-$ decay mode. 117

4.14 Pull distribution (left), return yield distribution (middle) and error distribution (right) for GSIM study for $B^0 \to \psi' K^+\pi^-$ decay mode. . 118

4.15 Pull distribution (left), return yield distribution (middle) and error distribution (right) for GSIM study for $B^0 \to X(3872)K^+\pi^-$ decay mode. 118

4.16 Top: Signal region projections of experimental data for $B^0 \to \psi' K^+\pi^-$ decay mode. Left (right) plot is the projection for $M_{J/\psi\pi\pi}$ (ΔE) signal region. Bottom: Projection plots in background enhanced regions of ΔE and $M_{J/\psi\pi\pi}$. Left (right) is for $M_{J/\psi\pi\pi}$ (ΔE) sidebands in ψ' mass region. The curves show the signal [red dotted] and the background components [black dotted for the component peaking in $M_{J/\psi\pi\pi}$ but non-peaking in ΔE, green dotted for the one peaking in ΔE but non-peaking in $M_{J/\psi\pi\pi}$, and magenta dotted for combinatorial background] as well as the overall fit [blue solid]. 120

4.17 Top: Signal region projections of experimental data for $B^0 \to X(3872)K^+\pi^-$ decay mode. Left (right) plot is the projection for $M_{J/\psi\pi\pi}$ (ΔE) signal region. Bottom: Projection plots in background enhanced regions of ΔE and $M_{J/\psi\pi\pi}$. Left (right) is for $M_{J/\psi\pi\pi}$ (ΔE) sidebands in $X(3872)$ mass region. The curves show the signal [red dotted] and the background components [black dotted for the component peaking in $M_{J/\psi\pi\pi}$ but non-peaking in ΔE, green dotted for the one peaking in ΔE but non-peaking in $M_{J/\psi\pi\pi}$, and magenta dotted for combinatorial background] as well as the overall fit [blue solid]. 121

4.18 Scan of $-2\ln(\mathcal{L}_0/\mathcal{L}_{\max})$ for whole range of yields for decay mode $B^0 \to X(3872)K^+\pi^-$ with blue curve (before systematic uncertainty) and red curve (after including systematic uncertainties which affects only signal yield). 123

5.1 Background subtracted distribution of $M_{K\pi}$. 132

5.2 Background subtracted signal MC yield for $B^0 \to \psi' K^*(892)^0$ (left), $B^0 \to \psi'(K^+\pi^-)_{NR}$ (middle) and $B^0 \to \psi' {K_2}^*(1430)^0$ (right) decay modes obtained from 2D extended UML fitting of ΔE and $M_{J/\psi\pi\pi}$ variables in each bin of $M_{K\pi}$. 135

5.3 Background subtracted signal MC yield for $B^0 \to X(3872)(K^+\pi^-)_{NR}$ (left) and $B^0 \to X(3872)K^*(892)^0$ (right) decay modes obtained from 2D extended UML fitting of ΔE and $M_{J/\psi\pi\pi}$ variables in each bin of $M_{K\pi}$. 135

5.4 Pull distribution (left), return yield distribution (middle) and error distribution (right) for $B^0 \to \psi' K^*(892)^0$ decay mode after dividing whole J/ψ inclusive MC into 100 pseudo-experiments after embedding all signals. 137

5.5 Pull distribution (left), return yield distribution (middle) and error distribution (right) for $B^0 \to X(3872)K^*(892)^0$ decay mode after dividing whole J/ψ inclusive MC into 100 pseudo-experiments after embedding all signals. 137

5.6 Pull distribution (left), return yield distribution (middle) and error distribution (right) for 1000 toy MC study for $B^0 \to \psi' K^*(892)^0$ decay mode. 138

5.7 Pull distribution (left), return yield distribution (middle) and error distribution (right) for 1000 toy MC study for $B^0 \to X(3872)K^*(892)^0$ decay mode. 139

5.8 Binned minimum χ^2 fitting of signal yield and custom errors in 51 MeV wide $M_{K\pi}$ bins for experimental data for ψ' mass region. Red curve represents $B^0 \to \psi' K^*(892)^0$, green curve is for $B^0 \to \psi'(K^+\pi^-)_{NR}$, magenta one is for $B^0 \to \psi' K_2^*(1430)^0$ and blue solid for overall fit. . 141

5.9 Binned minimum χ^2 fitting of signal yield and custom errors in 100 MeV wide $M_{K\pi}$ bins for experimental data for $X(3872)$ mass region. Red curve represents $B^0 \to X(3872)K^*(892)^0$, green curve is for $B^0 \to X(3872)(K^+\pi^-)_{NR}$ and blue solid for overall fit. 142

5.10 Background subtracted distributions of $M_{X(3872)K}$ (top), $M_{X(3872)\pi}$ (bottom). Left plots are for $M_{K\pi}$ in range [0.85, 0.95] and right plots are for ($M_{K\pi}$ <0.85 and $M_{K\pi}$ >0.95). All masses are in GeV/c^2. 147

6.1 Correctly reconstructed (CR) and self cross feed (SCF) events plots for signal MC sample in ΔE and $M_{J/\psi\pi\pi}$ (middle plots are zoomed plots for ΔE dimension) for $B^+ \to \psi' K^0_S\pi^+$ decay mode. Top plots are of $B^+ \to \psi' K^*(892)^+$ decay mode, middle one are of $B^+ \to \psi'(K^0_S\pi^+)_{NR}$ and bottom plots are of $B^+ \to \psi' {K_2}^*(1430)^+$ decay mode. 152

6.2 Correctly reconstructed (CR) and self cross feed (SCF) events plots for signal MC sample in ΔE and $M_{J/\psi\pi\pi}$ (middle plots are zoomed plots for ΔE dimension) for $B^+ \to X(3872)K^0_S\pi^+$ decay mode. Top plots are of $B^+ \to X(3872)(K^0_S\pi^+)_{NR}$ decay mode and bottom plots are of $B^+ \to X(3872)K^*(892)^+$ decay mode. 153

6.3 2D extended UML fit to signal MC events for $B^+ \to \psi' K^*(892)^+$ (top), $B^+ \to \psi'(K^0_S\pi^+)_{NR}$ (middle), $B^+ \to \psi' K^*_2(1430)^+$ (bottom) decay mode. Red dotted curve represents signal in both dimensions, green curve shows peaking background in the ΔE dimension and flat in $M_{J/\psi\pi\pi}$ distribution and vice-versa for black curve, while magenta curve shows combinatorial background in both dimensions with blue solid for overall fit. 154

6.4 2D extended UML fit to signal MC events for ΔE (left) and $M_{J/\psi\pi\pi}$ (right) dimensions for $B^+ \to X(3872)(K^0_S\pi^+)_{NR}$ (top) and $B^+ \to X(3872)K^*(892)^+$ (bottom) decay modes. Red curve represents signal in both dimensions. Green curve shows peaking background in the ΔE dimension and flat in $M_{J/\psi\pi\pi}$ distribution and vice-versa for black curve, while magenta curve shows combinatorial background in both dimensions with blue solid for overall fit. 155

6.5 Background estimation for $B^+ \to \psi' K^0_S\pi^+$ decay mode using J/ψ inclusive MC ($\sim 100\times$ experimental data) for ΔE (left) and $M_{J/\psi\pi\pi}$ (right) dimensions. 157

6.6 Background estimation for $B^+ \to X(3872)K^0_S\pi^+$ decay mode using J/ψ inclusive MC ($\sim 100\times$ experimental data) for ΔE (left) and $M_{J/\psi\pi\pi}$ (right) dimensions. 157

6.7 Signal region projections for only signal $B^+ \to \psi' K^*(892)^+$ from J/ψ inclusive MC sample (top) and whole J/ψ inclusive MC ($\sim 100\times$ experimental data) sample (bottom). Left plot is the projection for $M_{J/\psi\pi\pi}$ signal region $[3.675, 3.695]$ GeV/c^2 and right plot is the projection for ΔE signal region $[-11, 8]$ MeV. Red color represents signal in both dimensions, black color represents peaking background in $M_{J/\psi\pi\pi}$ dimension which is flat in ΔE dimension, green color represent peaking background in ΔE which is flat in $M_{J/\psi\pi\pi}$, magenta color represent combinatorial backgrounds in both dimensions with blue solid for overall fit. 159

6.8 Signal region projections for whole J/ψ inclusive MC ($\sim 100\times$ experimental data) sample. Left plot is the projection for $M_{J/\psi\pi\pi}$ signal region $[3.859, 3.882]$ GeV/c^2 and right plot is the projection for ΔE signal region $[-11, 9]$ MeV. Red color represents signal in both dimensions, green color represents peaking background in ΔE which is flat in $M_{J/\psi\pi\pi}$, magenta color represents combinatorial backgrounds in both dimensions with blue solid for overall fit. 160

6.9 Pull distribution (left), return yield distribution (middle) and error distribution (right) for 1000 toy MC study for $B^+ \to \psi' K^0_S \pi^+$ decay mode. 161

6.10 Pull distribution (left), return yield distribution (middle) and error distribution (right) for 1000 toy MC study for $B^+ \to X(3872) K^0_S \pi^+$ decay mode. 162

6.11 Pull distribution (left), return yield distribution (middle) and error distribution (right) for GSIM study for $B^+ \to \psi' K^0_S \pi^+$ decay mode. . 163

6.12 Pull distribution (left), return yield distribution (middle) and error distribution (right) for GSIM study for $B^+ \to X(3872) K^0_S \pi^+$ decay mode. 163

6.13 Top: Signal region projections of experimental data for $B^+ \to \psi' K^0_S \pi^+$ decay mode. Left (right) plot is the projection for $M_{J/\psi\pi\pi}$ (ΔE) signal region. Bottom: Projection plots in background enhanced regions of ΔE and $M_{J/\psi\pi\pi}$. Left (right) is for $M_{J/\psi\pi\pi}$ (ΔE) sidebands in ψ' mass region. Red color represents signal in both dimensions, black color represent peaking background in $M_{J/\psi\pi\pi}$ dimension which is flat in ΔE dimension, green color represent peaking background in ΔE which is flat in $M_{J/\psi\pi\pi}$, magenta color represent combinatorial backgrounds in both dimensions with blue solid for overall fit. 164

6.14 Top: Signal region projections of experimental data for $B^+ \to X(3872) K^0_S \pi^+$ decay mode. Left (right) plot is the projection for $M_{J/\psi\pi\pi}$ (ΔE) signal region. Bottom: Projection plots in background enhanced regions of ΔE and $M_{J/\psi\pi\pi}$. Left (right) is for $M_{J/\psi\pi\pi}$ (ΔE) sidebands in $X(3872)$ mass region. Red color represents signal in both dimensions, black color represent peaking background in $M_{J/\psi\pi\pi}$ dimension which is flat in ΔE dimension, green color represent peaking background in ΔE which is flat in $M_{J/\psi\pi\pi}$, magenta color represents combinatorial backgrounds in both dimensions with blue solid for overall fit. 166

6.15 Scan of $-2\ln(\mathcal{L}_0/\mathcal{L}_{\max})$ for whole range of yields for decay mode $B^+ \to X(3872)K^0_S\pi^+$ with blue curve (before systematic uncertainty) and red curve (after including those systematic uncertainties which affects only signal yield). 168

6.16 Correctly reconstructed (CR) and self cross feed (SCF) signal events plots for signal MC sample in ΔE and $M_{J/\psi\pi\pi}$ (middle plots are zoomed plots for ΔE dimension) for $B^+ \to \psi' K^+\pi^0$ decay mode. Top plots are for $B^+ \to \psi' K^*(892)^+$ decay mode, middle one are for $B^+ \to \psi'(K^+\pi^0)_{NR}$ and bottom plots are for $B^+ \to \psi' {K_2}^*(1430)^+$ decay mode. 172

6.17 Correctly reconstructed (CR) and self cross feed (SCF) signal events plots for signal MC sample in ΔE and $M_{J/\psi\pi\pi}$ (middle plots are zoomed plots for ΔE dimension) for $B^+ \to X(3872)K^+\pi^0$ decay mode. Top plots are for $B^+ \to X(3872)(K^+\pi^0)_{NR}$ decay mode and bottom plots are for $B^+ \to X(3872)K^*(892)^+$ decay mode. 173

6.18 2D extended UML fit to signal MC events for $B^+ \to \psi' K^*(892)^+$ (top), $B^+ \to \psi'(K^+\pi^0)_{NR}$ (middle), $B^+ \to \psi' K_2^*(1430)^+$ (bottom) decay mode, where signal is plotted with red dotted curve, black curve shows peaking SCF in $M_{J/\psi\pi\pi}$ dimension (flat in ΔE) and vice-versa for green curve, while magenta curve shows combinatorial background in both dimensions and blue solid for total fit. 174

6.19 2D extended UML fit to signal MC events for $B^+ \to X(3872)(K^+\pi^0)_{NR}$ (top), $B^+ \to X(3872)K^*(892)^+$ (bottom) decay mode, where signal is plotted with red dotted curve, black curve shows peaking SCF in $M_{J/\psi\pi\pi}$ dimension (flat in ΔE) and vice-versa for green curve, while magenta curve shows combinatorial background in both dimensions and blue solid for total fit. 175

6.20 Background estimation for $B^+ \to \psi' K^+\pi^0$ decay mode using J/ψ inclusive MC ($\sim 100\times$ experimental data) for ΔE (left) and $M_{J/\psi\pi\pi}$ (right) dimensions. 176

6.21 Background estimation for $B^+ \to X(3872)K^+\pi^0$ decay mode using J/ψ inclusive MC ($\sim$ 100$\times$ experimental data) for ΔE (left) and $M_{J/\psi\pi\pi}$ (right) dimensions. 177

6.22 Top: Signal region projections of experimental data for $B^+ \to \psi' K^+\pi^0$ decay mode. Left plot is the projection for $M_{J/\psi\pi\pi}$ signal region and right plot is the projection for ΔE signal region. Bottom: Projection plots in background enhanced regions of ΔE and $M_{J/\psi\pi\pi}$. Left (right) is for $M_{J/\psi\pi\pi}$ (ΔE) sidebands in ψ' mass region. Red color represents signal in both dimensions, black color represent peaking background in $M_{J/\psi\pi\pi}$ dimension which is flat in ΔE dimension, green color represent peaking background in ΔE which is flat in $M_{J/\psi\pi\pi}$, magenta color represents combinatorial backgrounds in both dimensions and blue solid for total fit. 178

6.23 Top: Signal region projections of experimental data for $B^+ \to X(3872)K^+\pi^0$ decay mode. Left plot is the projection for $M_{J/\psi\pi\pi}$ signal region and right plot is the projection for ΔE signal region. Bottom: Projection plots in background enhanced regions of ΔE and $M_{J/\psi\pi\pi}$. Left (right) is for $M_{J/\psi\pi\pi}$ (ΔE) sidebands in ψ' mass region. Red color represents signal in both dimensions, black color represent peaking background in $M_{J/\psi\pi\pi}$ dimension which is flat in ΔE dimension, green color represent peaking background in ΔE which is flat in $M_{J/\psi\pi\pi}$, magenta color represents combinatorial backgrounds in both dimensions and blue solid for total fit. 179

6.24 Relationship between input value of signal for Toy MC yield and confidence level for $B^+ \to X(3872)K^+\pi^0$ decay mode. 180

List of Tables

1.1 Properties of Quarks in the SM [1]. 3
1.2 Properties of Leptons in the SM [1]. 3
1.3 Properties of SM interactions and forces mediating bosons. 5
1.4 Charmonium states near the mass of $X(3872)$. The masses of predicted but unobserved states have no errors assigned. 22

2.1 B-factories in the world. 30
2.2 Masses and widths of Υ mesons. 32
2.3 Design parameters of KEKB accelerator. 34
2.4 Accumulated data set at Belle. 35
2.5 Summary of the parameters of the Belle detector. The performance is based on the measurement at a beam-test or a physics run. 38
2.6 Geometrical parameters of ECL. 57
2.7 Total cross-section and trigger rates with $L = 10^{34}\mathrm{cm}^{-2}\mathrm{s}^{-1}$ from various physics processes at $\Upsilon(4S)$. $*$: values prescaled by a factor 1/100. †: restricted condition of $P_t \geq 0.3$ GeV/c. 65
2.8 Sub-detectors which detect different particles. 69

3.1 EvtGen Models used for different signal MC samples. 76
3.2 The "`goodKs`" cuts of four variables depending upon momentum of K^0_S. 84
3.3 Multiple B-meson candidates for each decay mode. 87
3.4 Efficiencies of different BCS for the $B^0 \to \psi' K^*(892)^0 (\to K^+\pi^-)$, $B^0 \to \psi'(K^+\pi^-)_{NR}$ and $B^0 \to \psi' K^*_2(1430)^0 (\to K^+\pi^-)$ decay modes for $|\Delta E| < 0.1$ GeV. 88
3.5 Efficiencies of different BCS for the $B^0 \to X(3872) K^*(892)^0 (\to K^+\pi^-)$ and $B^0 \to X(3872)(K^+\pi^-)_{NR}$ decay modes for $|\Delta E| < 0.1$ GeV. . . . 89
3.6 Efficiencies of different BCS for the $B^+ \to \psi' K^*(892)^+ (\to K^0_S\pi^+)$, $B^+ \to \psi'(K^0_S\pi^+)_{NR}$ and $B^+ \to \psi' K^*_2(1430)^+ (\to K^0_S\pi^+)$ decay modes for $|\Delta E| < 0.1$ GeV. 89

3.7 Efficiencies of different BCS for the $B^+ \to X(3872)K^*(892)^+(\to K^0_S\pi^+)$ and $B^+ \to X(3872)(K^0_S\pi^+)_{NR}$ decay modes for $|\Delta E| < 0.1$ GeV. . . . 90

3.8 Various sources of systematic uncertainties. 95

4.1 Reconstruction efficiencies for different signal MC samples estimated from 2D extended unbinned maximum likelihood fit study. 107

4.2 Reconstruction efficiencies for different signal MC samples before and after Particle identification (PID) correction. 108

4.3 Fixed parameters (in GeV) for J/ψ inclusive MC and experimental data from signal MC sample of $B^0 \to \psi' K^*(892)^0$ for calibration sample. 113

4.4 $\mathcal{B}(B^0 \to \psi' K^*(892)^0)$ estimated from fit to the J/ψ inclusive MC with signal only and with signal + backgrounds. 115

4.5 Fixed parameters (in GeV) for J/ψ inclusive MC from signal MC simulated sample of $B^0 \to X(3872)(K^+\pi^-)_{NR}$ for concerned decay mode. 115

4.6 Fixed parameters (in GeV) for experimental data found using fudge factor. 122

4.7 Kaon identification systematic uncertainty for different modes under study. 124

4.8 Pion identification systematic uncertainty for different modes under study. 125

4.9 Lepton identification systematic uncertainty for different modes under study. 125

4.10 Systematic uncertainty due to limited statistics of the MC samples used for 2D fit study and having limited knowledge of actual model to generate signal MC simulated events. 126

4.11 Secondary branching fraction systematic uncertainty. 126

4.12 Estimation of systematic uncertainty for 2D fit (PDF modeling) as shown in Figure 4.16. Nominal value of the signal yield for $B^0 \to \psi' K^+\pi^-$ decay mode is 2599. 127

4.13 Estimation of systematic uncertainty for 2D fit (PDF modeling) as shown in Figure 4.17. Nominal value of the signal yield for $B^0 \to X(3872)K^+\pi^-$ decay mode is 116.48. 128

4.14 Systematic uncertainty due to the fit bias for 2D extended UML fit study. 129

4.15 The summary of systematic uncertainties used for 2D extended UML fit study. 129

5.1 Reconstruction efficiencies for $B^0 \to \psi' K^*(892)^0$ and $B^0 \to X(3872)K^*(892)^0$ decay modes before and after PID correction used for background subtracted binned fit study. 136

5.2 Systematic uncertainty due to the statistics of the MC samples. . . . 143

5.3 Estimation of systematic uncertainty from fit shown in Figure 5.8. Nominal value of the signal yield for $B^0 \to \psi' K^*(892)$ decay mode is 1708. 144

5.4 Estimation of systematic uncertainty from fit shown in Figure 5.9. Nominal value of the signal yield for $B^0 \to X(3872)K^*(892)^0$ decay mode is 37.58. 145

5.5 Systematic uncertainty due to the fit bias for background subtracted binned fit study. 146

5.6 Summary of systematic uncertainties used for background subtracted binned fit study. 146

6.1 Reconstruction efficiencies for different signal MC samples before and after Particle identification (PID) correction estimated from 2D extended UML fit study. 156

6.2 Fixed parameters (in GeV) for J/ψ inclusive MC and for experimental data from signal MC sample of $B^+ \to \psi' K^*(892)^+$ for ψ' mass region. 158

6.3 Fixed parameters (in GeV) for J/ψ inclusive MC from signal MC sample $B^+ \to X(3872)(K^0_S\pi^+)_{NR}$ for $X(3872)$ mass region. 160

6.4 Fixed parameters (in GeV) for experimental data found using fudge factor for $X(3872)$ mass region. 167

6.5 Estimation of systematic uncertainty from 2D extended UML fit shown in Figure 6.13. Nominal value of the signal yield for $B^+ \to \psi' K^0_S \pi^+$ decay mode is 629. 169

6.6 Estimation of systematic uncertainty from 2D extended UML fit from fit shown in Figure 6.14. Nominal value of the signal yield for $B^+ \to X(3872) K^0_S \pi^+$ decay mode is 34.85. 169

6.7 The Summary of systematic uncertainty used for 2D extended UML fit study. 170

6.8 Reconstruction efficiencies of different signal MC samples estimated from 2D extended UML fit study. 176

7.1 Signal yield (Y) from the fit, weighted efficiency (ϵ) after PID correction and measured branching fractions for $B^0 \to \psi' K^+ \pi^-$, $B^+ \to \psi' K^0_S \pi^+$ and $B^+ \to \psi' K^+ \pi^0$ decay modes. The first (second) uncertainty represents a statistical (systematic) contribution. 186

7.2 Signal yield (Y) from the fit, weighted efficiency (ϵ) after PID correction, significance (Σ) and measured branching fractions for $B^0 \to X(3872) K^+ \pi^-$, $B^+ \to X(3872) K^0_S \pi^+$ and $B^+ \to X(3872) K^+ \pi^0$ decay modes. The first (second) uncertainty represents a statistical (systematic) contribution. 186

7.3 Ratio of Branching fractions and its estimated value. The first (second) uncertainty represents a statistical (systematic) contribution. 190

7.4 Signal yield (Y) from the fit, efficiency (ϵ) after PID correction, significance (Σ) and measured branching fractions for $B^0 \to \psi' K^*(892)^0$ and $B^0 \to X(3872) K^*(892)^0$ decay modes. The first (second) uncertainty represents a statistical (systematic) contribution. 190

1

Introduction: Phenomenological and Experimental Review of $X(3872)$

Escalation in the number of fundamental particles during 1940's provided a strong challenge to the intellectual minds to create a model which can categorize these observed states, explain their properties along with the prediction of new states. Fermi and Yang, in 1949, thought of describing all the resonances as proton-neutron bound states, and Sakata extended this model to include newly discovered *strange* quark in 1956. Later on Gell-Mann and Zweig independently develop what we know today as the "Constituent Quark Model (CQM)". CQM remains a valid effective theory for classifying hadrons (Mesons $[q\bar{q}]$ and Baryons $[qqq]$), even after the introduction of heavy quarks (c, b, t). However, recently discovered states seem not to fit into the conventional mesons and baryons model: in particular, their internal structure seems to be different from conventional $[q\bar{q}]$ and $[qqq]$. From first principle tetraquark, pentaquark, mesonic molecules, hybrid states and glueballs are also allowed because Quantum Chromodynamics (QCD) is non-abelian in nature. Since none of these states have been observed for a long time after the theories were first published (around mid-1960s), it was chosen to label every non-basic state (except $[q\bar{q}]$ and $[qqq]$) as *"exotic"* state. Great excitement in hadron spectroscopy has come from the recent discovery of a whole host of unexpected states by the meson factories (specifically B-

factories), Belle and BaBar. These new states are called "charmonium-like states", not because they naturally fit into the spectrum of charmonium states, but because they seem to always decay into final states containing a charm quark and an anticharm quark.

The $X(3872)$, is such charmonium-like "exotic" state, was discovered by the Belle experiment (KEK, Japan) in 2003. It has attracted much theoretical and experimental interest because its properties don't match any expected state of charmonium spectroscopy and is a strong candidate for exotic states, which further opened the possibilities to more "exotic" interpretations. In this Chapter, we will first briefly review the concepts of the Standard Model (SM) and the Quark Model, with particular emphasis on the $c\bar{c}$ meson. The proposed theoretical models and known experimental facts on the $X(3872)$ will also be given in detail.

1.1 Standard Model

The Standard Model of particle physics is a Quantum Field Theory (QFT) describing the fundamental interactions between elementary particles. These basic interactions are Electromagnetic interaction, Weak interaction and Strong interaction. Gravitational force is not included in the SM. As it is insignificant at the level of particle physics, or at least at energies currently accessible in the laboratory.

The gauge symmetry group of the SM is $SU(3)_C \times SU(2)_L \times U(1)_Y$. $SU(3)_C$ is the symmetry group describing the strong (color) interactions, whereas $SU(2)_L \times U(1)_Y$ represents the symmetry group of the electro-weak sector describing the weak and electromagnetic interactions. The particle content of the model may be broadly classified in terms of two groups, namely the fundamental fermions (spin $\frac{1}{2}$) and the gauge vector bosons (spin 1). The fundamental fermions are in turn subdivided into two parallel classes of particles called quarks and leptons. There are three generations of quarks $\{1^{st}$ generation: [up (u), down (d)], 2^{nd} generation: [charm (c), strange (s)], 3^{rd} generation: [top (t) and bottom or beauty (b)]$\}$, with each type of quark exhibiting a further internal degree of freedom called color. A quark can take one of

the three colors (green, red, blue), while an antiquark takes an anticolor. The strongly interacting particles, actually observed in nature, are composites of the quarks and are collectively referred to as hadrons. Again, the hadrons are further classified as being either mesons or baryons. Table 1.1 list the known quarks as described by the SM. The leptons also come in three different families or generations and include: the electron, the muon, the tau and their corresponding neutrinos. Table 1.2 list the known leptons as described in the SM. The forces between above stated elementary particles are mediated by the gauge vector bosons. There are two basic theories which describe these interactions.

Table 1.1: Properties of Quarks in the SM [1].

Quark Flavor	Quark Charge	Quark Mass
Up	$+2/3$	$2.3^{+0.7}_{-0.5}$ (in MeV/c^2)
Down	$-1/3$	$4.8^{+0.5}_{-0.3}$ (in MeV/c^2)
Charm	$+2/3$	1275 ± 25 (in MeV/c^2)
Strange	$-1/3$	95 ± 5 (in MeV/c^2)
Top	$+2/3$	173.21 ± 0.87 (in GeV/c^2)
Bottom	$-1/3$	4.18 ± 0.03 (in GeV/c^2)

Table 1.2: Properties of Leptons in the SM [1].

Lepton	Charge	Lepton Mass (MeV/c^2) (central Value)
ν_e	0	$< 2.0 \times 10^{-6}$
e	-1	0.511
ν_μ	0	< 0.19
μ	-1	105.66
ν_τ	0	< 18.2
τ	-1	1776.82

1.1.1 Quantum Chromodynamics

Quantum chromodynamics is the theory of strong or nuclear interactions. This interaction is fundamental one, which describes the interactions between quarks and

gluons. The strong or nuclear interaction between quarks and gluons is described in terms of the gauge particles of $SU(3)_C$. These gauge vector bosons are $3^2 - 1 = 8$ in number and are called gluons. Gluons carry both a color and an anticolor. The $SU(3)_C$ symmetry of the color interaction is believed to be exact, so gluons are massless particles. However, the non-abelian nature of the color symmetry allows for these gluons to interact among themselves as well as mediate the strong nuclear force between the quarks. Theory of this sector is referred to as QCD [2]. Since no free quarks have ever been observed, it is postulated that only color-singlet states (the composite hadrons) can exist in nature. It is believed that QCD implies this requirement, known as color confinement. The color confinement principle requires hadrons to be colourless. The strength of the strong interaction is quantified in terms of the strong interaction coupling constant, α_s. Unlike the situation in Quantum Electrodynamics (QED), which is an abelian gauge field theory, an important consequence of the non-abelian nature of QCD is that α_s actually decreases with decreasing distance between strongly interacting partons (a generic term used to refer collectively to the quarks and gluons). This color anti-screening effect is called asymptotic freedom.

1.1.2 Electro-Weak Theory

The electro-weak sector of the SM is referred to as the Glashow-Weinberg-Salam (GWS) Model (in honor of the main architects of the theory) [3]. It is a gauge theory that unites the weak and electromagnetic interactions. The gauge symmetry group $SU(2)_L \times U(1)_Y$ requires $2^2 - 1 + (1^2) = 4$ massless gauge vector bosons. However, in order to describe weak interactions phenomenology, it is required that the vector bosons mediating this force acquire a non-zero mass. This is accomplished through the process of spontaneous symmetry breaking [4], which is implemented via the so-called Higgs mechanism [5]. The Higgs mechanism requires the introduction of scalar field. By allowing the scalar field to acquire a non-zero vacuum expectation value, 3 of the 4 gauge vector bosons acquire a mass and these are identified with the W^+, W^- (mediating charged-current weak interactions), and the Z^0 (mediating the neutral-current weak interactions). The remaining massless gauge vector boson is identified

with the photon, A (mediating the electromagnetic interactions). There remains one neutral scalar field which is called the Higgs Boson and recently observed by CMS [6,7] and ATLAS [8]. Table 1.3 presents a summary of the gauge vector bosons involved in the SM, known interactions of quarks and leptons.

Table 1.3: Properties of SM interactions and forces mediating bosons.

Interaction	Acts on	Particle	Gauge vector bosons with their masses (GeV/c^2)
Weak	Flavor	Quarks, Leptons	$W^{\pm}$: 80.385 ± 0.015, $Z : 91.1876 \pm 0.0021$
Electromagnetic	Electric charge	Charged particles	$\gamma : < 1.0 \times 10^{-27}$
Strong	Color charge	Quarks, Gluons	Gluons : 0

Although the SM successfully describes many aspects of high energy interactions, but still it is not complete. The model contains a large number (17) of free parameters. Further, the SM itself does not unite the strong interactions with the weak and electromagnetic in the same way that the Glashow-Weinberg-Salam model has united the weak and electromagnetic forces. There have been many attempts to unite all these forces to make Grand Unified Theory (GUT) [9]. In this sense, the SM is viewed as the low energy manifestation of the other fundamental theory which should take over at higher energies (i.e. shorter distances).

1.1.3 Discrete Symmetries

Symmetries play an important role in the SM. For each continuous symmetry, there is a corresponding conserved quantity. In the SM of particle physics, there are three related discrete symmetries.

Parity (P): Parity flips the sign of all spatial coordinates. In a three dimensional space, it is described as P(x, y, z) $\rightarrow$ (-x, -y, -z).

Charge Conjugation (C): This type of symmetry replaces each particle by its corresponding antiparticle.

Time Reversal (T): The time reversal operator leaves the spatial direction unchanged, but reverses the momentum and angular momentum. Time invariance implies that the physics does not change if the direction of time is made to run backwards instead of forward.

Among the above three discrete symmetries, charge conjugation has been known to be violated from the beginning because people found no left-handed anti-neutrinos, which are the charge conjugate partners for the left-handed neutrinos.

Parity conservation, on the contrary, was believed to be one of the fundamental conservation laws along with conservation of energy and momentum. This concept changed in 1957, when the study of beta decay of Cobalt-60 nuclei experiment, carried out by a group led by Chien-Shiung Wu, demonstrated conclusively that the parity symmetry is violated [10]. They found that when a specific nucleus was placed in a magnetic field, electrons from the beta decay were preferentially emitted in the direction opposite to that of the aligned angular momentum of the nucleus. Under the Parity transformation, however, it would look like the electrons prefer to be aligned with angular momentum, since the Parity transformation flips the direction of the electron but not that of the angular momentum. As a result, parity is not conserved.

Although charge conjugation and parity are violated separately, the symmetry of a quantum-mechanical system can still be restored if the combined symmetry CP remains unbroken. For example, a left handed neutrino, under the CP transformation will be turned into a right handed anti-neutrino, which exists. Therefore CP symmetry was proposed in 1957 by Lev Landau as the true symmetry between matter and antimatter.

Until 1964, it was thought that the combination CP was a valid symmetry of the universe. That year, Christenson, Cronin, Fitch, and Turlay observed the decay of the long-lived neutral K meson to pair of pions as well as three pions and thus concluding that CP symmetry is violated in the kaon system [11]. Now after B-factory data analysis, a large number of CP violation processes in B-meson system have been observed [1], which occurred by weak interactions.

Although C, P and CP are proven to be broken symmetries, the product CPT is firmly believed to be conserved till now. It is fundamental property of the Quantum Field Theory.

1.2 The Quark Model

Quarks are confined within composite particles called hadrons and bound by the strong interaction field. The quark model is a classification scheme for hadrons in terms of their valence quarks. Mainly there are two common types of hadrons: Baryons and Mesons.

1.2.1 Baryons

Baryons are composed of three quarks having unit baryon number. Their antiparticles are antibaryon having baryon number opposite to the previous one. Proton (p), neutron (n), lambda (Λ) etc. are examples of baryons.

1.2.2 Mesons

Mesons are composed of a quark-antiquark pair and thus have zero baryon number. Each meson has a corresponding antimeson, where quarks are replaced by their corresponding antiquarks and vice-versa. For example, the B^0 particle is a bottom meson, composed of a down quark (d) and a bottom antiquark ($\bar{b}$). Similarly, the B^+ meson is composed of an up quark (u) and a bottom antiquark ($\bar{b}$). The D^{*0} and the D^0 are charmed mesons both composed of a charm quark (c) and an up antiquark ($\bar{u}$). Other particles which appear in this thesis, such as kaons and pions, are also mesons and composed of the lighter quarks (u, d and s quarks).

1.2.3 Quarkonium

A flavorless meson composed of a heavy quark and its own antiquark is called a quarkonium. So quarkonia are mesons with hidden flavor. It is called a bottomonium

if it is a $b\bar{b}$ meson, such as the $\Upsilon(4S)$ produced at Belle; or a charmonium if it is a $c\bar{c}$ meson like the J/ψ, $\psi(2S)$ etc. Charmonium states have masses around 3 GeV/c^2, while the bottomonium states have masses around 10 GeV/c^2. The toponium doesn't exist, because the top quark is so heavy that it decays before the formation of a bound state.

1.3 Charmonium

First charmonium state was discovered in November 1974, when two experimental groups at SLAC and Brookhaven announced almost simultaneously the observation of a new narrow resonance, called J/ψ [12]. This was followed very shortly by the discovery of another narrow state by the SLAC group, which was called ψ' [13], which is radial excitation of J/ψ. These two resonances were interpreted as bound states of a new quark, called charm (c) quark and its antiquark ($\bar{c}$), whose existence had been predicted several years before to account for the non existence of strangeness changing neutral currents [14]. Since then charmonium has proven to be a powerful tool for the understanding the strong interactions.

Heavy quark combinations such as the charm-anticharm (called charmonium) is in particular interesting, as they can be treated *(a)* as non-relativistic systems and *(b)* perturbatively due to $m_Q >> \Lambda_{QCD}$, where $\Lambda_{QCD} \simeq 200$ MeV is the QCD scale.

Charmed quarks are heavy ($m_c \approx 1.3$ GeV/c^2), so the motion of the charm quark inside the bound states is slow, $v^2 \approx 0.3$, where v is the relative velocity between the c and $\bar{c}$. Thus charmonium system can be approximately considered as a non-relativistic bound state. The potential has two terms for short distance (1^{st} term represents asymptotic freedom) and long distance (2^{nd} represents confinement) [15].

$$V(r) = -\frac{4}{3}\frac{\alpha_s}{r} + kr. \tag{1.1}$$

The above simplest form of potential model does not include spin dependent central potential. Here first term is coulomb like potential which is due to single gluon exchange. This term is very similar to the Coulomb term in QED potentials e.g.

positronium or the hydrogen atom, except that here the coupling constant is given by α_s instead of α_{em}. Second term is for confinement of quarks within hadrons, which is because of non-abliean nature of QCD and it is completely absent in QED. Here parameters like α_s and k can be determined from fit to data. Using the above potential, charmonium spectrum is quite well reproduced (predicted ψ'' state). The non-relativistic treatment only describe feature of charmonium levels (without resolving the fine splitting between states with the same L and S quantum numbers but different J, and the hyperfine splitting between the spin-triplet and spin-singlet states).

If we include spin-dependent interaction term in Equation 1.1, then the total potential will become:

$$\begin{aligned} V(r) &= -\frac{4}{3}\frac{\alpha_s}{r} + kr \\ &+ \frac{32\pi\alpha_s}{9m_c^2}\tilde{\delta}_\sigma(r)\vec{S_c}.\vec{S_{\bar{c}}} \\ &+ \frac{1}{m_c^2}(\frac{2\alpha_s}{r^3} - \frac{k}{2r})\vec{L}\vec{S} \\ &+ \frac{1}{m_c^2}\frac{4\alpha_s}{r^3}(\frac{3\vec{S_c}\vec{r}\cdot\vec{S_{\bar{c}}}\vec{r}}{r^2} - \vec{S_c}\vec{S_{\bar{c}}}) \quad . \end{aligned} \tag{1.2}$$

Here the spin-spin term gives the spin-singlet splitting, while spin-orbit and the tensor terms describe the fine structure of states. and $\tilde{\delta}_\sigma(r) = (\sigma/\sqrt{\pi})^3 e^{-\sigma^2 r^2}$ and $(\alpha_s, k, m_c, \sigma)$ can be determined by fitting the spectrum [16].

After only including a Gaussian-smeared contact hyperfine interaction in the zeroth-order potential in non-relativistic potential in Equation 1.1, the central potential becomes

$$V(r) = -\frac{4}{3}\frac{\alpha_s}{r} + kr + \frac{32\pi\alpha_S}{9m_c^2}\tilde{\delta}_\sigma(r)\vec{S_c}.\vec{S_{\bar{c}}}. \tag{1.3}$$

The Godfrey-Isgur model is a "relativized" extension of the non-relativistic model. This model assumes a relativistic dispersion relation for the quark kinetic energy, a QCD motivated running coupling $[\alpha_s(r)]$, a flavor-dependent potential smearing parameter σ, and replaces factors of quark mass with quark kinetic energy [17]. The Hamiltonian consists of a relativistic kinetic term and a generalised quark-antiquark

potential

$$H = H_0 + V_{q\bar{q}}(\vec{p}, \vec{r}). \tag{1.4}$$

where

$$H_0 = \sqrt{\vec{p}_q^2 + m_q^2} + \sqrt{\vec{p}_{\bar{q}}^2 + m_{\bar{q}}^2}. \tag{1.5}$$

Just as in the non-relativistic model, the quark-antiquark potential $V_{q\bar{q}}(\vec{p}, \vec{r})$ assumed here incorporates the Lorentz vector one gluon exchange interaction at short distances and a Lorentz scalar linear confining interaction. To first order in $(v_q/c)^2$, $\mathrm{V}_{q\bar{q}}(\vec{p}, \vec{r})$ reduces to the standard non-relativistic result given by Equation 1.3 [with α_s replaced by a running coupling, $\alpha_s(r)$]. One important aspect of this model is that it gives reasonably accurate results of the spectrum for all quark flavors u, d, s, c, b, whereas the non-relativistic model is only fitted to $c\bar{c}$ system.

1.3.1 Charmonium Production

Charmonium states are produced in a variety of ways at e^+e^- colliders. The earlier studies of charmonium spectroscopy were performed almost exclusively at e^+e^- colliders. In these experiments e^+e^- annihilation proceeds primarily through an intermediate virtual photon, creating a bound $c\bar{c}$ state. Other production mechanisms include B-meson decay, two virtual photon production (photon-photon fusion), initial state radiation and double charmonium production.

- e^+e^- Annihilation or Direct formation

  In e^+e^- annihilations, direct charmonium production is allowed only for states with the quantum numbers $J^{PC} = 1^{--}$, namely the J/ψ, ψ', $\psi(3770)$ etc. shown in Figure 1.1(a). Precise measurements of the masses and widths of these states can be obtained from the energy of the electron and positron beams, which are known with good accuracy. All other states can be produced by radiative decays of the $J^{PC} = 1^{--}$ resonances.

$$e^+e^- \to \psi(2S) \to \gamma + X. \tag{1.6}$$

- B-meson decay

  Charmonium states can be produced at the B-factories in the color suppressed decays of the B-meson shown in Figure 1.1(b). The large data samples available at the B-factories make this a promising approach for the study of known states, as well as the discovery of new resonances: $X(3872)$, $X(3940)$, $Y(3940)$, $Z(4430)^+$ etc. are recent examples which illustrate well the discovery potential of the B-factories in the field of charmonium physics. The decays of the B-meson provide a clean production environment for charmonium production and states of any quantum number can be formed. The small production rates can be overcomes by restricting the study to specific exclusive final states, to take advantage of variables like: the B-meson mass, beam energy constraints etc. Decay modes under search in this thesis are propagated through this mode of production. e.g. $B^0 \to \psi' K^+\pi^-$, $B^0 \to X(3872)K^+\pi^-$, $B^+ \to \psi' K^0_S\pi^+$, $B^+ \to X(3872)K^0_S\pi^+$, $B^+ \to \psi' K^+\pi^0$ and $B^+ \to X(3872)K^+\pi^0$ decay modes.[†]We will exploit these decay modes in order to study the production of $X(3872)$ in $B \to X(3872)K\pi$ decays.

- Photon-photon ($\gamma\gamma$) fusion

  Electron-positron annihilations at higher energies can produce the J-even (0^{-+}, $0^{++}, 2^{-+}$ and 2^{++}) charmonium and charmonium-like states through two virtual photons via the process:

  $$e^+e^- \to e^+e^- + (c\bar{c}). \qquad (1.7)$$

  as shown in Figure 1.1(c). The production rate in this case decreases by a factor α^2 from the rate for a single photon, where α is the fine structure constant. The $(c\bar{c})$ state is usually identified by its hadronic decays. The cross section for process in Equation 1.7 scales linearly with the $\gamma\gamma$ partial width of the $(c\bar{c})$ state being studied [18]:

  $$\sigma(e^+e^- \to e^+e^-(c\bar{c})) = \int d^5\mathcal{L}_{\gamma\gamma}(\alpha_i)\sigma(\gamma\gamma \to (c\bar{c})). \qquad (1.8)$$

[†]Conjugate modes are also included in all analyses unless stated explicitly.

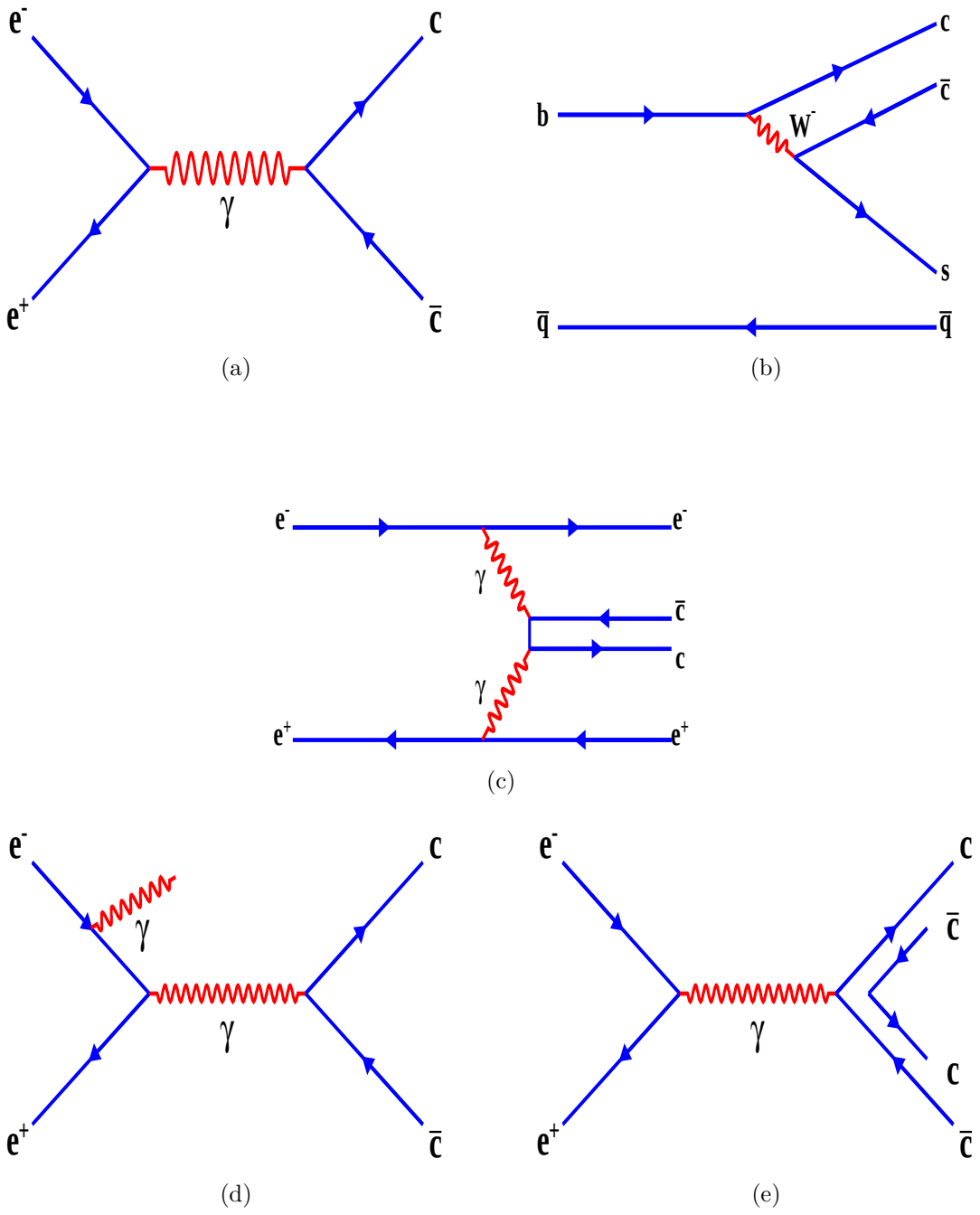

Figure 1.1: Charmonium production diagrams at e^+e^- colliders. (a) e^+e^- annihilation, (b) B-meson decay, (c) Photon-photon fusion, (d) Initial state radiation, (e) Double charmonium production.

where $\mathcal{L}(\alpha_i)$ is the luminosity function expressed in the variable α_i (for example, the four momenta of the outgoing leptons), and the two-photon cross section $\sigma(\gamma\gamma \to (c\bar{c}))$ is given (in natural units $\hbar = c = 1$) by:

$$\sigma(\gamma\gamma \to (c\bar{c})) = 8\pi \frac{2J+1}{M} \Gamma_{\gamma\gamma} \frac{M\Gamma}{(s-M^2)^2 + M^2\Gamma^2} F(q_1^2, q_2^2). \qquad (1.9)$$

Here J, M and Γ are the spin, mass and total width of the $c\bar{c}$ state under study, respectively; s is the center-of-mass energy of the colliding photon system; $\Gamma_{\gamma\gamma}$ is the two-photon partial width of the $c\bar{c}$ state; q_1 and q_2 are the four-momenta of the virtual photons and $F(q_1^2, q_2^2)$ is the factor describing the evolution of the cross section. e.g. $\gamma\gamma \to \eta_c(2S)$ or $\gamma\gamma \to Z(3930)$.

- Initial state radiation (ISR) or Radiative return

  In this process either the electron or the positron radiates a photon before the annihilation as shown in Figure 1.1(d), thereby lowering the effective CM energy. Only $J^{PC} = 1^{--}$ states can be produced in ISR. This process allows a large mass range to be explored and is very useful for the measurement of R,

$$R = \frac{\sigma(e^+e^- \to hadrons)}{\sigma(e^+e^- \to \mu^+\mu^-)}. \qquad (1.10)$$

  and for the search of new vector states. e.g. $e^+e^- \to \gamma_{ISR} Y(4260) \to J/\psi\pi^+\pi^-$.

- Double charmonium production

  The production of double charmonium states in e^+e^- annihilation as shown in Figure 1.1(e) was discovered by Belle Collaboration from a sample of data collected near the $\Upsilon(4S)$ resonance at a CM energy $\sqrt{s} = 10.6$ GeV, by studying the recoil momentum spectrum of the $J/\psi\eta_c$ [19]. The collaboration also found evidence for $J/\psi\chi_{c0}$ and $J/\psi\eta_c'$ production. With Belle data study [20], the $e^+e^- \to J/\psi c\bar{c}$ cross section measured in a model independent way comes out to be $(0.74 \pm 0.08 \pm 0.09)$pb. For the second charmonium with the mass below the open charm threshold, this fraction is $(16 \pm 3)\%$ [20]. Despite the small cross section value, these studies are possible, thanks to the high luminosity B-factories era. We can reconstruct one of two charmonium (e.g. J/ψ),

to observe the process of pair production. The second state can be seen in the spectrum of masses recoiling against the reconstructed ones, $M_{rec}(J/\psi) = \sqrt{(E_{CM} - E^*_{J/\psi})^2 - (p^*_{J/\psi})^2}$, where $E^*_{J/\psi}$ and $p^*_{J/\psi}$ are the energy and momentum of J/ψ. In the process of charmonium pair production in the e^+e^- annihilation, the final charmonium states have opposites charge parities. It was experimentally found that either scalar mesons with the quantum number $J^{PC} = 0^{++}(\chi_{c0})$ or pseudoscalar mesons with $J^{PC} = 0^{-+}$ [η_c and $\eta_c(2S)$] are produced together with J/ψ. The $J^{PC} = 1^{++}(\chi_{c1})$ and $J^{PC} = 2^{++}(\chi_{c2})$ are not seen. This could indicate that this process favors the production of $J = 0$ states over those with $J = 1$ and higher [21].

1.3.2 Charmonium Decays

Following are different ways through which charmonium can change its state:

(1) **Annihilation:** Annihilation of $c\bar{c}$ to leptons via photon is shown in Figure 1.2. It is generally suppressed for bound state. But decay to leptons is a clean experimental signal.
e.g. $\psi' \to e^+e^-$, $J/\psi \to \mu^+\mu^-$

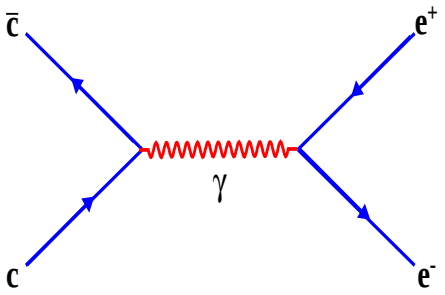

Figure 1.2: Annihilation of $c\bar{c}$.

(2) **Strong Decay:** Charmonium states below the open charm threshold decay via intermediate photons or gluons which are produced by the annihilation of $c\bar{c}$ pair. These type of decays are OZI violating but flavor conserving. Suppression of this

type of decays leads to (relatively) long lifetime and hence narrow width of J/ψ and ψ'.

e.g. $J/\psi(1^3S_1)$ or $\psi' \to$ ggg $\to$ hadrons

$J/\psi(1^3S_1)$ or $\psi' \to$ virtual $\gamma \to$ hadrons

$J/\psi(1^3S_1)$ or $\psi' \to$ virtual $\gamma \to$ leptons

$J/\psi(1^3S_1)$ or $\psi' \to \gamma$gg $\to$ hadrons

or Creation of one or more light $q\bar{q}$ pairs from vacuum to form light mesons.

e.g. $\psi(3770) \to \omega\pi^0$

$\psi(4160) \to \phi\pi^+\pi^-$

$\psi(3770) \to \pi^+\pi^-\pi^0$

These type of decays are shown in Figure 1.3.

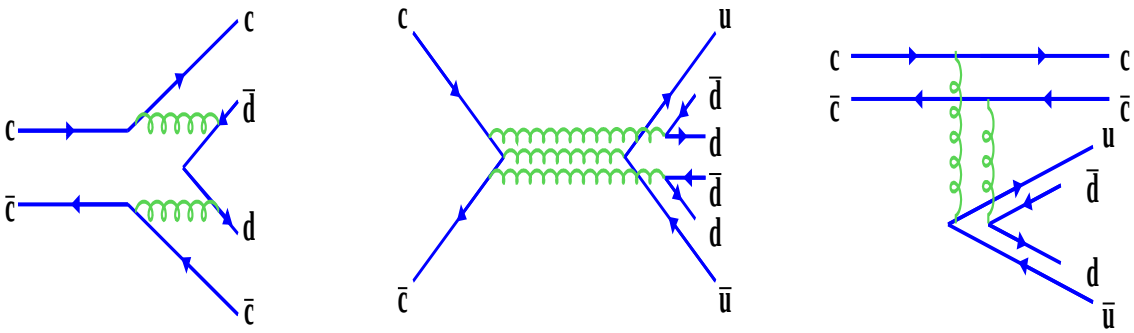

Figure 1.3: Strong decay of charmonium states.

(3) **Electromagnetic or Radiative Decay:** Radiative decay of charmonium is shown in Figure 1.4 e.g. $J/\psi \to \gamma\eta_c(1S)$, $\psi(4040) \to \chi_{c1}\gamma$

These type of decays are competitive and often most accessible transitions.

(4) **Weak Decay:** Weak decays of one or both heavy quarks, e.g.

- $J/\psi \to D_{s \text{ or } d}^- e^+\nu_e$ where D_s (D_d) decay mode is Cabbibo-favored (Cabbibo-suppressed).
- $J/\psi \to \bar{D}^0 e^+ e^-$.

Feynman diagrams are shown in Figure 1.5.

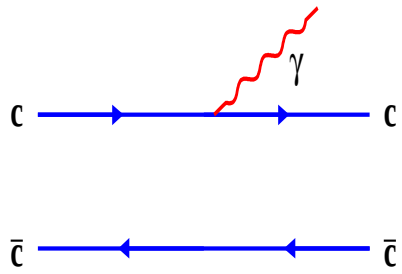

Figure 1.4: Radiative decay of charmonium states.

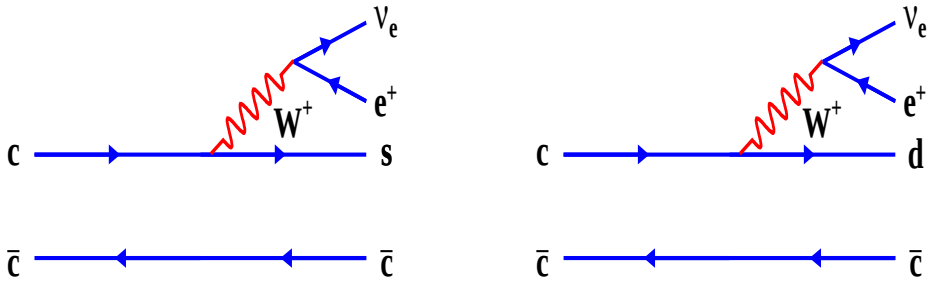

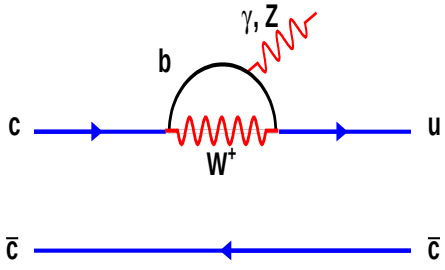

Figure 1.5: Weak decay of charmonium states.

1.3.3 Charmonium Spectroscopy

The $c\bar{c}$ system of two fermions is very much similar to the hydrogen atom. So it can be characterized with the same quantum numbers as that of hydrogen atom: n, L, S and J respectively the radial quantum number, the orbital quantum number, total spin and total angular momentum. Charmonium spectroscopy is an ideal place for

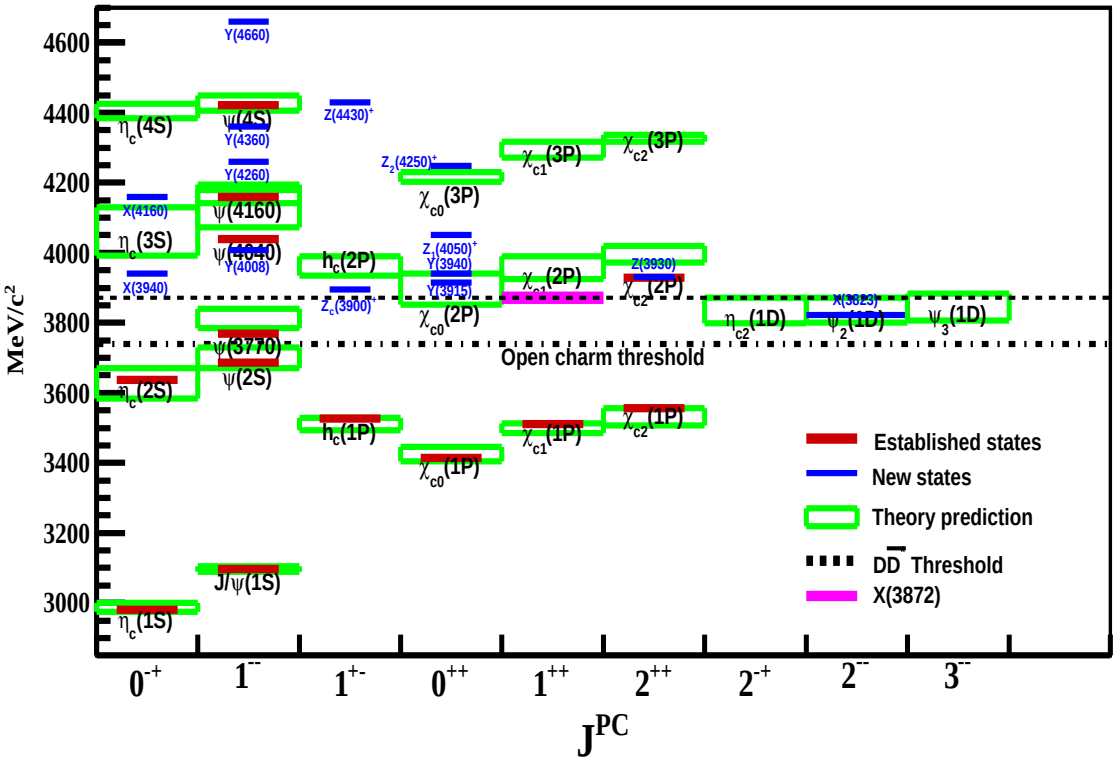

Figure 1.6: Charmonium spectrum for known, predicted and experimentally established charmonium and charmonium-like states.

studying the dynamics of QCD in the interplay of perturbative and non-perturbative QCD regime. Now, almost forty years after the discovery of J/ψ, charmonium physics continues to be an exciting and interesting field of research because of discoveries of new states and the exploitation of the B-factories which are rich source of charmonium and charmonium-like states. This field has grown very quickly, as exotic states continue to be found at the rate of about one or two new ones every year. Many thanks to B-factories for this achievement. Charmonium spectrum for well established, experimentally found and predicted charmonium and charmonium like states is shown in Figure 1.6 with J^{PC} of each state known till now. The charmonium states follow a pre-defined nomenclature. States with even J and $PC = -+$ are called $\eta_c(nL)$, states with odd J and $+-$ as PC are called $h_c(nL)$ states, states with

PC as $++$ are called $\chi_{cJ}(nL)$ and with $PC = --$ are called $\psi(nL)$ states except lowest ψ state which is known as J/ψ due to historical reasons. The spectrum consists of many narrow states below the threshold of $D^0\bar{D}^0$ (3.729 GeV/c^2) for open charm and several states above threshold, some of them wide (because they decay to $D^0\bar{D}^0$), some of them still narrow, because their decay to open charm is forbidden by some conservation rule. All predicted charmonium states below the $D^0\bar{D}^0$ threshold have been observed in experiment. While above this threshold, experimental information on the charmonium states is rather limited.

1.4 Charmonium-Like "Exotic" States

In recent years, new particle states have been found (like $X(3872)$, $Z(4430)^+$ etc.) which resembles like charmonium but seem to have different properties from that of conventional charmonium states. They come under the category of charmonium-like "exotic" states. These exotic states can be broadly classified with following models:

1.4.1 Multiquark

Multiquark model includes two types of states: Tetraquark (colorless combination of 4 quarks), pentaquark (colorless combination of 5 quarks). Below is the explanation of these two types of categories:

Tetraquark model assumes two quark-antiquark pairs. There have been no confirmed reports of a tetraquark state to date, although $\sigma(600)$, $f_0(980)$ and $a_0(980)$ states are considered by some authors to be a $J^{PC} = 0^{++}$ light tetraquark state [22]. The B-factories recently observed two very narrow states, the $D_{sJ}(2317)^{*\pm}$ and $D_{sJ}(2460)^{*\pm}$ [23, 24], which have also been interpreted as tetraquark states.

Pentaquark model assumes four quark and one antiquark or we can say baryon+a meson (a color-neutral). In 2003, the LEPS Collaboration [25] reported evidence for the Θ^+, a $uudud\bar{s}$ pentaquark candidate with a mass of 1540 ± 10 MeV/c^2, $\Gamma < 25$ MeV and a statistical significance of 4.6σ. The Θ^+ was then confirmed by ten experimental papers with significances ranging from 3 to 7σ including CLAS Collaboration [26].

But in a high-statistics repeat of their own measurement, CLAS Collaboration found that their earlier observation of Θ^+ was false and no evidence for the existence of the pentaquark exists [27]. However, it was not seen by the B-factories and other high-energy experiments. Because of these non-confirmations, it is doubted that Θ^+ really exists [28]. We end up this with a quote from PDG'08 summarizing the saga of the pentaquark: *"The whole story - the discoveries themselves, the tidal wave of papers by theorists and phenomenologists that followed, and the eventual* ***'undiscovery'*** *- is a curious episode in the history of science."*

1.4.2 Charmonium Hybrid

QCD suggests far richer spectrum of hadrons so called exotic hadrons such as hybrid mesons ($q\bar{q}g$). These are composed of color-octet quark-antiquark pair and an excited gluon. Hybrids and mesons can have common J^{PC} quantum numbers. But hybrids have additional gluonic degrees of freedom so they can have exotic quantum numbers (e.g. $J^{PC} = 0^{--}$, 0^{+-}, 1^{-+}, 2^{+-} etc.) which are not accessible for mesons. Heavy quarkonium hybrids have been studied using constituent gluon model [29], the flux tube model [30], the quasi-gluon model [31] and lattice QCD [32–37]. These studies broadly agree that heavy hybrids should exist in the same mass range as heavy quarkonia, suggesting that some of the XYZ states could be heavy hybrids.

1.4.3 Near-Threshold Enhancement

Due to the proximity of the $X(3872)$ mass to the $D^0\bar{D}^{*0}$ threshold, another possible scenario is that the $X(3872)$ is actually has cusp effect in the amplitude at the threshold. This effect would lead to a bump in the cross-section slightly above the threshold and also it affects kinematic distributions. The possible thresholds include the DD^*, D^*D^*, DD_1 and D^*D_1 at $E_{CM} \approx 3872$, 4020, 4287 and 4430 MeV, respectively. S-wave ($L = 0$) scattering dominates the cross section at the threshold, however in few cases, higher waves also become important. States in a relative S- wave with little relative momentum (which lives long on the time scale of strong interactions) will

have enough time to exchange pions and interact [38]. Molecular state is possible due to binding which is possible (via an attractive π exchange which could occurs through couplings such as $D \leftrightarrow D^*\pi^0$). It should be noted that there could also be a repulsive interaction which arises due to some strong interaction effects and it can result in a virtual state above threshold. Thus, near the kinematical threshold there can be a structure in the cross section which may or may not be a resonance. In addition, if there are $c\bar{c}$ states which are near a threshold, they can interact with the threshold and will result in a mass shift of both the $c\bar{c}$ resonance and the threshold-related enhancement. These effects could be quite significant in the observed cross section, particularly of the $c\bar{c}$ states close to the threshold [38, 39].

1.4.4 Glueballs

Glueballs contain only valence gluons and no quarks. Theoretical calculations show that glueballs could exist at energy ranges accessible to current colliders. However they are extremely difficult to identify because they mix with ordinary meson states. So far they have not been observed and identified with certainty; one possible candidate is the $f_J(1710)$ [40].

1.5 Review of "Exotic" X(3872) State

In 2003, the Belle Collaboration reported a narrow resonance in the $(J/\psi\pi^+\pi^-)$ mass spectrum in exclusive $B^\pm \to J/\psi\pi^+\pi^-K^\pm$ decay mode [41] with a mass of $3872.0 \pm 0.6 \pm 0.5$ MeV/c^2 shown in Figure 1.7. This announcement was very surprising because it was soon realised that the apparent quantum numbers, mass, quark content and decay patterns of this new state, called $X(3872)$, were not compatible with a standard charmonium state interpretation. Later on this state was also confirmed independently by many other experimental Collaborations like CDF [42], D0 [43], BaBar [44] and recently by LHCb [45] and CMS [46] experiments at LHC. Investigation of the nature of this state has received immense phenomenological and experimental attention. Among the "exotic" states, the X(3872) is the only one ob-

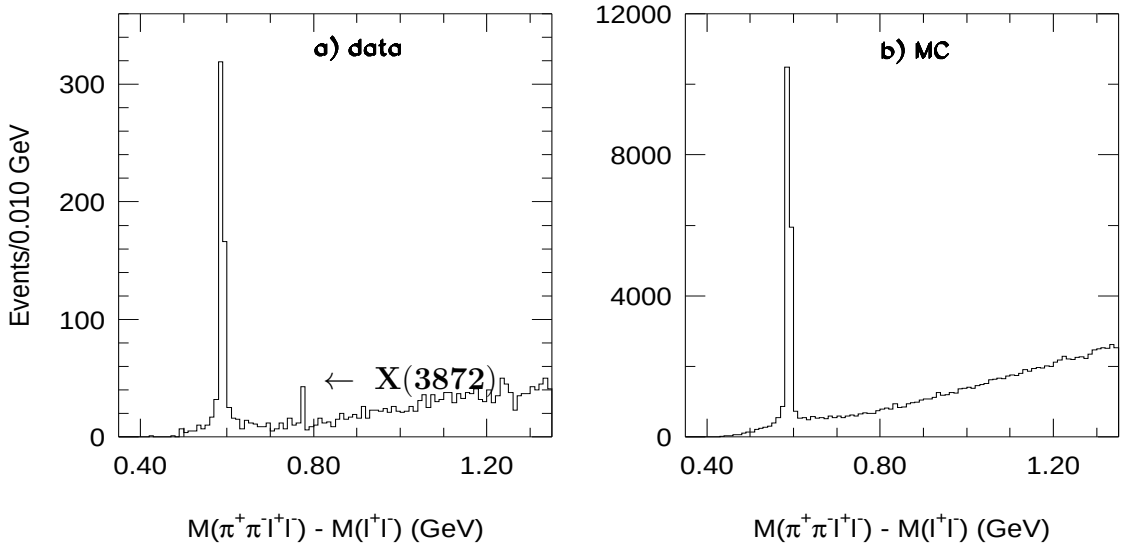

Figure 1.7: Observation of $X(3872)$, in left plot with experimental data (peak around 0.78 GeV/c^2) as compared to right plot in Monte Carlo.

served in number of decay modes like: $X(3872) \to J/\psi\pi^+\pi^-$ [41, 47], $X(3872) \to \gamma J/\psi$ [48, 49], $X(3872) \to \gamma\psi'$ [49, 50], $X(3872) \to J/\psi\omega(\to \pi^+\pi^-\pi^0)$ [51, 52], $X(3872) \to D^0\bar{D}^0\pi^0$ [53–55], and $X(3872) \to D^0\bar{D}^0\gamma$ [44, 55].

An surprising property of the X(3872) is isospin violation. It was found that in the decay X(3872)$\to J/\psi\pi^+\pi^-$, the invariant mass of $\pi^+\pi^-$ peaks at the mass of the ρ^0 meson with ρ and J/ψ in a relative S-wave. This is because it is found that dipion in $X(3872)$ have been coming from ρ meson [56, 57]. The ρ^0 carries isospin I=1, but the initial state (if assumed to be a pure $c\bar{c}$ state) has I=0 (as it would not contain any u or d valence quarks). One of the mechanisms to induce isospin violation is the u/d quark mass difference in strong interaction. However, as the mass difference is small, the effect should be very small, consistent with the measured branching fractions. Another possible mechanism to induce isospin violation is the u/d quark charge difference in electromagnetic interactions (EM). Isospin should only be conserved in strong interaction, but not in EM interaction. Thus one of the possible explanations might be, that the decay X(3872)$\to J/\psi\rho(\to\pi^+\pi^-)$ is proceeding via EM interaction, i.e. the ρ might not be created by sea quarks or by gluons coupling, but by

a virtual photon. On the other hand, the decay mode $X(3872) \to J/\psi\omega(\to \pi^+\pi^-\pi^0)$ is isospin conserving decay mode. But ratio of branching fractions of above decay modes estimated by Belle [51] and BABAR [52] are:

$$\frac{\mathcal{B}(X(3872) \to \pi^+\pi^-\pi^0 J/\psi)}{\mathcal{B}(X(3872) \to \pi^+\pi^- J/\psi)} = 1.0 \pm 0.4(\text{stat.}) \pm 0.3(\text{syst.}) \text{ (Belle).} \quad (1.11)$$

$$\frac{\mathcal{B}(X(3872) \to \pi^+\pi^-\pi^0 J/\psi)}{\mathcal{B}(X(3872) \to \pi^+\pi^- J/\psi)} = 0.8 \pm 0.3 \text{ (BABAR).} \quad (1.12)$$

Since above two branching fractions ($\mathcal{B}(X(3872) \to \pi^+\pi^-\pi^0 J/\psi)$ and $\mathcal{B}(X(3872) \to \pi^+\pi^- J/\psi)$) are comparable, so this indicates that isospin mixing occurs at large scale.

Earlier $X(3872)$ was thought to be a normal charmonium state [58]. The absence of a strong signal in the $\chi_{cJ}\gamma$ [59] decay channel disagree with potential model expectations for a conventional charmonium state.

Another possible interpretations for the $X(3872)$ nature include P- or D- wave charmonium, a tetraquark, a loosely bound molecule ($D^0\bar{D}^{*0}$) or molecule ($D^0\bar{D}^{*0}$) + charmonium ($c\bar{c}$) mixture.

The predicted and observed charmonium states [60] near the $X(3872)$ mass are listed in Table 1.4. The predicted masses of 2^1P_1 and 2^3P_1 are ~ 80 MeV/c^2 higher

Table 1.4: Charmonium states near the mass of $X(3872)$. The masses of predicted but unobserved states have no errors assigned.

State	$n^{2S+1}L_J$	J^{PC}	Mass (MeV/c^2)
$h_c(2P)$	2^1P_1	1^{+-}	~ 3956
$\chi_{c0}(2P)$	2^3P_0	0^{++}	3918.4 ± 1.9
$\chi_{c1}(2P)$	2^3P_1	1^{++}	~ 3953
$\chi_{c2}(2P)$	2^3P_2	2^{++}	3927.2 ± 2.6
$\eta_{c2}(1D)$	1^1D_2	2^{-+}	~ 3837
$\psi_{c1}(1D)$	1^3D_1	1^{--}	~ 3819
$\psi_{c2}(1D)$	1^3D_2	2^{--}	~ 3838
$\psi_{c3}(1D)$	1^3D_3	3^{--}	~ 3849

than the mass of the $X(3872)$. The observed 2^3P_0 mass which is lower than 2^3P_1 mass is still ~ 50 MeV/c^2 above the $X(3872)$ mass. The 2^3P_0 and 2^3P_2 states have

broad widths which are 20±5 MeV and 24±6 MeV, respectively [1]. However 2^3P_1 is expected to be narrower. The predicted masses of 1^1D_2, 1^3D_1, 1^3D_2 and 1^3D_3 are $\sim$ 30-50 MeV/c^2 lower than the $X(3872)$. The singlet 1^1D_2 ($J^{PC} = 2^{-+}$) state could be narrow and is closer in mass to the $X(3872)$ state. Thus exact state can be confirmed after its J^{PC} information. After analyzing angular distributions of $B^+ \to X(3872)K^+$, $X(3872) \to J/\psi\pi^+\pi^-$, CDF excluded all J^{PC} hypotheses except 2^{-+} and 1^{++} [47]. Recent analysis carried out by LHCb [61], using five-dimensional angular correlations of $B^+ \to X(3872)K^+$, where $X(3872) \to J/\psi\pi^+\pi^-$ and $J/\psi \to \mu^+\mu^-$ suggests $X(3872)$ J^{PC} to be 1^{++} and rejects 2^{-+} hypothesis with 8.2σ. So this J^{PC} rules out the explanation of the $X(3872)$ as a η_{c2} (1^1D_2) state. The remaining possibility, χ_{c1} (2^3P_1) charmonium, is disfavored by the $X(3872)$ mass.

Some authors have advanced a QCD-tetraquark [62] interpretation for the $X(3872)$, in which all four quarks interact with each other equally rather than in a bound state of bound states. In this model, a so-called diquark $[cq]$ and antidiquark $[\bar{c}\bar{q}']$ ($q, q' =$ u or d) act as composite antiquarks and quarks. In this interpretation, the $X(3872)$ is expected to be accompanied by isospin and $SU(3)$ multiplet partners (charged partners). In particular, the $X(3872)$ is considered an $I_3 = 0$ member of an isospin triplet and charged $I_3 = \pm 1$ partner states (e.g decay via $X^+ \to J/\psi\rho^+$) are expected to be produced at a rate in B decays that is twice that for the neutral $X(3872)$. Both BaBar [63] and Belle [56] Collaborations report negative results for its charged-partner and set upper limits on product of branching ratios.

In the same proposed interpretation, two neutral $X(3872)$ states (with orthogonal mixtures of $cu\bar{c}\bar{u}$ and $cd\bar{c}\bar{d}$) are expected to exist with mass difference of $\frac{(7\pm2)}{cos(2\theta)}$ MeV. These two different states might result in different $X(3872)$ mass in the neutral and charged B meson decay modes. But this mass difference estimation by BaBar [44], CDFII [64], Belle [56] reports negative results. Further search for C-odd partners by Belle with $B \to J/\psi\eta K$ [65] and $B \to \chi_{c1}\gamma K$ [66] didn't also match above interpretations. So experimental searches for charged- and C-odd partners report negative results. However, since these searches are restricted to states with narrow total widths and the published limits may not apply if the partner states access more decay chan-

nels and are thus broader.

Proximity of its mass to the D^0-$\bar{D}^{*0}$ threshold along with its measured decay rates suggests it to be a loosely-bound "molecule" of D^0 and $\bar{D}^{*0}$ mesons [67]. In this case, the binding energy E_b would be given by the mass difference $m(X(3872)) - (m(D^{*0})+m(D^0))$. Including the new Belle result, the new world average mass of the $X(3872)$ is m=3871.69±0.17 MeV [1]. The present value for the sum of the masses is $m(D^0)+m(D^{*0})$=3871.84±0.28 MeV [1], Thus, a binding energy of E_b=−0.15±0.33 MeV can be calculated, which is enormously small.

The remaining possibility for $X(3872)$ is molecule + charmonium mixture [67, 68]. This possibility can be checked using radiative decays of $X(3872)$, as these types of decays provide a valuable source of information to understand its nature. Studies of $X(3872) \to \gamma J/\psi$ also helped in establishing +ve C-parity of $X(3872)$. This decay mode has been observed by Belle [48] and BaBar [49]. $X(3872) \to \gamma\psi'$ was not observed by Belle [48], but the evidence of same decay mode was reported by BaBar [69] and LHCb [50] with significances 3.5σ and 4.4σ respectively. These Collaborations reports the ratio of branching fractions as follows:

LHCb result:

$$R = \frac{\mathcal{B}(X(3872) \to \gamma\psi')}{\mathcal{B}(X(3872) \to \gamma J/\psi)} = 2.46 \pm 0.64 \pm 0.29. \tag{1.13}$$

BaBar result:

$$R = \frac{\mathcal{B}(X(3872) \to \gamma\psi')}{\mathcal{B}(X(3872) \to \gamma J/\psi)} = 3.4 \pm 1.4. \tag{1.14}$$

Belle Collaboration only set upper limit on $R < 2.1$ at the 90% C.L. as they didn't observe a significant signal for $X(3872) \to \gamma\psi'$. After considering statistical and systematic uncertainties, this upper limit doesn't contradict BaBar and LHCb results.

After combining results form Belle, BaBar and LHCb [70], one can have:

$$\bar{R} = \frac{\mathcal{B}(X(3872) \to \gamma\psi')}{\mathcal{B}(X(3872) \to \gamma J/\psi)} = 2.31 \pm 0.57. \tag{1.15}$$

This $\bar{R}$ value seems to disfavor the pure $D^0\bar{D}^{0*}$ molecular interpretation of the $X(3872)$, as for pure $D^0\bar{D}^{0*}$, $\bar{R}$ value should be small [O(10^{-3})] [71,72]. However, mixing of $D^0\bar{D}^{0*}$ molecule and charmonium could explain this $\bar{R}$ value of $X(3872)$ [50,73].

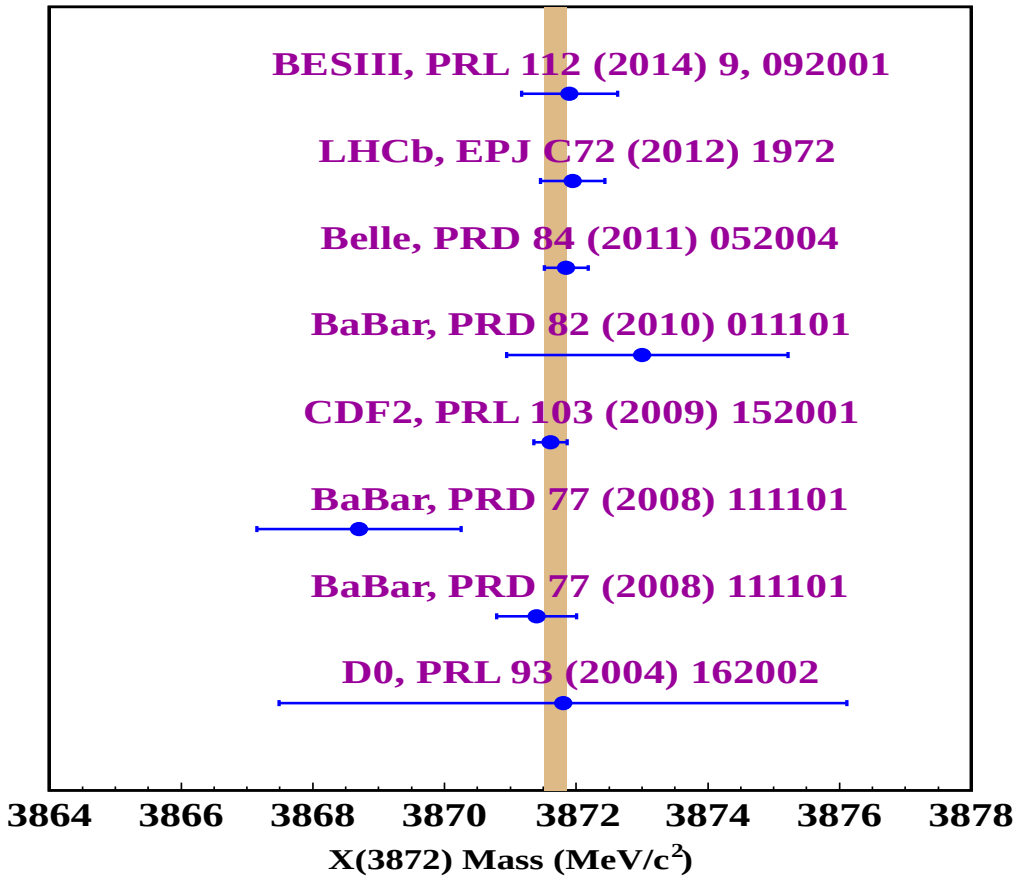

Figure 1.8: Mass measurements of the X(3872) state. Vertical band shows uncertainty in world average value (3871.69±0.17 MeV/c^2).

Considering the totality of phenomenological and experimental information on the $X(3872)$ at face value, this resonance seems to be very narrow with upper limit on total width $\Gamma_{X(3872)} < 1.2$ MeV [56], quantum numbers as $J^{PC} = 1^{++}$ and current world average mass as 3871.69±0.17 MeV/c^2. Measurements by different experiments on its mass is summarized in Figure 1.8 with vertical band shows uncertainty in world average value. Better understanding of the $X(3872)$ demands more experimental information and phenomenological insight.

In the present thesis work, we will try to understand in a better way the $X(3872)$

particle and perform its search in neutral and charged $B \to X(3872)K\pi$ decay modes with $B \to \psi' K\pi$ decays modes as the calibration decay modes.

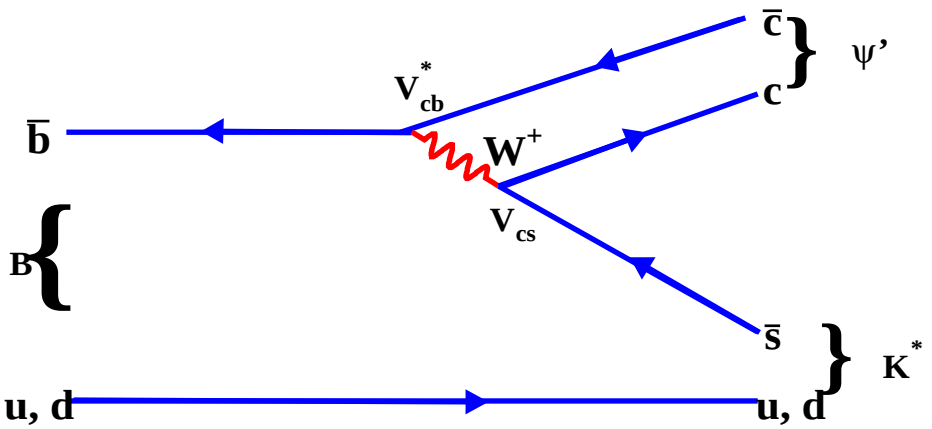

Figure 1.9: Tree diagram for $B \to \psi' K^*$ decay mode.

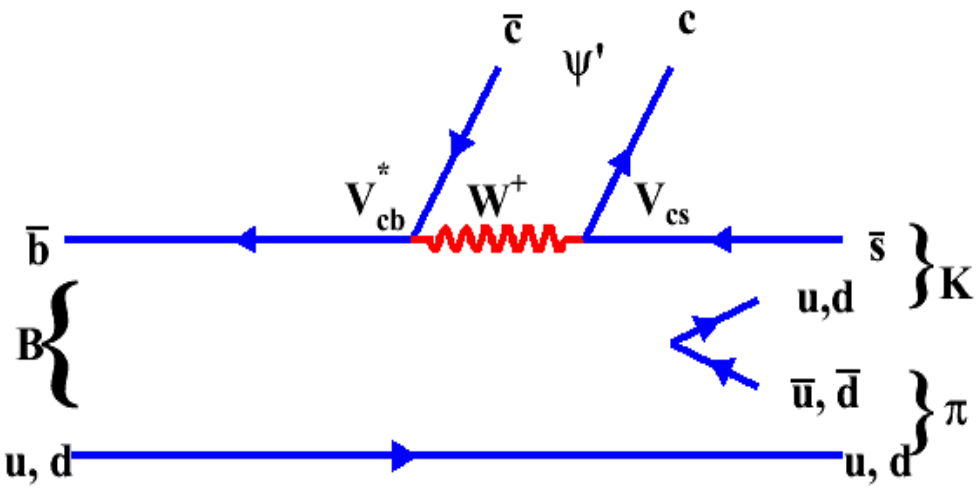

Figure 1.10: Tree diagram for $B \to \psi' K\pi$ decay mode.

1.6 Feynman Diagrams for $B \to \psi' K\pi$ decay modes

The $B \to \psi' K^*(\to K\pi)$ and $B \to \psi' K\pi$ (calibration decay modes) are color-suppressed and Cabibbo-favored two body and three body decay modes respectively,

which has already been observed and their branching fractions are well measured. In three body decay, this decay mode proceeds via the transition $\bar{b}q \to \bar{c}c\bar{s}u\bar{u}q$ or $\bar{b}q \to \bar{c}c\bar{s}d\bar{d}q$, here $q = u$ or d quark and $u\bar{u}$ or $d\bar{d}$ quark pairs are produced from either sea quarks or from coupling of gluons. Two body penguin proceeds via the transition $\bar{b}q \to c\bar{c}\bar{s}q$, where q can be either u or d quark and $c\bar{c}$ quark pair is produced from either virtual photon or Z^*. Tree diagram and penguin diagrams for calibrated decay modes are shown in Figure 1.9 to Figure 1.11.

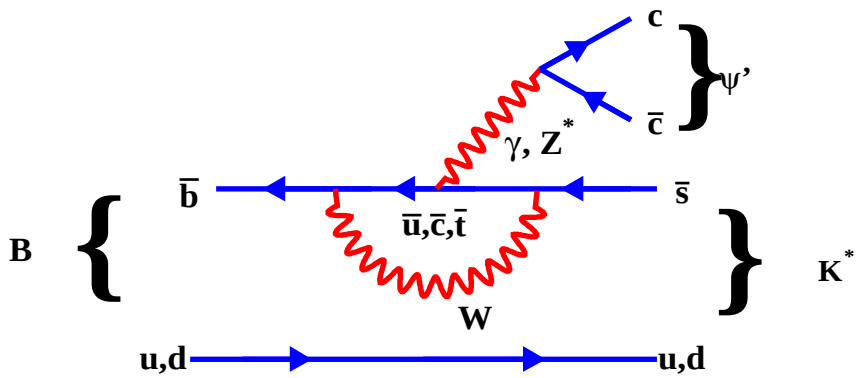

Figure 1.11: Penguin diagram for $B \to \psi' K^*$ decay mode.

1.7 $B \to X(3872)K\pi$ decay modes and Motivation

Concerned decay mode in this thesis is $B \to X(3872)K\pi$. Since $X(3872)$ is charmonium-like "exotic" state so one can have almost same Feynman diagrams as that of calibrated decay mode, except $X(3872)$ can have any type of structure (in deep any quark content).

$X(3872)$ state was never observed in three body decay dynamics of B-meson before this analysis. So our motive behind this decay mode is to first search for $X(3872)$ in neutral and charged $B \to X(3872)K\pi$ (three body) decay modes and then to search any resonant structure in background subtracted mass distributions of $M_{X(3872)K}$, $M_{X(3872)\pi}$ and $M_{K\pi}$ for observed $B \to X(3872)(K\pi)$ decay mode. After doing analy-

sis, it was found that for $X(3872)$ mass region, there is no structure in $M_{X(3872)K}$ and $M_{X(3872)\pi}$ distribution, but a clear structure is observed in $M_{K\pi}$ distribution. And further it is found that resonant $K^*(892)$ is not dominating as compared to $(K\pi)_{NR}$ one for $X(3872)$ mass region, which is not like normal charmonium state behaviour, like ψ', χ_{c1} mass regions.

1.8 Chapter in Compact

In this Chapter, author has tried to set up an introduction environment for the analysis work carried out in this thesis. Following decay modes are studied in this thesis:

- $B^0 \to X(3872)K^+\pi^-$

  Our main motive behind this study is to search for $X(3872)$ in $B^0 \to X(3872)K^+\pi^-$ decay mode as it has not been seen/measured yet. Further binned minimum χ^2 fit is performed to background subtracted $M_{K\pi}$ distribution to separate out resonant and non-resonant components of $K\pi$ mass system. From these studies, we may get some information about the nature of $X(3872)$ particle. For this study, we will take opportunity for utilization of $B^0 \to \psi' K^+\pi^-$ decay mode (acts as calibration sample).

- $B^+ \to X(3872)K^0_S\pi^+$ and $B^+ \to X(3872)K^+\pi^0$ decay modes.

  We have also taken up the search for $X(3872)$ in $B^+ \to X(3872)K^0_S\pi^+$ and the very preliminary study of $B^+ \to X(3872)K^+\pi^0$ decay modes. Strategy for searching these decay modes is same as previous one. Calibration modes for above decays modes are $B^+ \to \psi' K^0_S\pi^+$ and $B^+ \to \psi' K^+\pi^0$ (only preliminary results) decay modes respectively.

2

KEK B-Factory and Belle Detector

2.1 Introduction

In this Chapter, the technical details of the experimental project undertaken for this study are described. The experimental project undertaken utilizes the High Energy Physics Accelerator at KEK, Tsukuba, Japan, called KEK B-factory and the Belle detector for the study of B physics. It provides the clean and excellent environment to study B physics, charmonium like states and CP violation in B-meson system.

The CP violation phenomenon was first observed in $K^0\bar{K}$ system in 1964 [11]. Since then large amount of theoretical work has been carried out to understand this phenomenon. In a remarkable paper published in 1973, Kobayashi and Maskawa (KM) predicted that CP violation could be accommodated in the Standard Model (SM) only if there were at least six quark flavors, twice the number of quark flavors known at that time [74]. The subsequent experimental discoveries of c, b and t quarks [75–78] has substantiated the six-quark KM hypothesis and subsequently the KM model for CP violation is considered to be an essential part of the SM. In 1980, Sanda and Carter pointed out that the KM model contained the possibility of rather sizable CP violating asymmetries in certain decays of $B\bar{B}$ system [79]. The large amount of mixing in the neutral B-meson system and subsequent observation of a long b-quark lifetime [80] indicates that it would be experimentally feasible to carry

out the decisive tests of the KM model and CP violation by studying B-meson decays.

So, to observe the CP violation in the $B\bar{B}$ system and to determine the CKM matrix elements, two B-factories were proposed one at KEK (High Energy Accelerator Research Organisation), Japan and another at PEP at SLAC, USA in 1994. The B-factory at KEK is called KEK B-factory. For the present study the experimental setup consists of the KEKB accelerator [81, 82] and the Belle detector [83–85]. The KEKB is an asymmetric energy e^+e^- collider with e^- having energy 8 GeV and e^+ having energy 3.5 GeV. The center-of-mass (CM) energy $\sqrt{s}$ of this e^+ e^- collision at KEK B-factory is

$$\sqrt{s} = \sqrt{4E_{e^+}E_{e^-}} = 10.58 \text{ GeV}. \quad (2.1)$$

which is equal to the mass of $\Upsilon(4S)$ resonance. The $\Upsilon(4S)$ mainly decays to $B^0\bar{B}^0$ or B^+B^- in almost equal amount. Since the energy of e^+ and e^- is asymmetric, so the B-meson pairs are created with a Lorentz boost factor of

$$\beta\gamma = \frac{E_{e^-} - E_{e^+}}{\sqrt{s}} = 0.425. \quad (2.2)$$

Since the branching fractions of the B decays are very small, so large number of B

Table 2.1: B-factories in the world.

Institute	Accelerator	Type	Detector	Year
Cornell	CESR	e^+e^- sym.	CLEO II, III [86]	1995 – 2001
SLAC	PEP-II	e^+e^- asym.	BABAR [87]	1999 – 2008
KEK	KEK-B	e^+e^- asym.	Belle [88]	1999 – 2010
DESY	HERA	fixed (p+wires)	HERA-B [89]	1999 – 2003
CERN	LHC	pp	LHCb [90]	2007 –

mesons are necessary for the CP violation studies. The design luminosity of KEKB machine is 1×10^{34} cm^{-2}s^{-1} which corresponds to the production of 10^8 B mesons per year. Since at KEKB collider large number of B mesons are produced, thus it is often called as KEK B-factory (KEKB).

Table 2.1 displays the list of accelerators in the world to study B physics. However, KEKB and PEP-II are the only two B-factories.

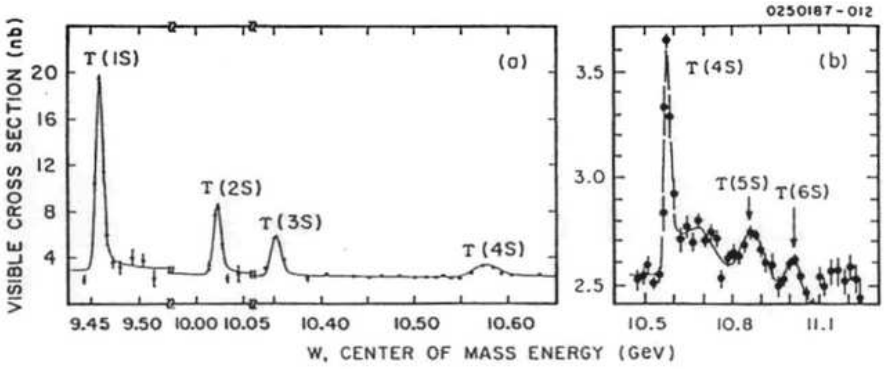

Figure 2.1: Total e^+e^- annihilation cross-section measured by CLEO. The energy regions (a) $\Upsilon(1S)$ through $\Upsilon(4S)$ (b) $\Upsilon(4S)$ through $\Upsilon(6S)$ are shown. Widths of $\Upsilon(1S)$, $\Upsilon(2S)$ and $\Upsilon(3S)$ are dominated by the beam energy resolution. A small bump between $\Upsilon(4S)$ and $\Upsilon(5S)$ is not clarified.

2.2 $\Upsilon(4S)$ Meson

The Υ mesons are the bound state of the $b\bar{b}$ with $J^{PC} = 1^{--}$. Experimental B physics study began in 1977 when the CFS (Columbia-Fermilab-Stony Brook) Collaboration at Fermilab observed a narrow resonance at an energy of about 9.5 GeV in the reaction $p + \text{nucleus} \to \mu^+\mu^- + \text{X}$ [77], resonance named as $\Upsilon(1S)$. Later on the Υ mesons were confirmed by experiments at CESR and DORIS. Figure 2.1 shows the total e^+e^- annihilation cross-section as a function of the CM energy in the region of Υ resonances measured by CLEO. The masses and widths of the resonances are listed in Table 2.2. The width of $\Upsilon(4S)$ resonance is significantly larger than the width of the three lighter resonances ($\Upsilon(1S)$, $\Upsilon(2S)$ and $\Upsilon(3S)$). The OZI (Okubo-Zweig-Iizuka) suppression of hadronic decays is responsible for the narrow width of the $\Upsilon(1S)$, $\Upsilon(2S)$ and $\Upsilon(3S)$ states.

The mass of $\Upsilon(4S)$ meson is just above the threshold of $B\bar{B}$ production. The cross-section of the $\Upsilon(4S)$ production at $\Upsilon(4S)$ peak position is about 1/3 of that of $q\bar{q}$ ($q = u, d, s, c$) ("continuum") production. Although KEKB machine is operated

Table 2.2: Masses and widths of Υ mesons.

Meson	Mass (MeV/c^2)	Total width (MeV)
$\Upsilon(1S)$	9460.30±0.26	0.05402±0.00125
$\Upsilon(2S)$	10023.26±0.31	0.03198±0.00263
$\Upsilon(3S)$	10355.2±0.5	0.02032±0.00185
$\Upsilon(4S)$	10579.4±1.2	20.5±2.5
$\Upsilon(5S)$	10876±11	55±28
$\Upsilon(6S)$	11019±8	79±16

at the $\Upsilon(4S)$ resonance to produce large number of $B\bar{B}$ pairs, it also produces three times more $q\bar{q}$ events that contribute as background to the B physics. In order to study the $q\bar{q}$ events background contribution, KEKB accelerator is also operated at 60 MeV below the $\Upsilon(4S)$ resonance. The operations at the $\Upsilon(4S)$ resonance and 60 MeV below this resonance are referred as "on-resonance" and "off-resonance" data respectively. Around 10% of data collected by Belle detector is off-resonance data. Due to the lower invariant mass of the $q\bar{q}$ pair, they are produced with a significant boost factor resulting in jets. Conversely, the $B\bar{B}$ pairs, being produced nearly at rest, have a spherical event shape. Event shape variable, which exploit this difference in topology is used to suppress continuum background events from signal events.

The branching fractions for $\Upsilon(4S)$ to $B\bar{B}$ pairs is more than 96% according to the measurement by CLEO [91]. The world average ratio of the branching fractions of $\Upsilon(4S)$ to B^+B^- and $B^0\bar{B}^0$ is given below [1]:

$$\frac{\mathcal{B}(\Upsilon(4S) \to B^+B^-)}{\mathcal{B}(\Upsilon(4S) \to B^0\bar{B}^0)} = 1.058 \pm 0.024. \tag{2.3}$$

which is consistent with equal production rate of charged and neutral pairs. In this study, the PDG convention is followed, which assumes an equal production rate.

2.3 KEKB Accelerator

The configuration of the KEKB storage ring is shown in Figure 2.2. It is necessary to measure the decay time of B as well as $\bar{B}$ mesons in order to observe the time dependent CP violation. So, B mesons are Lorentz boosted and their decay points are measured. In order to generate the Lorentz boosted B meson pairs, KEKB is

designed to be an asymmetric energy e^+e^- collider consisting of two rings. The ring for e^- having energy 8 GeV is called high energy ring (HER) while for e^+ having energy 3.5 GeV is called low energy ring (LER). The HER and LER were constructed side by side in the tunnel. The circumference of each ring is 3016 m, having four straight sections. In the KEKB accelerator, there is only one interaction point (IP) in the Tsukuba area. At the IP, the electron and positron beams are made to collide with a finite crossing angle of ± 11 mrad and Belle detector is located at IP to detect and measure the properties of the produced particles in the interaction. The straight section in Fuji area is used to inject 8 GeV electron and 3.5 GeV positron beams from Linac.

In a first stage of the linac, electrons are accelerated to an energy of 4 GeV. Positrons are then produced by hitting a thin tungsten monocrystal target with some of these electrons, which will radiate photons. These photons further create electron-positron pairs. Out of these, positrons are collected and accelerated to 3.5 GeV. The electron beam is then accelerated further to 8 GeV, and both beams are directly injected into the rings at full energies (3.5 GeV and 8 GeV respectively for LER (e^+) and HER (e^-)).

In order to compensate the energy loss of the beam due to synchrotron radiations, two kinds of RF cavities, normal cavities called ARES and superconducting cavities (SCC) [92] having frequency 508.9 MHz, are installed. There are 16 ARES cavities for LER in Fuji area while 10 ARES and 8 SCCs cavities for HER in Oho and Nikko area respectively. In order to reduce the longitudinal damping time of LER, wigglers magnets are installed in Oho and Nikko area. To achieve the higher luminosity the basic parameters of machine are determined. The designed parameters of KEKB accelerator are shown in the Table 2.3.

On June 2009, double luminosity was achieved ($2.1083 \times 10^{34}\ cm^{-2}s^{-1}$) in comparison with designed one. Accelerator stopped working on 30^{th} June, 2010 due to major upgrade to super-KEKB. Belle detector has accumulated data sample of ~ 1014 fb^{-1} (includes different Υ resonances and off-resonance data) which can be divided into different data sets as mentioned in Table 2.4.

Table 2.3: Design parameters of KEKB accelerator.

Ring		LER	HER	Unit
Particles		e^+	e^-	
Energy	E	3.5	8.0	GeV
Circumference	C	3016.26		m
Luminosity	L	1×10^{34}		$\mathrm{cm}^{-2}\mathrm{s}^{-1}$
Crossing angle	θ_x	± 11		mrad
Tune shift	ξ_x/ξ_y	0.039/0.052		
Beta function at the IP	β_x^*/β_y^*	33/1		cm
Beam Current	I	2.6	1.1	A
Natural bunch length	σ_x	0.4		cm
Energy spread	σ_E/E	7.1×10^{-4}	6.7×10^{-4}	
Number of bunches		~ 5000		
Bunch spacing	S_B	0.59		m
Particles/bunch		3.3×10^{10}	1.4×10^{10}	
Emittance	ϵ_x/ϵ_y	18/0.36		nm
Synchrotron tune	ν_s	$0.01 \sim 0.02$		
Betatron tune	ν_x/ν_y	45.52/45.08	47.52/43.08	
Momentum compaction factor	α_p	$1 \times 10^{-4} \sim 2 \times 10^{-4}$		
Energy loss/turn	U_0	$0.81^\dagger/1.5^\ddagger$	4.8	MeV
Total RF voltage	V_c	$5 \sim 10$	$10 \sim 20$	MV
RF frequency	f_{RF}	508.887		MHz
Harmonic number	h	5120		
Longitudinal damping time	τ_ϵ	$43^\dagger/23^\ddagger$	23	ms
Total beam power	P_b	$2.7^\dagger/4.5^\ddagger$	4.0	MW
Radiation power	P_{SR}	$2.1^\dagger/4.0^\ddagger$	3.8	MW
HOM power	P_{HOM}	0.57	0.15	MW
Bending Radius	ρ	16.3	104.5	m
Length of bending magnet	L_b	0.915	5.86	m

† without wigglers ‡ with wigglers

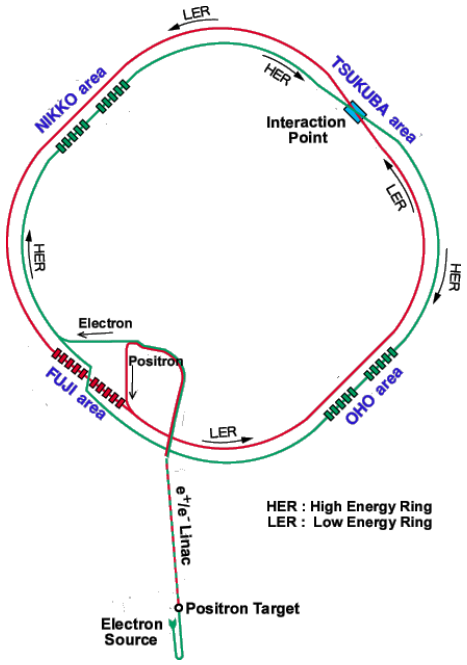

Figure 2.2: Configuration of the KEKB accelerator.

Table 2.4: Accumulated data set at Belle.

Resonance	Luminosity (fb^{-1})
$\Upsilon(1S)$	6
$\Upsilon(2S)$	24
$\Upsilon(3S)$	3
$\Upsilon(4S)$	711
$\Upsilon(5S)$	121
Off reson./scan	$\sim$ 100

2.4 The Belle Detector

At the KEK B-factory, the design of Belle detector was optimized to carry out quantitative studies of B-meson decays and in particular rare B-meson decay modes with very small branching fractions using an asymmetric e^+e^- collider operating at the $\Upsilon(4S)$ resonance. The Belle detector is configured around a 1.5 T superconducting solenoidal magnet. Figure 2.3 shows the side-view (top) and over-view (bottom) of the Belle detector.

The following coordinate system is used: the z axis is defined as the direction of

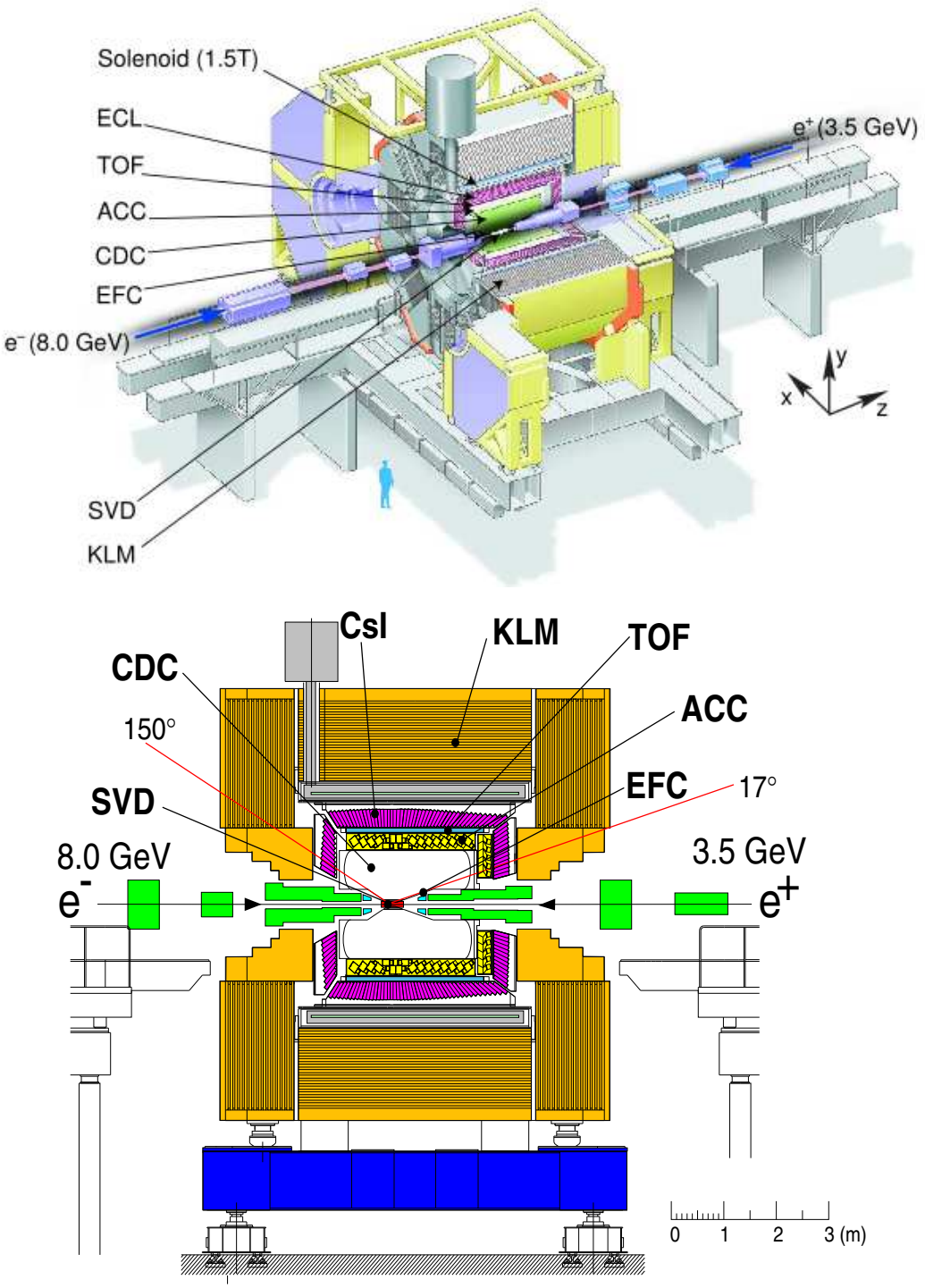

Figure 2.3: Side-view (top) and over-view (bottom) of Belle detector with the major components indicated.

the magnetic field within the solenoid, which is anti-parallel to the positron beam. The x and y axes are aligned horizontally and vertically respectively and corresponds to a right-handed coordinate system. The polar angle (θ) is subtended from the positive z axis. The azimuthal angle (ϕ) is subtended from the positive x axis, lies in the xy plane. The radius, defined in a cylindrical coordinate system, is measured from the origin in the xy plane, $r = \sqrt{x^2 + y^2}$. The origin is defined as the position of the nominal interaction point (IP). The Belle detector is timed with the KEKB Radio Frequency (RF), which governs the bunch crossing rate ($\sim$ 509 MHz, $\sim$ 2 ns interval).

The B mesons decay vertices are measured by a Silicon Vertex Detector (SVD) [93] situated just outside of the cylindrical beryllium beam pipe of the accelerator. Charged particle tracking is performed by a wire drift chamber known as Central Drift Chamber (CDC) [94] with the help of SVD. Particle identification (of charged particles) is provided by specific ionisation energy loss (dE/dx) measurements made with the CDC, light yield readings from Aerogel $\check{C}$erenkov Counter (ACC) [95] and time of flight information from Time-Of-Flight (TOF) [96] detector. The electromagnetic showers of electron/positron, photons and neutral pions are detected in an array of CsI(Tl) crystals of Electromagnetic Calorimeter (ECL) located inside the solenoid coil. The K_L^0 mesons and muons are identified by KLM detector which consists of arrays of Resistive Plate Counters (RPC) interspersed in the iron yoke. The detector covers the θ region extending from 17^o-150^o. The part of the uncovered small angle region is instrumented with a pair of BGO crystal arrays (EFC) placed on the surfaces of the QCS cryostats in the forward and backward directions. The summary of parameters of Belle detector are shown in Table 2.5. Details of each sub-detector part is described in the following sub-sections.

2.4.1 Beam Pipe

The precise determination of decay vertices is an essential feature of Belle experiment to observe CP violation. Multiple Coulomb scattering of produced particles in the beam pipe wall and first layer of the silicon vertex detector are the limiting factors

Table 2.5: Summary of the parameters of the Belle detector. The performance is based on the measurement at a beam-test or a physics run.

Detector	Type	Configuration	Readout	Performance
Beam pipe (SVDI)	Beryllium double-wall	Cylindrical, r = 20 mm 0.5 (Be)/2.5 (He)/0.5 (Be)mm		He gas cooled
SVDII		Inner r = 15 mm, 0.5 (Be)/2.5 (PF200)/0.5 (Be)mm		
SVDI	Double-sided Si-strip	300 μm thick 3-layers r = 3.0 - 6.05 cm	ϕ : 40.96 k θ: 40.99 k	$\sigma_{\Delta Z} \sim 100$ μm (MC)
SVDII	Double-sided Si-strip	300 μ m thick 4-layers r = 2.0 - 8.8 cm	ϕ : 55.296 k θ: 55.296 k	$\sigma_{\Delta Z} \sim 100$ μm (MC)
CDC	Small cell drift chamber	Anode: 50 layers Cathode: 3 layers r = 8.3 – 86.3 cm -77 cm $\leq z \leq$ 160 cm	Anode 8400 Cathode 1792	$\sigma_{r\phi} = 130$ μm $\sigma_z = 200 - 1400$ μm σ_{p_t}/p_t $= 0.3\%\sqrt{p_t^2+1}$ $\sigma_{dE/dx} = 6\%$
ACC	Silica Aerogel	960 barrel/228 endcap FM-PMT readout	1788	K/π separation at $1.2 < p < 3.5$ GeV/c
TOF/TSC	Plastic Scintillator	128 ϕ segmentations r = 120 cm, 3 m long TSC: 64 ϕ segmentations	TOF: 128×2 TSC: 64	$\sigma_t = 100$ ps K/π separation at $p < 1.2$ GeV/c
ECL	CsI(Tl) (towered structure)	Barrel: r = 125-162 cm Endcap: $z = -102$ cm and 196 cm	B: 6624 FE: 1152 BE: 960	$\sigma_E/E = (0.066\%/E \oplus 0.81\%/E^{1/4} \oplus 1.34)\%$ (E in GeV)
Magnet	Superconducting	inner radius (r) = 179 cm		B = 1.5 T
KLM	Resistive plate counters	14 layers (5 cm Fe + 4 cm gap) 2 RPCs in each gap	$\phi : 16k$ $\theta : 16k$	$\Delta\phi = \Delta\theta = 30$ mrad for K_L^0 1% hadron fake rate for μ
EFC	BGO crystal 14 layers	$2 \times 1.5 \times 12$ cm^3 Segmentation 32 in ϕ, 5 in θ	320	$\sigma_E/E = (0.3-1)\%/\sqrt{E}$

on the z-vertex position resolution. Thus it is very essential to minimize the beam pipe thickness and it should be enough thick so that it withstand the beam-induced heating, which can be up to several hundred watts. And this also requires an active cooling system for beam pipe and a mechanism for shielding the vertex detector from this heat, which is provided by helium gas channel. The helium gas cooling is adopted instead of water in order to minimize the material in the beam pipe. Figure 2.4 shows the cross-section of beam pipe at interaction point. The beam pipe consists of two concentric cylinders made of beryllium with different radii, 20.0 mm and 23.0 mm respectively. Each cylinder has 0.5 mm of thickness and the space between two cylinders is filled with helium gas for cooling.

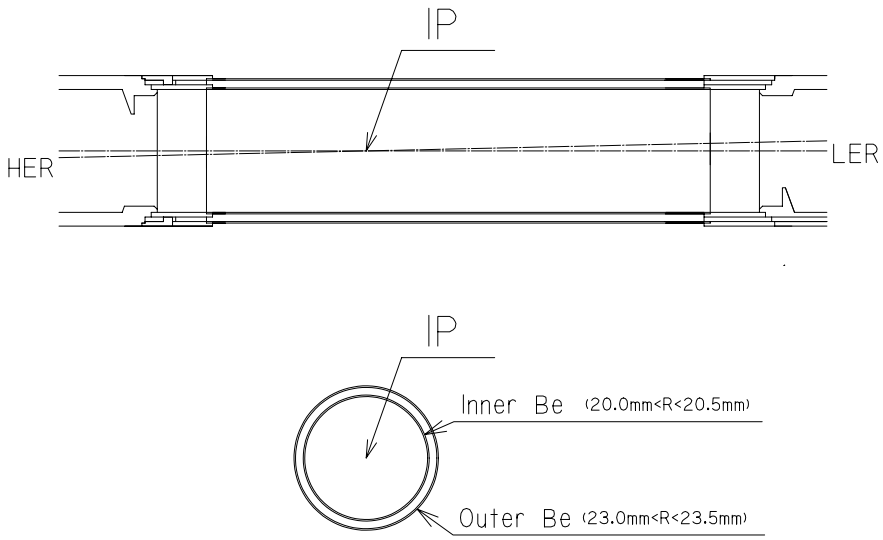

Figure 2.4: Cross-section of the beryllium beam pipe at the interaction point.

2.4.2 Silicon Vertex Detector (SVD)

The SVD provides precise measurement of the decay vertices of B-mesons which is essential for the time-dependent CP violation. It also helps to measure the flight length of the produced B mesons in z-direction with precise measurement ($\sim$ 100 μm). The SVD is used to measure the decay vertices of another particles such as D meson, τ

particles and it also contributes to the track reconstruction of charged particles and helps to improve the momentum resolution of the particles. The SVD is placed around the beam pipe to withstand the large beam background and vertex resolution should be dominated by multiple coulomb scattering as most particles of interest in Belle detector have momenta of 1 GeV/c. Also support structure must be low in mass but rigid and readout electronics must be placed outside the tracking volume. Moreover, since the vertex resolution improves inversely with the distance to the first detection layer, the vertex detector has to be placed as close as possible to the interaction point and thus to reduce the beam pipe wall. Figure 2.5 shows the cross-sectional and side view of SVDI. It consists of three cylindrical detection layers of "ladders" in a barrel-only design, where a ladder is composed of two, three or four double sided silicon strip detectors (DSSD). The DSSD is essentially a pn junction, operated under reverse bias to reach full depletion. A charged particle passing through the junction liberates electrons from the valence band into the conduction band creating electron-hole (e^-h^+) pairs. These pairs create currents in the p and n strips situated along the surface of the bulk on opposing sides of the DSSD. The p strips are aligned along the beam axis and measure the azimuthal angle ϕ. The n strips are aligned perpendicular to the beam axis and measure z. SVDI covers a solid angle $23^o < \theta < 139^o$; where θ is a polar angle from beam axis and it corresponds to ∼86% of the total solid angle. As shown in Figure 2.5, the three layers of SVDI consists of 8, 10 and 14 ladders for inner, middle and outer layers respectively. The radii of each ladder is 30.0 mm, 45.5 mm and 60.5 mm respectively. Each ladder is made of two half-ladders that are electrically independent, but mechanically joined by support ribs. The support ribs are made of boron-nitride (BN), sandwiched by carbon-fibre reinforced plastic (CFRP). In total, there are 32 ladders and 102 DSSDs. Each DSSD has 1280 sense strips and 640 readout pads on both the sides. Each DSSD size is 57.5×33.5 mm^2. Signal from DSSDs are read out by 128 channel VA1 chips [97] placed on both sides of the ladder. Inside the VA1 chip, signals are amplified and sent to shaping circuits, where the shaping time is adjusted to about 1 μs to minimize the occupancy due to the beam background. Then, the outputs of the shaper are held when the VA1 chips receive

a Level-0 (L0) trigger signal provided by TOF. This analog information is passed to fast analog-to-digital converters (FADC) in the electronic hut if a Level-1 (L1) trigger occurs. The total number of readout channels are 81,920. VA1 has excellent noise performance and reasonably good radiation tolerance of 200 kRad.

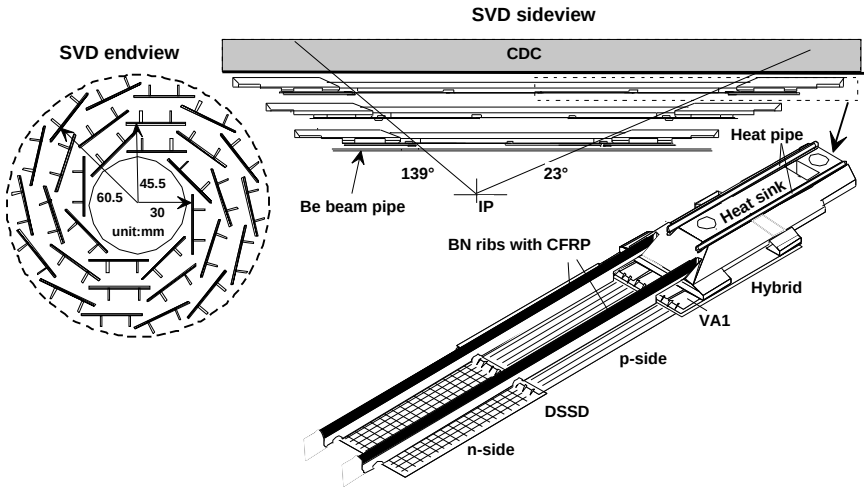

Figure 2.5: Detector configuration of first version of silicon vertex detector (SVDI) shown in a cross-section (left) and in a side-view (right).

The momentum and angular dependence of the impact parameter (closest approach of tracks to the interaction point) resolution can be well represented by the following formula:

$$\sigma_{xy} = 19 \oplus \frac{50}{(p\beta \sin^{3/2}\theta)}\mu\text{m}. \quad (2.4)$$

$$\sigma_{z} = 36 \oplus \frac{42}{(p\beta \sin^{5/2}\theta)}\mu\text{m}. \quad (2.5)$$

where $\oplus$ indicates a quadratic sum, the momentum p (track momentum) is given in units of GeV/c and the polar angle is θ.

SVDII

New SVD (SVDII) [98] was installed in the summer of 2003. There are many improvements of this one as compared to SVDI. The geometrical configuration of SVDII is

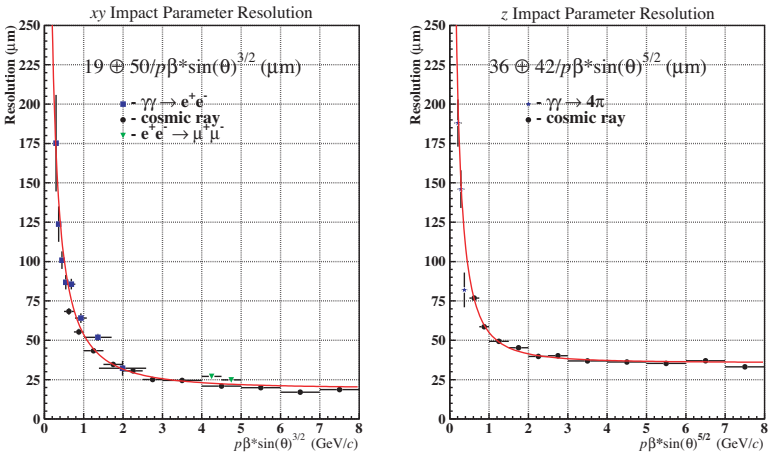

Figure 2.6: Impact parameter resolution of the SVDI.

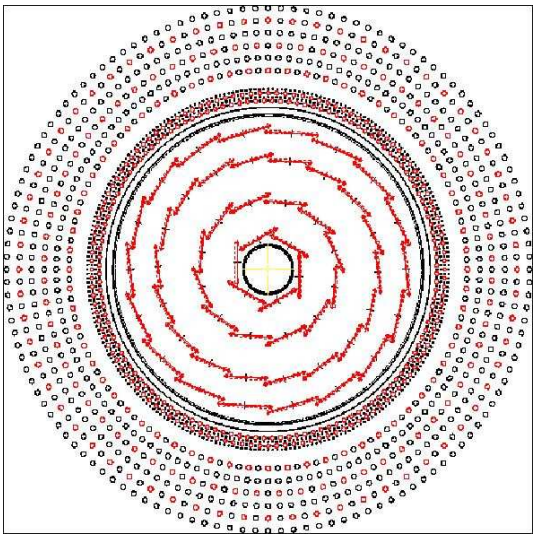

Figure 2.7: Detector configuration of the second version of silicon vertex detector (SVDII) shown in a cross-section.

shown in Figure 2.7 and Figure 2.8. For SVDII, the radius of the beam pipe has been reduced from 20 to 15 mm to put silicon closer to interaction point and to achieve better vertex resolution. The SVDII consists of four cylindrical layers whose radii are 20 mm, 43.5 mm, 70.0 mm and 88.0 mm from the IP. The angular acceptance has

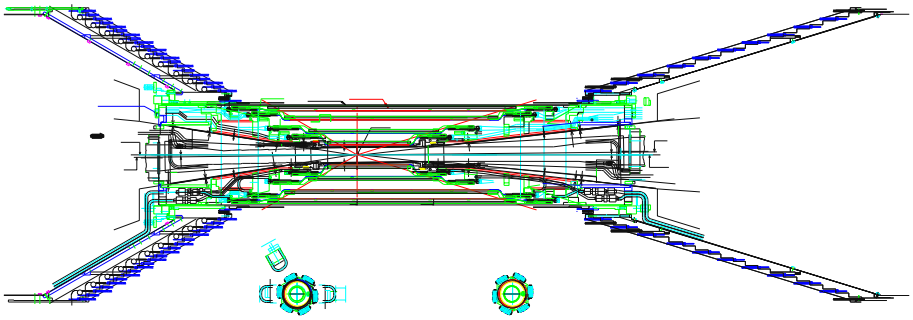

Figure 2.8: Side-view of SVDII.

been extended to $17^o < \theta < 150^o$, which is the same as CDC acceptance and it covers 92% of the total solid angle. In layer 1/2/3/4, we have 2/3/5/6 DSSDs along the z-direction in a ladder, and 6/12/18/18 ladders to cover all the ϕ region, respectively. There are two kinds of DSSDs. One is used in 1^{st}, 2^{nd} and 3^{rd} layers, the size is 28.4 $\times$ 79.6 mm^2, the strip pitch is 75 μm on p-side and 50 μm on n-side. The other one is used in 4^{th} layer, the size is 34.9 $\times$ 76.4 mm^2, the strip pitch is 73 μm on p-side and 65 μm on n-side. The n-side DSSDs is used for the measurement of the $r-\phi$ coordinate and the p-side is used for the measurement of the z-coordinate. The number of strip is 512 in both n-side and p-side. The total number of DSSDs is 246. Therefore the total number of readout channel is 1,10,592. As in SVDI each ladder is read out by four hybrids circuits. Each hybrid employs four VA1TA (VA1 with trigger functions) chips, each VA1TA chips reads and amplifies the signals from 128 strips, whose pulse heights are held and sent out serially to DAQ. To minimize the readout dead time the four chips on each hybrid are read in parallel, in contrast to SVDI where the chips were read sequentially. This represents a significant reduction in the overall dead time of the Belle DAQ system. The VA1TA also incorporated a fast shaper and discriminator that provide digital signals used in the trigger. The signals are de-multiplexed in the FADC boards housed in the electronics hut of Belle detector.

2.4.3 Central Drift Chamber (CDC)

The determination of three dimensional trajectories of charged particles and precise measurement of their momenta is the main motive of Central Drift Chamber (CDC). The 1.5 T magnetic field of superconducting solenoid bends the charged particle according to their momenta. The physics goal of the experiment require a momentum resolution of $\sigma_{p_t}/p_t \approx 0.5\%\sqrt{1+p_t^2}$ (where p_t is in GeV/c) for all charged particles with $p_t \geq 100$ MeV/c in the polar angle region $17^o \leq \theta \leq 150^o$. In addition, the CDC is used to measure the energy loss (dE/dx) of charged particles for their particle identification. The amount of dE/dx depends on $\beta = v/c$ of the charged particle (Bethe-Bloch formula). Another important role of the CDC is to provide an important information regarding trigger system in the $r-\phi$ and z dimensions.

The structure of CDC is shown in Figure 2.9. It consists of three geometrical sections, referred to as the cathode, the conical-shaped inner and toroidal-shaped outer. It is a cylindrical wire drift chamber having 50 layers (32 axial and 18 small angle stereo layers) of anode wires and three cathode strip layers. The CDC is asymmetric in the z-direction. Axial wires measure the $r-\phi$ position, while the stereo wires are slanted approximately ± 50 mrad. The stereo layers combined with axial layers provide z information of tracks. The cathode strips improve the z-measurement as well as produce a highly efficient fast z-trigger.

The CDC contains a total of 8400 drift cells. A drift cell is the functional unit of the CDC. It consists of a positively biased sense wire surrounded by eight negatively biased field wires strung along the beam direction. Each drift cell has a maximum drift distance between 8 mm to 10 mm. The sense wires are gold-plated tungsten wires of 30 μm in diameter to maximize the drift electric field. The field wires are of unplated aluminium of 126 μm in diameter are arranged to produce high electric field up to the edge of the cell and also to simplify the drift time-to-distance relation. The aluminium field wires are used to reduce the material of the chamber. The electric field strength at the surface of the aluminium field wires is always less than 20 kV/cm, a necessary condition for avoiding radiation damage.

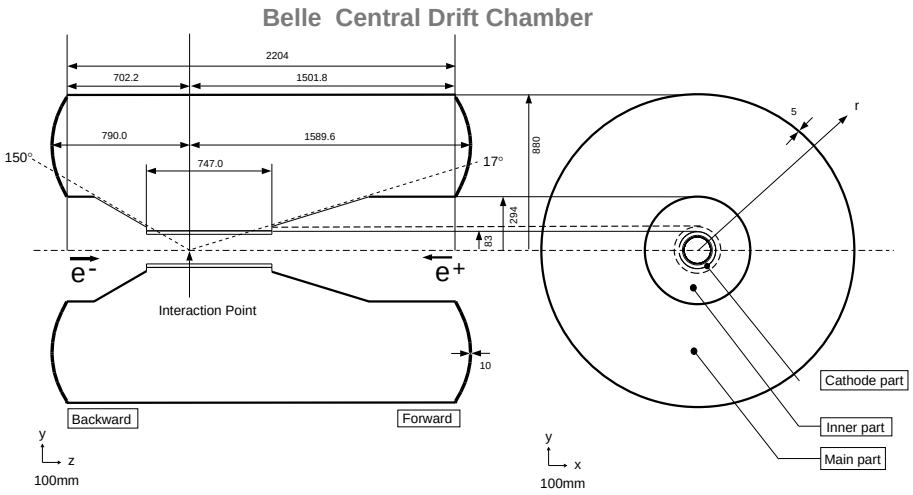

Figure 2.9: Structure of the CDC. Lengths in figure are in the unit of mm.

Three z-coordinate measurements at the inner-most radii are provided by cathode strips as shown in Figure 2.10. The cathode strip having width of 7.4 mm is divided into eight segments in the ϕ-direction and has an 8.2 mm pitch in the z-direction. The total number of cathode channels are 1792.

To minimize the multiple coulomb scattering contributions which affects the momentum resolution of the charged particles, a low Z (atomic number) gas is used, which is a mixture of 50% helium (He) and 50% ethane (C_2H_6) gas [99]. The drift cells are immersed in this mixture. This mixture has a long radiation length (640 m) and a drift velocity that saturates at 4 cm/μs at a relatively low electric field. Even though the gas mixture has a low Z, a good dE/dx resolution is provided by the large C_2H_6 component.

Signals from the chamber are amplified by pre-amplifiers and sent to Shaper/ Discriminator/QTC modules in the electronics hut via $\sim$ 30 m long twisted pair of cables. These modules receive shaped and discriminated signals and perform a charge (Q) -to-time (T) conversion (QTC) [100]. The modules internally generate the logic-level output where the leading edge corresponds to the drift time and width is proportional to the input pulse height. The output signals are read by time-to-

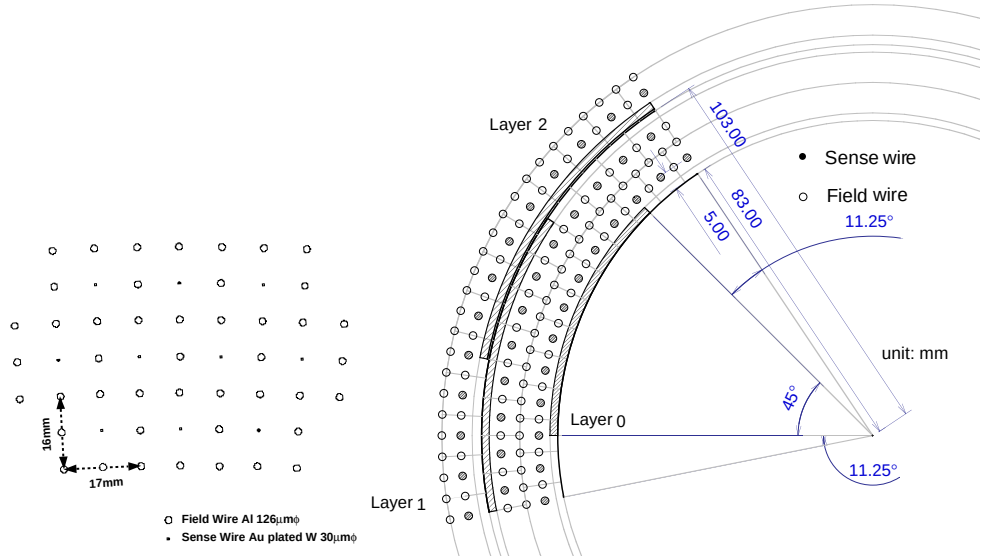

Figure 2.10: CDC Cell structure. Cathode sector configuration is also shown in the right figure.

digital converters (TDC). The input pulse height of the signal is used to measure dE/dx.

The spatial resolution as a function of the drift distance is shown in Figure 2.11. Near the sense wire and near the cell boundary the spatial resolution is significantly poorer. The spatial resolution for tracks passing near the middle of the drift space is approximately 130 μm. Figure 2.12 shows the p_t dependence on p_t resolution for cosmic rays. The solid curve indicates the result fitted to the data points to the transverse momentum resolution function σ_{p_t}/p_t is $((0.201\pm\ 0.003)p_t\oplus(0.290\pm\ 0.006)/\beta)\%$; where p_t is the transverse momentum measured in GeV/c. The dashed curve shows the ideal expectation for $\beta = 1$ particles.

Charged particle tracking is done by Kalman filtering method [101], taking into account the effect of multiple Coulomb scattering, energy loss, and non-uniformity of the magnetic field.

The average rate of energy loss (dE/dx) of a charged particle is given by the

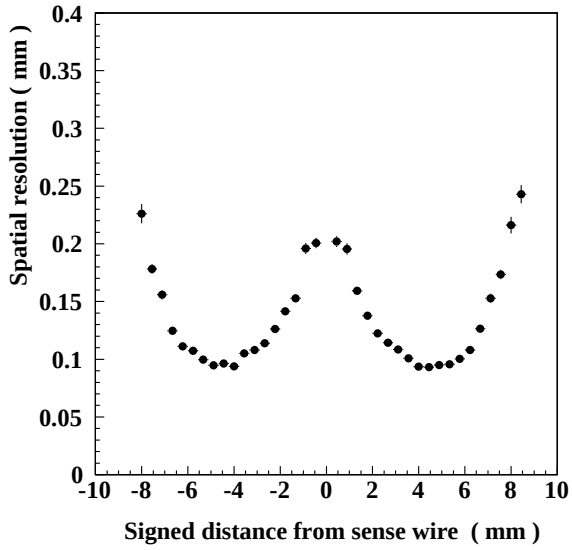

Figure 2.11: Spatial resolution as a function of the drift distance.

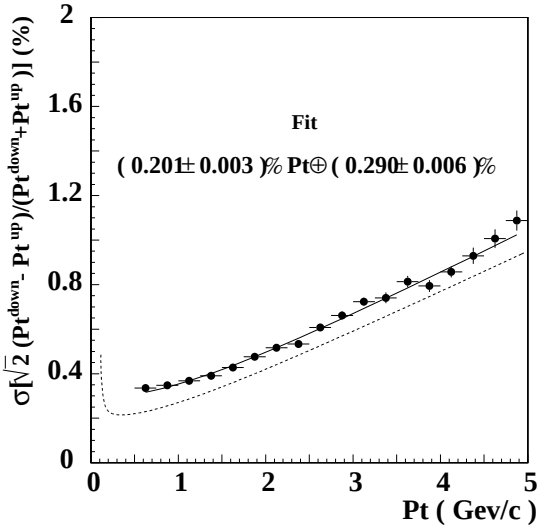

Figure 2.12: p_t dependence on p_t resolution for cosmic rays. The solid curve shows the fitted result $((0.201\pm\ 0.003)p_t\oplus(0.290\pm\ 0.006)/\beta)\%$ and the dotted curve shows the ideal expectation for $\beta = 1$ particles.

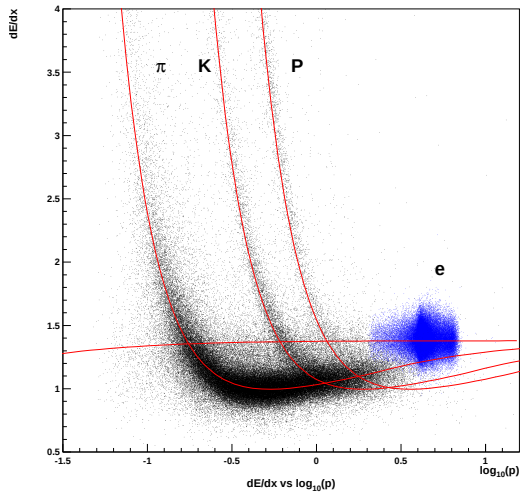

Figure 2.13: Scatter plot for momentum vs dE/dx taken during accelerator operations. Expected relation for π, K, p and e are shown by the solid curves. The momenta are given in units of GeV/c.

following Bethe-Bloch equation,

$$-\frac{dE}{dx} = 4\pi N_A r_e^2 m_e c^2 \frac{Z}{A}(\frac{z}{\beta})[\log\,(\frac{2m_e c^2\beta^2\gamma^2}{I})\;-\;\beta^2\;-\;\frac{\delta}{2}]. \qquad (2.6)$$

where N_A is the Avagadro's number, r_e is the classical electron radius, m_e is the mass of the electron. Z and A are the atomic number and mass number of the atoms of the medium, z and v are the charge (in units of e) and velocity of particle, $\beta = v/c$, $\gamma = 1/\sqrt{1-\beta^2}$, $I \approx 167Z^{0.9}$ eV is the mean excitation energy of the medium, and x is the path length in the medium, measured in gcm^{-2}. Equation 2.6 shows that the dE/dx is independent of the mass of the particle and depends on β. Therefore we can estimate β from a measurement of dE/dx. The measurement of β can provide a useful method for estimating the rest mass and thus differentiating particle species in conjunction with the momentum measurement.

Track parameters are improved by combining the SVD and CDC information.

The combined performance is given below:

$$\sigma_{xy} = 19 \oplus \frac{50}{(p\beta \sin^{3/2}\theta)}\mu\text{m}, \quad (2.7)$$

$$\sigma_z = 36 \oplus \frac{42}{(p\beta \sin^{5/2}\theta)}\mu\text{m}. \quad (2.8)$$

$$\frac{\sigma_{p_t}}{p_t} = (0.19 p_t \oplus 0.34)\%. \quad (2.9)$$

where momentum (p) and transverse momentum (p_t) are in GeV/c, β is the particle speed and θ is its polar angle.

The CDC is involved in the particle identification for the tracks with momentum $p < 0.8$ GeV/c and $p > 2.0$ GeV/c measuring dE/dx. Figure 2.13 shows the scattered plot of the measured dE/dx and the particle momentum. Expected relation for π, K, p and e are shown by the solid curves in Figure 2.13. The dE/dx resolution, measured in a sample of pions from K^0_S decays is 7.8%. The CDC can be used to distinguish pions from kaons of momenta up to 0.8 GeV/c with a 3σ separation.

2.4.4 Aerogel Čerenkov Counter (ACC)

Particle identification, specifically the identification of $\pi^\pm$ and $K^\pm$ plays an important role in the elucidation of CP violation in the B mesons system as well as for our analysis decay modes. For example, studies of $B^0 \to K^+\pi^-(\pi^+\pi^-)$, $B^0 \to \rho\gamma$ as well as our cocerned decay modes require good K/π separation. Pions are the most ubiquitous particles in hadronic events, so ACC performance is measured by its ability to identify kaons amongst pions. In the momentum region below 1 GeV/c, the K/π separations have been performed by dE/dx measurement from CDC and time of flight measurements. The ACC provides the K/π separation in momentum range of $1.2 < p < 3.5$ GeV/c by detection of the Čerenkov light from particle penetrating through silica aerogel radiator. Čerenkov light is emitted if the velocity of the charged particle, β satisfies:

$$\beta = \frac{p}{\sqrt{p^2 + m^2}} > 1/n. \quad (2.10)$$

where m and p are the particle mass and momentum respectively, and n is refractive

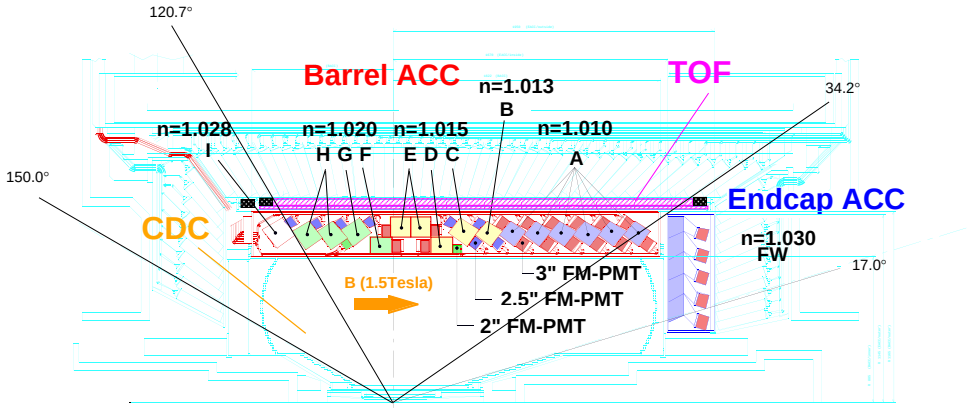

Figure 2.14: Transverse view of the ACC. Here n indicates the refractive index.

index of silica aerogel. Therefore there is a momentum region where pions emit $\check{C}$erenkov light while kaons do not, depending upon the refractive index of the matter, which is the basic concept for the particle identification by the ACC. For example, pions with momentum 2 GeV/c emit $\check{C}$erenkov light in the matter if n $>$ 1.002, while n $>$ 1.030 is necessary for kaons with the same momentum.

The ACC is divided into barrel and forward endcap regions. It spans a polar angle region of $17^o < \theta < 127^o$. The configuration of ACC is shown in Figure 2.14. The ACC consists of 960 counter modules segmented into 60 cells in the ϕ-direction for the barrel part and 228 modules arranged in 5 concentric layers for the forward endcap part of the detector. These modules are different for the barrel and endcap, and having different refractive indices. All the counters are arranged in a semi-tower geometry, pointing to the interaction point. The possible momentum range of charged particles from B decays depends on the polar angle at Belle due to the asymmetric beam energy i.e. particles with higher momentum will come into forward endcap part. In order to obtain good K/π separation for the kinematic range from 1.2 GeV/c to 3.5 GeV/c, the refractive indices of aerogels are selected between 1.01 and 1.028, depending on their polar angle region. A typical single ACC module is shown in

a) Barrel ACC Module

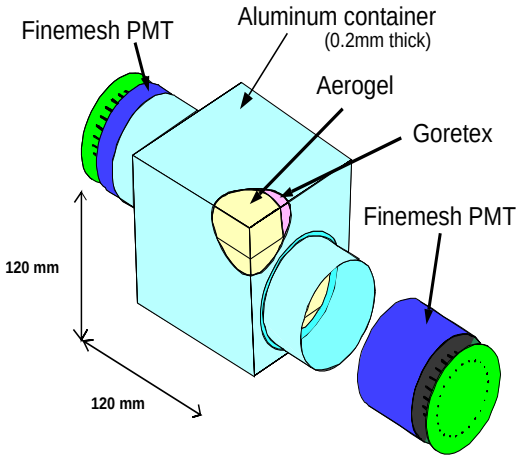

b) Endcap ACC Module

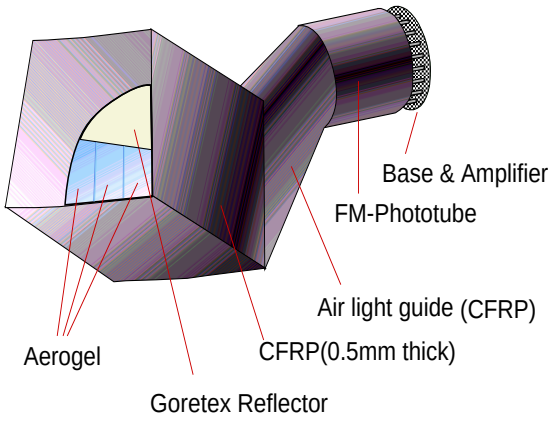

Figure 2.15: Schematic drawing of typical ACC module. (a) barrel and (b) endcap modules.

Figure 2.15 for barrel and endcap ACC respectively. The Čerenkov light generated in the silica aerogel is fed into one or two fine mesh photomultiplier's (FM-PMTs) attached to the aerogel radiator modules which are operated in the 1.5 T magnetic field [102]. The total number of PMTs readout channels are 1560 in barrel ACC and 228 in the endcap ACC.

Figure 2.16 shows the measured pulse height distribution for the barrel ACC for $e^{\pm}$ tracks in Bhabha events and $K^{\pm}$ candidates in hadronic events, which are selected by TOF and dE/dx measurements [95]. This figure clearly demonstrates a clear separation between high energy electrons and below-threshold particles. It also indicates good agreement between data and MC [103].

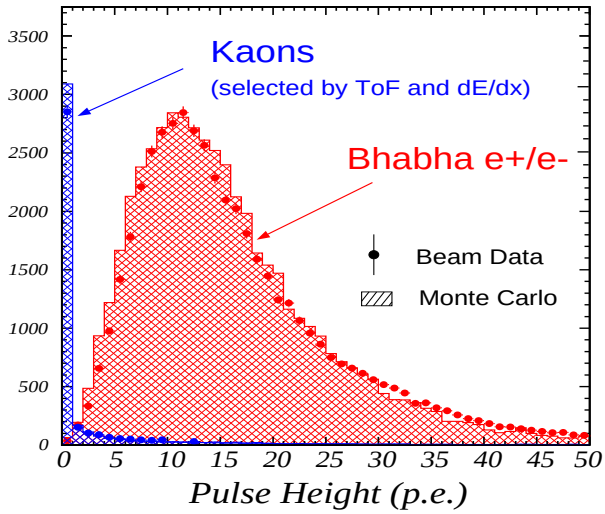

Figure 2.16: Pulse height spectrum for electrons and kaons in units of photoelectrons (p.e.) observed by the barrel ACC. Kaon candidates are obtained by dE/dx and TOF measurements. The MC expectation are superimposed.

2.4.5 Time of Flight Counter (TOF)

A time of flight (TOF) detector system, made of plastic scintillator counters, is used to distinguish kaons from pions having momentum below 1.2 GeV/c with time resolution 100 ps. This part of the detector is very interesting because 90% of the

particles produced in $\Upsilon(4S)$ decays are having above mentioned momentum. The TOF detector works on the principle of scintillation: the property of certain chemical compounds to emit short light pulses after excitation by the passage of charged particles or by photons of high energy. In addition to particle identification, TOF counters provide fast timing signals for trigger system to generate gate signals for ADCs and stop signals for TDCs. The trigger modules attached to the TOF are called Trigger Scintillation Counters (TSC). The counters measure the elapsed time between a collision at interaction point and the time when the particle hits the TOF layer. For the measured flight time (T) from TOF, and measured flight length and momentum by CDC track fit, one can estimate mass of each track in an event and therefore type of the particle.

Figure 2.17 shows the TOF/TSC module dimensions. One 5 mm thick TSC layer and one 4 cm thick TOF counter layer with a gap of 1.5 cm are arrayed cylindrically at the position (L) 1.2 m in radius from the interaction point (IP) cover a polar angle range 34^o to 120^o. The 1.5 cm gap between the TOF counters and TSC counters are introduced to isolate TOF from photon conversion backgrounds by taking the coincidence between the TOF and TSC counters. A particle with momentum atleast 0.28 GeV/c can reach the TOF counters. Scintillation light from a counter is collected by a PMT. Two PMTs are used for a TOF counter while only one is used for a TSC counter. The scintillators are wrapped with 45 μm thick polyvinyl film for light tightness and surface protection. A total number of 128 TOF counters are placed in ϕ-sectors and each counter is viewed by the FM-PMT at both ends. One FM-PMT is glued to each TSC at backward end. The total number of TSC counters are 64. The total number of readout channels are 256 for the TOF and 64 for the TSC. Each PMT signal is split into two. One is sent to Q-to-T and then to a multihit TDC for charge measurement. The other generates signals corresponding to two different, high level (HL) and low level (LL), threshold levels. The HL output provides a trigger signal and the LL output provides the TOF timing. Output pulse from the TOF pass the time-stretcher circuit, which expands the time difference of the TOF pulse and the 64 MHz reference clock by a factor of 20 with readout by the TDCs as shown in

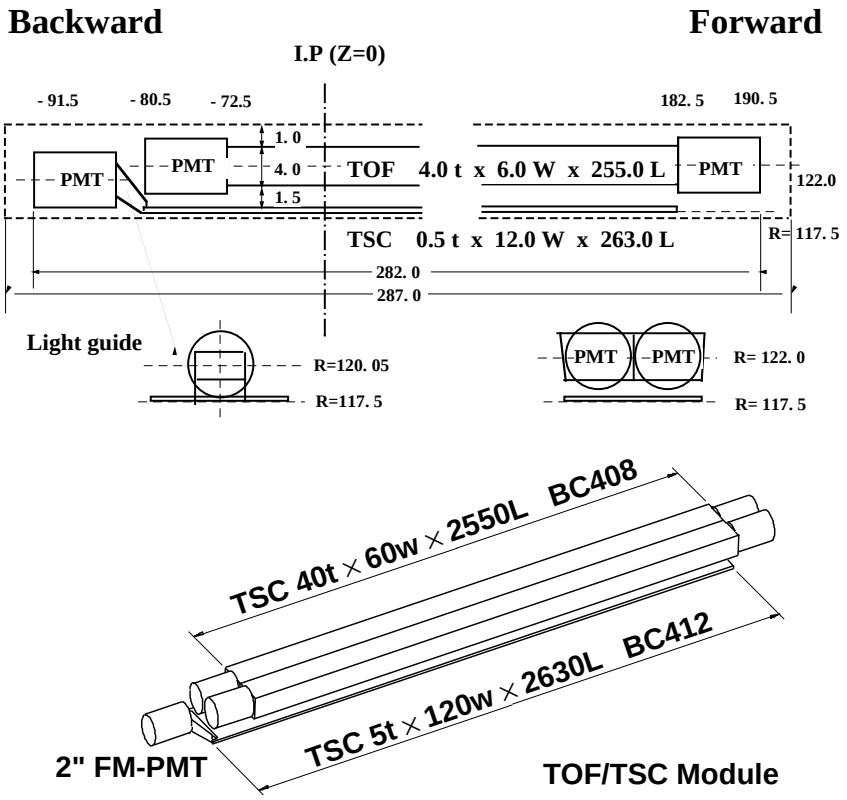

Figure 2.17: Configuration of a TOF module made of two TOF counters and one TSC.

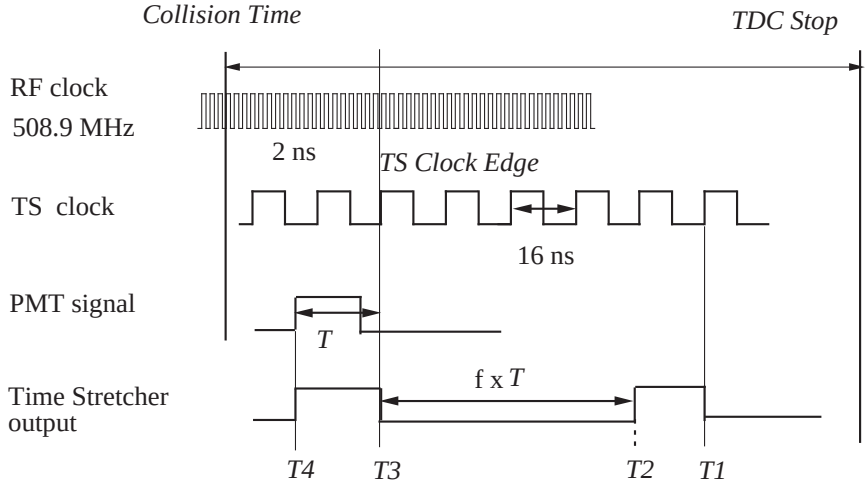

Figure 2.18: Scheme for the time stretcher for the TOF.

Figure 2.18 [96]. By this scheme the timing of the TOF pulse with 25 ps precision using the common TDCs (whose timing precision is 500 ns) can be measured.

Figure 2.19 shows the mass distribution for each track in hadron events, calculated by using the equation

$$m^2 = \left(\frac{1}{\beta^2} - 1\right)\frac{p^2}{c^2} = \left(\left(\frac{cT_{obs}^{twc}}{L_{path}}\right)^2 - 1\right)\frac{p^2}{c^2}. \quad (2.11)$$

where m is mass of the particle, p is the momentum and L_{path} is the path length of the particle determined from CDC track fit assuming the muon mass. From Figure 2.19 three clear peaks are evident, which corresponds to $\pi^{\pm}$, $K^{\pm}$ and protons (p). The data points are in good agreement with the Monte Carlo prediction (histogram) obtained by assuming $\sigma_{TOF} = 100$ ps.

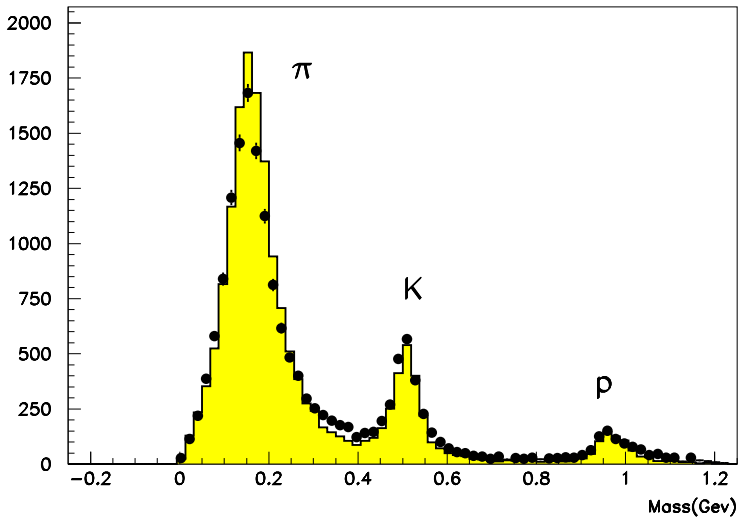

Figure 2.19: Mass distribution from TOF measurements for particles with momentum below 1.2 GeV/c. Points and histogram show the data and MC distributions respectively.

2.4.6 Electromagnetic Calorimeter (ECL)

The ECL is designed to measure the energy and position of photons and electrons produced in Belle. High energy electrons and photons entering the calorimeter in-

stigate an electromagnetic shower through subsequent bremsstrahlung and electron pair production. The main purpose of Electromagnetic Calorimeter (ECL) is the detection of these photons and electrons with high efficiency and good resolutions in energy and position. Since most of these photons are end products of cascade decays and have relatively low energies, and thus have good performance below 500 MeV is especially important. Important two body decay modes such as $B \to K^*\gamma$ and $B \to \pi^0\pi^0$ produce photon energies up to 4 GeV, so high resolution is needed to reduce background for these modes. Electron identification in our experiment relies primarily on a comparison of charged particle momentum and the energy deposited in ECL. Good electromagnetic energy resolution results in better hadron rejection. High momentum π^0 detection requires the separation of two nearby photons and a precise determination of their opening angle. This requires a fine-grained segmentation in the calorimeter.

The overall configuration of ECL is shown in Figure 2.20. It consists of a highly segmented array of CsI(Tl) crystals with silicon photodiode readout installed in a magnetic field of 1.5 T inside a superconducting solenoid. The purpose of Thallium is to shift excitation light into the visible spectrum. CsI(Tl) crystals have various nice features such as a large photon yield, weak hygroscopic nature, mechanical stability and moderate price. The barrel section of ECL is 3.0 m in length with inner radius of 1.25 m and annular endcaps at $z = +2.0$ m and -1.0 m from the interaction point. Each crystal has tower-like shape and is arranged so that it points almost to the interaction point. The calorimeter covers the polar angle region of $17^o < \theta < 150^o$, which corresponds to 91% of total solid-angle coverage of 4π. The geometrical parameters of ECL are given in Table 2.6. Small gaps between the barrel and end-cap crystals provide a pathway for cables and room for supporting members of the inner detectors. The loss of solid angle associated with these gaps is approximately 3% of the total acceptance. Typical size of CsI(Tl) crystals for the barrel region is 5.5 cm $\times$ 5.5 cm $\times$ 30 cm in the front face and 6.5 cm $\times$ 6.5 cm $\times$ 30 cm in the back face. The entire system contains 8736 CsI(Tl) counters. Each CsI(Tl) crystal length corresponds to 16.2 X_0, where X_0 is a radiation length.

Table 2.6: Geometrical parameters of ECL.

Item	θ coverage	θ seg.	ϕ seg.	No. of crytals
Forward endcap	12.4^o – 31.4^o	13	48–144	1152
Barrel	32.2^o – 128.7^o	46	144	6624
Backward endcap	130.7^o– 155.1^o	10	64 –144	960

The readout for each CsI(Tl) crystal is by independent pair of silicon PIN photodiodes and charge-sensitive pre-amplifiers attached at the end of the crystal. The energy resolution of ECL measured as a function of incident photon energy with 3 × 3 ECL matrices [104] is given by

$$\frac{\sigma_E}{E} = \frac{0.0066(\%)}{E} \oplus \frac{1.53(\%)}{E^{1/4}} \oplus 1.18\%. \tag{2.12}$$

where E is in GeV. Here, the first term is due to the contribution from electronic noise, and second and a part of the third term comes from the shower leakage fluctuations. The third term also indicates systematic effects such as the uncertainty of the calibration on crystals. The spatial resolution measured using the photon beams is given by

$$\sigma_X(mm) = 0.27 + \frac{3.4}{E^{1/2}} + \frac{1.8}{E^{1/4}}. \tag{2.13}$$

where E is measured in the units of GeV. Two-photon invariant mass distributions in hadronic events for π^0 and η are shown in Figure 2.21. The clear peaks of π^0 and η are seen at each nominal mass and the energy resolution has been achieved to be 4.8 MeV for π^0 and less than 12.1 MeV for η.

In addition to the measurement of energy of photons and electrons, the ECL plays an important role for the electron identification [105]. The electron identification is performed by combining the following informations:

- Matching between the position of the charged track measured by the CDC and that of the energy cluster measured by the ECL.
- E/p, i.e. the ratio of energy measured by the ECL to momentum measured by the CDC.

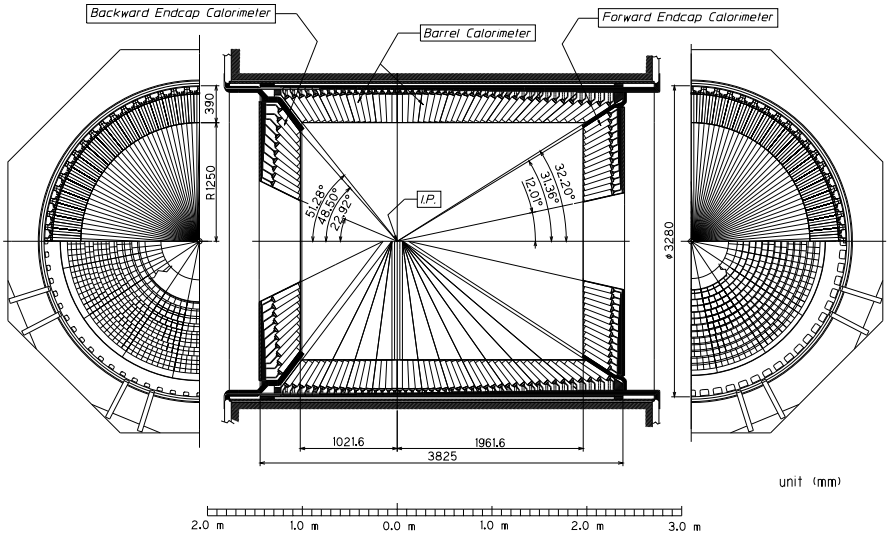

Figure 2.20: Configuration of the ECL.

- E_9/E_{25} at the ECL, i.e. the ratio of ECL shower energy in an array of 3×3 crystals to the energy in an array of 5×5 crystals.
- dE/dx measured by CDC.
- Light yield in the ACC.
- Time-of-flight measured by TOF.

The probability density functions (PDFs) for above parameters have been made and then a likelihood ratio for every track has been calculated. Figure 2.22 shows the data distributions for E/p and E_9/E_{25} for the electrons and charged pions. The PDF distributions for electrons are obtained from radiative Bhabha events ($e^+e^- \to e^+e^-\gamma$) and those for pions are obtained from $K^0_S \to \pi^+\pi^-$ decays. From the MC, the typical electron identification efficiency is estimated to be 92% with the pion mis-identification rate of 0.25% for electrons between 1 GeV/c and 3 GeV/c in the lab frame. The ECL also provides the trigger information and online luminosity information [106].

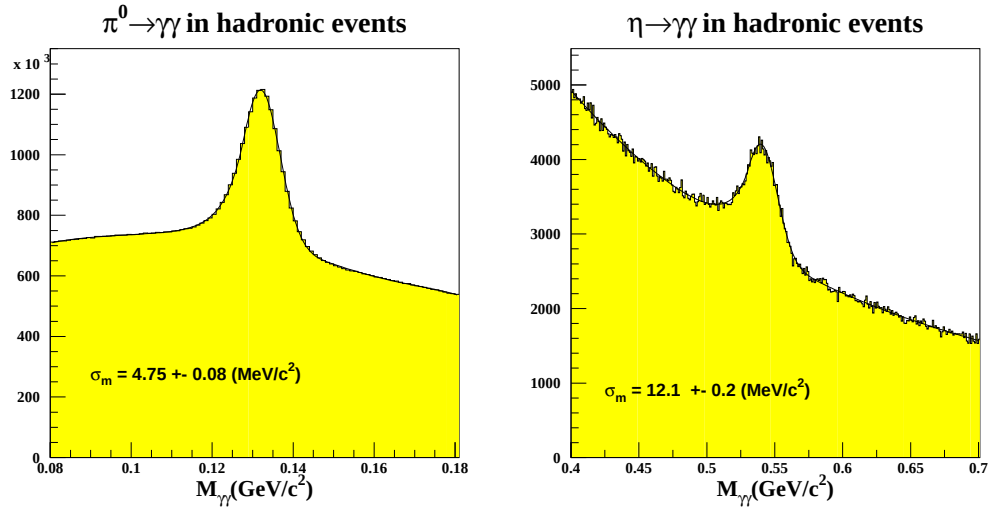

(a) (b)

Figure 2.21: Two photon invariant mass distribution for hadronic events: (a) $\pi^0 \to \gamma\gamma$, (b) $\eta \to \gamma\gamma$, where each of photon energy was required to be above 30 MeV in the barrel region.

2.4.7 Solenoid Magnetic Field

Magnetic field plays very important role for high energy physics detectors. It provides charge and momentum measurement of charged particles and separation of particle in the bunches. A charged particle with a momentum vector at an angle λ with respect to the magnetic field direction, will have a trajectory which is described by a helix. The magnitude of the momentum can be determined from the measured radius of curvature of the helix using following relation

$$p = 0.3 \times \frac{qBR}{\cos\lambda}. \tag{2.14}$$

where $q = \pm 1$ is the charge of the particle, B is magnetic field, R is radius of curvature and p is the momentum of particle. To measure particle momentum in the CDC, 1.5 T magnetic field is applied parallel to the beam pipe in the Belle detector. A superconducting solenoid provides a magnetic field of 1.5 T in a cylindrical volume of 3.4 m in diameter and 4.4 m in length. The coil is surrounded by a multilayer structure consisting of iron plates. The iron structure of the Belle detector serves as the return

path of the magnetic flux. The superconducting coils are chilled by the liquid helium. The iron structure also works as an absorber material for the KLM detector and also it provide support for all of the detector components inside the Solenoid. The configuration of superconducting magnetic coil is shown in Figure 2.23.

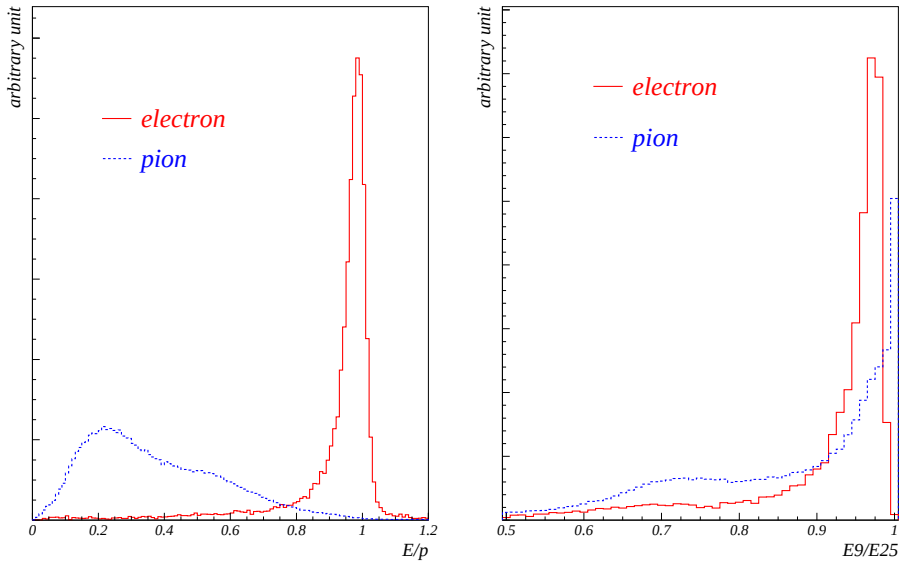

Figure 2.22: (a) E/p and (b) E_9/E_{25} distributions for electrons (solid) and charged pions (dashed). In (a), particle momenta limited to $0.5 < p < 3.0$ GeV/c.

2.4.8 K_L/μ Detector (KLM)

To identify K_L^0's and muons with high efficiency and low fake rate over a broad momentum range above 600 MeV/c, the K_L/μ Detector (KLM) is designed [107]. It is the only detector which is outside the solenoid magnetic field. It has two major parts, namely barrel KLM and endcaps (forward and backward) KLM shown in Figure 2.24. The barrel shaped region around the interaction point covers an angular range 45^o-125^o in the polar angle and endcaps in the forward and backward directions extend this range to 20^o-155^o. The KLM consists of alternating layers of glass resistive plate

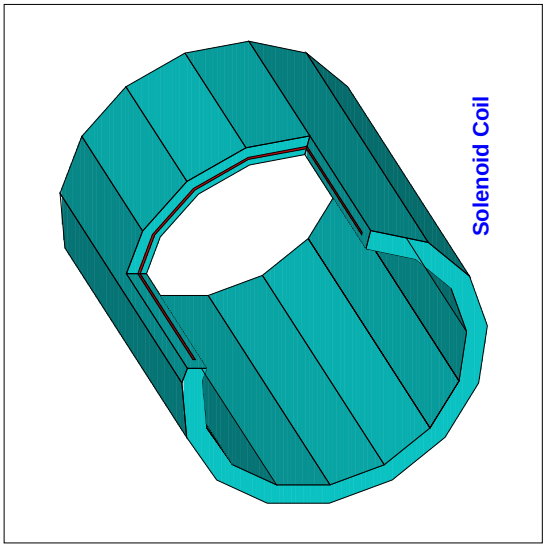

Figure 2.23: Configuration of the superconducting magnetic coil.

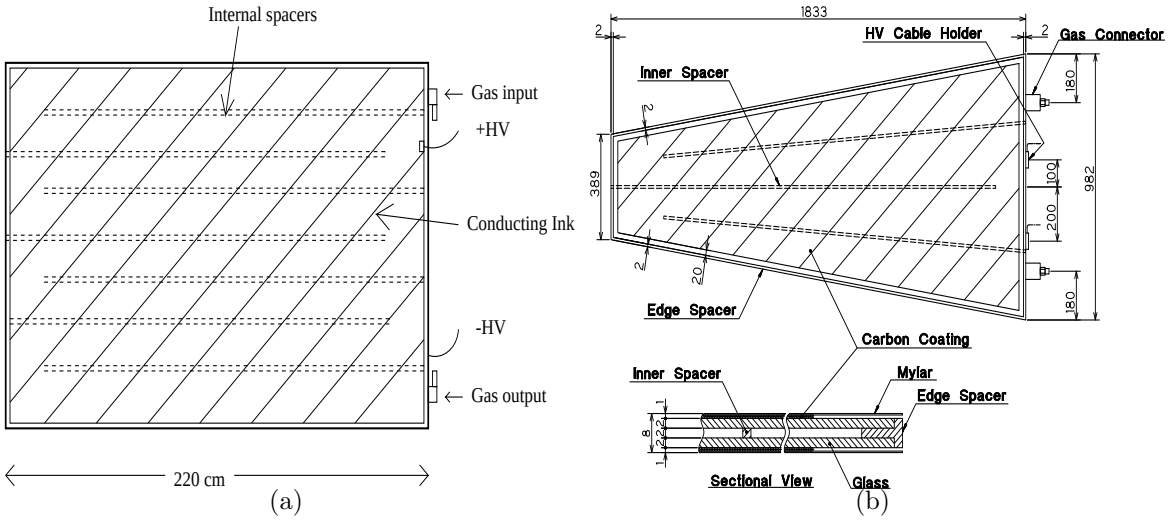

Figure 2.24: KLM detector plate diagram for a) Barrel RPC and b) Endcap RPC.

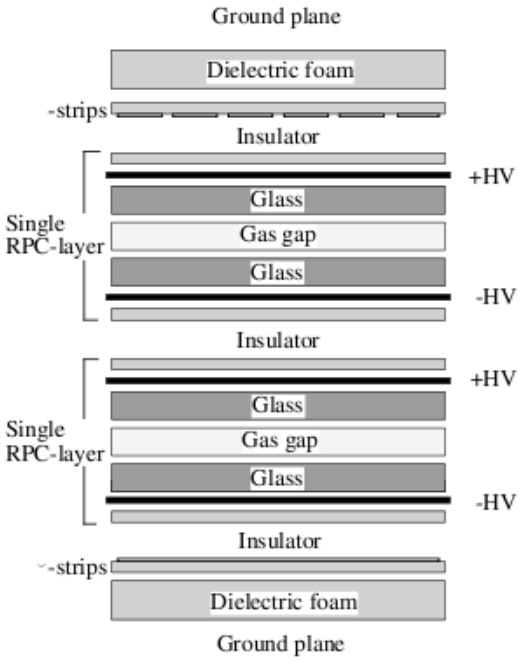

Figure 2.25: Cross-section of a KLM superlayer.

counters (RPCs) and 4.7 cm thick iron plates. There are 15 superlayers in barrel and 14 superlayers in both forward and backward endcaps. Figure 2.25 shows the cross-section of a superlayer. The iron plates provide a total of 3.9 interaction lengths of material for a particle travelling normal to the detector planes. In addition, ECL provides another 0.8 interaction length of material to convert K_L's. The K_L^0 particles live long enough and travels beyond the ECL and interact primarily via the strong force. They are detected by hadronic showers of ionising particles they decay to. Also showers initiated in the ECL will continue into the KLM; K_L^0 will deposit most of their energy within the iron of the KLM. The detector provides position information for the K_L^0 but no useful energy information is gained as a significant proportion of the shower will generally not be within the KLM.

Muons on the other hand, will not interact via the strong force but do have an electromagnetic interaction cross-section; they will lose energy mostly through ionisation process. They penetrate the ECL easily and will continue through most of all the KLM. KLM tracks that are able to be matched with a track in the CDC are

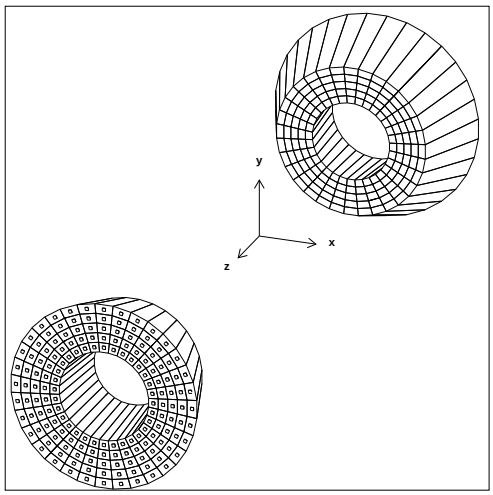

Figure 2.26: Configuration of the EFC.

identified as muons. This way KLM detector is able detect muons and K_L particles.

2.4.9 Extreme Forward Calorimeter (EFC)

In order to improve the experimental sensitivity to physics processes such as $B \to \tau\nu$, the extreme forward calorimeter (EFC) is needed to extend the polar angle coverage by ECL, $17^o < \theta < 150^o$. The EFC covers angular range from $6.4^o < \theta < 11.5^o$ in the forward direction and $163.3^o < \theta < 171.2^o$ in the backward direction. The EFC is attached to front faces of cryostats of the KEKB accelerator compensation solenoid magnets surrounding the beam pipe. The EFC is also required as a beam mask to reduce backgrounds for CDC. In addition, the EFC is used for a beam monitor in the KEKB control and a luminosity monitor for Belle experiment.

Since the EFC is placed in the very high radiation level area around the beam pipe near the interaction point, so it is required to be radiation hard. For this purpose, $Bi_4Ge_3O_{12}$ (BGO) crystal has been adopted which has the property of radiation hardness at megarad level and has excellent e/γ energy resolution of $(0.3 - 1.0)\%/\sqrt{E}$ GeV [108]. Both forward and backward EFC consist of BGO crystals segmented into 5 regions in θ-direction and 32 regions in the ϕ-direction in order to provide better

position resolution. Typical cross-section of a crystal is about $2\times$ 2 cm^2 with 12 X_0 for the forward and 10.5 X_0 in backward region, where X_0 is the radiation length. Each crystal is tower shaped and is aligned to point towards the IP. The arrangement is illustrated in Figure 2.26.

2.4.10 The Trigger

The acquisition and storage of data from the Belle detector is conducted by the trigger. The trigger decision is based on the need to keep physics events of interest and forward them to the Data Acquisition (DAQ) system, while rejecting the many uninteresting beam-related background events. Physics of interest includes hadronic, Bhabha, μ-pair, τ-pair and two photon events. Beam related backgrounds result from interactions between the beams and residual gas, interactions in the beam pipe, synchrotron radiation and cosmic ray events. Therefore, the trigger system which selects useful events from many unnecessary events at the online level plays an important role. The total cross-sections and trigger rates at the design luminosity of $10^{34}\text{cm}^{-2}s^{-1}$ for various physical processes of interest are listed in Table 2.7. Bhabha events and $\gamma\gamma$ events are useful for luminosity measurements and detector calibration, but triggers of such events should be prescaled due to their high rates. The total physics rate is expected to be around 100 Hz and trigger rate due to background is also estimated to be around 100 Hz, although it is difficult to make a reliable estimate. Therefore the trigger system is designed to keep the rate below 200 Hz and data acquisition (DAQ) system is designed to be tolerable to the trigger rate of 500 Hz. The Belle trigger system has been designed and developed to satisfy these requirements.

The Belle experiment adopted a hardware trigger called as Level-1 (L1) trigger and an online software trigger called Level-3 (L3) trigger. Figure 2.27 shows the schematic view of L1 trigger system which is composed of the sub-trigger system and the central trigger system called the Global Decision Logic (GDL) [109]. The GDL receives up to 48 sub-trigger signals and adjusts their timings by adding a delay to each channel. The sub-trigger system is based on two categories, track triggers and energy triggers. The CDC and TOF/TSC provide the trigger signals from charged particles, while

Table 2.7: Total cross-section and trigger rates with $L = 10^{34}\text{cm}^{-2}\text{s}^{-1}$ from various physics processes at $\Upsilon(4S)$. $*$: values prescaled by a factor 1/100. †: restricted condition of $P_t \geq 0.3$ GeV/c.

Physics Process	Cross-section (nb)	Rate (Hz)
$\Upsilon(4S) \to B\bar{B}$	1.2	12
Hadron production from $e^+e^- \to q\bar{q}$	2.8	28
$\mu^+\mu^-$	0.8	8
$\tau^+\tau^-$	0.8	8
Bhabha ($\theta_{lab} \geq 17^o$)	44	4.4*
$\gamma\gamma$ ($\theta_{lab} \geq 17^o$)	2.4	0.24*
2γ processes ($\theta_{\rm lab} \geq 17^{\rm o}$, $\rm P_t \geq 100$ MeV/c)	~ 15	$\sim 35^{\dagger}$
Total	~ 67	~ 96
Backgrounds	-	~ 100

the ECL trigger system provides triggers based on total energy deposit and cluster counting of crystal hits. The KLM and EFC trigger systems provide additional trigger information and the EFC triggers are used for tagging two-photon events as well as Bhabha events. The sub-triggers process event signals in parallel and provide trigger information to the GDL, where all information is combined to distinguish physics and background events and to characterize a physics event type. Information from the SVD is not implemented in the present trigger system. The trigger system provides the trigger signal with the fixed time of the 2.2 μs after the event occurrence. Since process time of GDL is 350 ns, the sub-triggers are required to issue the signal within 1.85 μs of the event occurrence. The Belle trigger system, including the sub-trigger system, is operated in a pipelined manner with clocks synchronized to the KEKB accelerator RF signal. The same figure shows view of GDL, which consists of Input Trigger Delay (ITD), Final Trigger Decision Logic (FTDL), Prescale and Mask (PSNM) and Timing Decision Logic (TDL) modules. Timing of the sub-trigger signals is adjusted to overlap each other, by the ITD module, which therefore assigns larger delay to the faster signal. Using thus adjusted signals the FTDL judges event occurrence or the type of the physics event with 32 MHz frequency. PSNM module

prescales the high rate input triggers for calibration and monitoring purpose and disables the unused triggers from FTDL. TDL finally generates the final trigger signal at 2.2 μs latency based on the timing information of the "timing trigger" from TSC and ECL. 40 logics are defined which express physics events, for example if CDC nearly back-to-back tracks and KLM hits signals are detected at the same time, the FTDL identifies $e^+e^- \to \mu^+\mu^-$ event occurrence and send a signal to the next stage. The trigger efficiency is monitored from the data using the redundant triggers. To keep hadronic events the GDL typically relies on three main trigger classes; multi-tracks, energy sums and isolated cluster counts. Each provide more than 95% efficiency for multi-hadronic data sample. As a result the combined efficiency is more than 99.5%. Belle has two trigger levels: Level-1 (implemented at hardware level) and Level-3 (implemented in software). Trigger system of Belle detector are given below in detail.

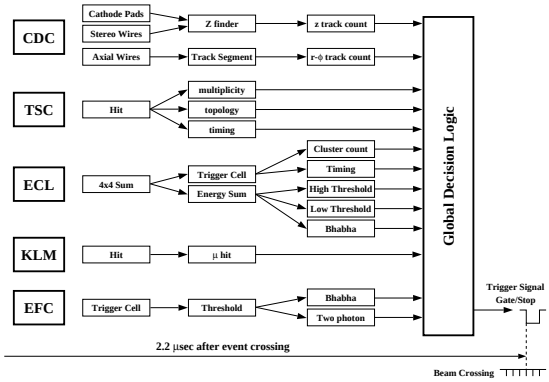

Figure 2.27: Overview of the Level-1 trigger system for the Belle detector.

Level-1 Trigger (Hardware Trigger)

This is based on the information in the form of track triggers and energy triggers from the following detectors:

- **CDC:** main trigger in the trigger system and is divided into an $r-\phi$ trigger and a z trigger. The $r-\phi$ trigger identify the tracks originating from the IP along

with discriminating the track transverse momentum p_t and on the direction and the number of tracks. The z trigger estimates the z position of the tracks to suppress tracks from beam-gas events, from interactions with material around the beam pipe or from cosmic rays.

- **TOF:** provides timing signals with a time jitter less than 10 ns and information on event multiplicity and topology.
- **ECL:** provides two complementary triggers based on total energy deposition and cluster multiplicity, each sensitive to different types of hadronic events.
- **KLM:** saves as many events containing muon tracks as possible.
- **EFC:** provides Bhabha scattering and $\gamma\gamma$ event samples used to monitor the luminosity.

Level-3 Trigger (Software Trigger)

The aim of the Level-3 trigger is to reduce the number of events to be stored. The L3 trigger first checks the L1 trigger information but passes some categories of events, such as Bhabha events and random trigger events. If an event does not belong to these categories, the L3 trigger performs a fast reconstruction and discards the event if it has no track with $|z| < 5$ cm at the IP. A large part of the beam background events are discarded by this procedure. The L3 software has been activated since Experiment 11 and results in a factor of two reduction of stored events while retaining an efficiency of more than 99% for hadronic and τ-pair events.

2.4.11 Data Acquisition System (DAQ)

In order to satisfy the data acquisition requirements so that it works at 500 Hz with a dead time fraction of less than 10%, the distributed-parallel system has been devised. The global scheme of the system is shown in Figure 2.28 [110]. The entire system is segmented into seven subsystems running in parallel, each handling the data from the sub-detector. Data from each subsystem is combined into a single event record by an

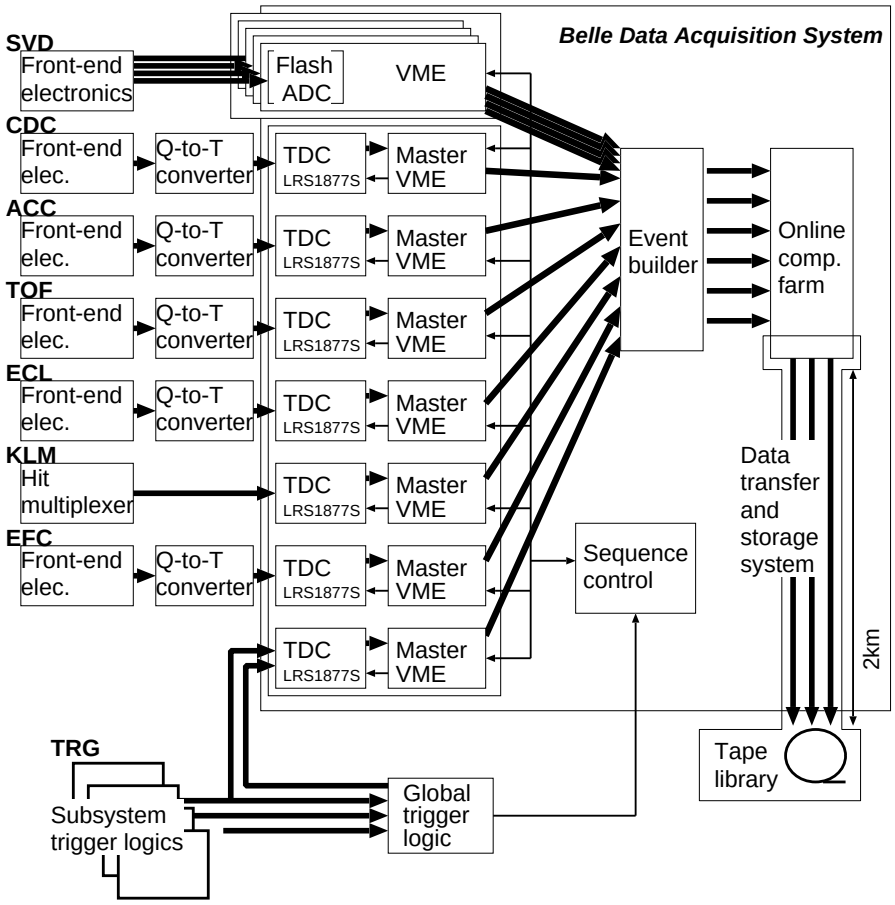

Figure 2.28: Overview of the Belle DAQ system.

event builder. Then event builder output is transferred to an online computer farm, where another level of filtering is done after fast event reconstruction. The data is then sent to a mass storage system located at the computer center via optical fibres. A typical data size of a hadronic event by $B\bar{B}$ or $q\bar{q}$ production is measure to be about 30 kB, which corresponds to the maximum data transfer rate of 15 MB/s.

The Level-4 trigger is then applied online to the raw data by a PC farm. Events passing this filter are converted from raw data to fully reconstructed data events, which are stored in DST files in the PANTHER [111] file format. To enact the L4 trigger an event is required to have at least one track with $p_T > 300$ GeV/c, an

impact parameter in r and $|z|$ less than 1 cm and 4 cm respectively and total energy deposited in ECL to be greater than 4 GeV.

The large quantities of data stored in the DST files are reduced to isolate specific physics processes and are stored in Mini-DST (MDST) files [112]. The analysis presented in this thesis uses the "HadronBJ" skim, which imposes loose requirements to select B-meson events [113]. Production of the (M)DST files, along with analysis of Belle data are performed in the Belle Analysis Software Framework (BASF) [114].

2.5 Detection of Different Particles for the Concerned Decay Modes

Table 2.8: Sub-detectors which detect different particles.

Particle	Energy	Momentum	Position	Particle Identification
$e^+(e^-)$	ECL	CDC	SVD, CDC	ECL, ACC, TOF, CDC
$\mu^+(\mu^-)$		CDC	SVD, CDC	KLM, ACC, TOF, CDC
$\pi^+(\pi^-)$		CDC	SVD, CDC	ACC, TOF, CDC
$K^+(K^-)$		CDC	SVD, CDC	ACC, TOF, CDC
γ	ECL		ECL	ECL, CDC

Due to short life time of B-meson, it decays and can't be detected directly in Belle detector. This Belle detector will be able to detect final state decay particles of B (fairly stable) like e, μ, π, K, γ etc. In Table 2.8, we have mentioned how detection of different particles takes place for our concerned decay modes by different sub-detectors.

2.6 Data Samples

- **Simulated Data**

  For a particular B-meson decay mode, the analysis procedure was established using Monte Carlo (MC) simulated events. The Software program packages

EvtGen [115] is used to simulate the decay processes, while the Belle detector response is simulated using GEANT3 [116] software. The PHOTOS package [117] is used to take into account final state radiations effect. The simulated decays are generated according to known branching fractions and all cross-sections are scaled according to the integrated luminosity recorded by the Belle detector. 2 Million simulated signal events are generated each decay mode. The simulated samples are used to implement and test the event reconstruction and study reconstruction efficiencies.

- **Experimental Data**

  The present analysis is based on the Belle full data sample of 711 fb^{-1} recorded at the $\Upsilon(4S)$ resonance collected with e^+e^- asymmetric KEKB collider. This data sample corresponds to $(771.6 \pm 10.6) \times 10^6 B\bar{B}$ pairs, referred to as $B\bar{B}$ events.

2.7 Chapter in Compact

In this Chapter, the introduction to KEKB accelerator and Belle detector has been provided. This e^+e^- asymmetric machine operates at 10.58 GeV CM energy at the $\Upsilon(4S)$ resonance which decays to pair of $B\bar{B}$. For the detection and measurement of decay products of B-meson, the Belle detector has been designed. It consists of various sub-detectors: Silicon Vertex Detector (SVD), Central Drift Chamber (CDC), Aerogel $\check{C}$erenkov Counter (ACC), Time-of-flight (TOF), Electromagnetic Calorimeter (ECL) and K_L and Muons detector (KLM). The detector covers the θ region extending from 17^o-150^o. The part of uncovered small angle region is instrumented with Extreme Forward Calorimeter (EFC). The detection of different particles takes place for our concerned decay modes by different sub-detectors of the Belle detector. A trigger system has been devised to record the events of the interest and data is recorded using Data Acquisition System.

3

Analysis Strategies and Software Tools

This Chapter summarizes the basic cuts and criteria used for the reconstruction of concerned B-meson decay modes ($B^0 \to X(3872)K^+\pi^-$ and $B^+ \to X(3872)K^0_S\pi^+$) using the recorded Belle data along with its calibration decay modes ($B^0 \to \psi' K^+\pi^-$ and $B^+ \to \psi' K^0_S\pi^+$)[†]. As already discussed in Chapter 2, for each event Belle detector records the response of particles from all sub-detectors. The digitized data collected by all the sub-detectors is then analyzed by reconstruction software packages, which provides all the useful information to the user for a particular event such as: number of charged tracks, momentum and energy deposited by each track, energy submitted by neutral tracks in the calorimeter and muon tracks in KLM. It also prepares the basic particles, which are commonly used for analyses of B-meson decays (e.g. K^0_S reconstruction from charged tracks of $\pi^+\pi^-$, π^0 and η from neutral clusters of $\gamma\gamma$ and K^0_L from $\pi^+\pi^-\pi^0$ etc.). The reconstruction software analyze these responses and provides, among other things, all reconstructed tracks and charged particles and a list of reconstructed K^0_S candidates. Using this information, reconstruction of B-meson takes place after identification and selection of particles in all events.

In order to optimize the selection criteria of concerned decay modes, signal MC samples are used. This provides a clean sample of signal events and allows to estimate the reconstruction efficiency (fraction of signal events left after applying all selections).

[†] $\psi(2S)$ is also frequently used in literature instead of ψ'.

By optimizing the selection criteria and the analysis on signal MC simulated events, one can avoid possible bias. The description about best calibration decay sample, software tools used for the present analyses, identification and reconstruction of the particles are explained in detail in this Chapter.

3.1 Calibration Decay Mode Sample

A valuable source for validating the analysis is the use of a calibration data sample which serves few purposes. It helps in gaining confidence in the analysis of interest without unblinding the region of interest (signal region). Possible problems with the method intended for the mode of interest can be seen on time and can be improved. As the calibration data sample shares the properties to the decay mode of interest, it helps in fine tuning and improves the physics parameter extraction without getting biased.

A perfect calibration sample should have the following characteristics:

- Should have roughly an order of magnitude more signal events than interested decay mode.
- Must topologically resemble with the mode of interest.
- Contain all the combinations of daughter decays as the mode of interest.
- Contain same final state particles (same phase space) as that to the decay mode of interest.

The most obvious and perfect choice for calibration decay modes for our concerned decay modes are $B \to \psi' K\pi$, as these decay modes are well established and well studied.

3.2 Tools and Framework

The Belle data analysis begins by working with Belle Analysis Software Framework (BASF). The BASF is used to access HadronBJ skimmed (filtered) data files (main

requirement for present analysis), to apply the topological pre-kinematic fitting cuts, and to carry out the kinematic fitting. The MC production also takes place in the same environment. The kinematic fitting module (a BASF user analysis module) saves the events in ROOT files format after applying the topological and selection cuts. The rest of the analysis is performed outside of the BASF framework with C++ programs based on the ROOT CERN program library. Below is the explanation of generation, simulation and reconstruction of particles.

3.2.1 Event Generation

The production of the signal Monte Carlo (MC) occurs mainly in two steps. First, the physical event is created using standard EvtGen package. This is done by simulating the full decay chain, taking into account the properties of intermediate particles/states. Then the response of the detector to the propagating particles is simulated using the GEANT3-based CERN program, a software package designed to simulate interactions of particles with matter.

Decay Simulation

To create a decay chain with the EvtGen package, it is necessary to define three components:

- **Particle properties** are defined in *particle definition lists*, that connect a particle name to its properties like mass, width, charge or spin. As these rarely change, a large default particle definition list is usually used.

- **Decay models** are independent modules, that handle the probability calculations in phase space for transitions from a given particle to decay products. For simple decays which are only restricted by energy and momentum conservation, a simple phase space model (PHSP) is found to be sufficient. The PHOTOS module is a special one, as it is used in addition to another module in an individual decay. It manages final state radiation by triggering the production of an additional photon. This analysis itself only uses standard decay models.

- **Decay tables** connect all components by defining the probability for a particle to decay into certain decay products via a given decay model. These have to be crafted individually for each required sample of signal Monte Carlo.

For each event, EvtGen has to start with an initial particle in a given state, which in case of our Monte Carlo is either an $\Upsilon(4S)$ with the same boost as the real ones produced in collisions at KEKB for on-resonance events, or a virtual photon carrying the four-momentum of the collision in the case of continuum (off-resonance) events. Starting from this particle, a decay time is determined using the properties of particles, and the decay tables are used to determine the decay products according to the individual decay probability. The kinematics of the decay products is then determined via the defined decay model. The procedure repeats for every non-stable decay product. The full information of the decay chain then consists of a list of particles and resonances, their mother-daughter relations, positions and momenta values.

Detector Simulation

The output of EvtGen is used to simulate the interactions of the generated particles with the Belle detector. For this purpose, the detector with its full geometry, materials and with magnetic field is modeled in the GEANT3 framework. It simulates the effects of interactions with the different detector components. Low energetic photons originating from the beam pipe - so called beam background - are also added, as they provide a major contribution to the noise in the detector. After the simulated digitalization of the detector response, further processing is identical with experimental data.

3.2.2 Event Reconstruction and Signal Extraction

Next step is reconstruction of particles with the help of same analysis module for both signal MC and experimental data. The signal efficiency is then obtained from signal yield which is obtained after fitting the variables like reconstructed mass, energy with the help of RooFit software using suitable PDF's (probability density function).

3.3 Blind Analysis

A blind analysis is an analysis in which the final result, and the individual data on which it is based, are not seen by the analyst until the analysis is essentially complete. The principal motivation behind this is to avoid experimenter's (subconscious) bias.

There are several different approaches for blind analysis, the method of choice depends on the type of analysis. Typically one has a MC sample and calibration decay mode taken from data to characterise the background to an analysis. Blind analysis in a counting analysis means optimising all the cuts using such samples, testing fitting procedures, and evaluating the systematic uncertainties before looking at the signal region.

All the analyses carried out in this Thesis are performed by blinding the signal region in data. Which means signal region (in data) is not seen until all the selections/criteria are optimized and also, it is demonstrated that the procedure in the study is sensitive and robust enough to search for the signal. Validation of measurements is done by checking results in a number of ways. Signal region (signal box) will be unblinded at the appropriate time in this Thesis.

3.3.1 Signal Monte Carlo Samples

As already mentioned, the reconstruction and analysis was first performed on the signal MC simulated events. The MC simulation can be very close description of the data, therefore MC is used primarily to understand resolution effects and mass biases for the two expected physics signals in the data, the ψ' and $X(3872)$. For this purpose, two different MC samples are used. The first sample consisted of calibration decay mode decaying in the same manner as that of concerned decay mode and second sample itself represented required decay mode. These simulated events are then passed through a detector simulator which simulates the outputs of the Belle detector and subsequently run through the reconstruction algorithm.

In any given event, only one B-meson decays generically and the other B decays exclusively into our concerned decay modes, where the products will continue to decay.

To calculate the reconstruction efficiencies, 2 Million events are generated for each decay mode. Following signal MC simulated samples are generated for this study:

(1) $B^0 \to \psi' K^*(892)^0 (\to K^+\pi^-)$

(2) $B^0 \to \psi' (K^+\pi^-)_{NR}$

(3) $B^0 \to \psi' {K_2}^*(1430)^0 (\to K^+\pi^-)$

(4) $B^0 \to X(3872) (K^+\pi^-)_{NR}$

(5) $B^0 \to X(3872) K^*(892)^0 (\to K^+\pi^-)$

where ψ' and $X(3872)$ both decays to $J/\psi\pi^+\pi^-$ and J/ψ is reconstructed from $\ell^+\ell^-$. Here ℓ is either e or μ (almost equal ratio). Decay modes consisting of ψ' are well known and ψ' mass is only $\approx$186 MeV/c^2 lower than $X(3872)$. Due to same final state as that of concerned channel, having large signal yield ($\approx$ 2600, 700 events respectively for neutral B and charged B-meson decays), these decays are used as calibration samples. For the generation of these samples, selected models are mentioned in Table 3.1. But due to few unfinished jobs, events actually generated are also mentioned in the same Table. The ψ' MC simulation uses the PDG values for

Table 3.1: EvtGen Models used for different signal MC samples.

Decay Channel	Model used	Events actually generated (for neutral decay mode)	Events actually generated (for charged decay mode)
$B^{0/+} \to \psi' K^*(892)^{0/+}$	SVV_HELAMP	2 Million	1939995
$B^{0/+} \to \psi' (K\pi)^{0/+}_{NR}$	PHSP	2 Million	2 Million
$B^{0/+} \to \psi' {K_2}^*(1430)^{0/+}$	PHSP[2]	2 Million	1939997
$B^{0/+} \to X(3872) (K\pi)^{0/+}_{NR}$	PHSP	2 Million	2 Million
$B^{0/+} \to X(3872) K^*(892)^{0/+}$	SVV_HELAMP	2 Million	2 Million

the input mass $m_{\psi'} = 3686.09$ MeV/c^2 and width $\Gamma_{\psi'} = 0.3$ MeV. For signal MC generation of all $X(3872)$ decay modes J^{PC} used is 1^{++}, as it is confirmed by LHCb Collaboration. Since very little is understood about the composition of $X(3872)$, this sample was created by simulating a "heavy" ψ'. Thus $X(3872)$ exotic mesons are generated similar to ψ' meson with mass 3871.4 MeV/c^2 and with zero natural width. Further decay model of $\psi' \to J/\psi\pi^+\pi^-$ is VVPIPI, while the $X(3872)$ also

assumes $J/\psi\pi^+\pi^-$ final state, but is entirely $X(3872) \to J/\psi\rho$ with the J/ψ and ρ in a relative S-wave. This is because it is found that di-pion in $X(3872)$ have been coming from ρ meson [56,57]. So these events are generated with PHSP model. Signal regions are different for ψ' [3.64, 3.74] GeV/c^2 and $X(3872)$ [3.82, 3.92] GeV/c^2 to avoid combinatorial backgrounds.

3.3.2 Background MC (J/ψ Inclusive MC Sample)

In order to understand (or estimate) the background source, officially generated J/ψ inclusive MC sample is used, which includes signal as well as possible backgrounds known at the time of its generation. Most of the background in our analyses is expected to come from an event which has a J/ψ, as we have $(J/\psi\pi^+\pi^- K\pi)$ in the final state. $B \to J/\psi X$ (here X can be anything) MC sample is officially generated by the Belle Collaboration using EvtGen, GEANT3 based simulation after taking into account different experimental conditions as that of experimental data. This sample has luminosity $\sim 100\times$luminosity as that of experimental data and included all the possible modes decaying into J/ψ in the final state. This sample is divided into two parts :

- **Mixed Inclusive J/ψ** : all possible neutral B-meson decays.
- **Charged Inclusive J/ψ** : all possible charged B-meson decays.

Both the data and the MC samples are processed using the belle library `b20090127_0910`.

3.3.3 Data Sample Analyzed

Analyses of all decay modes in this Thesis use full Belle data set available now i.e. 711 fb^{-1} ($\approx$ 771.6 Million $B\bar{B}$ pairs). The number of $B\bar{B}$ events in hadronic data sample can be calculated as,

$$N_{\mathrm{B\bar{B}}} = N_{\mathrm{on}} - \frac{\epsilon_{\mathrm{on}} \,.\, \mathcal{L}_{\mathrm{on}}}{\epsilon_{\mathrm{off}} \,.\, \mathcal{L}_{\mathrm{off}}} \, N_{\mathrm{off}}. \qquad (3.1)$$

[2]Since SVT model is not available in EvtGen, we are generating events with PHSP model.

Where $N_{\rm on}(N_{\rm off})$, $\epsilon_{\rm on}(\epsilon_{\rm off})$ and $\mathcal{L}_{\rm on}(\mathcal{L}_{\rm off})$ are the number of on-resonance events (off-resonance $q\bar{q}$ continuum), events detection efficiency and the luminosity in the on-resonance (off-resonance) data respectively.

The 151.96 Million $B\bar{B}$ pairs have been accumulated using 3-layers SVD (SVDI) configuration and the rest accumulated with a 4-layers SVD (SVDII) configuration. Due to this, extra care have to be taken while the calculation of efficiency correction, estimation of systematic uncertainty, as difference in particle identification will lead to different efficiency.

3.4 $B\bar{B}$ Event Selection

The Belle data consists of a large number of events which not only come from $e^+e^- \to \Upsilon(4S) \to B\bar{B}$, but also from several other processes such as τ pair, Bhabha, continuum events $e^+e^- \to q\bar{q}$ (where q stands for u, d, s and c), two-photon, and beam gas interactions. The cross-section of light quarks production has a smooth energy dependence and such decays form continuum events. These type of events has cross-section three times larger than the cross-section of the $B\bar{B}$ production events at the $\Upsilon(4S)$ mass. Such events can be misreconstructed as B mesons and contribute as background. Only relevant events need to be selected for the decay mode. There are hardware and software triggers to filter out the background events. For the current purpose, the ψ skim data based on HadronBJ event selection is used. Events with B-meson candidates are selected by first applying general hadronic events selection criteria which include the following requirements:-

- At least three charged tracks originating from an event vertex consistent with the interaction region.

- Sum of charged track's momenta and the sum of cluster energy (total visible energy in the rest frame, E_{vis}) to be greater than $0.2\sqrt{s}$ (where $\sqrt{s}$ is total CM energy).

- Absolute value of z-component sum for charged track momentum and clusters energy in the rest frame, $|(p_z)| \leq 0.5\sqrt{s}/c$.
- Total ECL energy between $0.025\sqrt{s}$ and $0.9\sqrt{s}$.
- Invariant mass of oppositely charged tracks with momentum > 0.8 GeV/c, in the range of 2.5 - 4.0 GeV/c^2, is counted as a ψ candidate. Here ψ refers to J/ψ or $\psi(2S)$. Number of such ψ candidates should be ≥ 1.
- All selected charged tracks are required to satisfy impact parameter cuts: distance of closest approach to the interaction point (IP) along the beam direction $|dz| < 5$ cm and in the transverse plane (xy-plane) $|dr| < 2.5$ cm.

3.5 Particle Identification

Data recorded during the experiment is processed by the reconstruction program. Charged particles are reconstructed using information from SVD and CDC. Particle momentum is calculated from the curvature radius of track in magnetic field. Particle identification is done using information from CDC (dE/dx), ACC and TOF. On the basis of this information the likelihood functions are constructed. Photon angles and energy are reconstructed using information from ECL.

In order to perform search for $B^0 \to X(3872)K^+\pi^-$, $B^0 \to \psi' K^+\pi^-$, $B^+ \to X(3872)K^0_S\pi^+$ and $B^+ \to \psi' K^0_S\pi^+$ decay modes, B candidate is reconstructed from the daughter and grand-daughter particles in the Belle detector. The particles required to reconstruct B-meson candidate for the present analyses are: π, K, e, μ, γ, K^0_S. In the following sub-sections a detailed procedure for selection of above particles is described.

3.5.1 Track Selection

For "normal" tracks, a loose selection criteria is applied to reject poorly reconstructed tracks. To remove those charged particle tracks that are poorly measured or do not come from the interaction region, we require their origin to be within 1.0 cm of the

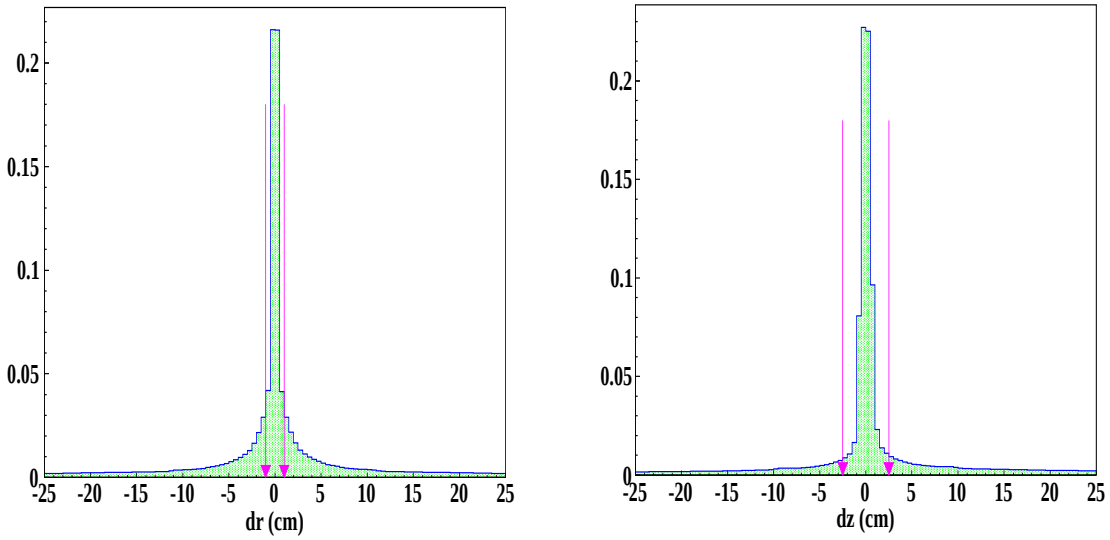

Figure 3.1: dr and dz of the tracks (plots are normalized to unity), with arrows showing cuts used in the analyses.

IP in the radial direction, and 2.5 cm along the beam direction (z-direction). These cuts are shown in Figure 3.1.

3.5.2 π/K Identification

Pions and kaons cannot be distinguished unambiguously. However these can be identified using energy loss (dE/dx) measurements in the CDC, cherenkov light yields in the ACC, and TOF information. The information from these detectors are combined to form π-K likelihood ratio, $\mathcal{R}(\pi/K) = \mathcal{L}_\pi/(\mathcal{L}_\pi + \mathcal{L}_K)$, where $\mathcal{L}_\pi(\mathcal{L}_K)$ is the likelihood that a pion (kaon) would produce the observed detector response.

In our analysis decay modes $B^0 \to X(3872)K^+\pi^-$, $B^0 \to \psi' K^+\pi^-$, $B^+ \to X(3872)K^0_S\pi^+$ and $B^+ \to \psi' K^0_S\pi^+$, charged tracks with $\mathcal{R}(\pi/K) > 0.6$ ($\mathcal{R}(K/\pi) > 0.6$) are identified as prompt charged-π (K). This selection is 95% (93%) efficient for π (K) with a fake rate of 7% (8%) for K (π). For pions which are daughters of $X(3872)$ or ψ', we impose $\mathcal{R}(\pi/K) > 0.4$; for which the corresponding pion identification efficiency is 99% and the misidentification probability is 8%. The resulting

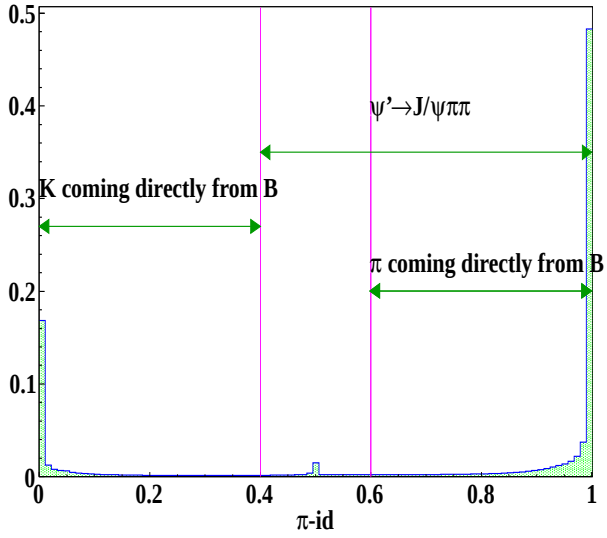

Figure 3.2: $R_{\pi/K}$ distribution (plots are normalized to unity), with arrows showing cuts used in the analyses. The peak at 0.5 is caused by tracks for which no particle ID information is available, such as tracks reconstructed only in the SVD.

likelihood ratio for all reconstructed tracks is shown in Figure 3.2.

3.5.3 Photon Selection

Being a neutral particle, it is not easy to detect γ candidate inside the detectors. However this is detected using cluster information in ECL detector. ECL clusters with no matching CDC track is identified as photon. Those photon candidates are rejected for which the ratio of the sum of the energy deposited in the array of the central 3×3 ECL cells to that in the array of 5×5 cells (E_9/E_{25}) is less than 0.85.

3.5.4 e, μ Identification

The electron track is identified with the criteria that electron likelihood to be greater than 0.01, where electron likelihood is calculated by combining dE/dx from the CDC, the ratio of the energy deposited in the ECL and the momentum measured by the SVD and the CDC, the shower shape in the ECL, ACC information and the position

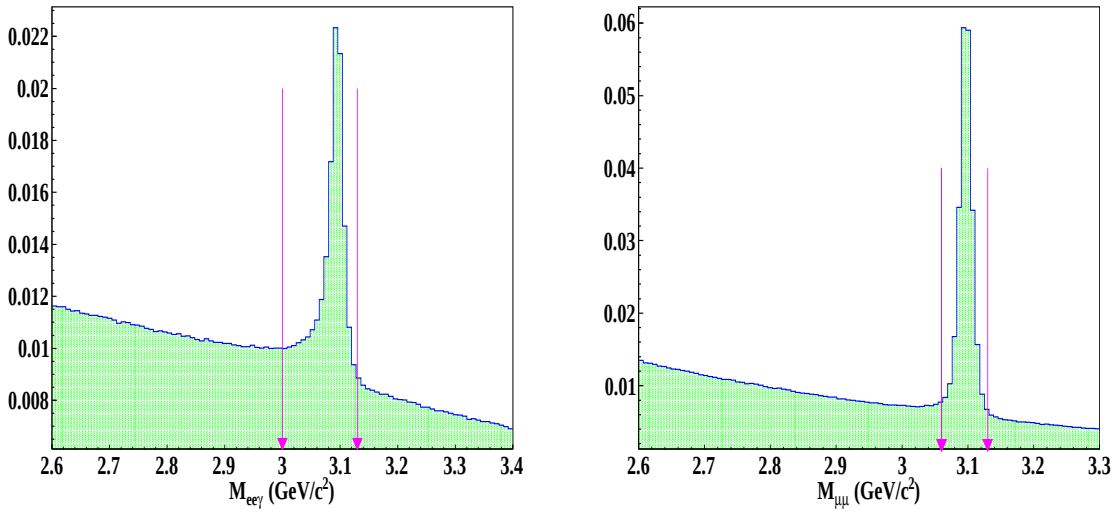

Figure 3.3: Reconstructed mass of J/ψ from e^+e^- and $\mu^+\mu^-$ decay modes (plots are normalized to unity), with arrows showing cuts used in the analyses.

matching between the shower and the track. For muon tracks, identification is based on track penetration depth and hit scatter pattern in the KLM detector. The track is identified as muon, if it satisfies the muon likelihood ratio of a track to be greater than 0.1, where the muon likelihood ratio is defined as $\mathcal{R}_\mu = \mathcal{L}(\mu)/(\mathcal{L}(\mu) + \mathcal{L}(\pi) + \mathcal{L}(K))$. With all above selections, the electron (muon) identification efficiency is above 90% and the hadron fake rate is less than 0.5% (4%).

3.5.5 J/ψ Reconstruction

The J/ψ state is reconstructed via the decay mode $J/\psi \to \ell^+\ell^-$, where ℓ is a electron or muon. In order to recover di-electron events in which one or both electrons radiate a photon, the four-momenta of all photons within 0.05 radians of the e^+ or e^- directions are included in the invariant mass calculation [hereinafter denoted as $e^+e^-(\gamma)$]. The invariant mass of the J/ψ candidate is required to satisfy 3.00 GeV/c^2 $< M_{e^+e^-(\gamma)} <$ 3.13 GeV/c^2 or 3.06 GeV/c^2 $< M_{\mu^+\mu^-} <$ 3.13 GeV/c^2. Lower energy cut on e^+e^- channel is used because electron tracks are more susceptible to energy loss due to the emission of bremsstrahlung photons. The momentum of J/ψ is taken to be less than

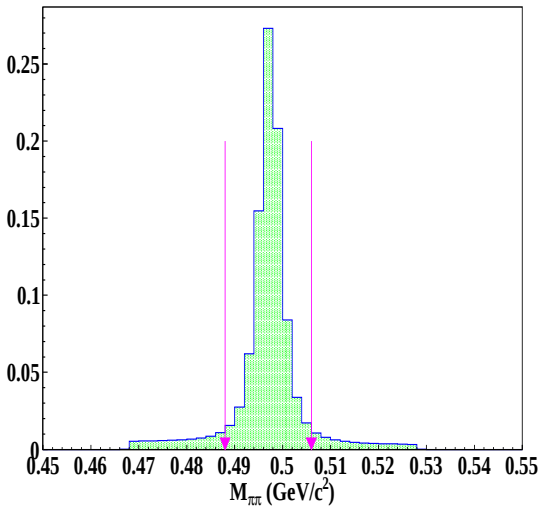

Figure 3.4: Reconstructed mass of $\pi^+\pi^-$ being identified as K^0_S (plots are normalized to unity), with arrows showing cuts used in the analyses.

1.8 GeV/c to avoid J/ψ coming directly from B-meson decay.

The invariant mass distributions of $J/\psi \to e^+e^-$ and $J/\psi \to \mu^+\mu^-$ candidates (before applying cuts and arrows are showing cuts applied) are shown in Figure 3.3. Vertex- and mass-constrained kinematic fits are performed to all selected J/ψ candidates to improve their momentum resolution.

3.5.6 K^0_S Reconstruction

K^0_S candidates are already provided by the Belle software. They are reconstructed from two charged tracks without any particle ID requirement and only a loose mass window of ± 30 MeV/c^2 around the PDG mass value is applied. In addition to above, all reconstructed K^0_S candidates are required to pass the "`goodKs`" selection criteria [118]. The selection criteria is based upon the following four dependent variables. These variables are very effective as a set of K^0_S quality cuts:

- ***dr*:** This is the smaller of $dr1$ and $dr2$, which are the smallest approach from the IP to the two tracks in the xy plane.

- ***dφ*:** This is the azimuthal angle between the momentum vector and the decay vertex vector of a K^0_S candidate.
- ***z*_dist:** This is the distance between the two daughter tracks at their interception point.
- ***fl*:** This is the flight length of K^0_S candidate in xy plane.

K^0_S is selected after applying momentum dependent cuts on above four variables, which are summarised in Table 3.2. Furthermore, those K^0_S candidates are selected which are having reconstructed mass within [0.488, 0.506] GeV/c^2. This window corresponds to $\pm 4\sigma$ around the nominal K^0_S mass as shown in Figure 3.4.

Table 3.2: The "goodKs" cuts of four variables depending upon momentum of K^0_S.

Momentum (GeV/c)	dr (cm)	$d\phi$ (rad)	z_dist (cm)	fl (cm)
< 0.5	> 0.05	< 0.30	< 0.8	-
0.5-1.5	> 0.03	< 0.10	< 1.8	> 0.08
> 1.5	> 0.02	< 0.03	< 2.4	> 0.22

3.5.7 Reconstruction of ψ' and $X(3872)$ Candidates

The reconstructed J/ψ candidate is combined with a $\pi^+\pi^-$ pair to form an ψ' [$X(3872)$] candidate whose mass must satisfy 3.64 GeV/c^2 $< M_{J/\psi\pi^+\pi^-} <$ 3.74 GeV/c^2 [3.82 GeV/c^2 $< M_{J/\psi\pi^+\pi^-} <$ 3.92 GeV/c^2]. These selections are shown in Figure 3.5. The di-pion mass must also satisfy $M_{\pi^+\pi^-} > M_{J/\psi\pi^+\pi^-} - (m_{J/\psi} + 0.2$ GeV/c^2), where $m_{J/\psi}$ is nominal mass and rest two are reconstructed masses. This criterion corresponds to $M_{\pi\pi} > 389$ [575] MeV/c^2 for the ψ' [$X(3872)$] mass region. This cut helps to reduce misidentified γ conversions combinatorial backgrounds [119], while also flattening the background shape distribution in $M_{J/\psi\pi^+\pi^-}$.

3.5.8 B-meson Reconstruction

Reconstruction of B-meson candidate is done after combining its daughter particles depending upon the analyses. Thus to reconstruct $B^0 \to XK^+\pi^-$ (where X is ψ'

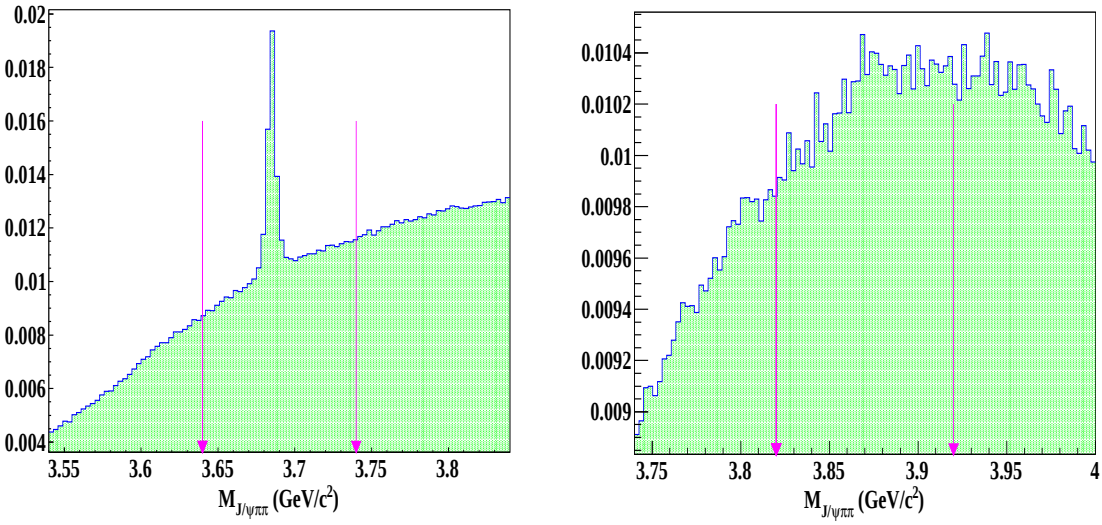

Figure 3.5: Reconstructed masses of ψ' and $X(3872)$ (plots are normalized to unity). Arrows shows cuts used in these analyses.

or $X(3872)$) decay modes, we combine a reconstructed X candidate with a $K^+\pi^-$ candidate and reconstructed X candidate is combined with a $K^0_S\pi^+$ for $B^+ \to XK^0_S\pi^+$ decay modes. A schematic of this principle is shown in Figure 3.6. From kinematical study, it is known that the energy of the B-meson in the $\Upsilon(4S)$ frame, E^*_B must be half the total energy of e^+e^- system in the same frame i.e. $E^*_{\rm beam}$. One can thus increase the resolution of invariant mass of the B-meson by constraining it to beam energy instead of measured energy. This term is also known as beam constrained mass ($M_{\rm bc}$) parameter.

$$M_{\rm bc} \equiv \sqrt{(E^*_{\rm beam})^2 - (p^*_B)^2}. \qquad (3.2)$$

In addition to above, the difference between the reconstructed energy and beam constrained energy is also used which can be defined as follows,

$$\Delta E \equiv E^*_B - E^*_{\rm beam}. \qquad (3.3)$$

Only those candidates are finally considered which are having $M_{\rm bc} > 5.27$ GeV/c^2 and $|\Delta E| < 0.1$ GeV.

Due to combinatorial nature of the reconstruction, there is a possibility of reconstructing more than one B-meson candidate per event, which can't be produced in

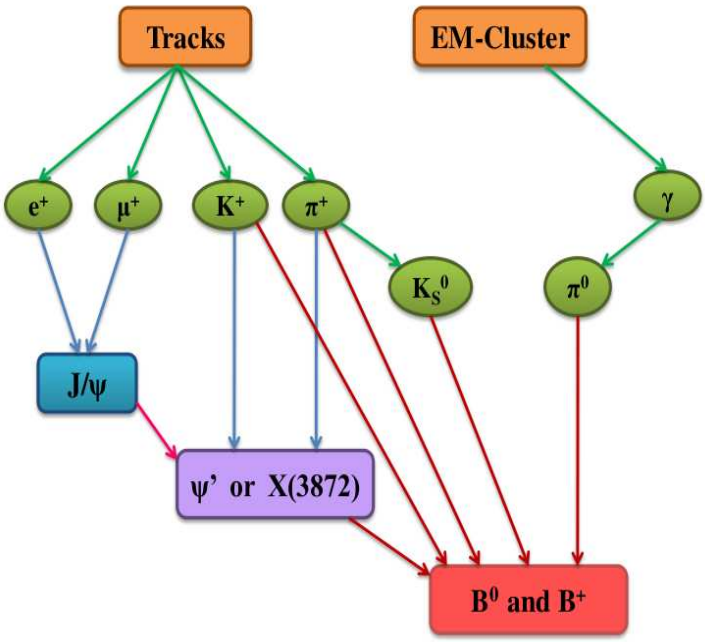

Figure 3.6: Schematic of the hierarchical reconstruction, starting from the lightest particles. Available particles are consecutively combined until a B-meson is reached.

an event. Number of multiple B-meson candidates estimated for signal MC events are mentioned in Table 3.3. However, there can only be one B-meson candidate per event. So it is necessary to choose the best candidate out of these multiple candidates using the so called "Best B" selection which is mentioned in detail in Section 3.6.

3.6 Best Candidate Selection (BCS)

As mentioned earlier, corresponding to one collision in signal MC and experimental data sample, one B-meson candidate is expected in the decay mode of interest per event. But due to several combinations, one can find multiple B candidates which satisfy same selection criteria. So the best candidate is selected out of these multiple

candidates. In that case, the best B candidate can be selected using parameters such as vertex quality, ΔE closest to zero, beam constrained mass closer to B-meson nominal mass, etc. or using their combination.

Table 3.3: Multiple B-meson candidates for each decay mode.

Decay Channel	Multiplicity in %
$B^0 \to \psi' K^*(892)^0 (\to K^+\pi^-)$	39
$B^0 \to \psi' (K^+\pi^-)_{NR}$	37
$B^0 \to \psi' {K_2}^*(1430)^0 (\to K^+\pi^-)$	34
$B^0 \to X(3872) (K^+\pi^-)_{NR}$	32
$B^0 \to X(3872) K^*(892)^0 (\to K^+\pi^-)$	33
$B^+ \to \psi' K^*(892)^+ (\to K^0_S\pi^+)$	43
$B^+ \to \psi' (K^0_S\pi^+)_{NR}$	39
$B^+ \to \psi' {K_2}^*(1430)^+ (\to K^0_S\pi^+)$	35
$B^+ \to X(3872) (K^0_S\pi^+)_{NR}$	37
$B^+ \to X(3872) K^*(892)^+ (\to K^0_S\pi^+)$	39

In order to select best B candidate out of the multiple B-meson candidates in one event, the following choices are considered:

(1) $|\Delta E|$ closest to zero.

(2) $M_{\rm bc}$ closest to the nominal B mass.

(3) Reduced ${\chi^2}_B$ vertex fitting.

(4) Reduced ${\chi^2}_{J/\psi\pi^+\pi^-}$ vertex fitting.

(5) Reduced ${\chi^2}_{\pi^+\pi^-}$ vertex fitting.

(6) Reduced ${\chi^2}_{K\pi}$ vertex fitting (defined only in neutral B meson decays because in charged B-meson decays there will only be one charged track).

(7) $M_{\rm bc}$ and ${\chi^2}_B$ vertex fitting.

(8) $M_{\rm bc}$ and ${\chi^2}_{J/\psi\pi^+\pi^-}$ vertex fitting.

MC truth matching (matching the mother and daughter using generation level information available in the MC) is performed to estimate how many fake B candidates survive after the best candidate selection (BCS) cut and which best candidate selection procedure is the most optimal one. Using this information, the BCS procedure is selected which provides us highest true B candidates (whose all daughters are properly reconstructed and combined). After this selection, the efficiency of BCS is calculated which depends upon how many times the correct B candidate is selected and can be defined as (1 - fake B)×100. Efficiencies for calibration samples and decay modes under study are mentioned in Tables 3.4 to Table 3.7.

Table 3.4: Efficiencies of different BCS for the $B^0 \to \psi' K^*(892)^0 (\to K^+\pi^-)$, $B^0 \to \psi'(K^+\pi^-)_{NR}$ and $B^0 \to \psi' K_2^*(1430)^0 (\to K^+\pi^-)$ decay modes for $|\Delta E| < 0.1$ GeV.

BCS	No. of truly reconstructed B candidates (%)		
	$B^0 \to \psi' K^*(892)^0$ $(\to K^+\pi^-)$	$B^0 \to \psi'(K^+\pi^-)_{NR}$	$B^0 \to \psi' K_2^*(1430)^0$ $(\to K^+\pi^-)$
1	64.04	62.40	60.46
2	62.65	60.83	58.89
3	62.11	60.36	58.47
4	61.56	60.07	58.36
5	61.16	59.58	57.78
6	61.11	59.30	57.34
7	62.93	62.22	59.37
8	62.65	61.12	59.38

From above Tables, it is clear that efficiency of BCS based on ΔE closest to zero is highest. Since ΔE variable is used for signal extraction, so it is difficult to choose same variable for BCS also as it will create some bias. So to avoid this bias, $M_{\rm bc}$ with ${\chi^2}_B$ vertex fitting (second best) is used to select correct (best) B candidate i.e.

$$\text{Reduced } \chi^2 = (\frac{(\mathrm{M_{bc}} - 5.2792 \text{ GeV/c}^2)}{\sigma_{\mathrm{M_{bc}}}})^2 + \frac{\chi^2_{\mathrm{B}}}{\mathrm{NDF}}. \text{ (for neutral B decay mode)} \quad (3.4)$$

Table 3.5: Efficiencies of different BCS for the $B^0 \to X(3872)K^*(892)^0(\to K^+\pi^-)$ and $B^0 \to X(3872)(K^+\pi^-)_{NR}$ decay modes for $|\Delta E| < 0.1$ GeV.

BCS	No. of truly reconstructed B candidates (%)	
	$B^0 \to X(3872)(K^+\pi^-)_{NR}$	$B^0 \to X(3872)K^*(892)^0$ $(\to K^+\pi^-)$
1	60.7	61.0
2	59.4	59.6
3	59.2	59.3
4	58.6	58.5
5	58.2	58.2
6	58.1	58.3
7	59.8	60.0
8	59.6	59.7

Table 3.6: Efficiencies of different BCS for the $B^+ \to \psi' K^*(892)^+(\to K^0_S\pi^+)$, $B^+ \to \psi'(K^0_S\pi^+)_{NR}$ and $B^+ \to \psi' K^*_2(1430)^+(\to K^0_S\pi^+)$ decay modes for $|\Delta E| < 0.1$ GeV.

BCS	No. of truly reconstructed B candidates (%)		
	$B^+ \to \psi' K^*(892)^+$ $(\to K^0_S\pi^+)$	$B^+ \to \psi'(K^0_S\pi^+)_{NR}$	$B^+ \to \psi' K^*_2(1430)^+$ $(\to K^0_S\pi^+)$
1	68.18	65.34	61.88
2	66.83	63.89	60.40
3	66.36	63.48	60.03
4	65.65	63.10	59.88
5	65.41	62.75	59.41
6	–	–	–
7	67.11	64.26	60.83
8	66.81	64.11	60.85

$$\text{Reduced } \chi^2 = \left(\frac{(\mathrm{M_{bc}} - 5.2792\ \mathrm{GeV/c^2})}{\sigma_{\mathrm{M_{bc}}}}\right)^2 + \frac{\chi^2_{\mathrm{B}}}{\mathrm{NDF}} + \chi^2_{\mathrm{K_S}}. \text{ (for charged B decay mode)} \quad (3.5)$$

Where $\sigma_{M_{\mathrm{bc}}}$ is estimated from the fit performed to M_{bc} distribution and value found

Table 3.7: Efficiencies of different BCS for the $B^+ \to X(3872)K^*(892)^+(\to K^0_S\pi^+)$ and $B^+ \to X(3872)(K^0_S\pi^+)_{NR}$ decay modes for $|\Delta E| < 0.1$ GeV.

BCS	No. of truly reconstructed B candidates (%)	
	$B^+ \to X(3872)(K^0_S\pi^+)_{NR}$	$B^+ \to X(3872)K^*(892)^+$ $(\to K^0_S\pi^+)$
1	64.0	64.7
2	62.5	63.2
3	62.2	62.8
4	61.5	61.8
5	61.2	61.5
6	–	–
7	62.9	63.6
8	62.7	63.3

to be 2.925 MeV/c^2. Probability distribution function (PDF) used for this fitting is single Gaussian for the signal, while background is parametrized by the Argus function [120]. χ^2_B is the χ^2 returned by vertex fit of all charged tracks and $\chi^2_{K_S}$ is the reduced χ^2 for K^0_S. NDF is number of degree of freedom which is equal to (2N-3), here N is the number of charged tracks considered for χ^2 vertex fitting. For a candidate to be a "best candidate" for neutral and charged B-meson decay mode, their reduced χ^2's, defined respectively in Equation 3.4 and Equation 3.5, should be smaller. Figure 3.7 shows a flow chart of the full reconstruction of the B-meson candidate which also give a quick overview of all cuts and reconstruction steps.

3.7 Analysis Procedure

In brief, the analysis procedure for these decay modes can be summarized using the flow chart as shown in Figure 3.8. For the present analysis two dimensional (2D) extended unbinned maximum likelihood fitting is performed using ΔE and $M_{J/\psi\pi^+\pi^-}$ variables. ΔE is very important variable as it is highly sensitive to the overall momentum of the B-meson candidate. It has dominant contribution from the track

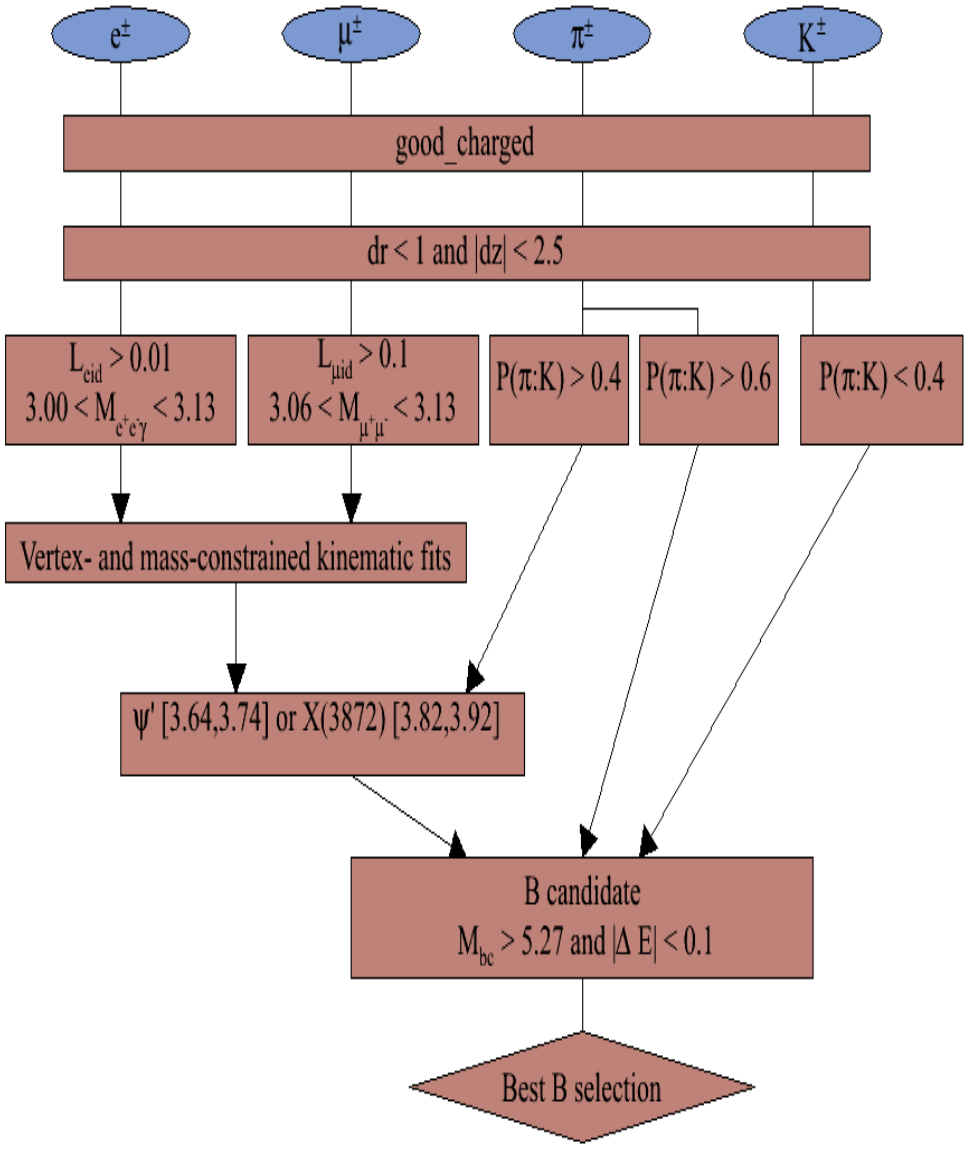

Figure 3.7: Flowchart of the full event selection and reconstruction.

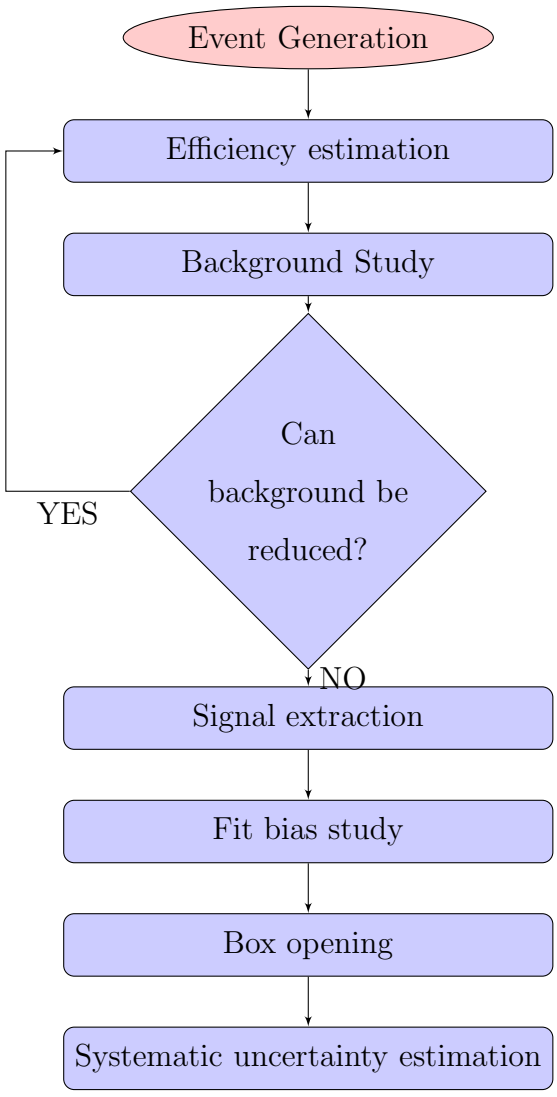

Figure 3.8: Flowchart for analysis procedure.

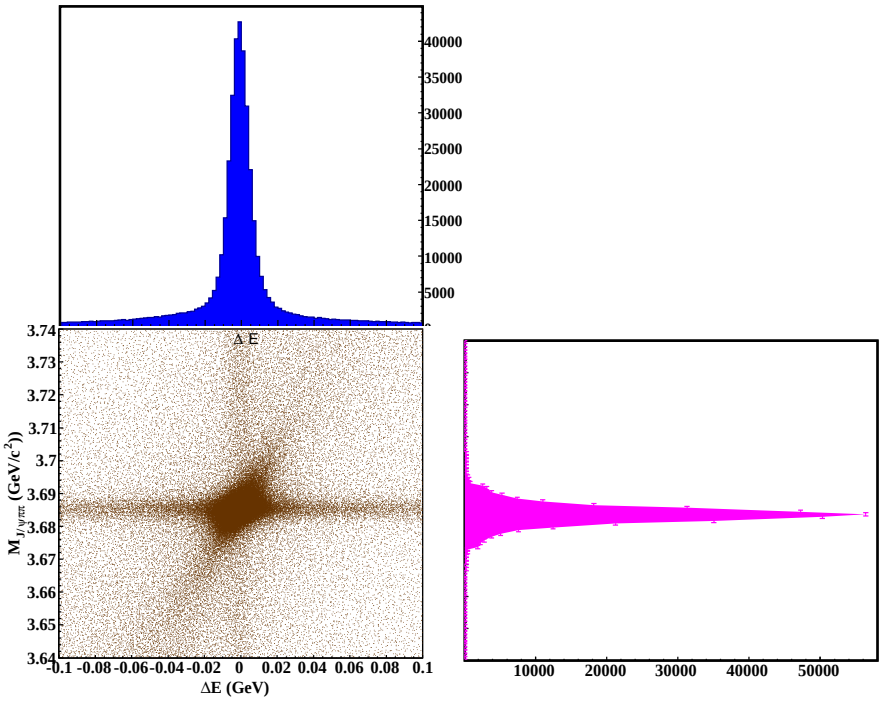

Figure 3.9: MC illustration of ΔE against $M_{J/\psi\pi^+\pi^-}$ distribution for signal events.

momentum and it has no effect of $E^*_{\rm beam}$ measurements because $E^*_{\rm beam}$ has very good resolution of about 3 MeV. The 2D probability distribution function (PDF) is a product of the individual one dimensional PDFs, as no sizable correlation is found as shown in Figure 3.9. All the events which have ΔE between ± 0.1 GeV and $M_{J/\psi\pi^+\pi^-}$ within 3.64 [3.82] GeV/c^2 and 3.74 [3.92] GeV/c^2 for $\psi'[X(3872)]$ mass regions with $M_{bc} > 5.27$ GeV/c^2 are considered for further analysis and this region is also referred to as fit-region. The signal events however populate a very small sub-region, termed as signal region or signal box.

3.7.1 $B^0 \to X(3872)K^+\pi^-$ and $B^+ \to X(3872)K^0_S\pi^+$ Decay Modes

As already mentioned, to extract the signal yield of $B^0 \to X(3872)K^+\pi^-$ and $B^+ \to X(3872)K^0_S\pi^+$, a 2D extended unbinned maximum likelihood (UML) fit is performed to the ΔE and $M_{J/\psi\pi^+\pi^-}$ variables. For the signal, the ΔE distribution

is parametrized by the sum of a Crystal Ball [121] and a Gaussian function while the $M_{J/\psi\pi^+\pi^-}$ distribution is modeled using the sum of two Gaussians having a common mean. For above analyses $B^0 \to \psi' K^+\pi^-$ and $B^+ \to \psi' K^0_S\pi^+$ decay modes are considered as calibration decay modes.

The main background contribution in $B \to (J/\psi\pi^+\pi^-)K\pi$ is expected to arise from inclusive B decays to J/ψ, which is confirmed by the low background found in the J/ψ mass sidebands in the experimental data. To study this background, a large Monte Carlo sample of $B \to J/\psi X$ events corresponding to 100 times the integrated luminosity of the experimental data sample is used and it is found that few backgrounds are peaking in the $M_{J/\psi\pi^+\pi^-}$ dimension (non-peaking in the ΔE dimension) and vice versa. The remaining backgrounds are combinatorial in nature in both dimensions (details are in Chapter 4).

3.8 Background Study and It's Reduction

To study backgrounds which are coming from B mesons, J/ψ inclusive MC sample is used which is about 100× experimental data (corresponds to $\sim$ 772×10^8 M $B\bar{B}$ pairs). The $B \to J/\psi X$ inclusive MC sample includes all the possible/known decay modes of B at the time of its production and having J/ψ meson in their final state. However in order to suppress backgrounds coming from non-$B\bar{B}$ (continuum) events, R_2 variable is used, which is the ratio of second to zeroth Fox-Wolfram moments [122]

$$R_2 = \frac{H_2}{H_0}, \quad \text{where } \mathrm{H_t} = \frac{\sum_{\mathrm{ij}} |\overrightarrow{p_i}|\,|\overrightarrow{p_j}|\,\mathrm{P_t}(\cos\theta_{\mathrm{ij}})}{(\sum_{\mathrm{i}} \mathrm{E_i})^2}. \tag{3.6}$$

which is 0 for perfect spherical events (like $B\bar{B}$ events) and 1 for non-spherical events (continuum backgrounds). Here P_t is the Legendre Polynomial and $\overrightarrow{p_i}(\overrightarrow{p_j})$ represents the four momentum of the particles while $\sum_i E_i$ represents the visible energy of the particles in the event. The $B\bar{B}$ mesons are produced almost at rest and their decay axis are uncorrelated. So, $B\bar{B}$ events are almost spherical in shape and can be distinguished from the jet like continuum events of u, d, s or c. To reduce the continuum background, R_2 variable is chosen to be less than 0.4. Further details about

background study will be given at appropriate time in next Chapters depending upon decay mode under consideration.

3.9 Systematic Uncertainty

The treatment of systematic uncertainties is one of the most demanding part of experimental physics. The sources of uncertainties which can add systematic shifts in the measurement/result can be sub-divided into four categories.

- Uncertainties in the **information from the previous measurements,** such as branching fractions for intermediate decays,
- Uncertainties due to inexact information about the **experimental setup,**
- Uncertainties involved in the **reconstruction procedure,** and
- Biases introduced due to the **fitting procedure**.

Various possible sources affecting the branching fraction measurement as well as other results are mentioned in Table 3.8. In this Section, systematic uncertainties estimation

Table 3.8: Various sources of systematic uncertainties.

Previous measurements	(a) Due to secondary branching fractions.
Experimental setup	(a) Charged tracking efficiency. (b) PID efficiency.
Signal reconstruction	(a) K_S^0 reconstruction.
Fit inputs	(a) Luminosity. (b) Reconstruction efficiencies due to limited MC statistics and due to the limited knowledge of the actual model to generate the signal MC events. (c) PDF modeling. (d) Fit bias.

(common to the analyses taken in this Thesis) is explained. Possible systematic uncertainties can come from the following sources:

3.9.1 K/π Identification

Kaons and pions have uncertainty on their identification and to estimate it Belle official PID group estimation, based upon the $D^{*+} \to D^0(K^-\pi^+)\pi_{\rm slow}{}^+$ decay [123] is used. A correction for the difference in kaon (pion) efficiency (between experimental data and MC) is then obtained. This correction is used to correct the efficiency while error on it is included as systematic uncertainty coming from K/π identification.

3.9.2 Charged Track Finding Efficiency

Charged particle track reconstruction has an uncertainty of about 0.35% per track which has been estimated on the basis of partially reconstructed $D^{*-} \to \bar{D}^0(K^0_S(\pi^-\pi^+)$ $\pi^+\pi^-)\pi^-$ study by Belle's official tracking group [124]. Due to correlation, the uncertainty due to each tracks are added linearly.

3.9.3 Secondary Branching Fraction ($\mathcal{B}$)

Secondary branching fractions [1] is used for the estimation of primary branching fraction. These secondary branching fractions have statistical and systematic uncertainties. These uncertainties are taken as the systematic coming from secondary branching fraction.

3.9.4 Lepton Identification

There can be a difference between lepton identification in experimental data and MC. This difference needs to be estimated. For lepton identification, systematic uncertainties are calculated from the comparison between the experimental data and MC for $2\gamma \to ee\mu\mu$. Efficiency correction and systematic uncertainties are calculated as a function of the momentum (p) and the polar angle (θ) in the laboratory rest frame [125].

3.9.5 Systematic Uncertainty due to K_S^0

The uncertainty on the reconstruction of K_S^0 is estimated to be 0.73%. This is also Belle official study given in [126] in detail.

3.9.6 Systematic Uncertainty due to Efficiency

This type of uncertainty arises from two sources in present analysis. First it is due to the limited statistical samples of signal MC, so there will be sizeable statistical errors on the calculated efficiency and this error is taken into account in the calculation of systematic uncertainty. And second systematic uncertainty in the efficiency is due to the fact that there is limited knowledge to generate MC samples for some of the decay modes.

3.9.7 Uncertainty on Number of $B\bar{B}$ Events ($N_{B\bar{B}}$)

This systematic is due to the uncertainty on $N_{B\bar{B}}$ value. Official $N_{B\bar{B}}$ for expt. 7-65 (data currently used) is $(771.6 \pm 10.6) \times 10^6$ which gives a systematic uncertainty of 1.4%.

3.9.8 Systematic Uncertainty due to PDF Modeling

Signal yield is extracted by performing a fit to the experimental data and it depends upon parameters fixed in fit. There is systematic uncertainty coming from the modeling of the different components of signal and background PDF. It will be different for each analyses depending upon the parametrization of the PDF.

3.10 Chapter in Compact

In this Chapter, introduction to the analysis tools utilized to perform the search for $X(3872)$ in three body decay $B \to X(3872)(K\pi)$ has been explained. The identified tracks of $e^{\pm}$, $\mu^{\pm}$, $K^{\pm}$, $\pi^{\pm}$ and γ are used to reconstruct the J/ψ, ψ', K_S^0 and $X(3872)$

particles. Also the reconstruction of neutral and charged B-meson from $\psi'(K\pi)$ or $X(3872)(K\pi)$ using $M_{bc} > 5.27$ GeV/c^2 and $|\Delta E| < 0.1$ GeV has been described. The 2D extended UML fitting is done using ΔE and $M_{J/\psi\pi^+\pi^-}$ variables. To perform the background study for these decay modes, large sample of $B \to J/\psi X$ inclusive MC is used, which includes all decay modes known at the time of its generation.

4

Search for $X(3872)$ in 3-body B^0 decay

In the current Chapter, the signal extraction procedure for $B^0 \to X(3872)K^+\pi^-$ decay mode using two dimensional extended unbinned maximum likelihood fit has been explained in detail. The first observation of $B^0 \to X(3872)K^+\pi^-$ decay mode along with the measurement of the product of branching fractions $\mathcal{B}(B^0 \to X(3872)K^+\pi^-) \times \mathcal{B}(X(3872) \to J/\psi\pi^+\pi^-)$ has been reported. In addition to the above stated analysis, the study of $B^0 \to \psi' K^+\pi^-$ decay mode is also presented in detail here.

4.1 Search for $B^0 \to X(3872)K^+\pi^-$ Decay Mode

In the following Sections, a detailed study about $B^0 \to X(3872)K^+\pi^-$ decay mode has been presented, which includes its signal MC study (only signal), J/ψ inclusive MC study (signal+backgrounds) and experimental data study.

4.2 Event Reconstruction Procedure

To observe $B^0 \to X(3872)K^+\pi^-$ decay mode, the B-meson reconstruction is done by combining the reconstructed $X(3872)$ particle with the tracks identified as K^+ and π^- as explained in Section 3.5. The $X(3872)$ is reconstructed via its decay mode $J/\psi\pi^+\pi^-$, here J/ψ is reconstructed using $\ell^+\ell^-$, where ℓ is e or μ. Reconstruction of $B^0 \to \psi' K^+\pi^-$ decay mode is also done on similar footing as that of concerned decay

mode as ψ' is also reconstructed from $J/\psi(\to \ell^+\ell^-)\pi^+\pi^-$.

4.3 Branching Fractions

Branching fraction of $\mathcal{B}(B^0 \to \psi' K^+\pi^-)$ decay mode after assuming equal production of $B^0\bar{B}^0$ and B^+B^- pairs (PDG convention) is defined as follows:

$$\mathcal{B}(B^0 \to \psi' K^+\pi^-) = \frac{Y(B^0 \to \psi' K^+\pi^-)}{\epsilon(B^0 \to \psi' K^+\pi^-) \times \mathcal{B}(\psi' \to J/\psi\pi^+\pi^-) \times \mathcal{B}(J/\psi \to \ell^+\ell^-) \times N(B\bar{B})}. \quad (4.1)$$

The product of the branching fractions of $\mathcal{B}(B^0 \to X(3872)K^+\pi^-) \times \mathcal{B}(X(3872) \to J/\psi\pi^+\pi^-)$ under the similar assumption as stated above is given by:

$$\mathcal{B}(B^0 \to X(3872)K^+\pi^-) \times \mathcal{B}(X(3872) \to J/\psi\pi\pi) = \frac{Y(B^0 \to X(3872)K^+\pi^-)}{\epsilon(B^0 \to X(3872)K^+\pi^-) \times \mathcal{B}(J/\psi \to \ell\ell) \times N(B\bar{B})}. \quad (4.2)$$

The signal yield $Y(B^0 \to X(3872)K^+\pi^-)$ is the number of fitted $B^0 \to X(3872)K^+\pi^-$ events found in the total experimental data set $N(B\bar{B})$ with suitable PDFs. It is to be noted that for whole $X(3872)$ mass region in $B \to X(3872)K\pi$ decay modes, the product of branching fractions is estimated because $\mathcal{B}(X(3872) \to J/\psi\pi^+\pi^-)$ is not known till date.

Since reconstruction of all signal events is not 100% efficient because of detector acceptance and the software reconstruction limitations, so it is required to estimate the reconstruction efficiency $\epsilon(B^0 \to X(3872)K^+\pi^-)$ for the estimation of branching fractions. This term is the probability of detecting any $B^0 \to X(3872)K^+\pi^-$ decay event. It also includes the fact that we are able to reconstruct only a small part of the possible $B^0 \to X(3872)K^+\pi^-$ decay mode.

4.3.1 Efficiency Estimation from Signal MC study and PDF Parametrization

Due to the multi-body tracks (six tracks) in this decay mode, the efficiency of observing each track multiplies and results in a lower reconstruction efficiency. In order to estimate the reconstruction efficiency, signal Monte Carlo (MC) simulated events are

generated according to the luminosity of the experimental data collected by different detector environment and conditions like beam backgrounds etc. For each decay mode of interest, 2 Million signal events are generated, which is many order magnitude larger than what is expected in experimental data in order to have better control and understanding. Generated events for each decay mode are already mentioned in Table 3.1. In order to estimate the reconstruction efficiency, large number of signal MC events are generated for ψ' and $X(3872)$ mass regions. Following signal MC simulated samples are generated:

(1) $B^0 \to \psi' K^*(892)^0 (\to K^+\pi^-)$

(2) $B^0 \to \psi' (K^+\pi^-)_{NR}$

(3) $B^0 \to \psi' {K_2}^*(1430)^0 (\to K^+\pi^-)$

(4) $B^0 \to X(3872)(K^+\pi^-)_{NR}$

(5) $B^0 \to X(3872) K^*(892)^0 (\to K^+\pi^-)$

It is to be noted that for $X(3872)$ mass region, $B^0 \to X(3872){K_2}^*(1430)^0 (\to K^+\pi^-)$ decay mode is kinematically suppressed due to phase space limitation. To extract the signal events, two dimensional (2D) extended Unbinned Maximum Likelihood (UML) fit was performed on the ΔE and $M_{J/\psi\pi^+\pi^-}$[†] variables. As there can be situations, where few of the particles are missed (escaped) due to detector acceptance or random combinations, which resulted in poor reconstruction of signal events. In order to study them, each particle is first tagged and its history (mother, grandmother etc.) is checked using MC truth matching. Properly reconstructed and corrected final state events are known as correctly reconstructed (CR) events. Poorly reconstructed and partially reconstructed events come under the category of SCF events. Figure 4.1 and Figure 4.2 show CR and SCF events for ψ' and $X(3872)$ mass regions respectively.

Based on above study and in order to avoid any bias, the following strategy was found to be the best one.

[†]From now onwards $M_{J/\psi\pi\pi}$ is used as short-hand notation for $M_{J/\psi\pi^+\pi^-}$.

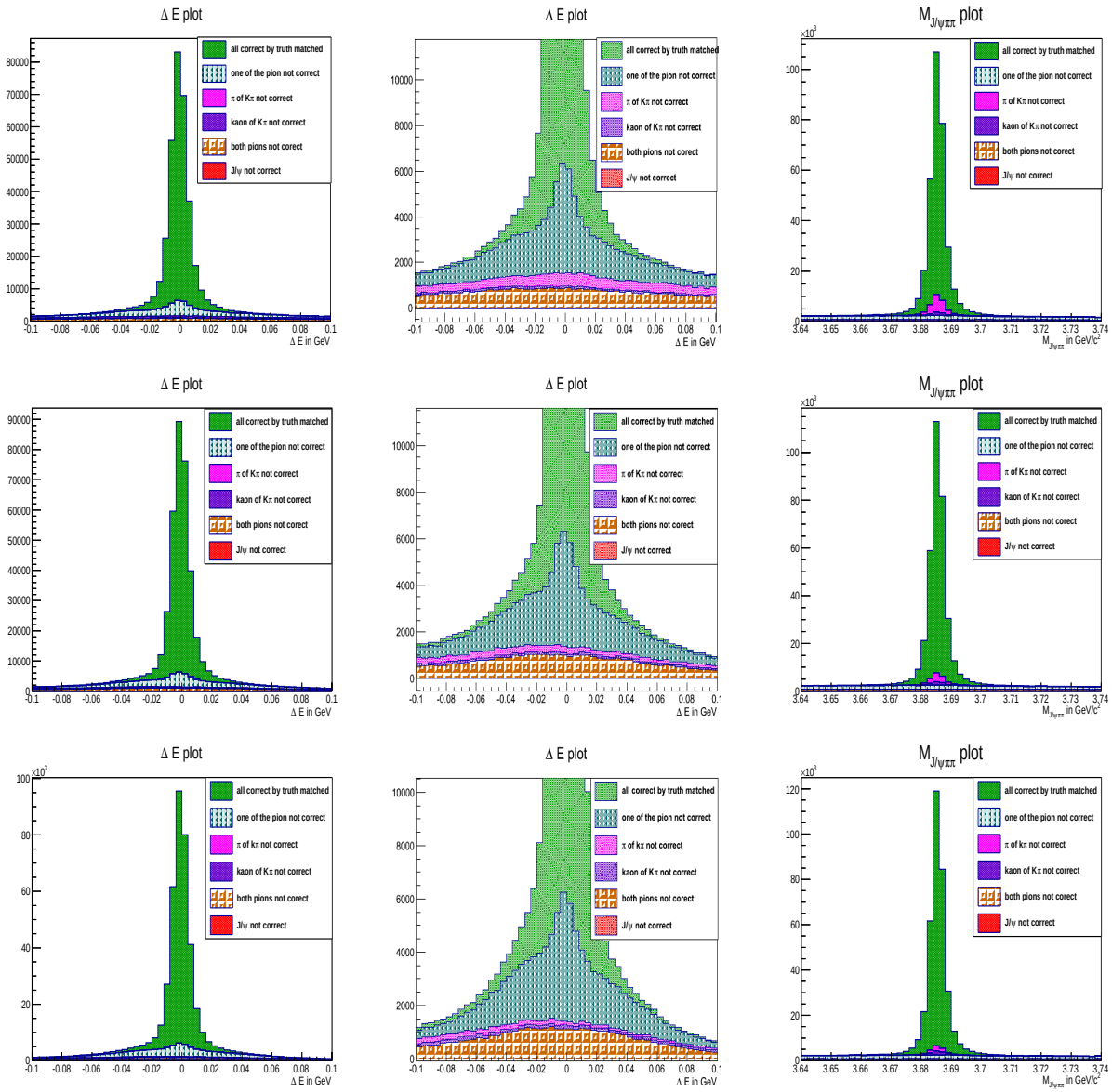

Figure 4.1: Correctly reconstructed (CR) and self cross feed (SCF) events plots for signal MC simulated samples in ΔE and $M_{J/\psi\pi\pi}$ dimensions (middle plots are zoomed plots for ΔE dimension) for $B^0 \to \psi' K^+\pi^-$ decay mode. Top plots are of $B^0 \to \psi' K^*(892)^0$ decay mode, middle ones are of $B^0 \to \psi'(K^+\pi^-)_{NR}$ and bottom plots are of $B^0 \to \psi' {K_2}^*(1430)^0$ decay mode.

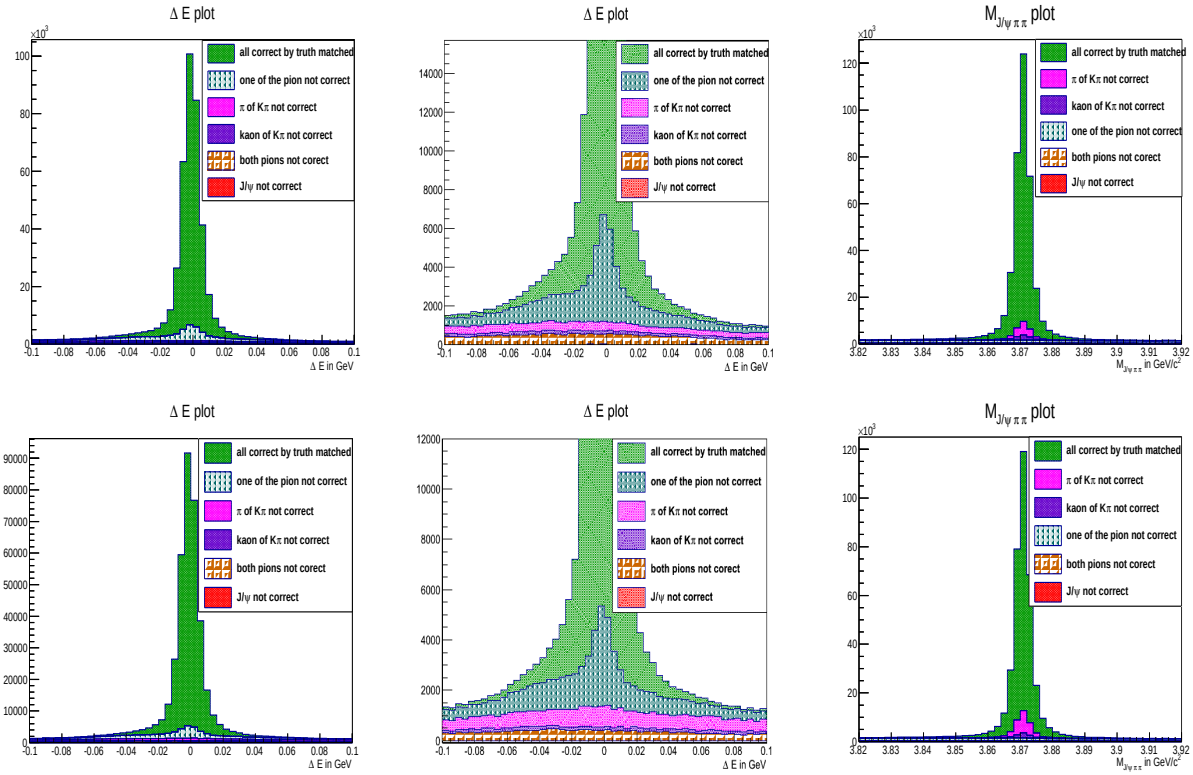

Figure 4.2: Correctly reconstructed (CR) and self cross feed (SCF) events plots for signal MC simulated samples in ΔE and $M_{J/\psi\pi\pi}$ dimensions (middle plots are zoomed plots for ΔE dimension) for $B^0 \rightarrow X(3872)K^+\pi^-$ decay mode. Top plots are for $B^0 \rightarrow X(3872)(K^+\pi^-)_{NR}$ decay mode and bottom plots are for $B^0 \rightarrow X(3872)K^*(892)^0$ decay mode.

(a) Signal events PDF: These are our CR events. As, one can see in Figure 4.1 and Figure 4.2, these type of events are having peak in both ΔE and $M_{J/\psi\pi\pi}$ dimensions. In order to properly model them, sum of core Gaussian with the Crystal Ball [121] (tail parameter) was used to model signal events in ΔE dimension, while in the case of $M_{J/\psi\pi\pi}$ dimension, sum of two Gaussian with common mean was found to be sufficient. The 2D extended UML fit is performed on variables ΔE and $M_{J/\psi\pi\pi}$. As no sizeable correlation is found, so 2D probability distribution function (PDF) is a product of individual one dimensional (1D) PDF.

(b) Peaking events PDF: Due to wrong or multiple combinations, some events are found with missing final state and having peak in only one dimension (while they are almost flat in other dimension). These types of events can be further sub-divided into two parts.

- Peaking only in ΔE dimension: There are SCF events which are peaking in ΔE dimension and these events are not peaking in $M_{J/\psi\pi\pi}$ dimension. These events originates from a B^0 with the final state $(J/\psi\pi^+\pi^-K^+\pi^-)$ where $J/\psi\pi^+\pi^-$ is not from $\psi'/X(3872)$ for $B^0 \to \psi' K^+\pi^-/B^0 \to X(3872)K^+\pi^-$ decay modes.
- Peaking only in $M_{J/\psi\pi\pi}$ dimension: Due to correct combination of $J/\psi\pi^+\pi^-$ but wrongly combining with K^+ or (and) π^-, few events are found to be peaking in $M_{J/\psi\pi\pi}$ dimension, while flat in ΔE distribution.

  These type of events (peaking in one variable (dimension) and flat in other variable (dimension)) are found to have same resolution as that of the signal. So keeping this thing in mind, PDF similar to the signal PDF is used for the peaking dimension, while the other dimension is parametrized by 1^{st} order Chebychev polynomial. This slope in other dimension was allowed to vary in fit for ψ' mass region. For $X(3872)$ mass region, everything is same except the slope of Chebychev polynomial, which is fixed to be zero in ΔE dimension (for the backgrounds which are peaking in $M_{J/\psi\pi\pi}$ dimension). This strategy was chosen from signal MC study (this type of background (SCF) has no structure), background study (negligible background of this nature) and from fit bias study.

(c) Combinatorial background events PDF: The remaining background events are found to be combinatorial in nature and flat in both dimensions. These type of events are parametrized by 1^{st} order Chebychev polynomial for both variables (dimensions).

Fitting strategy for signal MC simulated events is following for ψ' and $X(3872)$ mass regions:

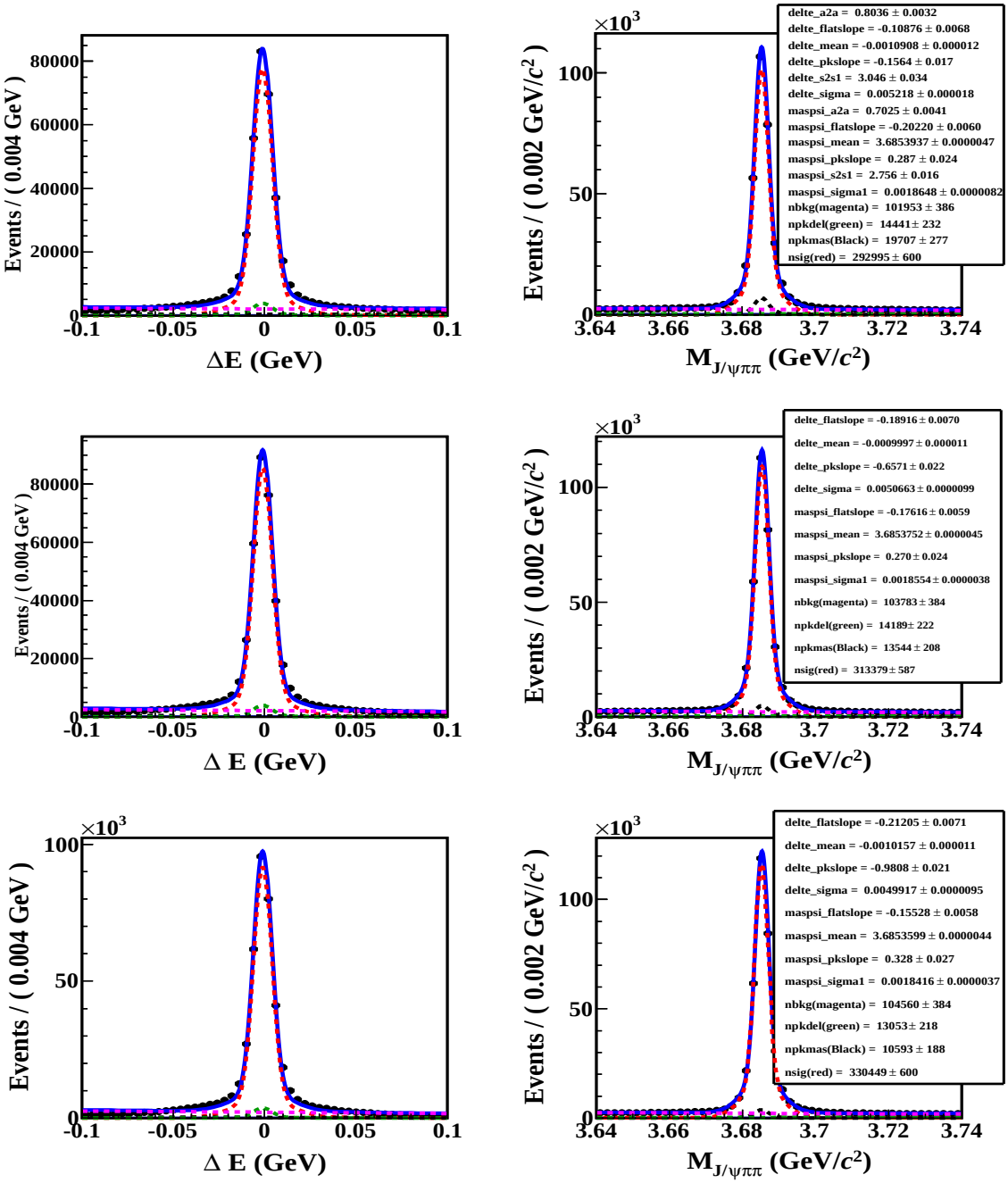

Figure 4.3: 2D extended UML fit to signal MC simulated samples for ΔE (left) and $M_{J/\psi\pi\pi}$ (right) dimensions for $B^0 \to \psi' K^*(892)^0$ (top), $B^0 \to \psi'(K^+\pi^-)_{NR}$ (middle) and $B^0 \to \psi' K_2{}^*(1430)^0$ (bottom) decay modes. The curves show the signal [red dotted] and the background components [black dotted for the component peaking in $M_{J/\psi\pi\pi}$ but non-peaking in ΔE, green dotted for the one peaking in ΔE but non-peaking in $M_{J/\psi\pi\pi}$, and magenta dotted for combinatorial background in both dimensions] as well as the overall fit [blue solid].

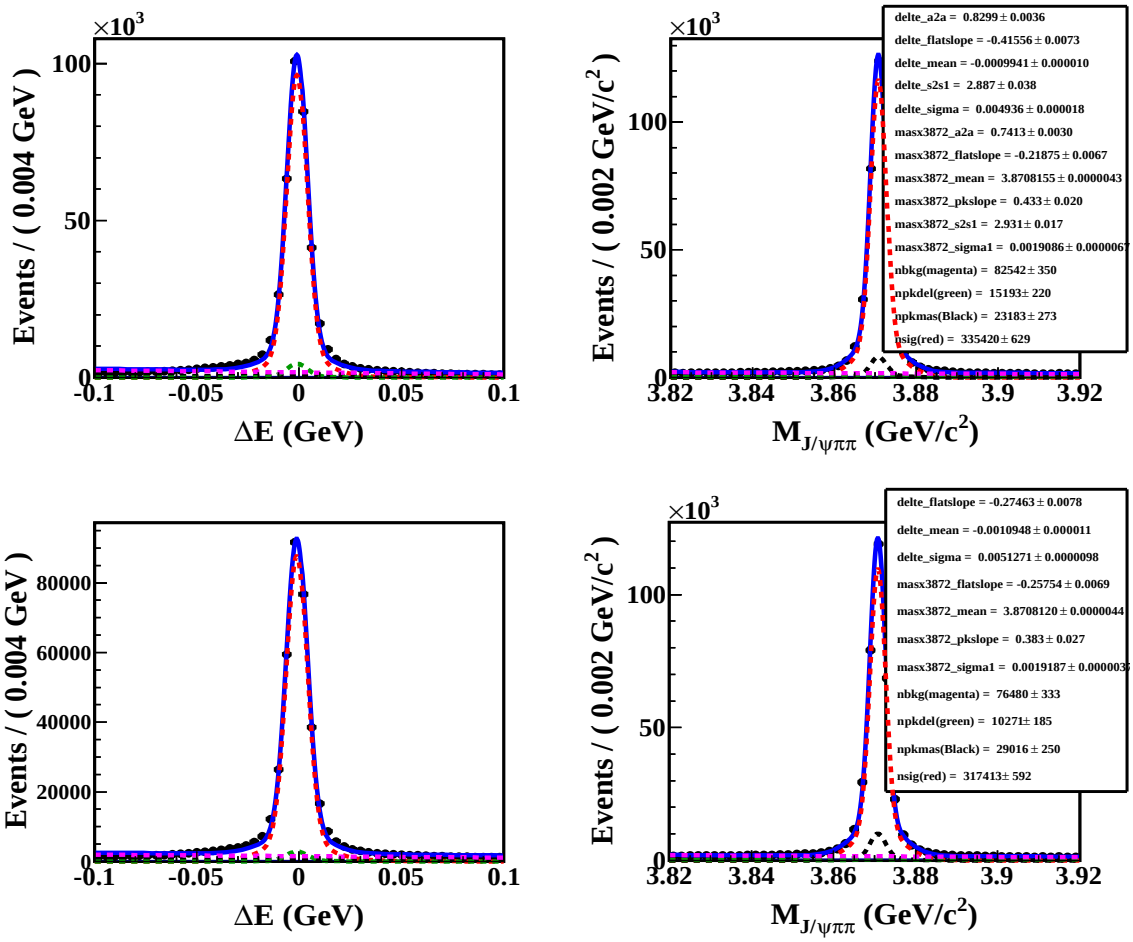

Figure 4.4: 2D extended UML fit to signal MC simulated samples for ΔE (left) and $M_{J/\psi\pi\pi}$ (right) dimensions for $B^0 \to X(3872)(K^+\pi^-)_{NR}$ (top) and $B^0 \to X(3872)K^*(892)^0$ (bottom) decay modes. The curves show the signal [red dotted] and the background components [black dotted for the component peaking in $M_{J/\psi\pi\pi}$ but non-peaking in ΔE, green dotted for the one peaking in ΔE but non-peaking in $M_{J/\psi\pi\pi}$, and magenta dotted for combinatorial background in both dimensions] as well as the overall fit [blue solid].

- 2D extended UML fit is performed on truth matched signal MC simulated sample of $B^0 \to \psi' K^*(892)^0$ using signal and combinatorial backgrounds PDF's to find the value of tail parameters (α and n) of Crystal Ball function. Both of these parameters are fixed now onwards for every fit of ψ' and $X(3872)$ mass

Table 4.1: Reconstruction efficiencies for different signal MC samples estimated from 2D extended unbinned maximum likelihood fit study.

Decay Mode	Reconstruction Efficiency in %
$B^0 \to \psi' K^*(892)^0$	(14.65 ± 0.03)
$B^0 \to \psi'(K^+\pi^-)_{NR}$	(15.67 ± 0.03)
$B^0 \to \psi' {K_2}^*(1430)^0$	(16.52 ± 0.03)
$B^0 \to X(3872)(K^+\pi^-)_{NR}$	(16.77 ± 0.03)
$B^0 \to X(3872)K^*(892)^0$	(15.87 ± 0.03)

region in neutral B-meson decay mode.

- 2D extended UML fit is then performed on signal MC simulated sample of $B^0 \to \psi' K^*(892)^0$ and $B^0 \to X(3872)(K^+\pi^-)_{NR}$ to find the value of rest tail parameters (fraction of areas and fraction of sigmas), while core parameters (mean and sigma) are floated in both dimensions for ψ' and $X(3872)$ mass regions respectively. Reconstruction efficiencies are thus estimated from these fits for $B^0 \to \psi' K^*(892)^0$ and $B^0 \to X(3872)(K^+\pi^-)_{NR}$ decay modes.

- Then fitting is performed on $B^0 \to \psi'(K^+\pi^-)_{NR}$, $B^0 \to \psi' K_2^*(1430)^0$ and $B^0 \to X(3872)K^*(892)^0$ samples to estimate reconstruction efficiencies after fixing variables mentioned above (α, n, fraction of area's and fraction of sigma's for both ΔE and $M_{J/\psi\pi\pi}$ dimension).

In all above stated samples, there is no difference in background parametrization. Fitting of these signal MC simulated samples are shown in Figure 4.3 and Figure 4.4 respectively for ψ' and $X(3872)$ mass regions.

Reconstruction efficiencies are estimated using signal MC simulated samples and are given in Table 4.1. It should be noted that these efficiencies are before any particle identification (PID) correction.

Further PID correction has been applied to incorporate small differences in the signal MC reconstruction efficiency because of particle identification differences between signal MC simulated events and experimental data. This difference is due to leptons [electron and muon], kaon and pion (in all due to charged tracks). All these

corrections are mentioned in detail in Section 4.4. After applying these corrections, corrected reconstruction efficiencies are summarized in Table 4.2.

Table 4.2: Reconstruction efficiencies for different signal MC samples before and after Particle identification (PID) correction.

Decay Mode	MC Efficiency (%)	PID correction Factor	Corrected Efficiency (%)
$B^0 \to \psi' K^*(892)^0$	14.65	0.94	13.77
$B^0 \to \psi'(K^+\pi^-)_{NR}$	15.67	0.94	14.73
$B^0 \to \psi' K_2^*(1430)^0$	16.52	0.94	15.53
$B^0 \to X(3872)(K^+\pi^-)_{NR}$	16.77	0.97	16.27
$B^0 \to X(3872)K^*(892)^0$	15.87	0.97	15.39

4.3.2 Background Study

The main background contribution in $B^0 \to (J/\psi\pi^+\pi^-)K^+\pi^-$ decay mode is expected to arise from inclusive B decays to J/ψ. To study this type of background, a large simulated MC sample of $B \to J/\psi X$ events is used, which corresponds to almost 100 times the integrated luminosity of the experimental data sample, where X can be any particle. We also performed J/ψ mass sidebands study in experimental data to study non-J/ψ background and found that these types of events are negligible. So main contribution to background is the decay modes having real J/ψ. All background study is given below in details.

J/ψ mass sidebands study

To study the possible background coming from the non-J/ψ component, experimental data sidebands of leptonic invariant mass ($M_{\ell^+\ell^-}$) are used. Sidebands which are considered to do above study are 2.54 GeV/c^2 $< M_{\ell^+\ell^-} <$ 2.6 GeV/c^2 and 3.2 GeV/c^2 $< M_{\ell^+\ell^-} <$ 3.5 GeV/c^2, where ℓ = e or μ. These plots are shown in Figure 4.5 and Figure 4.6 for ψ' and $X(3872)$ mass regions respectively. From sideband study it is found that these events are negligible. Hence most of the background has real J/ψ. So explanation of J/ψ inclusive MC sample is presented here in detail.

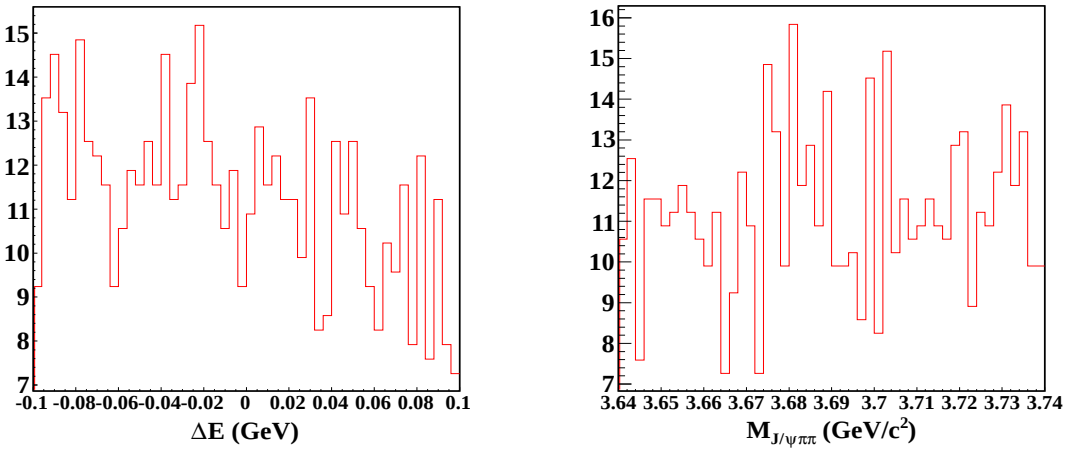

Figure 4.5: J/ψ mass sidebands for $B^0 \to \psi' K^+\pi^-$ decay mode.

J/ψ Inclusive MC study

As mentioned above, in order to estimate the background for $B^0 \to \psi' K^+\pi^-$ and $B^0 \to X(3872)K^+\pi^-$ decay modes, officially generated J/ψ inclusive MC sample is used. This sample is processed through the analysis code and different sources of background (different decay modes) are tagged using MC truth matching. For $B^0 \to$

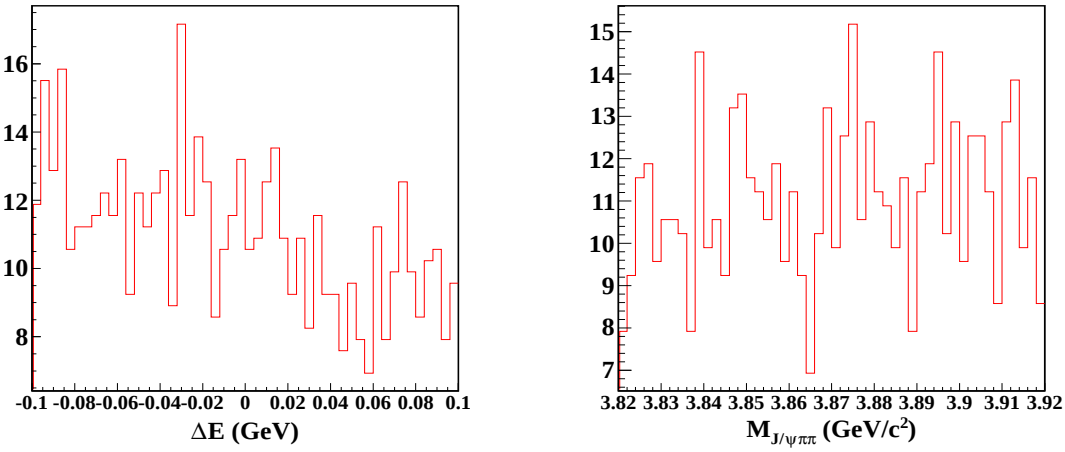

Figure 4.6: J/ψ mass sidebands for $B^0 \to X(3872)K^+\pi^-$ decay mode.

$\psi' K^+\pi^-$ decay, signal and expected background in ΔE and $M_{J/\psi\pi\pi}$ dimension are shown in Figure 4.7. In these figures, $B \to \psi' X_{sd}$ (green color) and $B^0 \to \psi' K^*(892)^0$ (red color) are two components of our signal (peaking in both dimensions), where X_{sd} includes $K^{*+}\pi^-\eta$, $K^{*0}\pi^+\pi^-$, $K^+\pi^-$, $K^0\pi^0$, $K^{*0}\pi^0$, $K^+\pi^-\omega$, $K^+\rho^-$, $K^{*+}\pi^-$ and $K^0\rho^0$ decay modes etc. In the ΔE dimension, major peaking backgrounds are coming from $B^0 \to J/\psi K^{*0}\pi^+\pi^-$ (pink color) and $B \to J/\psi X_{sd}$ (crossed blue lines) decay modes, but are found to be flat in $M_{J/\psi\pi\pi}$ dimension. In the $M_{J/\psi\pi\pi}$ dimension, the peaking background is coming from $B^+ \to \psi' K^+\pi^+\pi^-$ (light brown color) and $B^+ \to \psi' K^*(892)^+$ (blue color) decay modes, but they are not peaking in the ΔE distribution. There are other minor peaking backgrounds in this region, but all of them are found to be flat in ΔE distribution. Rest of the background has combinatorial nature in both distributions (ΔE and $M_{J/\psi\pi\pi}$) and has no peaking structure.

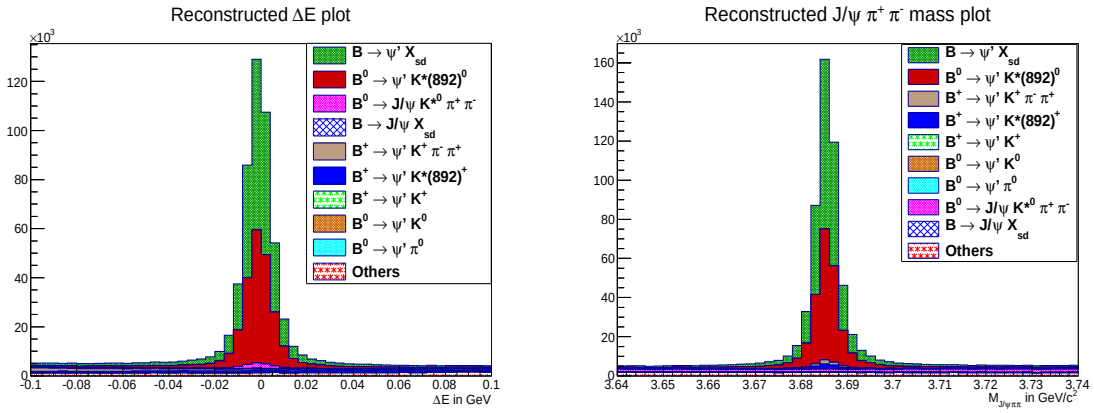

Figure 4.7: Background estimation for $B^0 \to \psi' K^+\pi^-$ decay mode using J/ψ inclusive MC ($\sim 100\times$ experimental data) for ΔE (left) and $M_{J/\psi\pi\pi}$ (right) dimensions.

For $B^0 \to X(3872)K^+\pi^-$ decay mode, the backgrounds in the ΔE and $M_{J/\psi\pi\pi}$ dimensions are shown in Figure 4.8. The peaking backgrounds in the ΔE distribution are $B^0 \to J/\psi K^{*0}\pi^+\pi^-$ (green color), $B \to \psi' X_{sd}$ (red color), $B^0 \to \psi' K^*(892)^0$ (light brown color) and $B \to J/\psi X_{sd}$ (blue color), but all these backgrounds are flat in the $M_{J/\psi\pi\pi}$ dimension. Rest backgrounds have combinatorial nature and flat in both $M_{J/\psi\pi\pi}$ and ΔE dimensions.

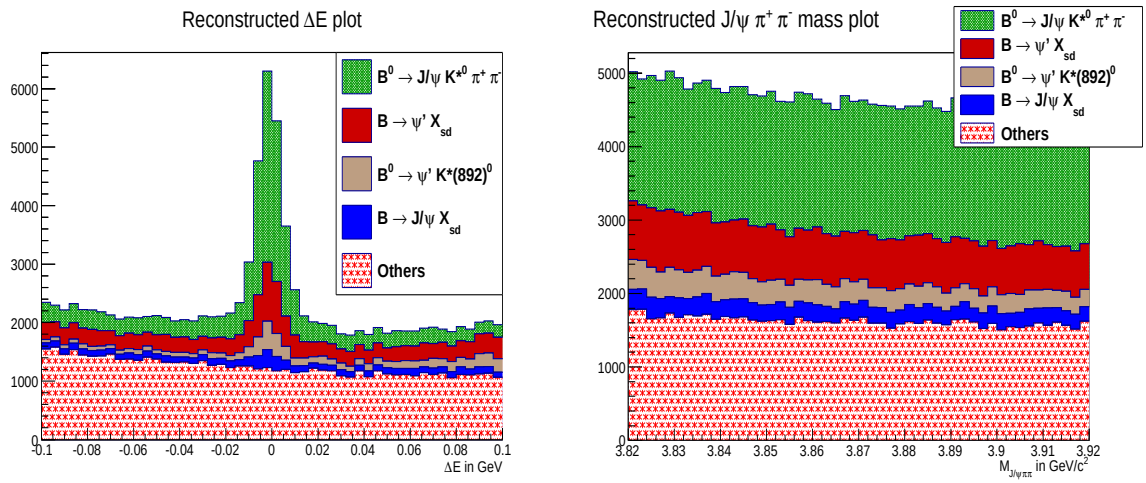

Figure 4.8: Background estimation for $B^0 \to X(3872)K^+\pi^-$ decay mode using J/ψ inclusive MC ($\sim 100\times$ experimental data) for ΔE (left) and $M_{J/\psi\pi\pi}$ (right) dimensions.

Comparison of experimental data with J/ψ Inclusive MC for calibration decay mode

Before extracting signal yield, we compared $M_{K\pi}$ mass distribution of experimental data and J/ψ inclusive MC for calibration decay mode (after normalizing as it is $100\times$ more than experimental data). While comparing, it is found that there is some discrepancy between them as shown in Figure 4.9 (left). The generation of $B \to \psi' X_{sd}$ is found to be the reason behind this discrepancy.

After removing this component, experimental data and J/ψ inclusive MC match quite well with each other (Figure 4.9 (right)). The remaining discrepancy (above 1.2 GeV/c^2) is explained by the absence of $B^0 \to \psi' K_2{}^*(1430)^0$ decay mode in officially generated J/ψ inclusive MC sample. Hence for J/ψ inclusive MC sample after removing $B \to \psi' X_{sd}$ decay mode, only $B^0 \to \psi' K^*(892)^0$ decay mode remains as a signal decay mode.

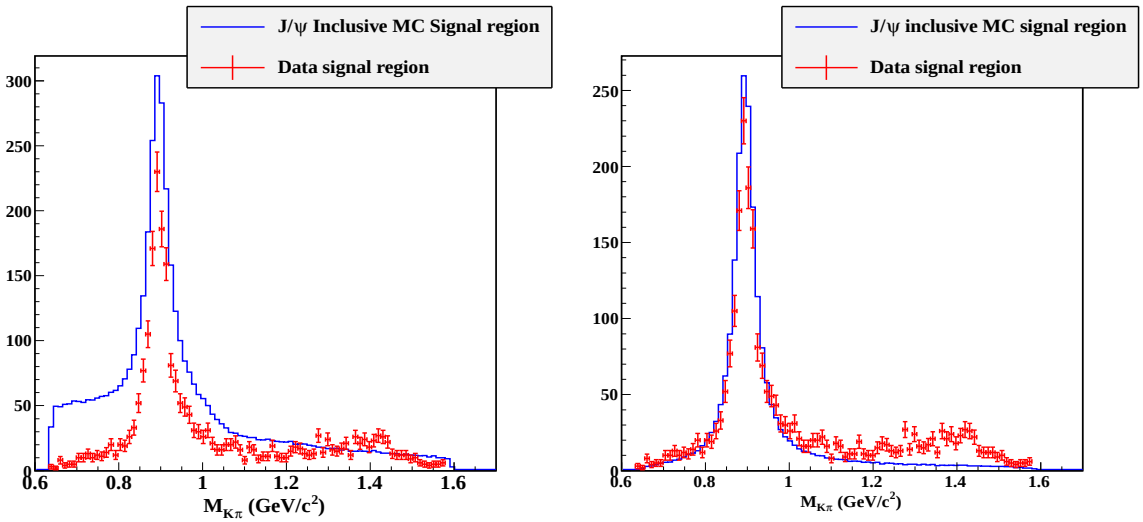

Figure 4.9: Comparison of experimental data and J/ψ inclusive MC sample before (left) and after (right) removing $B \to \psi' X_{sd}$ decay mode for ψ' mass region.

4.3.3 Branching Fraction Estimation for J/ψ Inclusive MC Sample

PDFs used for signal extraction is divided into two parts: signal and background on the similar lines as that of signal MC simulated samples. Explanation of them is the following:

• **Signal:** Product of sum of Crystal Ball and Gaussian function (used for ΔE dimension fitting) and sum of two Gaussian (used for $M_{J/\psi\pi\pi}$ dimension fitting) is used for signal PDF (as discussed in previous Section 4.3.1). The tail parameters of Crystal Ball function (α and n) are fixed from fitting of truth matched signal MC simulated events of $B^0 \to \psi' K^*(892)^0$ decay mode for both ψ' and $X(3872)$ mass regions. The rest tail parameters (fraction of areas and fraction of sigmas) are fixed from signal MC simulated sample $B^0 \to \psi' K^*(892)^0[X(3872)(K^+\pi^-)_{NR}]$ after fixing α and n for $\psi'[X(3872)]$ mass region, while core Gaussian parameters (mean and sigma) are floated in the fit for ΔE dimension. For $M_{J/\psi\pi\pi}$ dimension, tail parameters (fraction of areas and fraction of sigmas) are fixed from signal MC simulated sample $B^0 \to \psi' K^*(892)^0[X(3872)(K^+\pi^-)_{NR}]$ for $\psi'[X(3872)]$ mass region, while core

parameters (mean and sigma's) are floated in fit.

Table 4.3: Fixed parameters (in GeV) for J/ψ inclusive MC and experimental data from signal MC sample of $B^0 \to \psi' K^*(892)^0$ for calibration sample.

Parameter name	Value from signal MC
delte_alpha (from truth matching of $B^0 \to \psi' K^*(892)^0$ decay mode)	-2.0454 ± 0.042
delte_n (from truth matching of $B^0 \to \psi' K^*(892)^0$ decay mode)	1.42 ± 0.15
maspsi_a2a	0.7025 ± 0.0041
maspsi_s2s1	2.756 ± 0.016
delte_a2a	0.8036 ± 0.0032
delte_s2s1	3.046 ± 0.034

The parameters which are fixed for J/ψ inclusive MC sample and for experimental data are shown in Table 4.3.

• **Backgrounds:** Total background is further divided into two parts: peaking and combinatorial part. Peaking background should have same PDF as of the signal, so PDF is fixed in a similar way to the one of signal PDF. This peaking background is flat in other dimension. So Chebychev polynomial of 1^{st} order is used to parametrize flat background in $M_{J/\psi\pi\pi}$ distribution (peaking in ΔE distribution and for its vice-versa). While, the combinatorial background in both $M_{J/\psi\pi\pi}$ and ΔE dimensions can be easily parametrized by product of Chebychev polynomial 1^{st} order.

Using the above mentioned strategy to fit signal and background components, a 2D extended UML fit is performed to the whole J/ψ inclusive MC sample (which consists both of signal and backgrounds after removing the $B \to \psi' X_{sd}$ component). Fitting of only signal events ($B^0 \to \psi' K^*(892)^0$) from whole J/ψ inclusive MC sample is shown in Figure 4.10 (top). Total fit to whole J/ψ inclusive MC sample is shown in Figure 4.10 (bottom). Signal yield (203539 ± 542 events) extracted from the total fit comes out to be consistent to the one extracted from signal part only (205353 ± 483 events), which provides confidence in the fitter.

Since $B^0 \to \psi' X_{sd}$ decay mode is removed from J/ψ inclusive MC sample, so $B^0 \to \psi' K^*(892)^0$ decay mode is only signal, which is left in this sample and $\mathcal{B}(B^0 \to \psi' K^*(892)^0)$ is estimated and it is found to be consistent for the signal fit with and without background as summarized in Table 4.4.

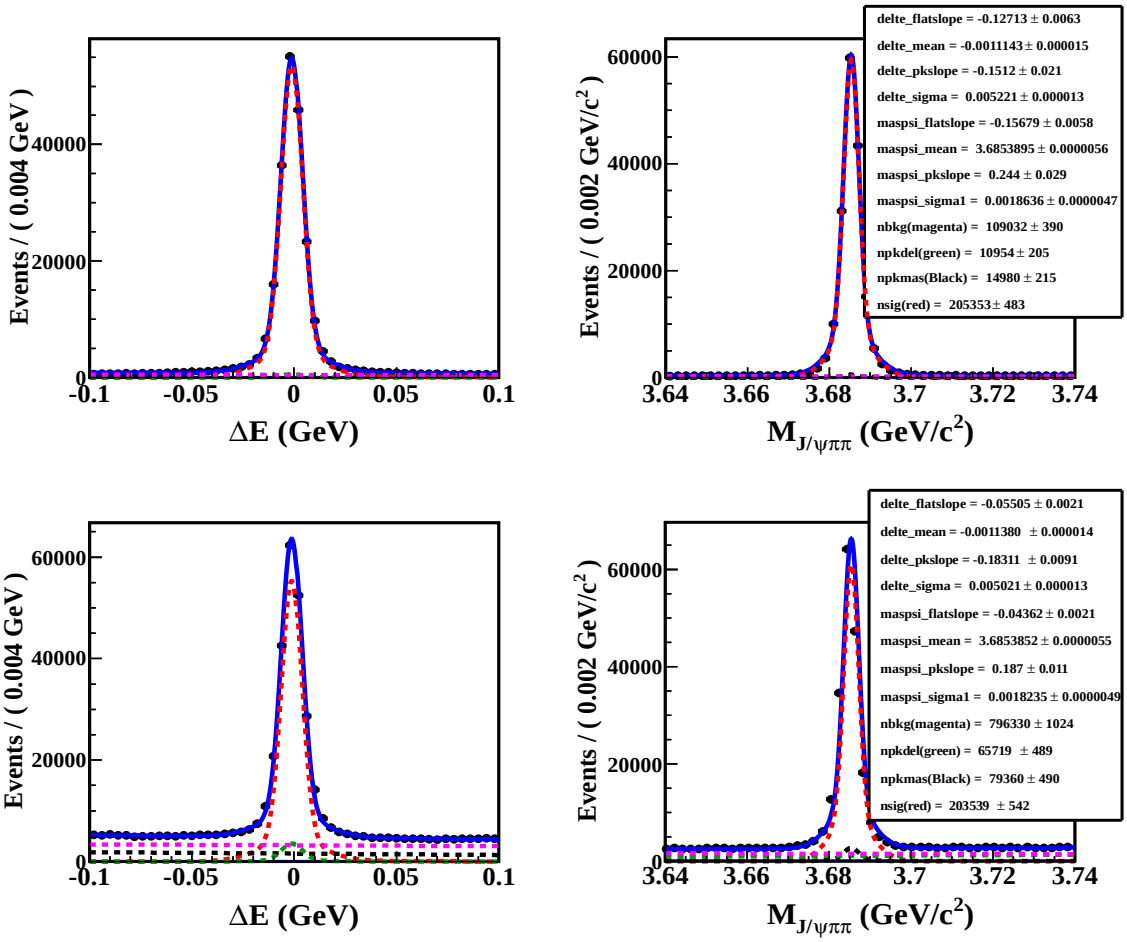

Figure 4.10: Signal region projections for only signal $B^0 \to \psi' K^*(892)^0$ from J/ψ inclusive MC sample (top) and whole J/ψ inclusive MC ($\sim 100\times$ experimental data) sample (bottom). Left plot is the projection for $M_{J/\psi\pi\pi}$ signal region $[3.675, 3.695]$ GeV/c^2 and right plot is the projection for ΔE signal region $[-11, 8]$ MeV. The curves show the signal [red dotted] and the background components [black dotted for the component peaking in $M_{J/\psi\pi\pi}$ but non-peaking in ΔE, green dotted for the one peaking in ΔE but non-peaking in $M_{J/\psi\pi\pi}$, and magenta dotted for combinatorial background in both dimensions] as well as the overall fit [blue solid].

Table 4.4: $\mathcal{B}(B^0 \to \psi' K^*(892)^0)$ estimated from fit to the J/ψ inclusive MC with signal only and with signal + backgrounds.

Fit Sample	$\mathcal{B}(\times 10^{-4})$ From fit	$\mathcal{B}(\times 10^{-4})$ DECAY.DEC (Generated value)
Only signal	7.30 ± 0.02	7.20
With background	7.24 ± 0.02	7.20

Similar to calibration decay mode study, J/ψ inclusive MC sample is divided into two parts for $B^0 \to X(3872)(K^+\pi^-)$ decay mode: 1^{st} part having only signal & 2^{nd} part having peaking and combinatorial backgrounds.

• **Signal:** Since there is no decay mode in J/ψ inclusive MC which peaks in $X(3872)$ mass region in both dimensions (ΔE as well as $M_{J/\psi\pi\pi}$) as shown in Figure 4.8. So signal PDF is fixed in J/ψ inclusive MC for $X(3872)$. Ideally signal events should be zero.

• **Backgrounds:** Background is further divided into two parts: peaking and combinatorial part. Peaking backgrounds PDF are fixed as that of signal PDF because of same resolution. Chebychev polynomial of 1^{st} order is used to parametrize flat background in $M_{J/\psi\pi\pi}$ distribution (peaking in ΔE dimension). While, the combinatorial background is flat in both dimensions and can be parametrized by product of Chebychev polynomial 1^{st} order for both $M_{J/\psi\pi\pi}$ and ΔE dimension. The total fit to the J/ψ inclusive MC sample is shown in Figure 4.11 as there is no signal for $X(3872)$

Table 4.5: Fixed parameters (in GeV) for J/ψ inclusive MC from signal MC simulated sample of $B^0 \to X(3872)(K^+\pi^-)_{NR}$ for concerned decay mode.

Parameter name	Value from signal MC
maspsi_mean	3.8708155 ± 0.0000043
maspsi_sigma1	0.0019086 ± 0.0000067
maspsi_a2a	0.7413 ± 0.003
maspsi_s2s1	2.931 ± 0.017
delte_alpha (from truth matching of $B^0 \to \psi' K^*(892)^0$ decay mode)	-2.0454 ± 0.042
delte_n (from truth matching of $B^0 \to \psi' K^*(892)^0$ decay mode)	1.42 ± 0.15
delte_sigma	0.004936 ± 0.000018
delte_a2a	0.8299 ± 0.0036
delte_s2s1	2.887 ± 0.038

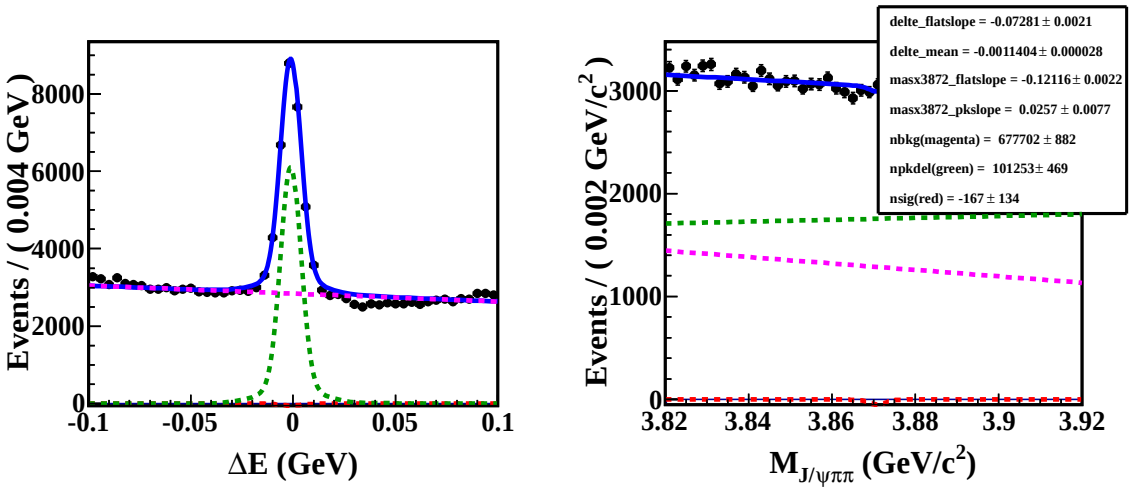

Figure 4.11: Signal region projections for whole J/ψ inclusive MC ($\sim 100\times$ experimental data) sample. Left plot is the projection for $M_{J/\psi\pi\pi}$ signal region $[3.860, 3.881]$ GeV/c^2 and right plot is the projection for ΔE signal region $[-11, 8]$ MeV. The curves show the signal [red dotted] and the background components [green dotted for the one peaking in ΔE but non-peaking in $M_{J/\psi\pi\pi}$, and magenta dotted for combinatorial background] as well as the overall fit [blue solid].

in J/ψ inclusive MC. Parameters which are fixed for J/ψ inclusive MC sample are shown in Table 4.5. As one can observe in Figure 4.11, signal events are consistent with zero.

4.3.4 Fit Validation

In order to determine the stability of fit procedure and to correct for any possible fit bias, toy MC simulations study and GSIM study is performed.

- **Toy MC study**: To perform this study, the expected number of events (allowing for Poisson fluctuations) of fit model under consideration are generated according to the PDFs of the fit for each experiment. 1000 toy MC samples are generated using signal and background PDFs. All Signal events [$(K^*(892)^0$, $K_2{}^*(1430)^0$ and $(K^+\pi^-)_{NR}$ in ψ' mass region) ($K^*(892)^0$ and $(K^+\pi^-)_{NR}$ in $X(3872)$ mass region)] as well as background events are generated using experimental data results shown in

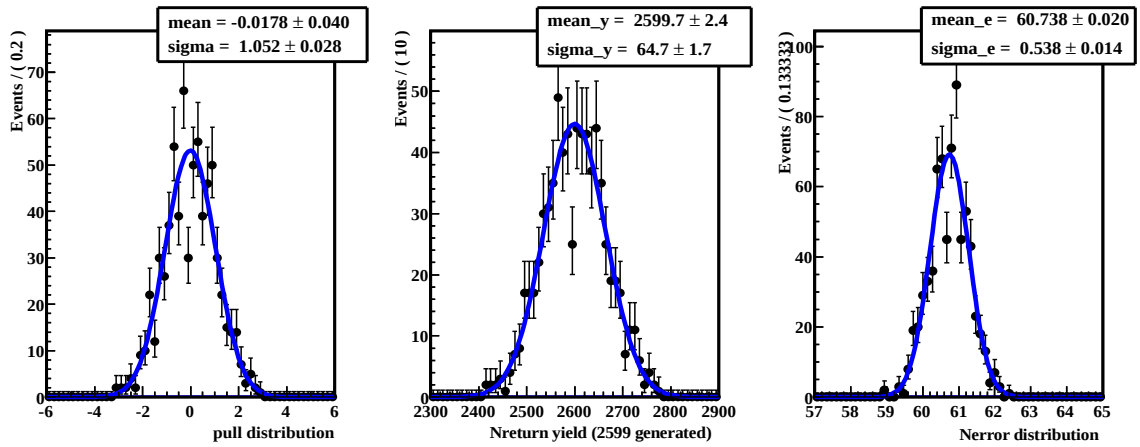

Figure 4.12: Pull distribution (left), return yield distribution (middle) and error distribution (right) for 1000 toy MC study for $B^0 \to \psi' K^+\pi^-$ decay mode.

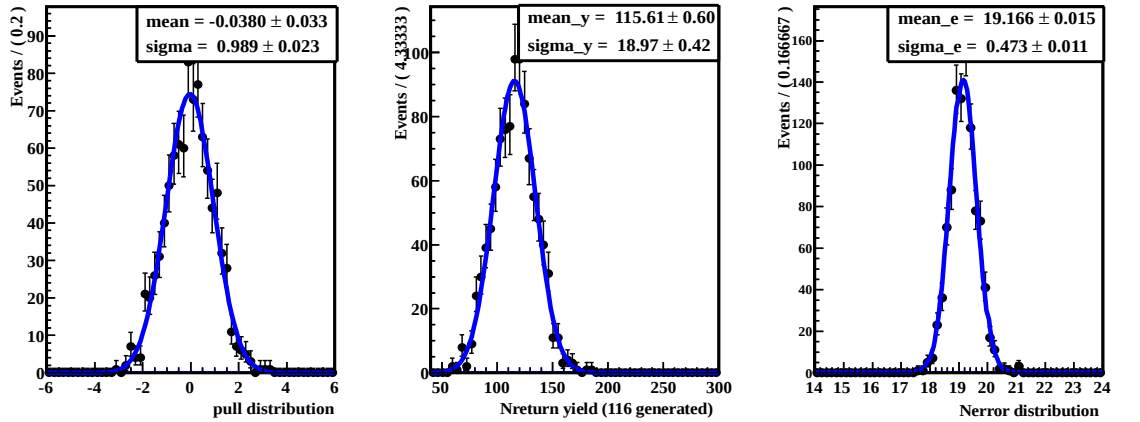

Figure 4.13: Pull distribution (left), return yield distribution (middle) and error distribution (right) for 1000 toy MC study for $B^0 \to X(3872) K^+\pi^-$ decay mode.

Figure 4.16 and Figure 4.17 respectively for ψ' and $X(3872)$ mass regions and using PDFs. Signal yield is extracted from each toy MC sample using same final fitter. The possible bias in our signal extraction procedure has been estimated by calculating the pull from each fit defined as:

$$\text{Pull} = \frac{\text{Yield}_{\text{Fitted}} - \text{Yield}_{\text{Expected}}}{\sigma_{\text{Fitted Yield}}}. \qquad (4.3)$$

Figure 4.12 and Figure 4.13 shows the pull distribution (left), return yield distribution (middle) and error distribution (right) respectively for ψ' and $X(3872)$ mass regions,

which demonstrates that there is no significant bias in the final fitter.

- **GSIM study**: GSIM (Geant SIMulation) study has also been performed using ac-

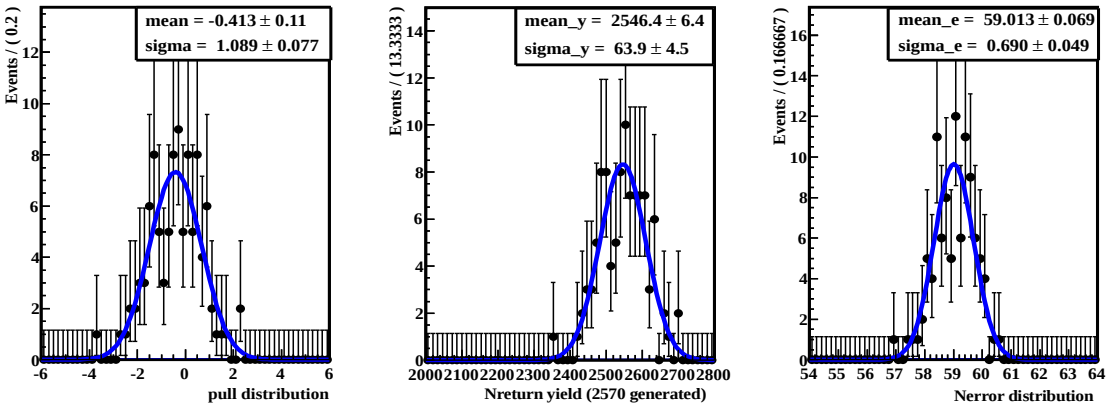

Figure 4.14: Pull distribution (left), return yield distribution (middle) and error distribution (right) for GSIM study for $B^0 \to \psi' K^+\pi^-$ decay mode.

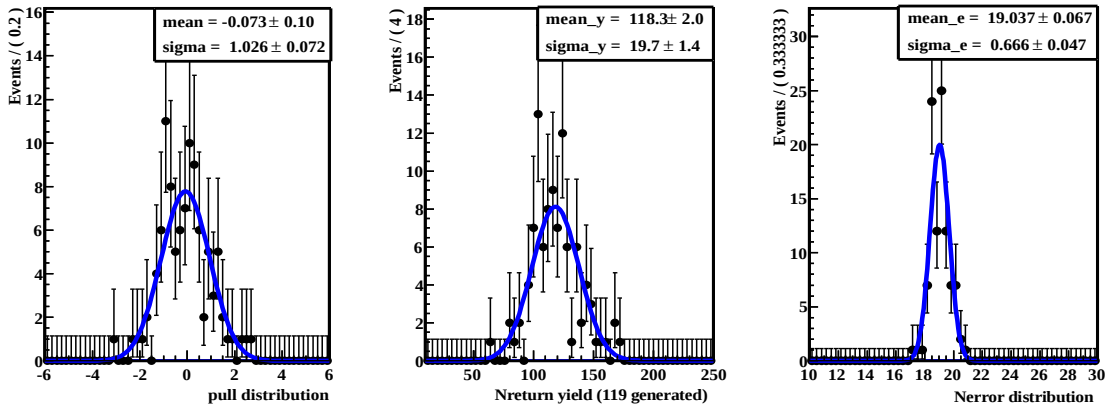

Figure 4.15: Pull distribution (left), return yield distribution (middle) and error distribution (right) for GSIM study for $B^0 \to X(3872)K^+\pi^-$ decay mode.

tual signal MC simulated events and background events. As Belle MC team officially generated huge sample of J/ψ inclusive MC ($\sim$100$\times$ the experimental data) under similar detector environment conditions and same type of expected backgrounds as that of experimental data. Full advantage of this whole sample has been taken. Whole J/ψ inclusive MC sample is divided into 100 samples and all signal events are embed-

ded in each sample according to background subtracted $M_{K\pi}$ distribution extracted from the fit shown in Figure 5.8 and Figure 5.9 for ψ' and $X(3872)$ mass regions, respectively. GSIM study will actually reflect true fit bias, if any. Figure 4.14 and Figure 4.15 shows the pull distribution (left), return yield distribution (middle) and error distribution (right) for ψ' and $X(3872)$ mass regions, respectively after performing GSIM study. From these distributions, it is clear that there is no significant bias in the final fitter. However due to conservation, insignificant bias has been added in the systematic uncertainty estimation.

4.3.5 Extraction of Signal Yield from Experimental Data and Results

From J/ψ inclusive MC study and from fit bias study, it can be concluded that estimation of signal yield is neither under-estimated nor over-estimated, also systematic uncertainty is very small, so same procedure can be used to extract signal yield from actual experimental data. All PDFs (Signal PDF + Background PDFs) for the fitting of experimental data are same as that of J/ψ inclusive MC. Fitting of experimental data for $B^0 \to \psi'(K^+\pi^-)$ in signal and background enhanced regions is shown in Figure 4.16. Signal yield extracted from fit to the experimental data is (2599 ± 61) events and branching fraction (B.F) comes out to be $(5.44 \pm 0.13(\text{stat.})) \times 10^{-4}$. Here weighted efficiency is considered (mentioned in Appendix A) by assuming each $K\pi$ component according to Figure 5.8. After including PID efficiency correction and systematic uncertainty mentioned in Table 4.2 and Table 4.15 respectively, $\mathcal{B}(B^0 \to \psi' K^+\pi^-)$ comes out to be $(5.79 \pm 0.14(\text{stat.}) \pm 0.31(\text{syst.})) \times 10^{-4}$. while PDG B.F for this decay mode is $(5.8 \pm 0.4) \times 10^{-4}$ [128], here the error is the combination of systematic as well as statistical uncertainties.

For fitting of experimental data for $X(3872)$ mass region, all parameters of fitting function except mean and width are fixed to that from signal MC sample. Difference between experimental data and signal MC for the mean and width is calculated and are called fudge factors. The calibrated mean ($\mu_{\text{calibrated}}$) and width ($\sigma_{\text{calibrated}}$) due

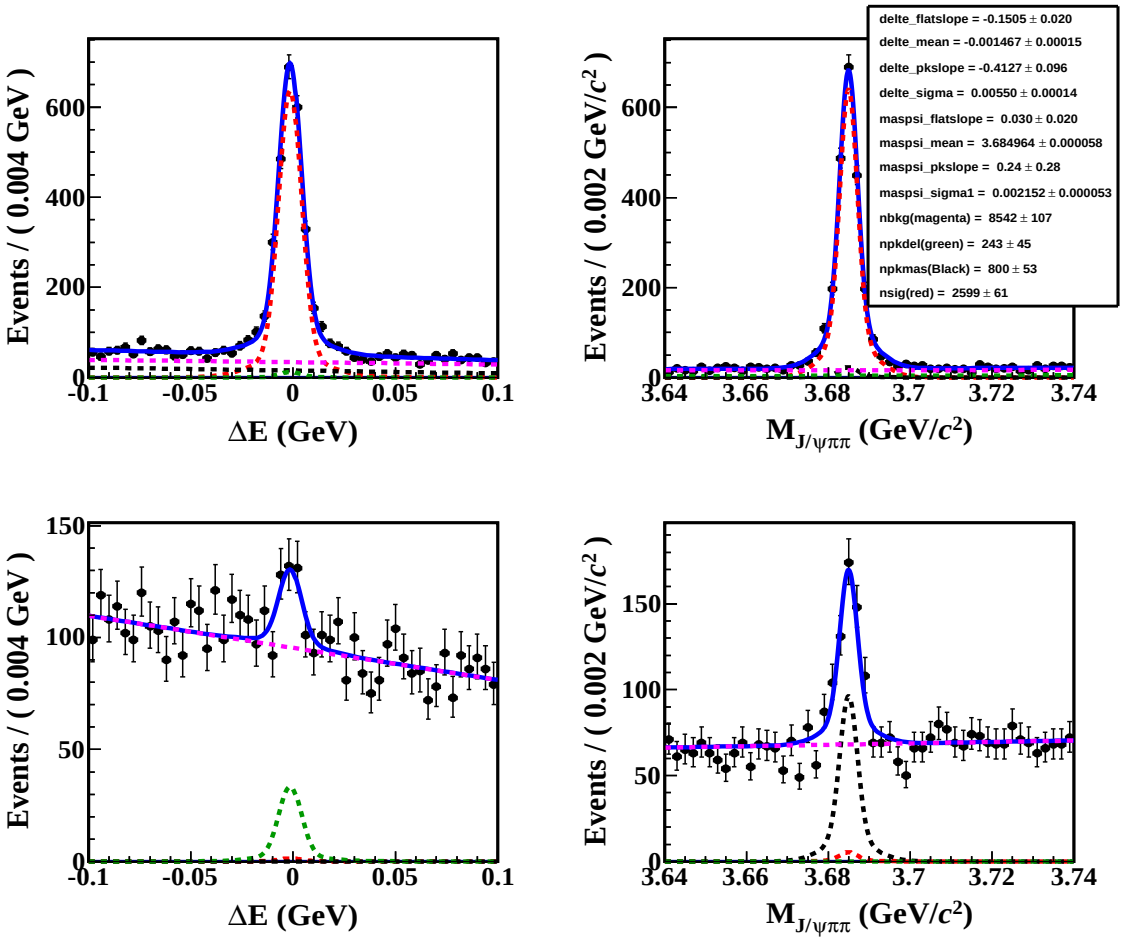

Figure 4.16: Top: Signal region projections of experimental data for $B^0 \to \psi' K^+\pi^-$ decay mode. Left (right) plot is the projection for $M_{J/\psi\pi\pi}$ (ΔE) signal region. Bottom: Projection plots in background enhanced regions of ΔE and $M_{J/\psi\pi\pi}$. Left (right) is for $M_{J/\psi\pi\pi}$ (ΔE) sidebands in ψ' mass region. The curves show the signal [red dotted] and the background components [black dotted for the component peaking in $M_{J/\psi\pi\pi}$ but non-peaking in ΔE, green dotted for the one peaking in ΔE but non-peaking in $M_{J/\psi\pi\pi}$, and magenta dotted for combinatorial background] as well as the overall fit [blue solid].

to misidentification are calculated by using the fudge factors as,

$$\mu_{\text{calibrated}} = \mu_{\text{MC}} + (\mu_{\text{data}} - \mu_{\text{MC}})_{\text{calibration sample}}; \quad (4.4)$$

$$\sigma_{\text{calibrated}} = (\frac{\sigma_{\text{data}}}{\sigma_{\text{MC}}})_{\text{calibration sample}} \times \sigma_{\text{MC}}. \quad (4.5)$$

From experimental results, it is found that dynamics of $X(3872) \to J/\psi\pi^+\pi^-$ and $\psi' \to J/\psi\pi^+\pi^-$ is different, as former proceeds through an intermediate state $J/\psi\rho$, where ρ further decays to $\pi^+\pi^-$, so there is a shift in mass between ψ' and $X(3872)$ [129], which has to be corrected. This correction is applied to mass of $(J/\psi\pi^+\pi^-)$. Pa-

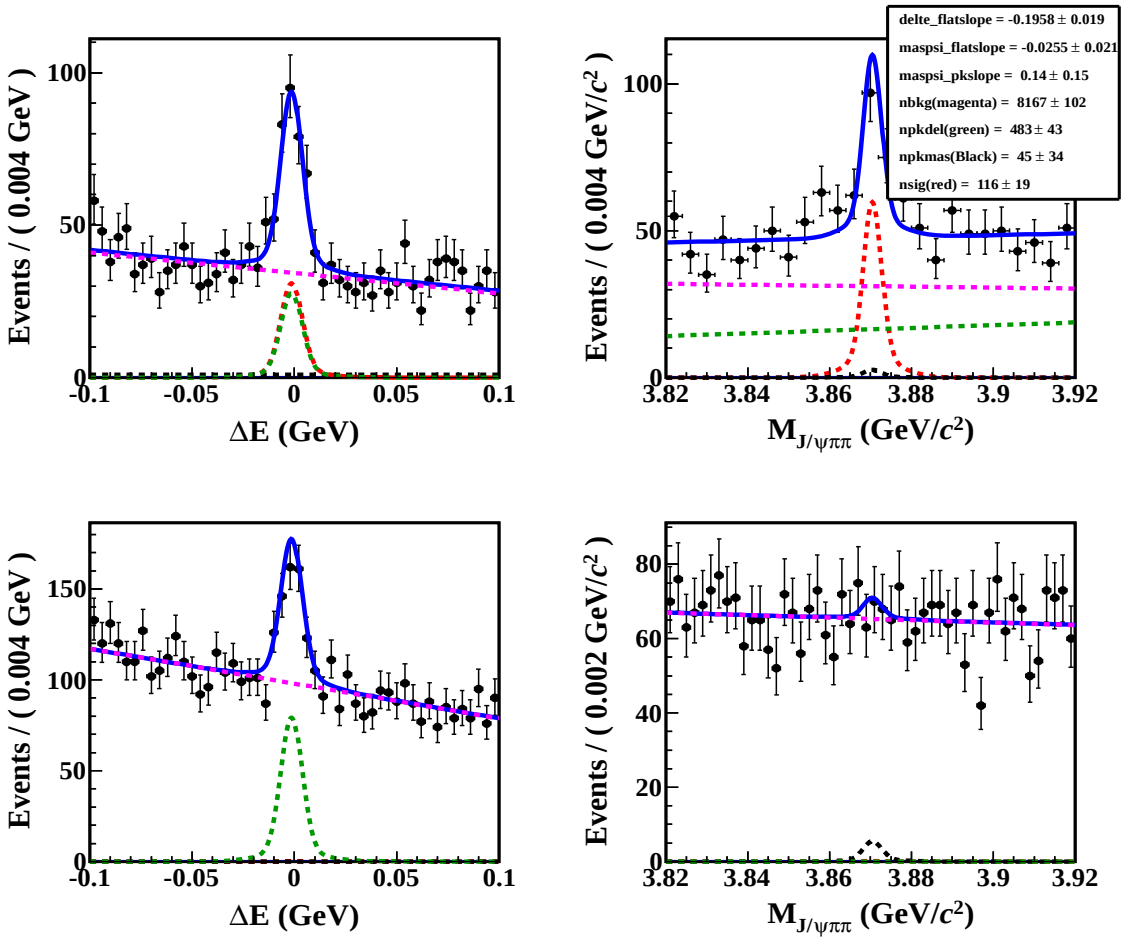

Figure 4.17: Top: Signal region projections of experimental data for $B^0 \to X(3872)K^+\pi^-$ decay mode. Left (right) plot is the projection for $M_{J/\psi\pi\pi}$ (ΔE) signal region. Bottom: Projection plots in background enhanced regions of ΔE and $M_{J/\psi\pi\pi}$. Left (right) is for $M_{J/\psi\pi\pi}$ (ΔE) sidebands in $X(3872)$ mass region. The curves show the signal [red dotted] and the background components [black dotted for the component peaking in $M_{J/\psi\pi\pi}$ but non-peaking in ΔE, green dotted for the one peaking in ΔE but non-peaking in $M_{J/\psi\pi\pi}$, and magenta dotted for combinatorial background] as well as the overall fit [blue solid].

Table 4.6: Fixed parameters (in GeV) for experimental data found using fudge factor.

Parameter name	Value from signal MC
maspsi_mean	3.8705 ± 0.0000583488
maspsi_sigma1	$0.00220231 \pm 0.0000556364$
maspsi_a2a	0.7413 ± 0.003
maspsi_s2s1	2.931 ± 0.017
delte_alpha (from truth matching of $B^0 \to \psi' K^*(892)^0$ decay mode)	-2.0454 ± 0.042
delte_n (from truth matching of $B^0 \to \psi' K^*(892)^0$ decay mode)	1.42 ± 0.15
delte_mean	$-0.0013691 \pm 0.000150811$
delte_sigma	$0.00519977 \pm 0.000134906$
delte_a2a	0.8299 ± 0.0036
delte_s2s1	2.887 ± 0.038

rameters which are fixed for experimental data are shown in Table 4.6.

Experimental data fit for $B^0 \to X(3872)K^+\pi^-$ in signal and background enhanced regions is shown in Figure 4.17 using similar PDFs as that for calibration sample and after fixing all parameters mentioned in Table 4.6. Thus a clear peak in $X(3872)$ mass region as well as in ΔE signal region with signal yield (116 ± 19) events has been observed for $B^0 \to X(3872)(K^+\pi^-)$ decay mode with full Belle data sample. The product branching fractions is also measured as:

$$\mathcal{B}(B^0 \to X(3872)(K^+\pi^-)) \times \mathcal{B}(X(3872) \to J/\psi\pi^+\pi^-) = (7.67 \pm 1.25(\text{stat.})) \times 10^{-6}. \quad (4.6)$$

After including PID correction in Table 4.2 and systematic uncertainty mentioned in Table 4.15, product of $\mathcal{BR}$ comes out to be:

$$\mathcal{B}(B^0 \to X(3872)(K^+\pi^-)) \times \mathcal{B}(X(3872) \to J/\psi\pi^+\pi^-) = (7.91 \pm 1.29(\text{stat.})^{+0.43}_{-0.42}(\text{syst.})) \times 10^{-6}. \quad (4.7)$$

Here also weighted efficiency is considered by assuming same fraction of each $K\pi$ component as in Figure 5.9 (details are in Appendix A).

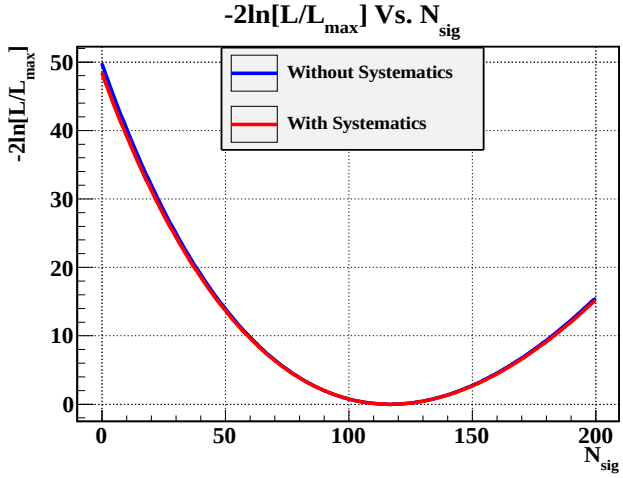

Figure 4.18: Scan of $-2\ln(\mathcal{L}_0/\mathcal{L}_{\max})$ for whole range of yields for decay mode $B^0 \to X(3872)K^+\pi^-$ with blue curve (before systematic uncertainty) and red curve (after including systematic uncertainties which affects only signal yield).

4.3.6 Significance of Signal Yield for $B^0 \to X(3872)K^+\pi^-$ Decay Mode

Method used for significance estimation is mentioned in detail in Appendix B. The statistical significance is estimated using the value of $\sqrt{-2\ln(\mathcal{L}_0/\mathcal{L}_{\max})}$ where $\mathcal{L}_{\max}$ ($\mathcal{L}_0$) denotes the likelihood value when the yield is allowed to vary (fixed to zero). The significance of $B^0 \to X(3872)K^+\pi^-$ decay mode with current experimental data is found to be 7.1σ and 7.0σ respectively for before and after including systematic uncertainties (which affects only signal yield) also shown in Figure 4.18. One can understand 7.0σ significance as out of one trillion events, getting this result as fake is only 2 events.

4.4 Systematic Uncertainty Study

In addition to the statistical uncertainty, there is also an uncertainty which can affects results or estimations. These uncertainties are known as systematic uncertainties. Main sources of the systematic uncertainties for all decay modes under consideration

are due to kaon-identification, pion-identification, charged track finding efficiency, lepton-identification, due to limited statistics, having limited knowledge of the actual model to generate signal MC events, secondary branching fractions, number of $B\bar{B}$ ($N_{B\bar{B}}$) events, due to PDF modeling, fit bias etc. We describe them below.

Table 4.7: Kaon identification systematic uncertainty for different modes under study.

Mode	Correction with error		Efficiency	Syst. error(%)
	SVD1	SVD2	correction	
$B^0 \to \psi' K^+\pi^-$	1.0032 ± 0.0107	1.0114 ± 0.0109	1.0098	1.0860
$B^0 \to X(3872)K^+\pi^-$	1.0037 ± 0.0124	1.0158 ± 0.0107	1.0350	1.1035

4.4.1 Kaon Identification

In $B^0 \to (J/\psi\pi^+\pi^-)(K^+\pi^-)$ decay, kaons have uncertainty on their identification and to estimate it, official PID group estimation is used, which is based upon the $D^{*+} \to D^0(K^-\pi^+){\pi_{\rm slow}}^+$ decay [123]. A correction for the difference in kaon efficiency between experimental data and MC is then obtained. This correction is used to correct the efficiency while error on it, is included as systematic error coming from kaon's identification. Table 4.7 summarizes the kaon's systematic uncertainty study.

4.4.2 Pion Identification

Similar procedure is applied for pion as that of kaon (Table 4.8) to find systematic uncertainty and PID correction.

4.4.3 Charged Track Finding Efficiency

Charged particle track reconstruction has an uncertainty of about 0.35% per track which has been estimated on the basis of partially reconstructed $D^{*-} \to \bar{D}^0(\to K^0_S(\to \pi^-\pi^+)\pi^+\pi^-)\pi^-$ decay mode study by tracking group [124]. Due to correlation, the errors are added linearly. For $B^0 \to \psi'(K^+\pi^-)$ and $B^0 \to X(3872)(K^+\pi^-)$ decay modes, this uncertainty comes out to be 2.1%.

Table 4.8: Pion identification systematic uncertainty for different modes under study.

Mode	Correction with error		Efficiency	Syst. error(%)
	SVD1	SVD2	Correction	
$B^0 \to \psi'(K^+\pi^-)$ (π of $K\pi$)	0.9873 ± 0.0055	0.9826 ± 0.0118	0.9835	1.056
$B^0 \to X(3872)(K^+\pi^-)$ (π of $K\pi$)	0.9915 ± 0.0061	0.9885 ± 0.0120	0.9891	1.083
$B^0 \to \psi'(K^+\pi^-)$ (π of ψ')	0.9983 ± 0.0061	1.0018 ± 0.0131	1.0011	1.172
$B^0 \to X(3872)(K^+\pi^-)$ (π of $X(3872)$)	0.9973 ± 0.0070	1.0004 ± 0.0126	0.9998	1.149

4.4.4 Lepton Identification

There can be a difference between lepton identification in experimental data and in MC. This difference needs to be estimated. For lepton identification, systematic uncertainties are calculated from the comparison between the experimental data and MC for $2\gamma \to ee\mu\mu$. Efficiency correction and systematic uncertainties are calculated as a function of the momentum (p) and the polar angle (θ) in the laboratory rest frame. Table 4.9 summarizes the electron and muon identification systematic error and lepton identification correction.

Table 4.9: Lepton identification systematic uncertainty for different modes under study.

Mode	Correction with error			Syst. error(%)		
$J/\psi \to$	e^+e^-	$\mu^+\mu^-$	l^+l^-	e^+e^-	$\mu^+\mu^-$	l^+l^-
$B^0 \to \psi'(\to J/\psi\pi^+\pi^-)(K^+\pi^-)$	0.9833	0.9625	0.9729	1.51	1.84	1.68
$B^0 \to X(3872)(\to J/\psi\pi^+\pi^-)(K^+\pi^-)$	0.9837	0.9637	0.9737	1.47	1.83	1.65

4.4.5 Systematic Uncertainty due to Efficiency

This type of uncertainty arises from two sources in present analysis. First it is due to the limited statistical samples of signal MC, so there will be sizeable statistical errors on the calculated efficiency and this error is taken into account in the calculation of systematic uncertainty. And second systematic uncertainty in the efficiency is due to

the limited knowledge of the actual model to generate signal MC sample and hence to calculate weighted efficiency, which is further used for branching fractions estimation. This systematic uncertainty is given in Table 4.10 and also mentioned in Appendix A.

Table 4.10: Systematic uncertainty due to limited statistics of the MC samples used for 2D fit study and having limited knowledge of actual model to generate signal MC simulated events.

Decay mode	$B^0 \to \psi' K^+\pi^-$	$B^0 \to X(3872)K^+\pi^-$
Syst. (%)	0.26	0.6

4.4.6 Secondary Branching Fraction

Secondary branching fractions from PDG'14 [1] are used for the estimation of primary branching fractions. These secondary branching fractions also have errors, which are considered as the source of systematic coming from secondary branching fraction. Table 4.11 summarizes the systematic uncertainty coming from the secondary branching fraction. We are using the following secondary branching fractions

a) $\Longrightarrow \mathcal{B}(J/\psi \to e^+e^-) = 0.05971 \pm 0.00032$ (0.54%)

b) $\Longrightarrow \mathcal{B}(J/\psi \to \mu^+\mu^-) = 0.05961 \pm 0.00033$ (0.55%)

c) $\Longrightarrow \mathcal{B}(J/\psi \to \ell^+\ell^-) = 0.11932 \pm 0.00046$ (0.39%) (combining a and b)

d) $\Longrightarrow \mathcal{B}(\psi' \to J/\psi\pi^+\pi^-) = 0.3445 \pm 0.003$ (0.87%)

e) $\Longrightarrow \mathcal{B}(K_S \to \pi^+\pi^-) = 0.6920 \pm 0.0005$ (0.07%)

Table 4.11: Secondary branching fraction systematic uncertainty.

Decay Mode	Contribution	Syst(%)
$B^0 \to \psi'(K^+\pi^-)$	c and d	0.95
$B^0 \to X(3872)(K^+\pi^-)$	c	0.39

4.4.7 Uncertainty on Number of $B\bar{B}$ Events ($N_{B\bar{B}}$)

This systematic uncertainty is due to the uncertainty on number of $B\bar{B}$ events ($N_{B\bar{B}}$) estimation value. Official $N_{B\bar{B}}$ for expt. 7-65 (experimental data currently used) is $(771.6 \pm 10.6) \times 10^6$ events which gives a systematic uncertainty of 1.4%.

4.4.8 Systematic Uncertainty due to PDF Fitting Model

Signal yield extraction is performed by fitting to the experimental data. Fixed parameters in the fit affects signal yield as these fixed parameters have some uncertainty on it. To estimate this PDF modeling systematic uncertainty, variation of fixed parameters of the fit is done by $+1\sigma/-1\sigma$ (one at a time).

The systematic uncertainty due to the PDF modeling is estimated to be $^{+0.20}_{-0.13}\%$ and $^{+1.81\%}_{-1.53\%}$ for $B^0 \to \psi' K^+\pi^-$ and $B^0 \to X(3872)K^+\pi^-$ respectively for 2D extended UML fit study as shown in Table 4.12 and Table 4.13.

Table 4.12: Estimation of systematic uncertainty for 2D fit (PDF modeling) as shown in Figure 4.16. Nominal value of the signal yield for $B^0 \to \psi' K^+\pi^-$ decay mode is 2599.

Variable	Value Error	+Variation -Variation	Yield	ΔYield	-(Δ Yield)	+(Δ Yield)
maspsi_a2a	0.7025	0.7066	2599	0	0	1
	0.0041	0.6984	2600	1		
maspsi_s2s1	2.756	2.772	2601	2	-1	2
	0.016	2.740	2598	-1		
delte_alpha	-2.0454	-2.0034	2601	2	-1	2
	0.042	-2.0874	2598	-1		
delte_n	1.42	1.57	2598	-1	-1	2
	0.15	1.27	2601	2		
delte_a2a	0.8036	0.8068	2597	-2	-2	2
	0.0032	0.8004	2601	2		
delte_s2s1	3.046	3.080	2602	3	-2	3
	0.034	3.012	2597	-2		
				Total	-0.13%	+0.20%

Table 4.13: Estimation of systematic uncertainty for 2D fit (PDF modeling) as shown in Figure 4.17. Nominal value of the signal yield for $B^0 \to X(3872)K^+\pi^-$ decay mode is 116.48.

Variable	Value Error	+Variation -Variation	Yield	ΔYield	-(Δ Yield)	+(Δ Yield)
maspsi_mean	3.8705	3.8705583488	116.45	-0.03	-0.03	0.16
	5.83488E-05	3.8704416512	116.64	0.16		
maspsi_sigma	0.00220231	0.0022579464	118.13	1.65	-1.47	1.65
	5.56364E-05	0.0021466736	115.01	-1.47		
maspsi_a2a	0.7413	0.7443	116.25	-0.23	-0.23	0.36
	0.003	0.7383	116.84	0.36		
maspsi_s2s1	2.931	2.948	116.75	0.27	-0.13	0.27
	0.017	2.914	116.35	-0.13		
delte_mean	-0.0013691	-0.001218289	116.28	-0.20	-0.20	0.31
	1.50811E-04	-0.001519911	116.79	0.31		
delte_sigma	0.00519977	0.005334676	117.59	1.13	-0.92	1.13
	1.34906E-04	0.005064864	115.56	-0.92		
delte_alpha	-2.0454	-2.0034	116.51	0.03	-0.03	0.03
	0.0420	-2.0874	116.45	-0.03		
delte_n	1.42	1.57	116.45	-0.03	-0.03	0.04
	0.15	1.27	116.52	0.04		
delte_a2a	0.8299	0.8335	116.29	-0.19	-0.19	0.38
	0.0036	0.8263	116.86	0.38		
delte_s2s1	2.887	2.925	116.61	0.13	-0.12	0.13
	0.038	2.849	116.36	-0.12		
				Total	-1.53%	+1.81%

4.4.9 Systematic Uncertainty due to Fit Bias

Due to small bias in the final fitter, there can be systematic uncertainty which is mentioned in Table 4.14.

Table 4.14: Systematic uncertainty due to the fit bias for 2D extended UML fit study.

Decay mode	$B^0 \to \psi' K^+\pi^-$	$B^0 \to X(3872)K^+\pi^-$
Syst. (%)	0.92	0.59

4.4.10 Total Systematic Uncertainty

All systematic uncertainties contributions are summarized in Table 4.15. All these individual systematic uncertainties are added in quadrature to obtain total systematic uncertainty of $\pm 5.29\%$ and $^{+5.41}_{-5.33}\%$, respectively for $B^0 \to \psi' K^+\pi^-$ and $B^0 \to X(3872)K^+\pi^-$ decay modes.

Table 4.15: The summary of systematic uncertainties used for 2D extended UML fit study.

Systematic Uncertainty(%)		
Mode $\to$	$B \to \psi' K^+\pi^-$	$B \to X(3872)K^+\pi^-$
Source $\downarrow$		
K-id	1.1	1.1
π-id π of $K\pi$	1.1	1.1
π-id pions of ψ' or $X(3872)$	2×1.2	2×1.1
Tracking	2.1	2.1
ℓ id	2×1.7	2×1.7
MC statistics	0.26	0.59
Sec. $\mathcal{B}$	0.95	0.39
$N_{B\bar{B}}$	1.4	1.4
PDF	$^{+0.20}_{-0.13}$	$^{+1.81}_{-1.53}$
Fit bias	0.92	0.59
Total	± 5.29	$^{+5.41}_{-5.33}$

4.5 Chapter in Compact

In this Chapter, $B^0 \to X(3872)K^+\pi^-$ has been described along with the analysis of calibration decay mode $B^0 \to \psi' K^+\pi^-$. Branching fraction is estimated for this calibration decay mode $B^0 \to \psi' K^+\pi^-$ to be $(5.79 \pm 0.14(\text{stat.}) \pm 0.31(\text{syst.})) \times 10^{-4}$ which is well consistent with the world measurement. We have performed search for $B^0 \to X(3872)K^+\pi^-$ decay mode with the analysis of full Belle data set, a clear observation of $B^0 \to X(3872)K^+\pi^-$ decay mode has been seen having significance of 7σ (after including systematic uncertainties). The product of branching fractions $\mathcal{B}(B^0 \to X(3872)(K^+\pi^-)) \times \mathcal{B}(X(3872) \to J/\psi\pi^+\pi^-)$ has been measured, which comes out to be $(7.91 \pm 1.29(\text{stat.})^{+0.43}_{-0.42}(\text{syst.})) \times 10^{-6}$.

5

Search for Resonant structures in $B^0 \to X(3872)K^+\pi^-$

In this Chapter, the study for the search of possible resonant structures in $B^0 \to X(3872)K^+\pi^-$ decay mode has been explained in detail. To elucidate the nature of the signal observed, especially whether there are contributions from the decays with intermediate resonant states, a fit study is performed using possible combinations in decay mode $B^0 \to X(3872)K^+\pi^-$ (e.g. using background subtracted mass distributions of $K\pi$, $X(3872)K$ and $X(3872)\pi$). Detail study of the background subtracted $(K\pi)$ mass distribution is performed to get possible $K\pi$ resonant and non-resonant components. In order to get maximum information, background subtracted $M_{K\pi}$ ($K\pi$-mass) distribution is used and binned minimum χ^2 fit is performed to separate out the different $K\pi$ components. Before performing this study on $B^0 \to X(3872)K^+\pi^-$, the fit is first verified on our calibration decay mode $B^0 \to \psi' K^+\pi^-$.

5.1 Search for Resonances in $(K\pi)$ System

To check the production mechanism of three body decay mode $B^0 \to X(3872)K^+\pi^-$, different combinations are checked. In this Section, we check $K\pi$ mass distribution to

find any resonant or non-resonant component. For this purpose, 2D extended UML fit is performed to ΔE and $M_{J/\psi\pi\pi}$ variables in each bin of $M_{K\pi}$. From this fitting, we get background subtracted distribution of $M_{K\pi}$ with its errors are also returned by 2D fit. This distribution is shown in Figure 5.1. From this distribution, it seems a clear pattern of resonant and non-resonant component. Hence we perform detail study on this background subtracted $(K\pi)$ mass distribution to extract different $(K\pi)$ components.

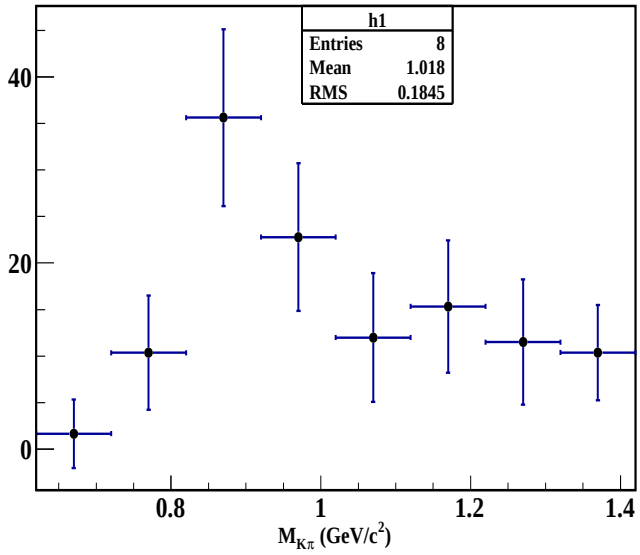

Figure 5.1: Background subtracted distribution of $M_{K\pi}$.

5.2 $(K\pi)$ Components and its Background Subtracted Binned Fit Study

† The signal extraction procedure explained in Chapter 4 based upon 2D extended UML fit provides total signal yield for $B^0 \to \psi' K^+\pi^-$ and $B^0 \to X(3872)K^+\pi^-$ decay modes. Extracting different $(K\pi)$ resonant and non-resonant components is

†This study with root version 34.07 to take into account custom errors, which was not available in the previous versions of root.

not possible there (because $K\pi$ can have any fraction of different resonant and non-resonant states). In order to extract different components of $(K\pi)$ system, a fit to $M_{K\pi}$ mass distribution is necessary. So for this method, 2D extended UML fit is performed to the variables ΔE and $M_{J/\psi\pi\pi}$ in the each bins of $M_{K\pi}$ distribution. In the end, background subtracted distribution of $M_{K\pi}$ is obtained. Then, one can perform binned minimum χ^2 fit (due to binning, statistics and because of custom errors provided by 2D extended UML fit) to separate out the different contribution of $K\pi$ resonant and non-resonant components.

5.2.1 Branching Fractions and Ratio of Branching Fractions

Branching fraction for $B^0 \to \psi' K^*(892)^0$ decay mode is defined as follows:

$$\mathcal{B}(B^0 \to \psi' K^*(892)^0) = \frac{Y(B^0 \to \psi' K^*(892)^0)}{\epsilon \times \mathcal{B}(\psi' \to J/\psi\pi\pi) \times \mathcal{B}(J/\psi \to \ell\ell) \times \mathcal{B}(K^*(892)^0 \to K^+\pi^-) \times N(B\bar{B})}. \quad (5.1)$$

The product of the branching fractions $\mathcal{B}(B^0 \to X(3872)K^*(892)^0) \times \mathcal{B}(X(3872) \to J/\psi\pi^+\pi^-)$ is given by:

$$\mathcal{B}(B^0 \to X(3872)K^*(892)^0) \times \mathcal{B}(X(3872) \to J/\psi\pi^+\pi^-) = \frac{Y(B^0 \to X(3872)K^*(892)^0)}{\epsilon(B^0 \to X(3872)K^*(892)^0) \times \mathcal{B}(J/\psi \to \ell^+\ell^-) \times \mathcal{B}(K^*(892)^0 \to K^+\pi^-) \times N(B\bar{B})}. \quad (5.2)$$

The signal yield $Y(B^0 \to X(3872)K^*(892)^0)$ is the number of fitted $B^0 \to X(3872)$ $K^*(892)^0$ events found in the total experimental data set $N(B\bar{B})$ with suitable PDFs.

Reconstruction of all signal events is not 100% efficient due to the software detector reconstruction limitations, so it is required to estimate the reconstruction efficiency ϵ for the estimation of branching fractions.

Further in this Chapter, a measurement of ratio of branching fractions is done, which can be defined as follows:

$$R_{\psi'} = \frac{\mathcal{B}(B^0 \to \psi' K^*(892)^0) \times \mathcal{B}(K^*(892)^0 \to K^+\pi^-)}{\mathcal{B}(B^0 \to \psi' K^+\pi^-)_{\text{2D fit}}}. \quad (5.3)$$

$$R_{X(3872)} = \frac{\mathcal{B}(B^0 \to X(3872)K^*(892)^0) \times \mathcal{B}(K^*(892)^0 \to K^+\pi^-)}{\mathcal{B}(B^0 \to X(3872)K^+\pi^-)_{\text{2D fit}}}. \quad (5.4)$$

From these ratio's, there can be some interpretation for different nature of $X(3872)$ as compared to ordinary charmonium states e.g. ψ' mass region.

5.2.2 Signal MC Study - Efficiency Estimation and PDF Modeling

Large number of signal MC events are already generated for different decay modes mentioned in Section 4.3.1. Then a 2D extended UML fit is performed on ΔE and $M_{J/\psi\pi\pi}$ variables in each mass bin of $M_{K\pi}$ with 51 MeV wide bins and $M_{K\pi}$ range is [0.6-1.569] GeV/c^2 (total 19 bins) for ψ' mass region. Same strategy is applied for $X(3872)$ mass region as adopted for ψ' for signal yield extraction in each bin, except the change of bin width. Due to the limitation of the signal events in $B^0 \to X(3872)K^+\pi^-$ decay mode (≈ 120 events), we ran out of luxury of choosing fine bins and were forced to use 100 MeV wide bins of $M_{K\pi}$ based upon number of expected events and resolution of $K^*(892)^0$ resonance. Range selected for $M_{K\pi}$ is from 0.62-1.42 GeV/c^2 for $X(3872)$ mass region (total 10 bins). Resolution of ΔE and $M_{J/\psi\pi\pi}$ is checked in each bins of $M_{K\pi}$ and is found to be consistent. In light of which, the mean and width for ΔE and $M_{J/\psi\pi\pi}$ are fixed to the one estimated from the global fit performed on respective samples. In order to have a good control over the fit, the slope of the flat background (for the one which is peaking in other dimension) is fixed as global fit result. This is done after performing the fit bias studies.

Signal MC yield obtained from 2D fit for each signal in the bins of $M_{K\pi}$ are shown in Figure 5.2 and Figure 5.3 for ψ' and $X(3872)$ mass regions respectively. These signal yields are obtained after performing 2D fitting on ΔE and $M_{J/\psi\pi\pi}$ in each bin of $M_{K\pi}$. From these extracted yields, RooHistPdfs are obtained which are further used to fit different signal component in J/ψ inclusive MC sample and in experimental data. For ψ' mass region, major $(K\pi)$ components are $K^*(892)^0$, $K_2^*(1430)^0$ and $(K^+\pi^-)_{NR}$ as shown in Figure 5.2. For $X(3872)$ mass region, two $(K\pi)$ components are there shown in Figure 5.3 except $K_2^*(1430)^0$, because it is

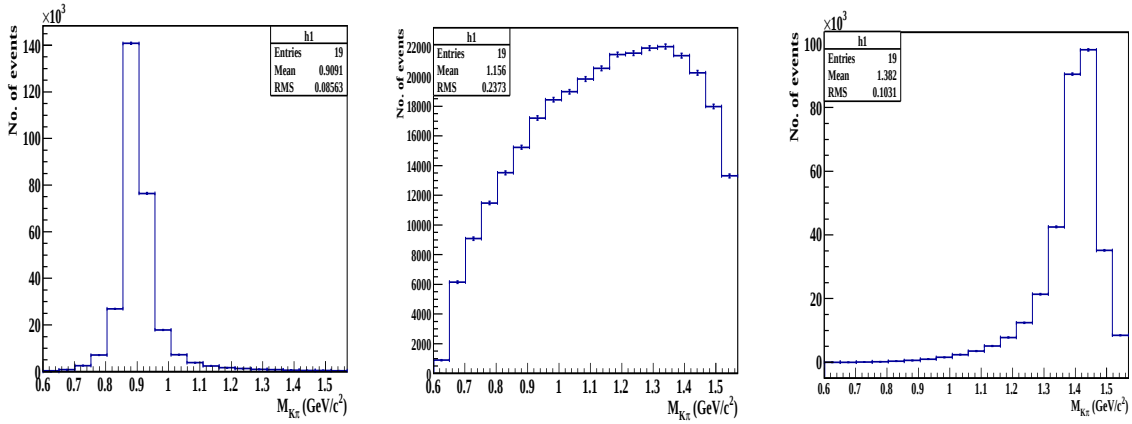

Figure 5.2: Background subtracted signal MC yield for $B^0 \to \psi' K^*(892)^0$ (left), $B^0 \to \psi'(K^+\pi^-)_{NR}$ (middle) and $B^0 \to \psi' {K_2}^*(1430)^0$ (right) decay modes obtained from 2D extended UML fitting of ΔE and $M_{J/\psi\pi\pi}$ variables in each bin of $M_{K\pi}$.

kinematically suppressed.

These distributions are background subtracted ones, so reconstruction efficiencies can be estimated from total yield obtained for each sample. Reconstruction efficiencies without and with PID corrections are mentioned in Table 5.1.

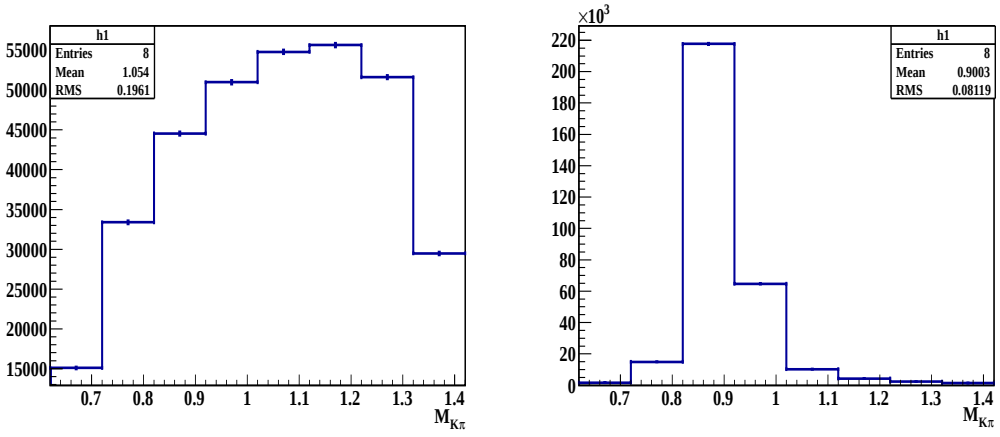

Figure 5.3: Background subtracted signal MC yield for $B^0 \to X(3872)(K^+\pi^-)_{NR}$ (left) and $B^0 \to X(3872)K^*(892)^0$ (right) decay modes obtained from 2D extended UML fitting of ΔE and $M_{J/\psi\pi\pi}$ variables in each bin of $M_{K\pi}$.

Table 5.1: Reconstruction efficiencies for $B^0 \to \psi' K^*(892)^0$ and $B^0 \to X(3872)K^*(892)^0$ decay modes before and after PID correction used for background subtracted binned fit study.

Decay Mode	MC Efficiency (%)	PID correction Factor	Corrected Efficiency (%)
$B^0 \to \psi' K^*(892)^0$	14.62	0.94	13.74
$B^0 \to X(3872)K^*(892)^0$	15.86	0.97	15.38

5.2.3 J/ψ Inclusive MC Study

Official J/ψ inclusive MC sample has backgrounds for $X(3872)$ mass region. But to perform background subtracted binned fit study, one required signal events. So to perform the study with Official J/ψ inclusive MC sample, one has to embed signal MC events. Following is the description of calibration decay mode as well as concerned decay mode:

• **For $B^0 \to \psi' K^+\pi^-$ decay mode:**

Official J/ψ inclusive MC sample is divided into 100 pseudo-experiments (luminosity equivalent to experimental data) after removing signal decay mode i.e. $B^0 \to \psi' K^*(892)^0$. In each sample, signals $B^0 \to \psi' K^*(892)^0$, $B^0 \to \psi'(K^+\pi^-)_{NR}$ and $B^0 \to \psi' {K_2}^*(1430)^0$ are embedded according to fraction got from $M_{K\pi}$ fit as shown in Figure 5.8. For each sample 2D extended UML fit is performed in each bin of $M_{K\pi}$. Then binned minimum χ^2 fit is performed on background subtracted $M_{K\pi}$ signal yield and custom errors (both provided by 2D fit), which is obtained from each sample, using RooHistPdf's got from signal MC study. Thus one can compare embedded yield and extracted signal yield from binned minimum χ^2 fit for these 100 samples.

Pull distribution (left), return yield distribution (middle) and error distribution (right) is shown in Figure 5.4 for $B^0 \to \psi' K^*(892)^0$ decay mode. As one can see, there is no significant fit bias in this study.

• **For $B^0 \to X(3872)K^+\pi^-$ decay mode:**

Same strategy is applied for $X(3872)$ mass region as that of calibration decay mode by embedding both signals ($B^0 \to X(3872)K^*(892)^0$ as well as $B^0 \to X(3872)(K^+\pi^-)_{NR}$)

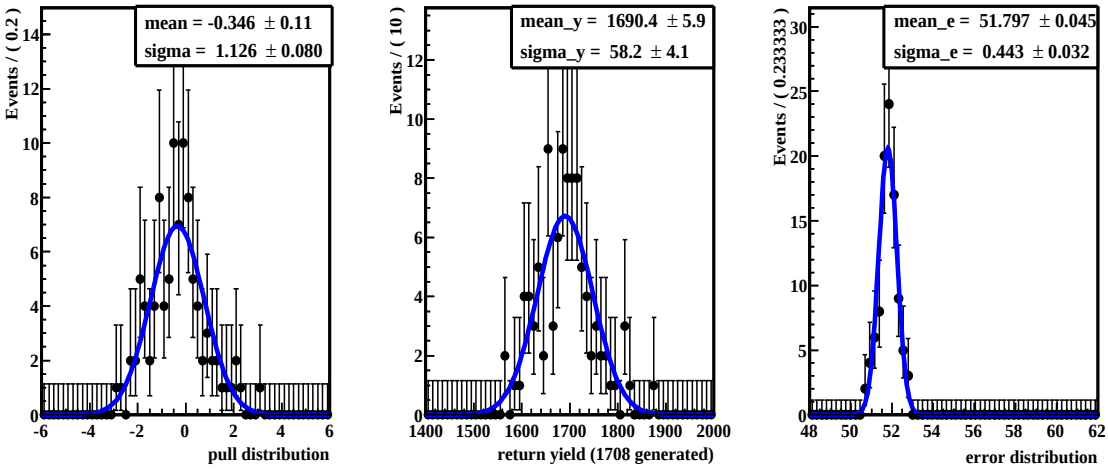

Figure 5.4: Pull distribution (left), return yield distribution (middle) and error distribution (right) for $B^0 \to \psi' K^*(892)^0$ decay mode after dividing whole J/ψ inclusive MC into 100 pseudo-experiments after embedding all signals.

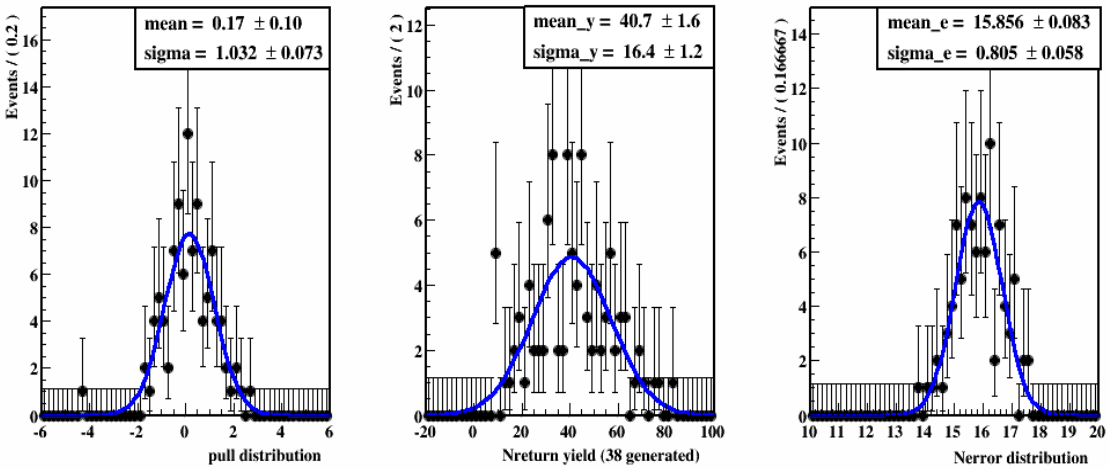

Figure 5.5: Pull distribution (left), return yield distribution (middle) and error distribution (right) for $B^0 \to X(3872) K^*(892)^0$ decay mode after dividing whole J/ψ inclusive MC into 100 pseudo-experiments after embedding all signals.

to J/ψ inclusive MC. Fitting is done to $M_{K\pi}$ distribution by using binned minimum χ^2 method with RooHistPdf's obtained from signal MC study. Pull distribution (left),

return yield distribution (middle) and error distribution (right) is shown in Figure 5.5 for $B^0 \to \psi' K^*(892)^0$ decay mode.

Insignificant biases from these distributions (Figure 5.4 and Figure 5.5) are added as source of systematic uncertainty arises from fit bias study.

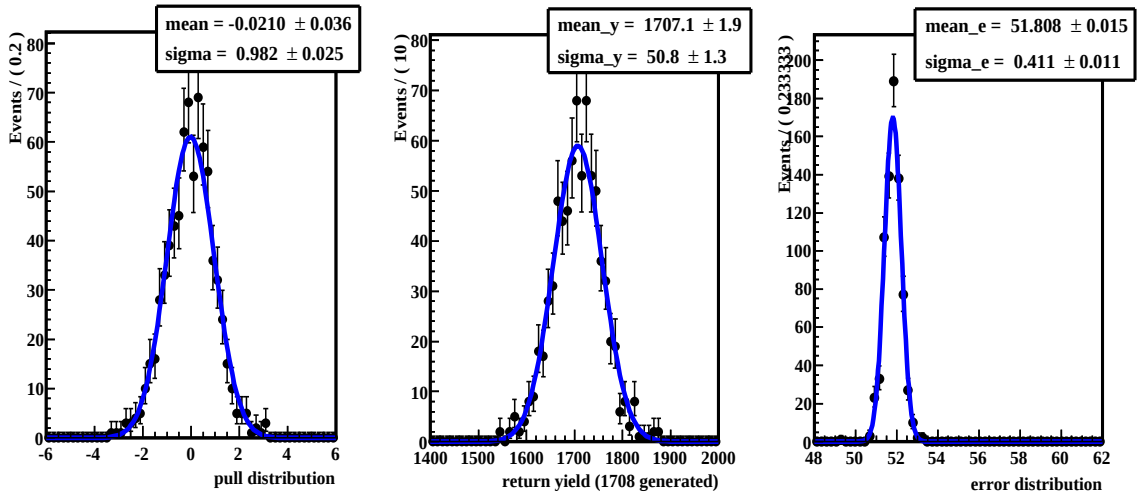

Figure 5.6: Pull distribution (left), return yield distribution (middle) and error distribution (right) for 1000 toy MC study for $B^0 \to \psi' K^*(892)^0$ decay mode.

5.2.4 Fit Validation

• Toy MC study for $B^0 \to \psi' K^+\pi^-$ decay mode:

In order to validate the estimation of signal yield and to check for any kind of fit bias, 1000 toy MC samples are generated using the signal and the background PDF in each bin. Total of 1708, 160 and 703 events are generated for $B^0 \to \psi' K^*(892)^0$, $B^0 \to \psi' K_2^*(1430)^0$ and $B^0 \to \psi'(K^+\pi^-)_{NR}$ decay modes respectively, while for backgrounds, events are generated according to yield obtained from experimental data by 2D fitting as shown in Figure 4.16. The 2D extended UML fit is performed for each sample in each bin. Background subtracted signal yield and custom errors are then fitted using binned minimum χ^2 method by using RooHistPdf's got from signal MC study to estimate the possible bias in fitting procedure by calculating the pulls

from each fit. Figure 5.6 shows the pull distribution (left), return yield distribution (middle) and error distribution (right) for $B^0 \to \psi' K^*(892)^0$ decay mode.

No significant bias has been found from toy MC study for our calibration decay mode.

- **Toy MC study for $B^0 \to X(3872)K^+\pi^-$ decay mode:**

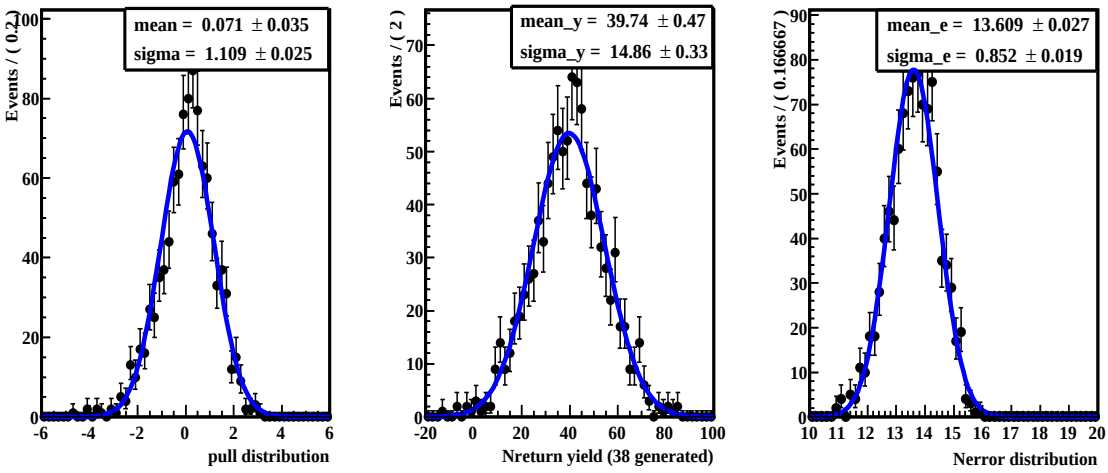

Figure 5.7: Pull distribution (left), return yield distribution (middle) and error distribution (right) for 1000 toy MC study for $B^0 \to X(3872)K^*(892)^0$ decay mode.

Here also the same strategy has been adopted as that of calibration decay mode. In order to validate measured estimate, 1000 toy MC samples are generated using the signal and the background PDF in each bin. Total of 38 and 82 events are generated respectively for $B^0 \to X(3872)K^*(892)^0$ and $B^0 \to X(3872)(K^+\pi^-)_{NR}$ decay modes, while for backgrounds events are generated according to yield obtained from experimental data 2D fitting as shown in Figure 4.17. The 2D extended UML fit is performed for each sample in each bin. Background subtracted signal yield and custom errors are then fitted using binned minimum χ^2 method by using RooHistPdf's got from signal MC study to estimate the possible bias in fitting procedure by calculating the pull from each fit. Figure 5.7 shows the pull distribution (left), return yield distribution (middle) and error distribution (right). Again no significant bias has been observed from this toy MC study and insignificant bias has been added as

a source of systematic uncertainty for conservation.

5.2.5 Extraction of Signal Yield from Experimental Data and Results

• For $B^0 \to \psi' K^+\pi^-$decay mode:

The same strategy has been applied as previously explained for pseudo-experiments and toy MC study. The 2D extended UML fit to ΔE and $M_{J/\psi\pi\pi}$ variables has been performed for experimental data in each bin of $M_{K\pi}$ to obtain signal yield as well as custom errors. As already stated all parameters (except slope of combinatorial background) are fixed as that of 2D global fit of experimental data for ψ' as well as $X(3872)$ mass regions during the extraction of signal yield as well as custom errors. Then binned minimum χ^2 fit is performed to this obtained signal yield and custom errors (both are provided by 2D fit) using RooHistPdf's got from signal MC study. Fitting to this experimental data is shown in Figure 5.8. Sum of yields obtained for each $(K\pi)$ component is consistent with total yield obtained from 2D fit of ΔE and $M_{J/\psi\pi\pi}$ (Figure 4.16) variables and the branching fractions (B.F) of $B^0 \to \psi' K^*(892)^0$ decay mode obtained from experimental data is $(5.53 \pm 0.17) \times 10^{-4}$. After including PID correction mentioned in Table 5.1 and systematic uncertainty (Table 5.6) B.F of $B^0 \to \psi' K^*(892)^0$ from experimental data comes out to be $(5.88 \pm 0.18 \pm 0.31) \times 10^{-4}$, while the branching fraction from PDG is $(6.0 \pm 0.4) \times 10^{-4}$, here the error is the combination of statistical and systematic uncertainties. So estimation of branching fraction by binned minimum χ^2 method is consistent within errors to world average value.

From above branching fraction, in the ψ' mass region, $R_{\psi'}$ variable is estimated as:

$$R_{\psi'} = \frac{\mathcal{B}(B^0 \to \psi' K^*(892)^0) \times \mathcal{B}(K^*(892)^0 \to K^+\pi^-)}{\mathcal{B}(B^0 \to \psi' K^+\pi^-)_{\text{2D fit}}} = 0.68 \pm 0.01(\text{stat.}) \pm 0.01(\text{syst.}). \quad (5.5)$$

For estimating this ratio, many of the common systematic uncertainties are cancelled out except systematic due to PDF modeling, fit bias and efficiency variation due to

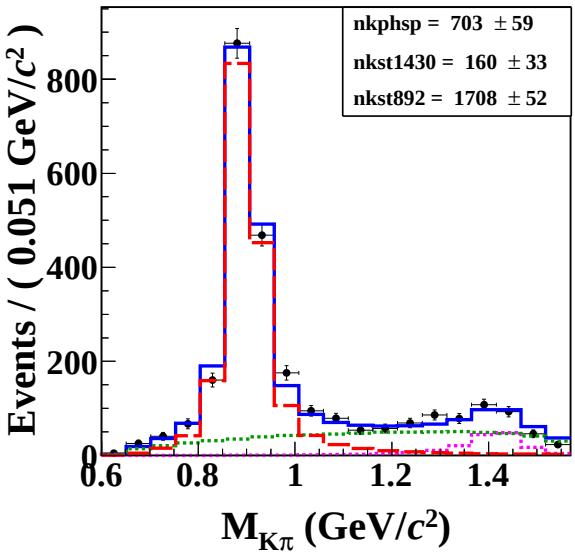

Figure 5.8: Binned minimum χ^2 fitting of signal yield and custom errors in 51 MeV wide $M_{K\pi}$ bins for experimental data for ψ' mass region. Red curve represents $B^0 \to \psi' K^*(892)^0$, green curve is for $B^0 \to \psi'(K^+\pi^-)_{NR}$, magenta one is for $B^0 \to \psi' K_2^*(1430)^0$ and blue solid for overall fit.

limited knowledge to generate signal MC samples. This ratio is consistent with the one measured by Belle using full amplitude analysis [128].

From the fit bias study as well as from calibration decay mode study, confidence is gained to extract signal yield for concerned decay mode using the same strategy as that of calibration decay mode.

• **For $B^0 \to X(3872)K^+\pi^-$decay mode**

For the experimental data, the fitting of background subtracted $M_{K\pi}$ distribution for $X(3872)$ mass region, using same strategy as that of calibration decay mode, is shown in Figure 5.9. The signal yields obtained from the fitting to the experimental data are (38 ± 14) and (82 ± 21) events for $B^0 \to X(3872)K^*(892)^0$ and $B^0 \to X(3872)(K^+\pi^-)_{NR}$ decay modes respectively. The total yield "$38+82$" events obtained from the $M_{K\pi}$ fit is close to the result from 2D fit (Figure 4.17) of ΔE and $M_{J/\psi\pi\pi}$ variables. So there is major contribution of these two components to the

whole ($K\pi$) system. As one can see in same Figure 5.9, for $B^0 \to X(3872)K^+\pi^-$ decay mode, non-resonant component is dominating as compared to resonant one. The product of branching fractions $\mathcal{B}(B^0 \to X(3872)K^*(892)^0) \times \mathcal{B}(X(3872) \to J/\psi\pi^+\pi^-)$ for experimental data is estimated to be $(3.87 \pm 1.44(\text{stat.})) \times 10^{-6}$ before including systematic uncertainties. However after including PID correction mentioned in Table 5.1 and systematic uncertainties from Table 5.6 for experimental data, the product of branching fractions comes out to be $\mathcal{B}(B^0 \to X(3872)K^*(892)^0) \times \mathcal{B}(X(3872) \to J/\psi\pi^+\pi^-) = (3.99 \pm 1.48(\text{stat.}) \pm 0.28(\text{syst.})) \times 10^{-6}$.

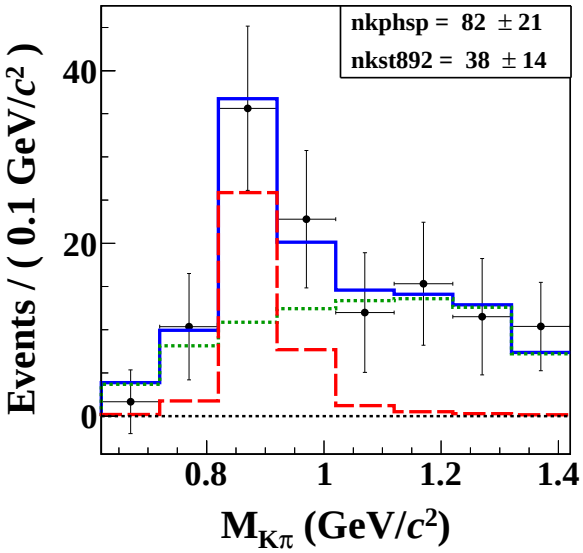

Figure 5.9: Binned minimum χ^2 fitting of signal yield and custom errors in 100 MeV wide $M_{K\pi}$ bins for experimental data for $X(3872)$ mass region. Red curve represents $B^0 \to X(3872)K^*(892)^0$, green curve is for $B^0 \to X(3872)(K^+\pi^-)_{NR}$ and blue solid for overall fit.

The statistical significance of above signal yield for $B^0 \to X(3872)K^*(892)^0$ is found to be 3.0σ before and after including systematic uncertainties (only those affecting our signal yield). For estimating above mentioned significance, large number of toy MC samples are generated keeping signal yield of $B^0 \to X(3872)K^*(892)^0$ to be zero. And to include systematic uncertainties, convolution is done to this statistical significance with a Gaussian function of width equals to the systematic error.

Estimation of $R_{X(3872)}$ variable is as follows from branching fractions:

$$R_{X(3872)} = \frac{\mathcal{B}(B^0 \to X(3872)K^*(892)^0) \times \mathcal{B}(K^*(892)^0 \to K^+\pi^-)}{\mathcal{B}(B^0 \to X(3872)K^+\pi^-)_{\text{2D fit}}} \quad (5.6)$$
$$= 0.34 \pm 0.09(\text{stat.}) \pm 0.02(\text{syst.}).$$

Here also same systematic uncertainties are used as for $R_{\psi'}$ variable calculation.

It is clear from Equation 5.5 and Equation 5.6 that for $X(3872)$ mass region, $K^*(892)^0$ component is not dominating as compared to ψ' mass region. The $X(3872)$ seems to be not behaving like ordinary charmonium states. But with more statistics, knowledge about quark content of $X(3872)$, one can clearly observe this difference.

5.3 Systematic Uncertainty Study

Few uncertainties are same as mentioned in previous Chapter like kaon-identification, pion-identification, charged track finding efficiency, lepton identification, secondary branching fraction, number of $B\overline{B}$ ($N_{B\overline{B}}$) events. So here only those uncertainties are described which are different.

5.3.1 Systematic Uncertainty due to Efficiency

Due to the limited statistical samples of signal MC, there will be sizeable statistical errors on the calculated efficiency and this error is taken into account given in Table 5.2.

Table 5.2: Systematic uncertainty due to the statistics of the MC samples.

Decay mode	$B^0 \to \psi' K^*(892)^0$	$B^0 \to X(3872)K^*(892)^0$
Syst. (%)	0.2	0.2

5.3.2 Systematic Uncertainty due to PDF Modeling

Signal yield is extracted by performing a fit to the experimental data. Signal yield depends upon parameters fixed in fit. For estimating this systematic uncertainty, the

Table 5.3: Estimation of systematic uncertainty from fit shown in Figure 5.8. Nominal value of the signal yield for $B^0 \to \psi' K^*(892)$ decay mode is 1708.

Variable	Value Error	+Variation -Variation	Yield	ΔYield	-(Δ Yield)	+(Δ Yield)
maspsi_mean	3.684964	3.685022	1708	0	0	0
	5.8E-05	3.684906	1708	0		
maspsi_sigma	0.002152	0.002205	1713	5	-6	5
	5.3E-05	0.002099	1702	-6		
maspsi_a2a	0.7025	0.7066	1707	-1	-1	1
	0.0041	0.6984	1709	1		
maspsi_s2s1	2.756	2.772	1709	1	-1	1
	0.016	2.74	1707	-1		
maspsi_pkslope	0.24	0.52	1710	2	-1	2
	0.28	-0.04	1707	-1		
delte_mean	-0.001467	-0.001317	1707	-1	-1	0
	0.00015	-0.001617	1708	0		
delte_sigma	0.0055	0.00564	1714	6	-6	6
	1.4E-04	0.00536	1702	-6		
delte_alpha	-2.0454	-2.0034	1709	1	-1	1
	0.042	-2.0874	1707	-1		
delte_n	1.42	1.57	1707	-1	-1	1
	0.15	1.27	1709	1		
delte_a2a	0.8036	0.8068	1706	-2	-2	1
	0.0032	0.8004	1709	1		
delte_s2s1	3.046	3.08	1709	1	-1	1
	0.034	3.012	1707	-1		
delte_pkslope	-0.4127	-0.3167	1708	0	0	0
	0.096	-0.5087	1708	0		
				Total	-0.53%	+0.49%

Table 5.4: Estimation of systematic uncertainty from fit shown in Figure 5.9. Nominal value of the signal yield for $B^0 \to X(3872)K^*(892)^0$ decay mode is 37.58.

Variable	Value Error	+Variation -Variation	Yield	ΔYield	-(Δ Yield)	+(Δ Yield)
maspsi_mean	3.8705	3.8705583488	37.59	0.01	-0.02	0.01
	5.83488E-05	3.8704416512	37.56	-0.02		
maspsi_sigma	0.00220231	0.0022579464	38.05	0.47	-0.37	0.47
	5.56364E-05	0.0021466736	37.21	-0.37		
maspsi_a2a	0.7413	0.7443	37.63	0.05	0.00	0.06
	0.003	0.7383	37.64	0.06		
maspsi_s2s1	2.931	2.948	37.67	0.09	0.00	0.09
	0.017	2.914	37.63	0.05		
maspsi_pkslope	0.14	0.29	37.60	0.02	0.00	0.05
	0.15	-0.01	37.63	0.05		
delte_mean	-0.0013691	-0.001218289	37.33	-0.25	-0.25	0.21
	1.50811E-04	-0.001519911	37.79	0.21		
delte_sigma	0.00519977	0.005334676	37.78	0.20	-0.25	0.20
	1.34906E-04	0.005064864	37.33	-0.25		
delte_alpha	-2.0454	-2.0034	37.57	-0.01	-0.04	0.00
	0.042	-2.0874	37.54	-0.04		
delte_n	1.42	1.57	37.53	-0.05	-0.05	0.00
	0.15	1.27	37.55	-0.03		
delte_a2a	0.8299	0.8335	37.51	-0.07	-0.07	0.05
	0.0036	0.8263	37.63	0.05		
delte_s2s1	2.887	2.925	37.60	0.02	-0.04	0.02
	0.038	2.849	37.54	-0.04		
				Total	-1.39%	+1.51%

variation of fixed parameters of PDF model are done by varying the parameters of PDF's by $+1\sigma/-1\sigma$ (one at a time).

The systematic uncertainty due to the fitting model is estimated to be $^{+0.49}_{-0.53}\%$ and $^{+1.51}_{-1.39}\%$ respectively for $B^0 \to \psi' K^*(892)^0$ and $B^0 \to X(3872)K^*(892)^0$ for background subtracted binned fit study as shown in Table 5.3 and Table 5.4.

5.3.3 Systematic Uncertainty due to Fit Bias

Although there is insignificant bias in the final fitter, but this small systematic uncertainty is also added, which is mentioned in Table 5.5.

Table 5.5: Systematic uncertainty due to the fit bias for background subtracted binned fit study.

Decay mode	$B^0 \to \psi' K^*(892)$	$B^0 \to X(3872)K^*(892)$
Syst. (%)	1.03	4.58

5.3.4 Total Systematic Uncertainty

All systematic uncertainties contributions are summarized in Table 5.6. All these individual systematic uncertainties are added in quadrature to obtain total systematic uncertainty of $^{+5.32}_{-5.33}\%$ and $^{+7.04}_{-7.01}\%$, respectively for $B^0 \to \psi' K^*(892)^0$ and $B^0 \to X(3872)K^*(892)^0$ decay modes.

Table 5.6: Summary of systematic uncertainties used for background subtracted binned fit study.

Systematic Uncertainty(%)		
Mode $\to$	$B^0 \to \psi' K^*(892)^0$	$B^0 \to X(3872)K^*(892)^0$
Source $\downarrow$		
K-id	1.1	1.1
π-id π of $K\pi$	1.1	1.1
π-id pions of ψ' or $X(3872)$	2×1.2	2×1.2
Tracking	2.1	2.1
ℓ id	2×1.7	2×1.7
MC statistics	0.2	0.2
Sec. $\mathcal{B}$	0.95	0.39
$N_{B\overline{B}}$	1.4	1.4
PDF	$^{+0.49}_{-0.53}$	$^{+1.51}_{-1.39}$
Fit bias	1.03	4.58
Total	$^{+5.32}_{-5.33}$	$^{+7.04}_{-7.01}$

5.4 Search for Resonances in $X(3872)K$ and $X(3872)\pi$ Systems

Search has also been performed for other resonances in $X(3872)K$ and $X(3872)\pi$ mass distributions in $X(3872)$ mass region in the $B^0 \to X(3872)K^+\pi^-$ decay mode, like

5.4. SEARCH FOR RESONANCES IN $X(3872)K$ AND $X(3872)\pi$ SYSTEMS

Belle already found resonance in ψ' mass region ($Z(4430)^+$). Background subtracted mass distributions of $X(3872)K$ and $X(3872)\pi$ are shown in Figure 5.10. Here 2D extended UML fit is performed (ΔE and $M_{J/\psi\pi\pi}$ variables) in bins of $M_{X(3872)K}$ and $M_{X(3872)\pi}$. Same strategy has been implemented as previous background subtracted binned fit study but with a cut on $M_{K\pi}$ to enhance the $B^0 \to X(3872)K^*(892)^0$ ($M_{K\pi}$ in the range [0.85,0.95] GeV/c^2) and the $B^0 \to X(3872)(K\pi)_{NR}$ ($M_{K\pi}$ <0.85 GeV/c^2 and $M_{K\pi}$ >0.95 GeV/c^2). At the current level of statistics and with our analysis strategy, no clear pattern is observed in the background subtracted mass distributions of $X(3872)K$ and $X(3872)\pi$ as shown in Figure 5.10.

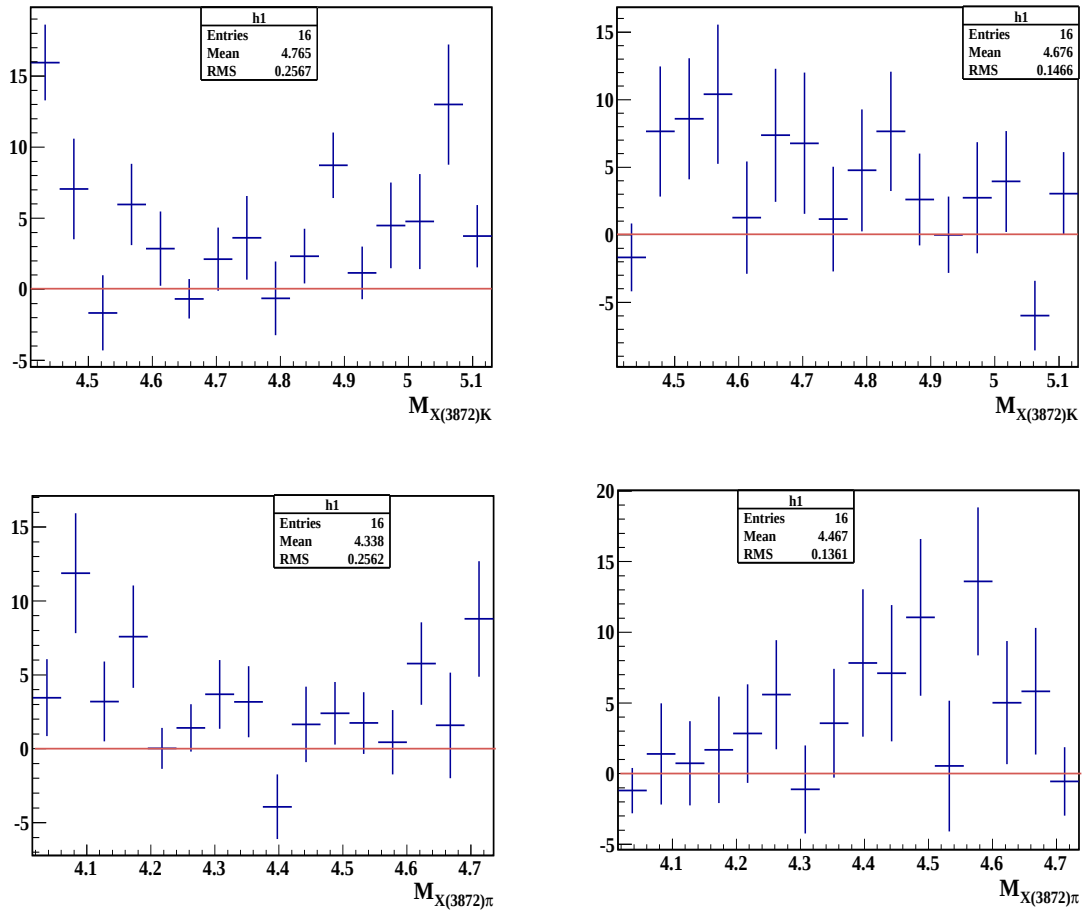

Figure 5.10: Background subtracted distributions of $M_{X(3872)K}$ (top), $M_{X(3872)\pi}$ (bottom). Left plots are for $M_{K\pi}$ in range [0.85, 0.95] and right plots are for ($M_{K\pi}$ <0.85 and $M_{K\pi}$ >0.95). All masses are in GeV/c^2.

5.5 Chapter in Compact

In brief, different components of $(K\pi)$ are discussed in this Chapter and it is found that non-resonant component of $(K\pi)$ is dominating as compared to resonant component for $X(3872)$ mass region which is in contrast with other charmonium states like ψ'. Branching fraction of $B^0 \to \psi' K^*(892)^0$ decay mode is estimated to be $(5.88 \pm 0.18(\text{stat.}) \pm 0.31(\text{syst.})) \times 10^{-4}$ which is consistent with world average value. Measurement on the product of branching fractions $\mathcal{B}(B^0 \to X(3872)K^*(892)^0) \times \mathcal{B}(X(3872) \to J/\psi\pi^+\pi^-)$ comes out to be $(3.99 \pm 1.48(\text{stat.}) \pm 0.28(\text{syst.})) \times 10^{-6}$. At the current level of statistics, no clear pattern is found in background subtracted mass distributions of $X(3872)K$ and $X(3872)\pi$.

6

Search for $X(3872)$ in 3-body B^+ decay

In this Chapter, the search for the charged B-decay modes $B^+ \to X(3872)K^0_S\pi^+$ and $B^+ \to X(3872)K^+\pi^0$ are explained in detail. Signal extraction procedure and systematic uncertainty study for these decay modes has also been explained. The first evidence of $B^+ \to X(3872)K^0_S\pi^+$ decay mode has been found and accordingly the measurement of the product of branching fractions $\mathcal{B}(B^+ \to X(3872)K^0\pi^+) \times \mathcal{B}(X(3872) \to J/\psi\pi^+\pi^-)$ is estimated. Along with this study, the calibration decay mode $B^+ \to \psi' K^0_S\pi^+$ is also studied. A very preliminary study of $B^+ \to X(3872)K^+\pi^0$ decay mode has also been presented along with its calibration decay mode $B^+ \to \psi' K^+\pi^0$.

6.1 Search for $B^+ \to X(3872)K^0_S\pi^+$ Decay Mode

In the following Sections, a detailed study about $B^+ \to X(3872)K^0_S\pi^+$ decay mode has been presented, which includes its signal MC study, J/ψ inclusive MC study and experimental data study.

6.2 Event Reconstruction Procedure

For the search of $B^+ \to X(3872)K^0_S\pi^+$ decay mode, the B-meson reconstruction is performed by combining the reconstructed $X(3872)$ particle with the tracks identi-

fied to be coming from K^0_S decay (reconstructed from $\pi^+\pi^-$) and π^+, as explained in Section 3.5. The $X(3872)$ reconstruction is done via its decay mode $X(3872) \to J/\psi\pi^+\pi^-$, here J/ψ is reconstructed using $\ell^+\ell^-$, where ℓ is a e or μ. In order to estimate the reconstruction efficiency for above decay modes, 2 Million signal MC events are generated using EvtGen and these events are then processed through detector environment using GEANT3. Same selection criteria has been applied to the experimental data.

6.3 Branching Fractions

Branching fraction of $B^+ \to \psi' K^0\pi^+$ decay mode, after assuming equal production of neutral and charged B-meson pairs, is defined as follows:

$$\mathcal{B}(B^+ \to \psi' K^0\pi^+) = \frac{Y(B^+ \to \psi' K^0_S\pi^+)}{\epsilon(B^+ \to \psi' K^0_S\pi^+) \times \mathcal{B}(\psi' \to J/\psi\pi^+\pi^-) \times \mathcal{B}(J/\psi \to \ell^+\ell^-) \times N(B\bar{B}) \times f_K}. \quad (6.1)$$

The product of the branching fractions $\mathcal{B}(B^+ \to X(3872)K^0\pi^+) \times \mathcal{B}(X(3872) \to J/\psi\pi^+\pi^-)$ is given by:

$$\mathcal{B}(B^+ \to X(3872)K^0\pi^+) \times \mathcal{B}(X(3872) \to J/\psi\pi^+\pi^-) = \frac{Y(B^+ \to X(3872)K^0_S\pi^+)}{\epsilon(B^+ \to X(3872)K^0_S\pi^+) \times \mathcal{B}(J/\psi \to \ell^+\ell^-) \times N(B\bar{B}) \times f_K}. \quad (6.2)$$

Where, $f_K = \mathcal{B}(K^0 \to K^0_S) \times \mathcal{B}(K^0_S \to \pi^+\pi^-)$. The signal yield $Y(B^+ \to X(3872)K^0_S\pi^+)$ is the number of fitted $B^+ \to X(3872)K^0_S\pi^+$ signal events found in the total experimental data set $N(B\bar{B})$ ($\sim$771.6 Million $B\bar{B}$). Reconstruction efficiency $\epsilon(B^+ \to X(3872)K^0_S\pi^+)$ is required to be estimated from signal MC simulated samples. As by using different selections (cuts), due to acceptance of detector and due to software limitations some particles can get missed and it resulted in lower reconstruction efficiency.

6.3.1 Efficiency Estimation from Signal MC Study and PDF Parametrization

In order to estimate the reconstruction efficiency, 2 Million signal MC events are generated for:

- $B^+ \to \psi' K^*(892)^+ (\to K^0_S \pi^+)$
- $B^+ \to \psi' (K^0_S \pi^+)_{NR}$
- $B^+ \to \psi' {K_2}^*(1430)^+ (\to K^0_S \pi^+)$
- $B^+ \to X(3872) (K^0_S \pi^+)_{NR}$
- $B^+ \to X(3872) K^*(892)^+ (\to K^0_S \pi^+)$

Signal yield is extracted from 2D extended UML fitting of ΔE and $M_{J/\psi\pi\pi}$ variables. Correctly reconstructed (CR) and self cross feed (SCF) events plots for these two dimensions are shown in Figure 6.1 and Figure 6.2 respectively for ψ' and $X(3872)$ mass regions. From these Figures, it is clear that there are two types of events.

(1) Correctly reconstructed events: As these are correctly reconstructed events, they are accumulating and forming peak at ΔE and $M_{J/\psi\pi\pi}$ signal region distributions. One can model ΔE distribution using sum of core Gaussian with the Crystal Ball (tail parameter), while $M_{J/\psi\pi\pi}$ distribution can be modeled using sum of two Gaussian with common mean.

(2) Self cross feed events: These types of events can be categorises into two subdivision:

   - Peaking backgrounds in one dimension (flat in other): As some of the few final state particles miss detection or wrongly combine (which has very low probability as per our signal MC study), due to the wrong kinematical reconstruction, these decay modes are seen to have tendency to peak in one dimension but having flat distribution in other. This property helps us in separating these decay modes from fully reconstructed decay mode.

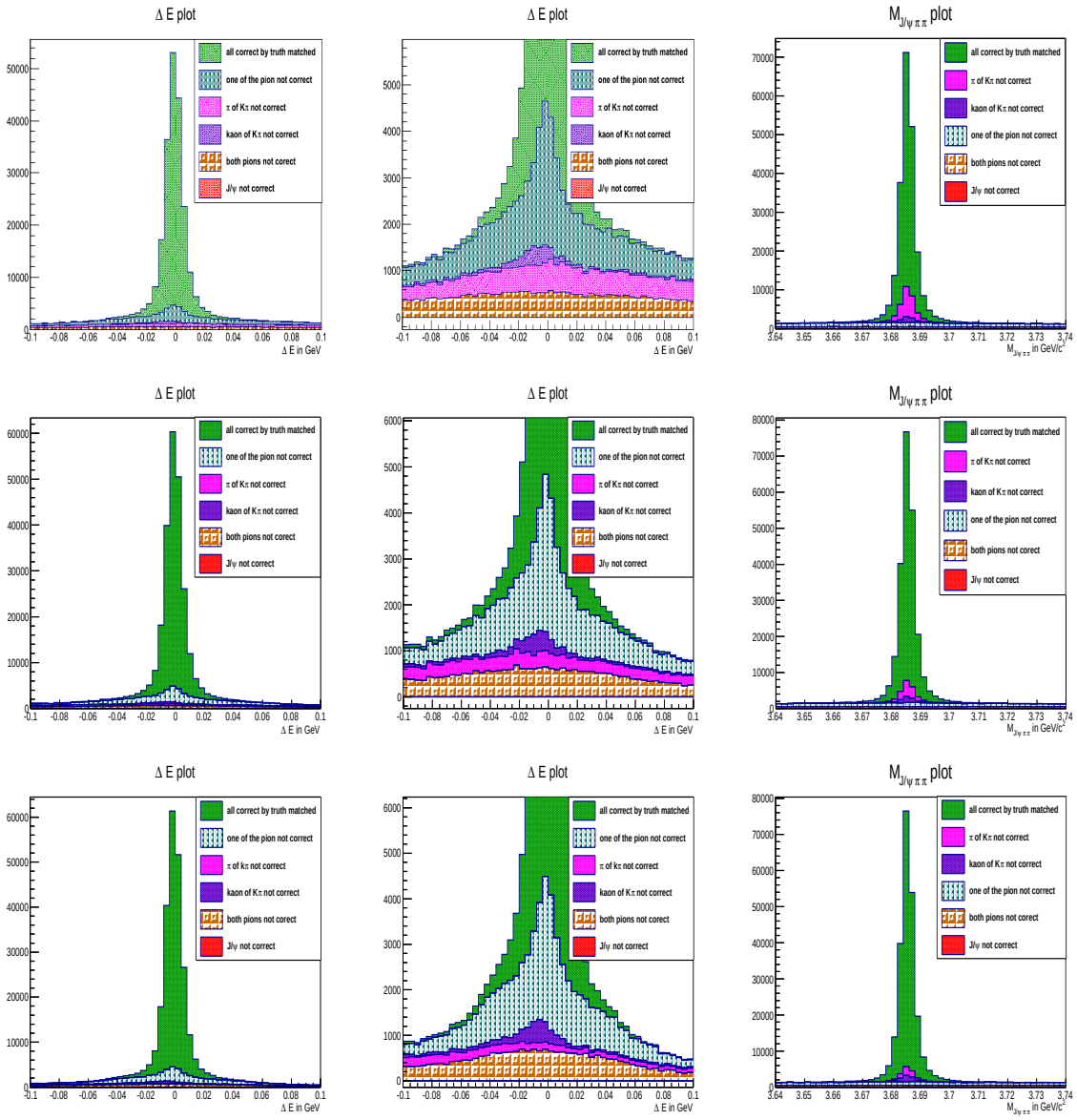

Figure 6.1: Correctly reconstructed (CR) and self cross feed (SCF) events plots for signal MC sample in ΔE and $M_{J/\psi\pi\pi}$ (middle plots are zoomed plots for ΔE dimension) for $B^+ \to \psi' K^0_S \pi^+$ decay mode. Top plots are of $B^+ \to \psi' K^*(892)^+$ decay mode, middle one are of $B^+ \to \psi'(K^0_S\pi^+)_{NR}$ and bottom plots are of $B^+ \to \psi' {K_2}^*(1430)^+$ decay mode.

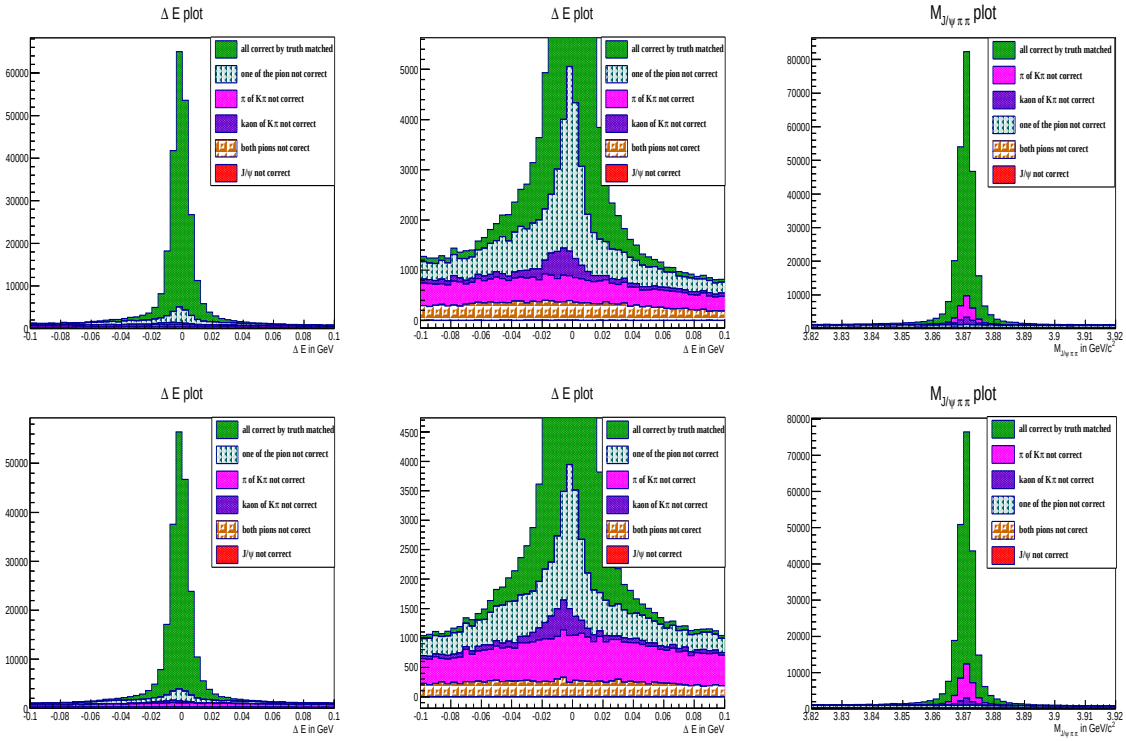

Figure 6.2: Correctly reconstructed (CR) and self cross feed (SCF) events plots for signal MC sample in ΔE and $M_{J/\psi\pi\pi}$ (middle plots are zoomed plots for ΔE dimension) for $B^+ \to X(3872)K^0_S\pi^+$ decay mode. Top plots are of $B^+ \to X(3872)(K^0_S\pi^+)_{NR}$ decay mode and bottom plots are of $B^+ \to X(3872)K^*(892)^+$ decay mode.

These peaking background events (in one dimension and flat in other dimension) and vice-versa are found to have same resolution as that of the signal PDF. In light of which, PDF similar to the signal PDF is used for the peaking dimension, while the other dimension is parametrized by 1^{st} order Chebychev polynomial. This slope in other dimension is allowed to vary in fit for ψ' mass region. For $X(3872)$ mass region, strategy and PDF modeling is same as that of calibration sample except the slope of Chebychev polynomial is fixed to be zero in ΔE dimension (which is peaking in $M_{J/\psi\pi\pi}$ dimension). This type of strategy is chosen from signal MC study (this type of background (SCF) has no structure), background study (negligible background of this nature) and from fit bias study.

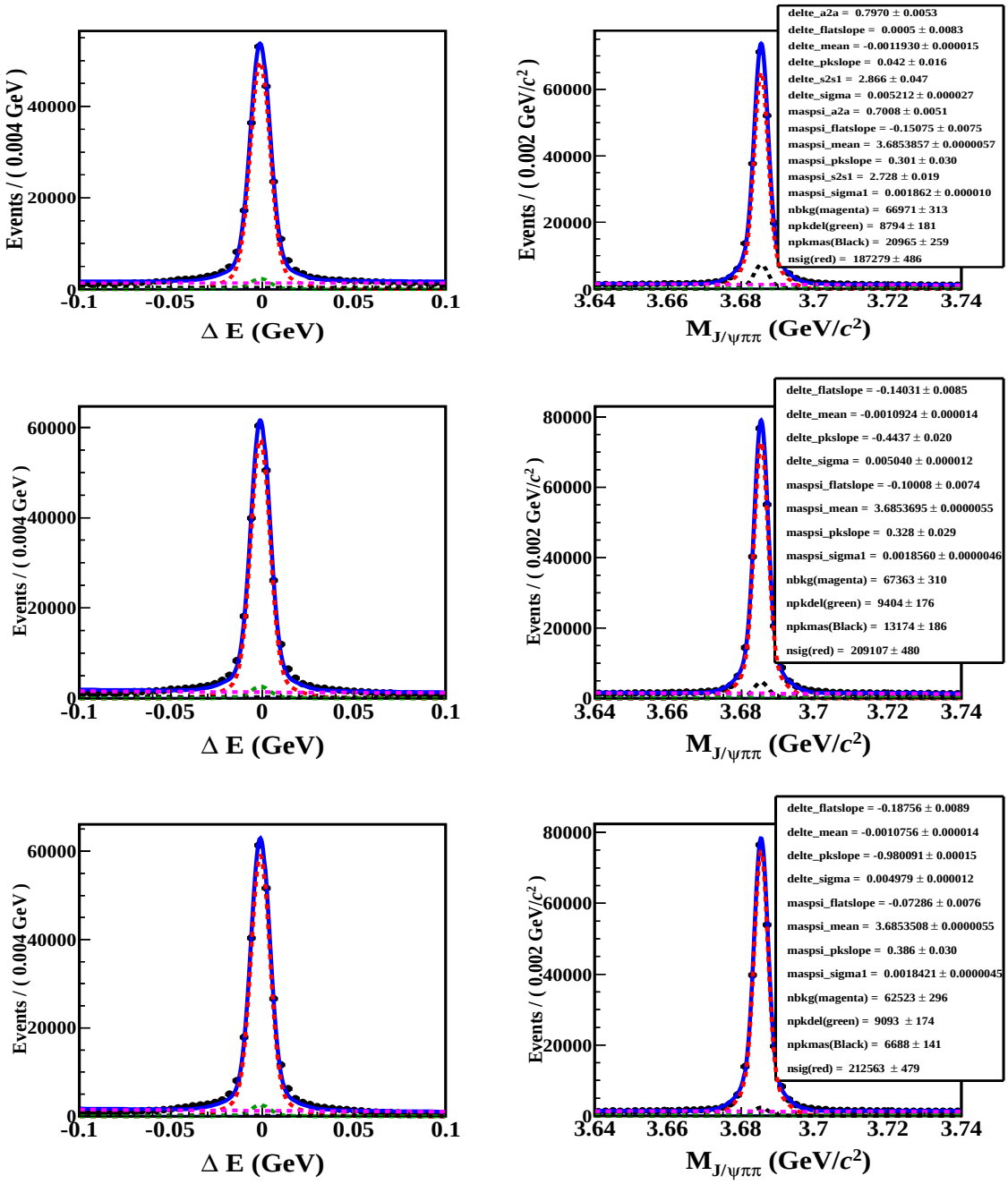

Figure 6.3: 2D extended UML fit to signal MC events for $B^+ \to \psi' K^*(892)^+$ (top), $B^+ \to \psi'(K^0_S\pi^+)_{NR}$ (middle), $B^+ \to \psi' K^*_2(1430)^+$ (bottom) decay mode. Red dotted curve represents signal in both dimensions, green curve shows peaking background in the ΔE dimension and flat in $M_{J/\psi\pi\pi}$ distribution and vice-versa for black curve, while magenta curve shows combinatorial background in both dimensions with blue solid for overall fit.

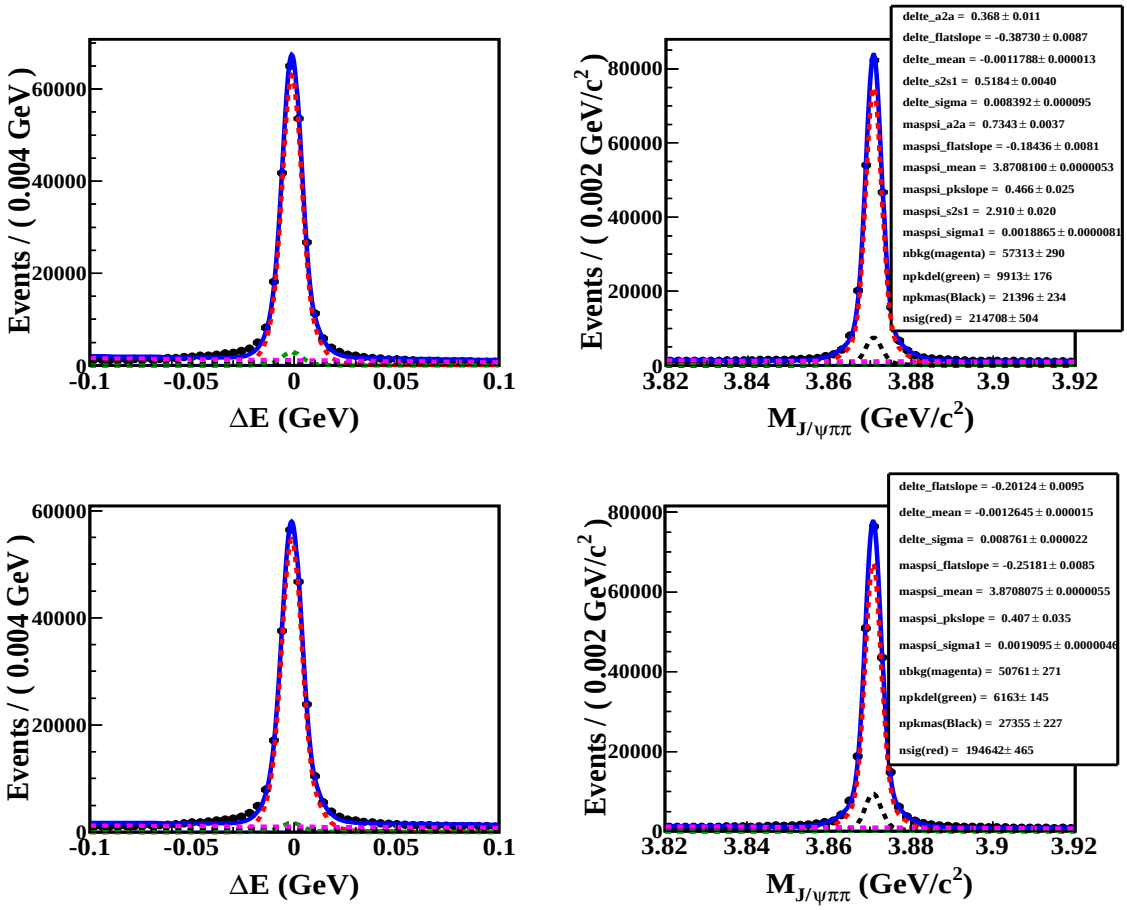

Figure 6.4: 2D extended UML fit to signal MC events for ΔE (left) and $M_{J/\psi\pi\pi}$ (right) dimensions for $B^+ \to X(3872)(K^0_S\pi^+)_{NR}$ (top) and $B^+ \to X(3872)K^*(892)^+$ (bottom) decay modes. Red curve represents signal in both dimensions. Green curve shows peaking background in the ΔE dimension and flat in $M_{J/\psi\pi\pi}$ distribution and vice-versa for black curve, while magenta curve shows combinatorial background in both dimensions with blue solid for overall fit.

- Combinatorial backgrounds (flat in both ΔE and $M_{J/\psi\pi\pi}$ dimensions): The remaining events are found to be combinatorial in nature and flat in both dimensions. These type of events are parametrized easily by 1^{st} order Chebychev polynomial for both dimensions.

As the final state kinematics is similar for $B^+ \to \psi' K^0_S\pi^+$ and $B^+ \to X(3872)K^0_S\pi^+$, same PDFs are used to extract signal events for $B^+ \to X(3872)K^0_S\pi^+$ decay mode.

Table 6.1: Reconstruction efficiencies for different signal MC samples before and after Particle identification (PID) correction estimated from 2D extended UML fit study.

Decay Mode	MC Efficiency (%)	PID correction	Corrected efficiency (%)
$B^+ \to \psi' K^*(892)^+$	9.65	0.96	9.26
$B^+ \to \psi'(K^0_S\pi^+)_{NR}$	10.46	0.96	10.04
$B^+ \to \psi' {K_2}^*(1430)^+$	10.96	0.96	10.52
$B^+ \to X(3872)(K^0_S\pi^+)_{NR}$	10.74	0.99	10.63
$B^+ \to X(3872)K^*(892)^+$	9.73	0.99	9.63

The 2D fitting plots on similar strategy as that of previous neutral B-meson decay ($B^0 \to X(3872)K^+\pi^-$) analysis explained in Section 4.3.1 are shown in Figures 6.3 and Figure 6.4 for ψ' and $X(3872)$ mass regions respectively. Reconstruction efficiencies for different signal MC samples before and after PID corrections are mentioned in Table 6.1. Here one thing to be noted that PID correction is also for K^0_S reconstruction because it is also reconstructed from two oppositely charged pions.

6.3.2 Background Study

Since $B^+ \to \psi' K^0_S\pi^+$ as well as $B^+ \to X(3872)K^0_S\pi^+$ decay mode has J/ψ in the final state, the background is expected to come mainly from B decays with a real J/ψ in the final state.

For the $B^+ \to \psi' K^0_S\pi^+$ decay mode, signal and background in ΔE and $M_{J/\psi\pi\pi}$ dimension are shown in Figure 6.5. In this Figure, $B^+ \to \psi' K^*(892)^+$ (green color) is our signal (peaking in both dimensions). In the $M_{J/\psi\pi\pi}$ region, the peaking background is coming from $B \to \psi' X_{sd}$ (pink color), $B^0 \to \psi' K^*(892)^0$ (brown color), $B^+ \to \psi' K^+\pi^+\pi^-$ (Red color) and $B^+ \to \psi' K^0_S$ (violet color) decay modes, but they are not peaking in the ΔE dimension. Rest of the background comprises of combinatorial events in both dimensions (ΔE and $M_{J/\psi\pi\pi}$) and has no peaking structure. But signal in both dimensions includes SCF which is peaking in ΔE and flat in $M_{J/\psi\pi\pi}$ (due to the fact that the pions coming from the ψ' getting swapped with the pions coming from the K^0_S. As the final state is same, a peak is observed at ΔE dimension, while background in $M_{J/\psi\pi\pi}$ dimension is flat).

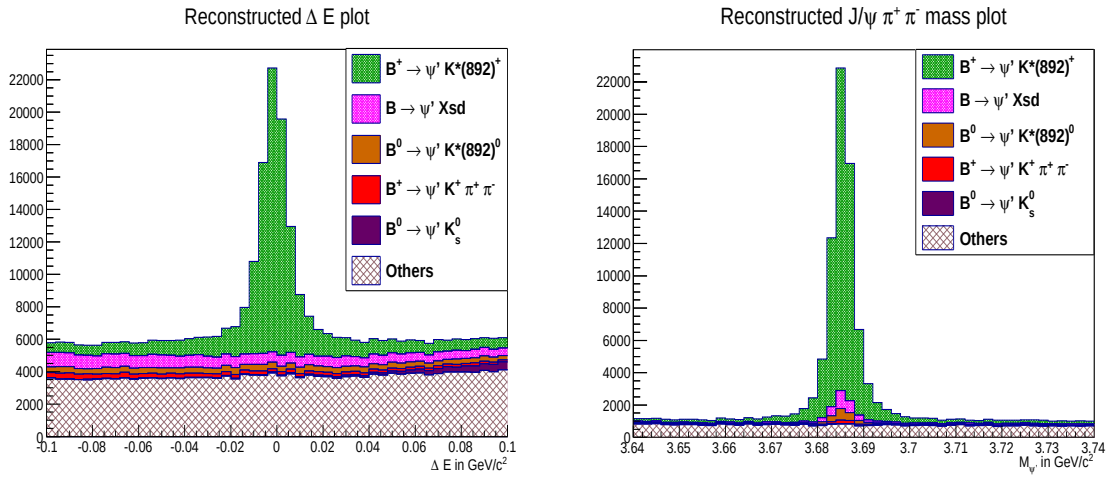

Figure 6.5: Background estimation for $B^+ \to \psi' K_S^0 \pi^+$ decay mode using J/ψ inclusive MC ($\sim 100\times$ experimental data) for ΔE (left) and $M_{J/\psi\pi\pi}$ (right) dimensions.

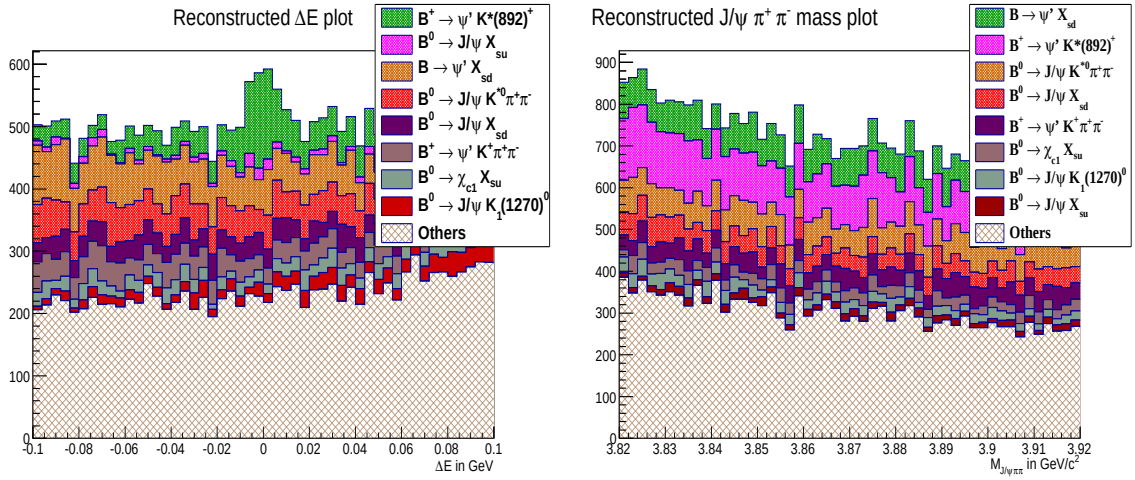

Figure 6.6: Background estimation for $B^+ \to X(3872) K_S^0 \pi^+$ decay mode using J/ψ inclusive MC ($\sim 100\times$ experimental data) for ΔE (left) and $M_{J/\psi\pi\pi}$ (right) dimensions.

For $B^+ \to X(3872)K^0_S\pi^+$ decay mode, same type of behaviour has been observed as that of calibration decay mode. The backgrounds from J/ψ inclusive MC sample study in the ΔE and $M_{J/\psi\pi\pi}$ dimensions are shown in Figure 6.6. The peaking background in the ΔE dimension is $B^+ \to \psi' K^*(892)^+$ (green color), but this background is flat in the $M_{J/\psi\pi\pi}$ distribution. Rest of the background is combinatorial in nature and is flat in both ΔE as well as in $M_{J/\psi\pi\pi}$ dimensions. All the PDFs are added and 2D extended UML fit is performed to extract signal yield from experimental data. Before performing the fit to experimental data, testing is done on the J/ψ inclusive MC sample using same strategy.

6.3.3 Branching Fractions Estimation for J/ψ Inclusive MC Sample

The PDF's for 2D extended UML fitting of J/ψ inclusive MC sample are same as for its signal MC sample. Parameters which are fixed for J/ψ inclusive MC and for experimental data from signal MC sample of $B^+ \to \psi' K^*(892)^+$ for ψ' mass region are shown in Table 6.2.

Table 6.2: Fixed parameters (in GeV) for J/ψ inclusive MC and for experimental data from signal MC sample of $B^+ \to \psi' K^*(892)^+$ for ψ' mass region.

Parameter name	Value from signal MC
delte_alpha (from truth matching of $B^+ \to \psi' K^*(892)^+$)	-2.1466 ± 0.051
delte_n (from truth matching of $B^+ \to \psi' K^*(892)^+$)	1.25 ± 0.14
maspsi_a2a	0.7008 ± 0.0051
maspsi_s2s1	2.728 ± 0.019
delte_a2a	0.797 ± 0.0053
delte_s2s1	2.866 ± 0.047

For the J/ψ inclusive MC sample, fitting is first performed on tagged signal from whole J/ψ inclusive MC sample. This fit is shown in Figure 6.7 (top). From the fit the branching fraction $\mathcal{B}(B^+ \to \psi' K^*(892)^+)$ comes out to be $((9.31 \pm 0.04) \times 10^{-4})$ for this signal only. Then 2D extended UML fit is performed on whole J/ψ inclusive MC sample as shown in Figure 6.7 (bottom) and branching fraction of the decay mode $B^+ \to \psi' K^*(892)^+$ is estimated to be $((9.24 \pm 0.05) \times 10^{-4})$, which is consistent

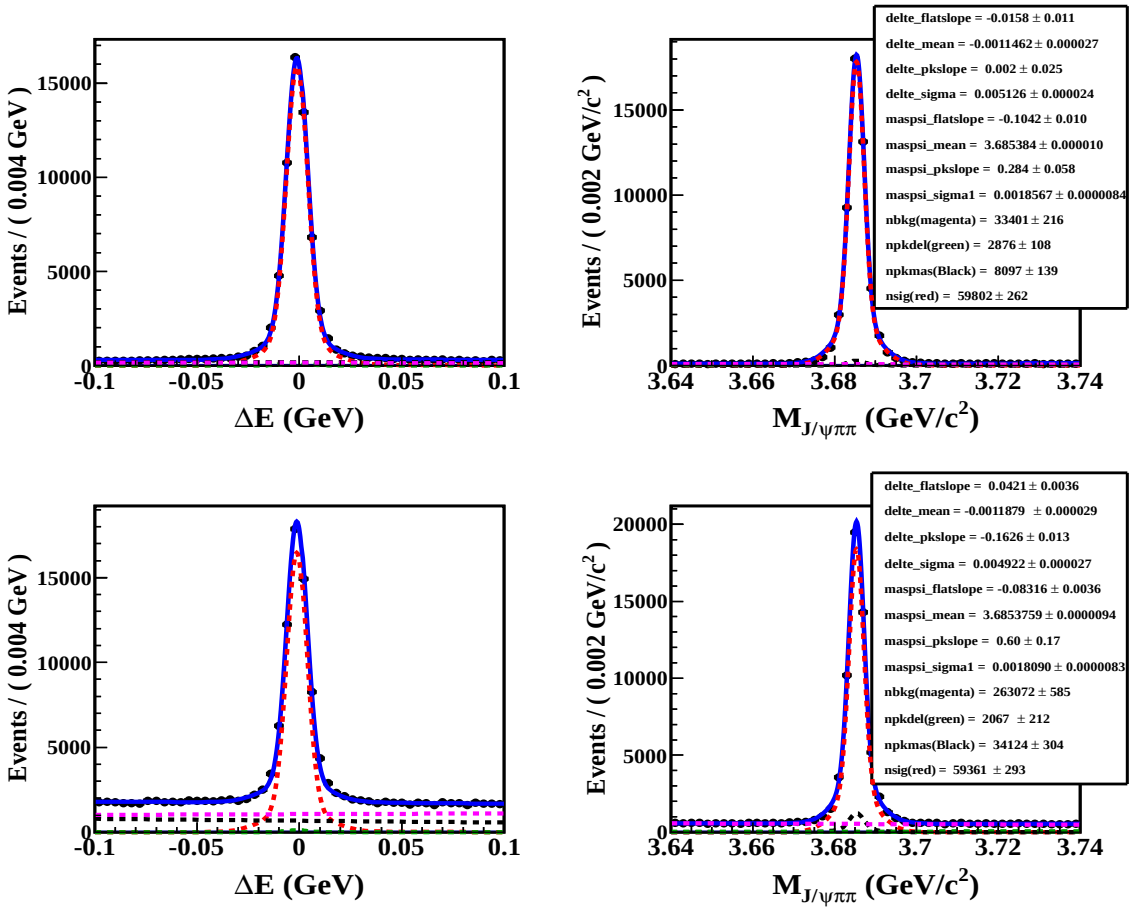

Figure 6.7: Signal region projections for only signal $B^+ \to \psi' K^*(892)^+$ from J/ψ inclusive MC sample (top) and whole J/ψ inclusive MC ($\sim 100\times$ experimental data) sample (bottom). Left plot is the projection for $M_{J/\psi\pi\pi}$ signal region $[3.675, 3.695]$ GeV/c^2 and right plot is the projection for ΔE signal region $[-11, 8]$ MeV. Red color represents signal in both dimensions, black color represents peaking background in $M_{J/\psi\pi\pi}$ dimension which is flat in ΔE dimension, green color represent peaking background in ΔE which is flat in $M_{J/\psi\pi\pi}$, magenta color represent combinatorial backgrounds in both dimensions with blue solid for overall fit.

with generated value given in DECAY.DEC i.e. (9.20×10^{-4}).

Similar to the calibration decay mode sample study, for $X(3872)$ mass region, parametrization can be done with same PDF's as kinematics of these two decays modes is same. Since there is no decay mode in J/ψ inclusive MC which peaks in

$X(3872)$ mass region as shown in Figure 6.6. So signal PDF in J/ψ inclusive MC for $X(3872)$ mass region is fixed for $M_{J/\psi\pi\pi}$ dimension. Ideally signal events from fitted result should come out to be zero.

Table 6.3: Fixed parameters (in GeV) for J/ψ inclusive MC from signal MC sample $B^+ \to X(3872)(K^0_S\pi^+)_{NR}$ for $X(3872)$ mass region.

Parameter name	Value from signal MC
maspsi_mean	3.8708100 ± 0.0000053
maspsi_sigma1	0.0018865 ± 0.0000081
maspsi_a2a	0.7343 ± 0.0037
maspsi_s2s1	2.91 ± 0.020
delte_alpha (from truth matching of $B^+ \to \psi' K^*(892)^+$)	-2.1466 ± 0.051
delte_n (from truth matching of $B^+ \to \psi' K^*(892)^+$)	1.25 ± 0.14
delte_sigma	0.008392 ± 0.000095
delte_a2a	0.368 ± 0.011
delte_s2s1	0.5184 ± 0.004

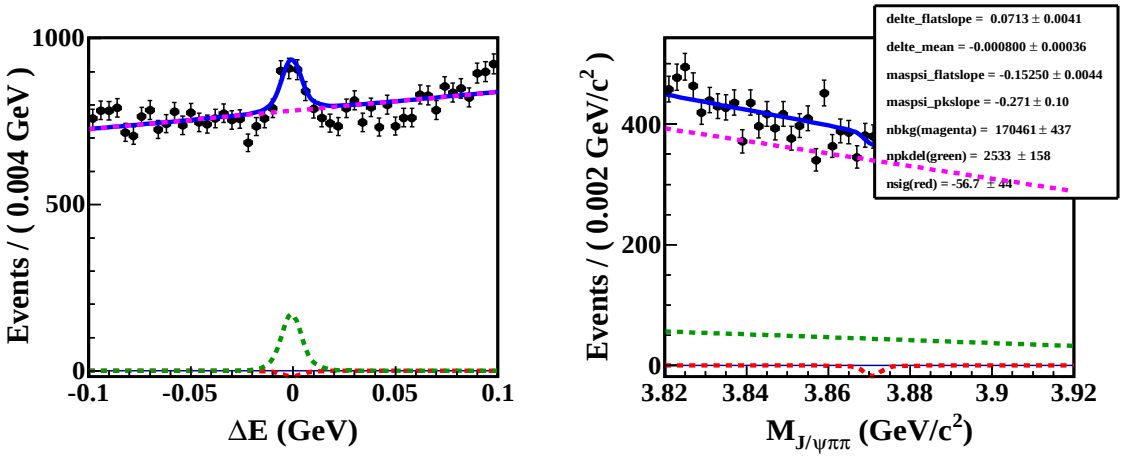

Figure 6.8: Signal region projections for whole J/ψ inclusive MC ($\sim 100\times$ experimental data) sample. Left plot is the projection for $M_{J/\psi\pi\pi}$ signal region $[3.859, 3.882]$ GeV/c^2 and right plot is the projection for ΔE signal region $[-11, 9]$ MeV. Red color represents signal in both dimensions, green color represents peaking background in ΔE which is flat in $M_{J/\psi\pi\pi}$, magenta color represents combinatorial backgrounds in both dimensions with blue solid for overall fit.

Parameters which are fixed for J/ψ inclusive MC for $X(3872)$ mass region are

shown in Table 6.3. The total fit to the J/ψ inclusive MC sample for $X(3872)$ mass region is shown in Figure 6.8. As one can see in this Figure, signal yield is consistent with zero as there is no $X(3872)$ decay mode in officially generated J/ψ inclusive MC sample.

6.3.4 Fit Validation

In order to determine the stability of fit procedure and to correct for any possible fit bias, two types of studies have been performed.

- **Toy MC study**: To perform this study, the expected number of events (allowing

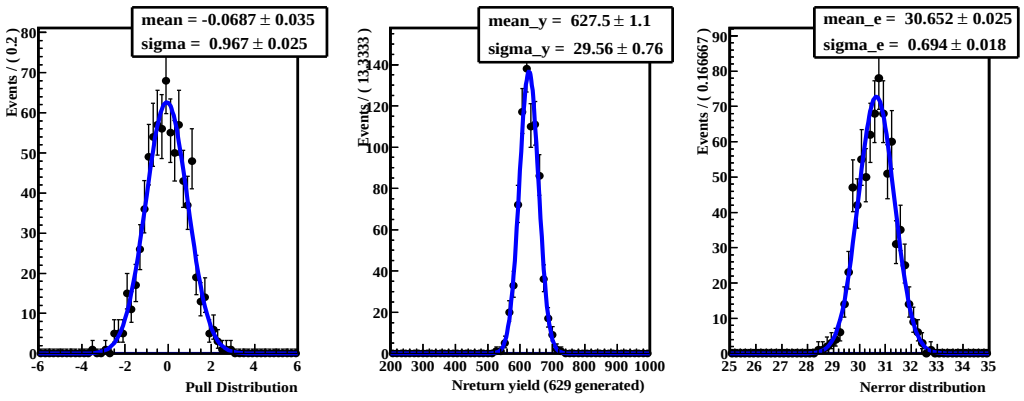

Figure 6.9: Pull distribution (left), return yield distribution (middle) and error distribution (right) for 1000 toy MC study for $B^+ \to \psi' K^0_S \pi^+$ decay mode.

for Poisson fluctuations) of fit model under consideration are generated according to the PDFs of the fit for each experiment. 1000 toy MC samples are generated using signal and background PDFs. All Signal events [$(K^*(892)^+$, $K_2{}^*(1430)^+$ and $(K^0_S\pi^+)_{NR}$ for ψ' mass region) ($K^*(892)^+$ and $(K^0_S\pi^+)_{NR}$ for $X(3872)$ mass region)] as well as background events are generated using experimental data results shown in Figure 6.13 and Figure 6.14 respectively for ψ' and $X(3872)$ mass regions and using PDFs. Signal yield is extracted from each toy MC sample using same final fitter. The possible bias in our signal extraction procedure has been estimated by calculating the

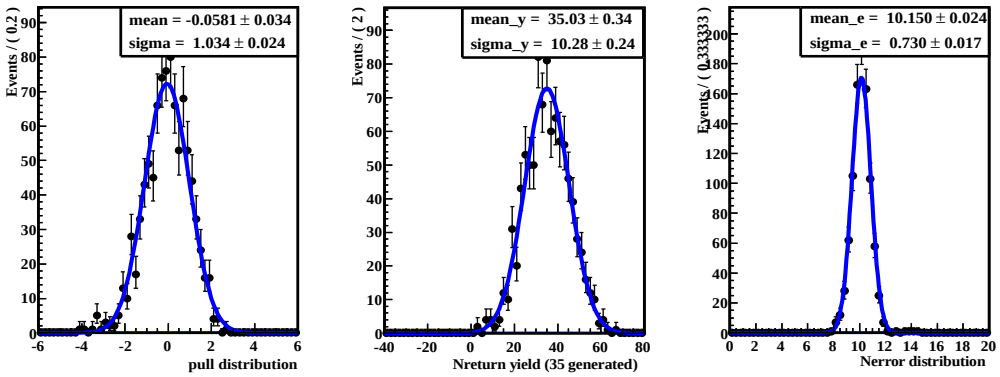

Figure 6.10: Pull distribution (left), return yield distribution (middle) and error distribution (right) for 1000 toy MC study for $B^+ \to X(3872)K^0_S\pi^+$ decay mode.

pull from each fit defined as:

$$\text{Pull} = \frac{\text{Yield}_{\text{Fitted}} - \text{Yield}_{\text{Expected}}}{\sigma_{\text{Fitted Yield}}} \tag{6.3}$$

Figure 6.9 and Figure 6.10 shows the pull distribution (left), return yield distribution (middle) and error distribution (right) for ψ' and $X(3872)$ mass regions respectively, which demonstrates that there is no significant bias in the final fitter.

•**GSIM study**: GSIM study has also been performed using actual signal MC simulated events and background events. As Belle MC team officially generated huge sample of J/ψ inclusive MC ($\sim$100$\times$ the experimental data) under similar detector environment conditions and same type of expected backgrounds as that of experimental data. Full advantage of this whole sample has been taken. Whole J/ψ inclusive MC sample is divided into 100 samples and all signal events are embedded in each sample according to $M_{K\pi}$ distribution extracted from the fit shown in Figure 5.8 and Figure 5.9. The GSIM study will actually reflect true fit bias, if any. Figure 6.11 and Figure 6.12 shows the pull distribution (left), return yield distribution (middle) and error distribution (right) after performing GSIM study for ψ' and $X(3872)$ mass regions respectively. From these distributions, it is clear that no significant bias is there in the final fitter. However, for conservation insignificant bias has been added in the systematic uncertainty estimation.

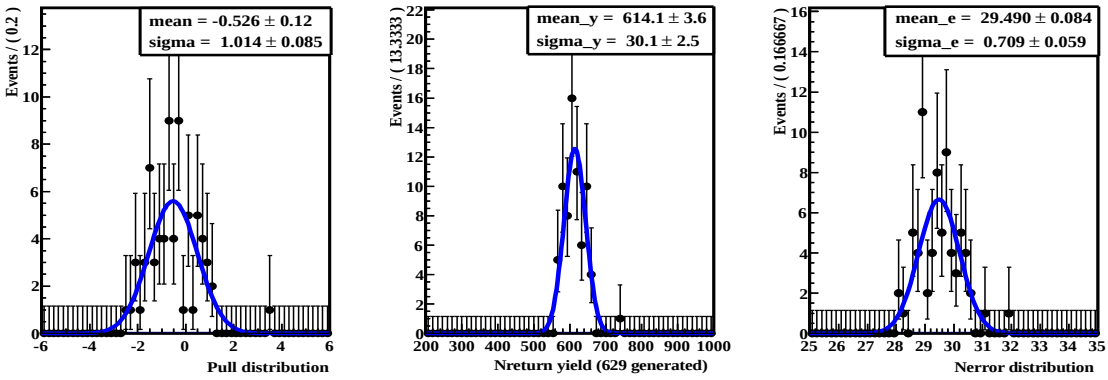

Figure 6.11: Pull distribution (left), return yield distribution (middle) and error distribution (right) for GSIM study for $B^+ \to \psi' K_S^0 \pi^+$ decay mode.

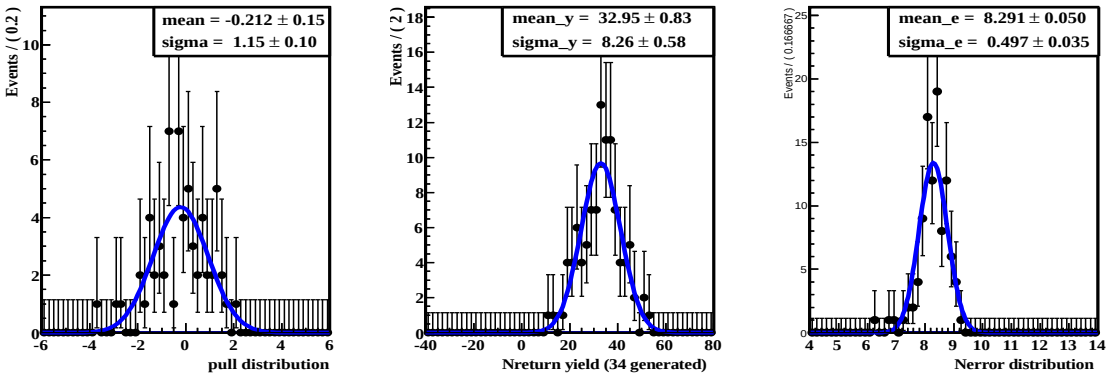

Figure 6.12: Pull distribution (left), return yield distribution (middle) and error distribution (right) for GSIM study for $B^+ \to X(3872) K_S^0 \pi^+$ decay mode.

6.3.5 Extraction of Signal Yield from Experimental Data and Results

Negligible fit bias and consistent results of branching fractions for J/ψ inclusive MC motivated us to apply same strategy to extract signal yield from experimental data too. Thus PDFs for the fitting of experimental data are same as that of J/ψ inclusive MC.

The fit to the experimental data for the $B^+ \to \psi' K_S^0 \pi^+$ decay in signal and back-

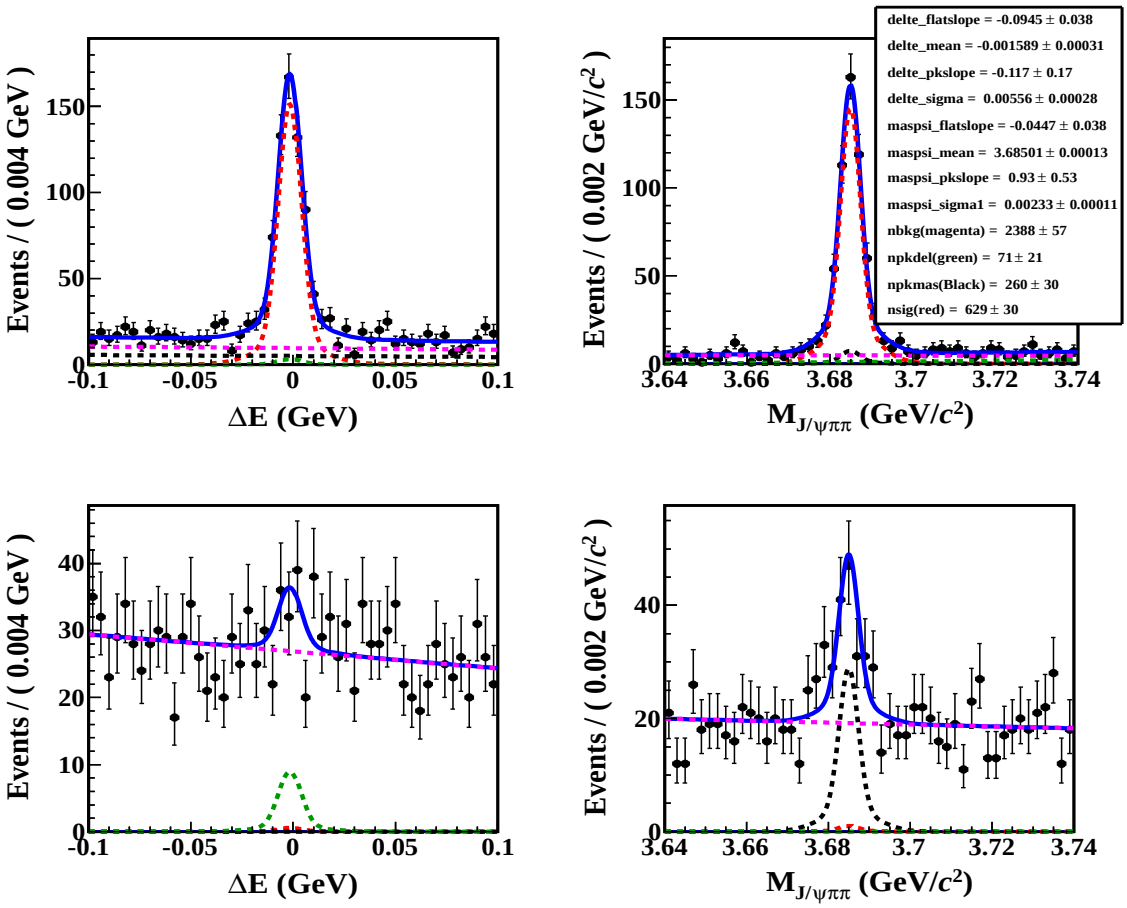

Figure 6.13: Top: Signal region projections of experimental data for $B^+ \to \psi' K^0_S \pi^+$ decay mode. Left (right) plot is the projection for $M_{J/\psi\pi\pi}$ (ΔE) signal region. Bottom: Projection plots in background enhanced regions of ΔE and $M_{J/\psi\pi\pi}$. Left (right) is for $M_{J/\psi\pi\pi}$ (ΔE) sidebands in ψ' mass region. Red color represents signal in both dimensions, black color represent peaking background in $M_{J/\psi\pi\pi}$ dimension which is flat in ΔE dimension, green color represent peaking background in ΔE which is flat in $M_{J/\psi\pi\pi}$, magenta color represent combinatorial backgrounds in both dimensions with blue solid for overall fit.

ground enhanced regions is shown in Figure 6.13. The branching fraction (B.F) obtained for experimental data from 2D extended UML fitting comes out to be $(5.76 \pm 0.27(\text{stat.})) \times 10^{-4}$. After including PID correction in Table 6.1 and systematic uncertainties reported in Table 6.7, the branching fraction (B.F) comes out to be $(6.00 \pm 0.28(\text{stat.}) \pm 0.35(\text{syst.})) \times 10^{-4}$, while the PDG value of this branching fraction is $(5.88 \pm 0.34) \times 10^{-4}$. As one can see, our measured result is consistent with PDG value within 1σ. For estimating branching fraction, weighted efficiency is used, which is calculated by assuming same fraction of each $K\pi$ bins as in Figure 5.8 (details are in Appendix A).

For the fitting to the experimental data in the $X(3872)$ mass region, all parameters of fitting function, except mean and width, are fixed to that from signal MC sample. Mean and width values are estimated from signal MC study and using fudge factor (estimated from calibration decay mode). The calibrated mean ($\mu_{\text{calibrated}}$) and width ($\sigma_{\text{calibrated}}$) is calculated by using the fudge factors as,

$$\mu_{\text{calibrated}} = \mu_{\text{MC}} + (\mu_{\text{data}} - \mu_{\text{MC}})_{\text{calibration sample}}; \tag{6.4}$$

$$\sigma_{\text{calibrated}} = (\frac{\sigma_{\text{data}}}{\sigma_{\text{MC}}})_{\text{calibration sample}} \times \sigma_{\text{MC}}. \tag{6.5}$$

Further correction is applied on mass (mean) of $M_{J/\psi\pi\pi}$ because of different dynamics of ψ' and $X(3872)$ decaying to $J/\psi\pi^+\pi^-$.

Parameters which are fixed for experimental data are given in Table 6.4.

The fit to the experimental data for $B^+ \to X(3872)K^0_S\pi^+$ decay, in the signal and background enhanced regions, is shown in Figure 6.14. In this Figure, there is a clear observation of peak in $X(3872)$ signal region and ΔE signal region with signal yield (35 ± 10) events having significance of 3.7σ (after including systematic uncertainties). The product of branching fractions is measured as:

$$\mathcal{B}(B^+ \to X(3872)K^0\pi^+) \times \mathcal{B}(X(3872) \to J/\psi\pi^+\pi^-) = (10.54 \pm 3.01(\text{stat.})) \times 10^{-6}. \tag{6.6}$$

After including PID correction from Table 6.1 and systematic uncertainties reported

in Table 6.7, the product of branching fraction is measured as:

$$\mathcal{B}(B^+ \to X(3872)K^0\pi^+)\times\mathcal{B}(X(3872) \to J/\psi\pi^+\pi^-) = (10.64\pm3.04(\text{stat.})^{+0.81}_{-0.86}(\text{syst.}))\times10^{-6}. \quad (6.7)$$

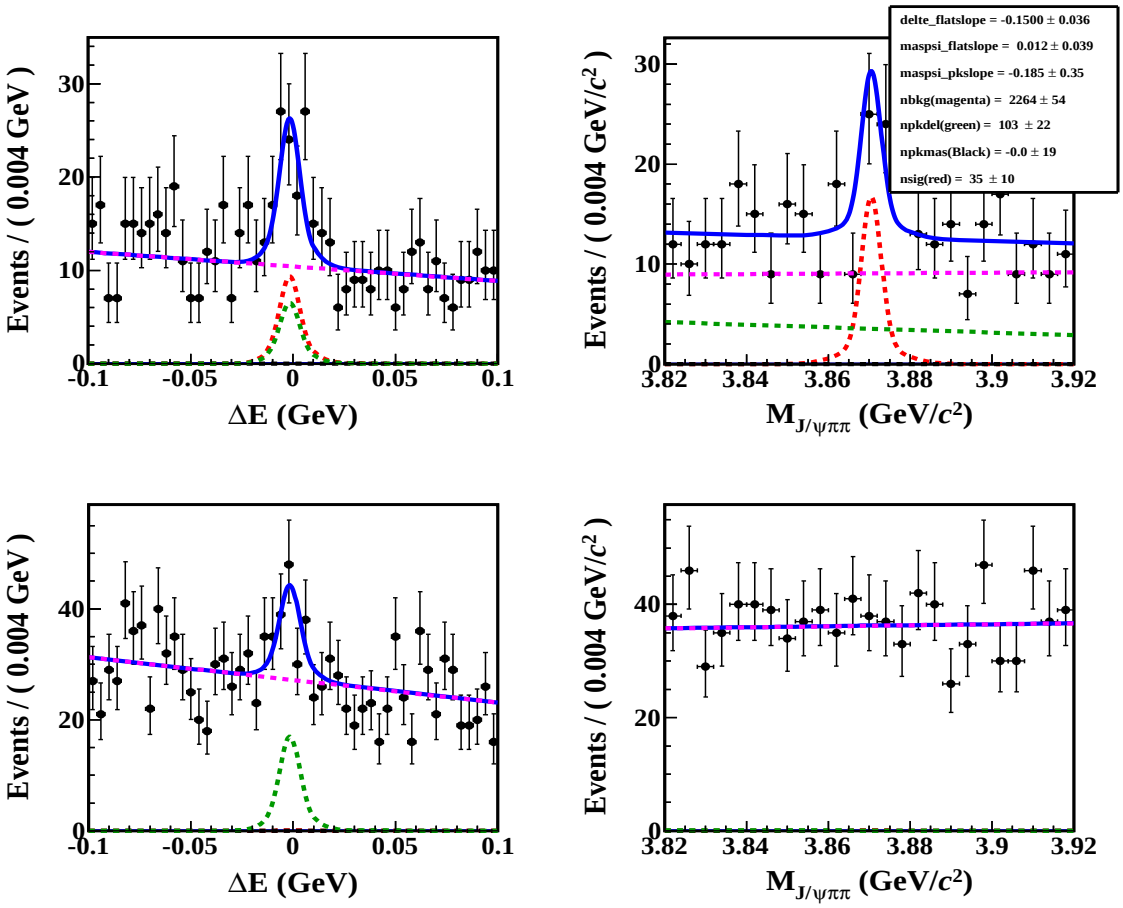

Figure 6.14: Top: Signal region projections of experimental data for $B^+ \to X(3872)K^0_S\pi^+$ decay mode. Left (right) plot is the projection for $M_{J/\psi\pi\pi}$ (ΔE) signal region. Bottom: Projection plots in background enhanced regions of ΔE and $M_{J/\psi\pi\pi}$. Left (right) is for $M_{J/\psi\pi\pi}$ (ΔE) sidebands in $X(3872)$ mass region. Red color represents signal in both dimensions, black color represent peaking background in $M_{J/\psi\pi\pi}$ dimension which is flat in ΔE dimension, green color represent peaking background in ΔE which is flat in $M_{J/\psi\pi\pi}$, magenta color represents combinatorial backgrounds in both dimensions with blue solid for overall fit.

Here also the weighted efficiency is taken by assuming same fraction of each $K\pi$ component as shown in Figure 5.9 (Appendix A).

Table 6.4: Fixed parameters (in GeV) for experimental data found using fudge factor for $X(3872)$ mass region.

Parameter name	Value from signal MC
maspsi_mean	3.87055 ± 0.000130233
maspsi_sigma1	$0.00236066 \pm 0.000112623$
maspsi_a2a	0.7343 ± 0.0037
maspsi_s2s1	2.91 ± 0.020
delte_alpha (from truth matching of $B^+ \to \psi' K^*(892)^+$)	-2.1466 ± 0.051
delte_n (from truth matching of $B^+ \to \psi' K^*(892)^+$)	1.25 ± 0.14
delte_mean	$-0.0015748 \pm 0.0000310635$
delte_sigma	$0.00895233 \pm 0.000464408$
delte_a2a	0.368 ± 0.011
delte_s2s1	0.5184 ± 0.004

6.3.6 Significance of Signal Yield for $B^+ \to X(3872)K^0_S\pi^+$ Decay Mode

As per the results obtained above, there is a clear evidence of $B^+ \to X(3872)K^0_S\pi^+$ decay. The statistical significance of $B^+ \to X(3872)K^0_S\pi^+$ decay mode with current data is estimated to be 3.9σ and 3.7σ respectively before and after including systematic uncertainties. This has also been shown in Figure 6.15. Details of method used for considering systematic uncertainty for significance calculations are mentioned in Appendix B.

6.4 Systematic Uncertainty Study

Common systematic uncertainties like kaon-identification, pion-identification, charged track finding efficiency, lepton-identification, due to limited statistics, variation of efficiency due to limited knowledge to generate signal MC samples, secondary branching

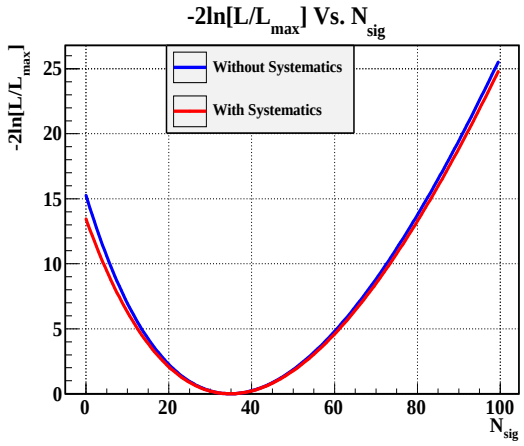

Figure 6.15: Scan of $-2\ln(\mathcal{L}_0/\mathcal{L}_{\max})$ for whole range of yields for decay mode $B^+ \to X(3872)K^0_S\pi^+$ with blue curve (before systematic uncertainty) and red curve (after including those systematic uncertainties which affects only signal yield).

fractions, number of $B\bar{B}$ ($N_{B\bar{B}}$) events, fit bias are already explained in the Section 4.4. In addition to that following systematic uncertainties are also included:

6.4.1 Systematic Uncertainty due to K^0_S Reconstruction

In $B^+ \to (J/\psi\pi^+\pi^-)(K^0_S\pi^+)$ decay, the K^0_S have uncertainty on its reconstruction, which can be estimated from the $D^{*0} \to D^0(\to K^0_S(\to \pi^+\pi^-)\pi^+\pi^-)\pi_{\rm slow}$ decay mode. Correction factor for the difference in K^0_S efficiency (between MC and experimental data) is used to correct the efficiency (this correction comes out to be 0.9789), while error on it is included as systematic uncertainty due to K^0_S (it is 0.73%) reconstruction.

6.4.2 Systematic Uncertainty due to PDF Modeling

As explained in the Section 4.4.8, the systematic uncertainty is estimated on our signal extraction procedure to be $^{+0.36\%}_{-0.22\%}$ and $^{+4.17\%}_{-4.85\%}$ for ψ' and $X(3872)$ mass regions respectively. Details of this uncertainty are provided in the Table 6.5 and Table 6.6.

Table 6.5: Estimation of systematic uncertainty from 2D extended UML fit shown in Figure 6.13. Nominal value of the signal yield for $B^+ \to \psi' K_S^0 \pi^+$ decay mode is 629.

Variable	Value Error	+Variation -Variation	Yield	ΔYield	-(Δ Yield)	+(Δ Yield)
maspsi_a2a	0.7008	0.7059	629	0	0	0
	0.0051	0.6957	629	0		
maspsi_s2s1	2.728	2.747	630	1	0	1
	0.019	2.709	629	0		
delte_alpha	-2.1466	-2.0956	630	1	0	1
	0.051	-2.1976	629	0		
delte_n	1.25	1.39	629	0	0	1
	0.14	1.11	630	1		
delte_a2a	0.797	0.8023	628	-1	-1	1
	0.0053	0.7917	630	1		
delte_s2s1	2.866	2.913	630	1	-1	1
	0.047	2.819	628	-1		
				Total	-0.22%	+0.36%

Table 6.6: Estimation of systematic uncertainty from 2D extended UML fit from fit shown in Figure 6.14. Nominal value of the signal yield for $B^+ \to X(3872) K_S^0 \pi^+$ decay mode is 34.85.

Variable	Value Error	+Variation -Variation	Yield	ΔYield	-(Δ Yield)	+(Δ Yield)
maspsi_mean	3.87055	3.870680233	35.66	0.81	-0.84	0.81
	1.30233E-04	3.870419767	34.01	-0.84		
maspsi_sigma	0.00236066	0.002473283	35.44	0.59	-0.53	0.59
	1.12623E-04	0.002248037	34.32	-0.53		
maspsi_a2a	0.7343	0.738	34.76	-0.09	-0.09	0.11
	0.0037	0.7306	34.96	0.11		
maspsi_s2s1	2.91	2.93	34.90	0.05	-0.04	0.05
	0.02	2.89	34.81	-0.04		
delte_mean	-0.0015748	-0.001264165	35.20	0.35	-0.39	0.35
	3.10635E-04	-0.001885435	34.46	-0.39		
delte_sigma	0.00895233	0.009416738	35.79	0.94	-1.04	0.94
	4.64408E-04	0.008487922	33.81	-1.04		
delte_alpha	-2.1466	-2.0956	34.99	0.14	-0.12	0.14
	0.051	-2.1976	34.73	-0.12		
delte_n	1.25	1.39	34.69	-0.16	-0.16	0.17
	0.14	1.11	35.02	0.17		
delte_a2a	0.368	0.379	35.01	0.16	-0.13	0.16
	0.011	0.357	34.72	-0.13		
delte_s2s1	0.5184	0.5224	34.95	0.10	-0.76	0.10
	0.004	0.5144	34.09	-0.76		
				Total	-4.85%	+4.17%

6.4.3 Total Systematic Uncertainty

All systematic uncertainties contributions, which can affect our measurement for branching fractions, are summarized in Table 6.7. After adding all these individual systematic uncertainties in quadrature, we obtain total systematic uncertainty of $^{+5.82}_{-5.81}\%$ and $^{+7.65}_{-8.05}\%$, respectively for $B^+ \to \psi' K^0_S \pi^+$ and $B^+ \to X(3872) K^0_S \pi^+$ decay modes.

Table 6.7: The Summary of systematic uncertainty used for 2D extended UML fit study.

Systematic Uncertainty(%)		
Mode $\rightarrow$	$B^+ \to \psi' K^0_S \pi^+$	$B^+ \to X(3872) K^0_S \pi^+$
Source $\downarrow$		
K^0	0.73	0.73
π-id π of $K^0\pi$	1.1	1.2
π-id pions of ψ' or $X(3872)$	2×1.2	2×1.5
Tracking	2.45	2.45
ℓ id	2×1.7	2×1.7
MC statistics	0.35	1.0
Sec. $\mathcal{B}$	0.96	0.40
$N_{B\overline{B}}$	1.4	1.4
PDF	$^{+0.36}_{-0.22}$	$^{+4.17}_{-4.85}$
Fit bias	2.37	3.09
Total	$^{+5.82}_{-5.81}$	$^{+7.65}_{-8.05}$

6.5 Search for $B^+ \to X(3872) K^+ \pi^0$ Decay Mode

In order to search for $B^+ \to X(3872) K^+ \pi^0$ decay mode, a quick and very preliminary study is performed using full and final data set accumulated by the Belle Experiment. Due to the fact that whole $M_{K\pi}$ phase space is allowed, having π^0 (two gammas) in the final state, a large range for $M_{J/\psi\pi\pi}$ (which includes ψ' and $X(3872)$ mass regions) as well as the wide ΔE region, all these factors results in a high rate of multiple B candidates in an event while reconstructing this decay mode. As it is already seen, multiplicity of multiple B candidates is already large for $B^+ \to X(3872) K^0_S \pi^+$ decay mode and it becomes too large in $B^+ \to X(3872) K^+ \pi^0$ decay mode. Therefore, it

becomes difficult to handle backgrounds for this decay mode at same footing as that of previous decay modes. However, we are presenting here, our preliminary study and providing 90% C.L. upper limit on the product of branching fractions for the $\mathcal{B}(B^+ \to X(3872)K^+\pi^0) \times \mathcal{B}(X(3872) \to J/\psi\pi^+\pi^-)$ because of less significance of this mode. In addition to the above stated analysis, the results of the analysis of $B^+ \to \psi' K^+\pi^0$ decay mode is also presented which is the calibration decay mode for this decay mode.

6.6 Event Reconstruction Procedure

To observe $B^+ \to X(3872)K^+\pi^0$ decay mode, the B-meson reconstruction is done by the reconstructed $X(3872)$ particle with K^+ and π^0 candidates as shown in Figure 3.6. The $X(3872)$ is reconstructed via its decay mode $J/\psi\pi^+\pi^-$, here J/ψ is reconstructed using $\ell^+\ell^-$, where ℓ is e or μ. Selection criteria for J/ψ, charged pion and charged kaon is similar to the one used in previously studied decay mode, while the π^0 decays to $\gamma\gamma$ in $\approx 99\%$ of its decay. π^0 is reconstructed using two-photon showers having deposited energy of 60 MeV in the ECL crystals. Further, only those two-photons are selected whose invariant mass lies within ± 15 MeV/c^2 of the nominal π^0 mass. In an attempt to improve the resolution of our final B-meson, we constraint the mass of the reconstructed π^0 to the world average π^0 mass. Reconstruction of calibration decay mode $B^+ \to \psi' K^+\pi^0$ is also done on similar footing as that of concerned decay mode.

6.6.1 Efficiency Estimation from Signal MC Study and PDF Parametrization

For $B^+ \to \psi' K^+\pi^0$ and $B^+ \to X(3872)K^+\pi^0$ decay modes, correctly reconstructed events (signal events peaking in both ΔE and $M_{J/\psi\pi\pi}$ reconstructed correctly) and self cross feed events (due to wrongly reconstruction or exchange of daughter particles of tag B with other B-meson daughters) for signal MC are shown in Figures 6.16 and Figure 6.17. Also its 2D extended UML fitting is shown in Figure 6.18 and Figure 6.19

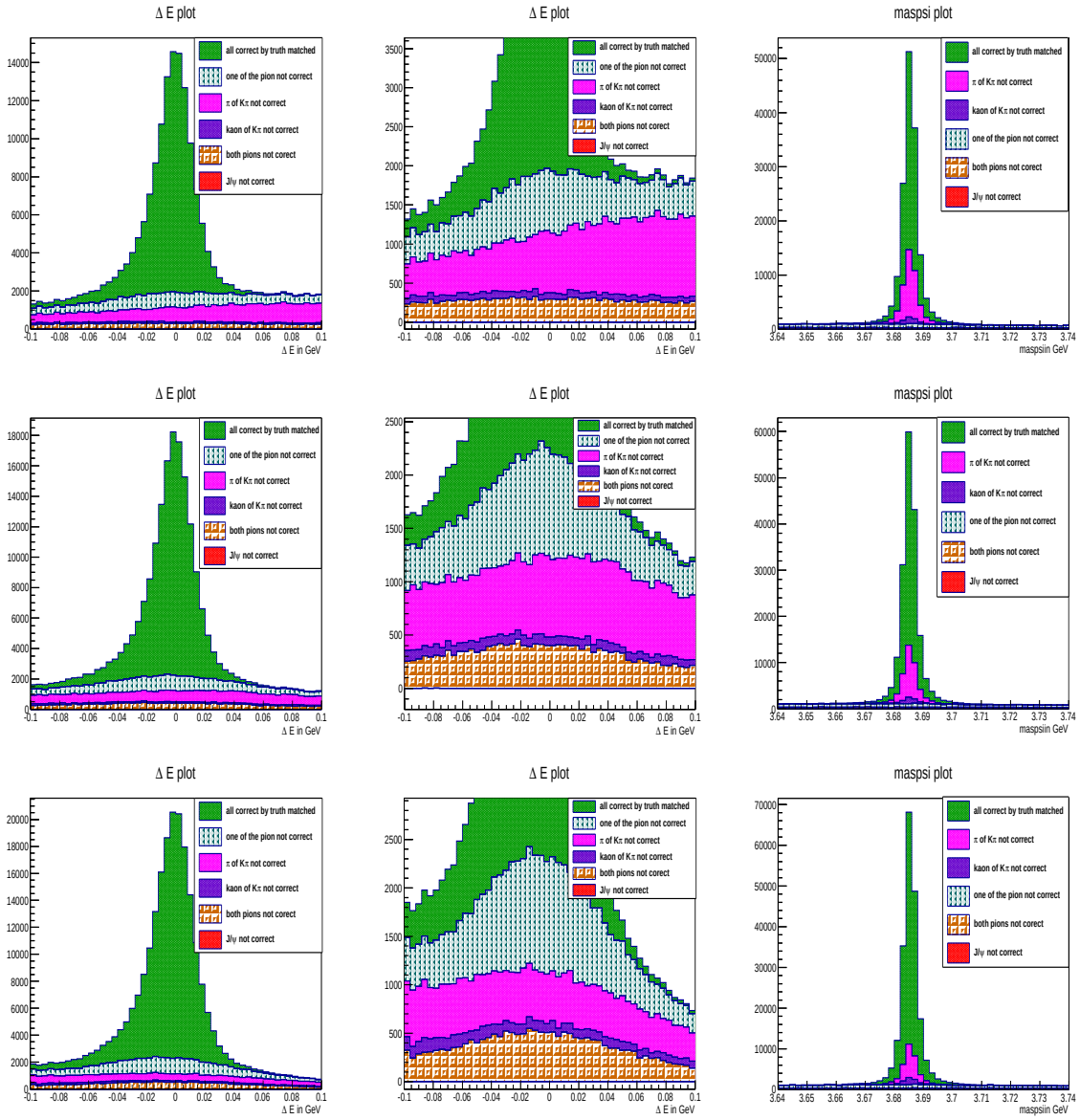

Figure 6.16: Correctly reconstructed (CR) and self cross feed (SCF) signal events plots for signal MC sample in ΔE and $M_{J/\psi\pi\pi}$ (middle plots are zoomed plots for ΔE dimension) for $B^+ \to \psi' K^+\pi^0$ decay mode. Top plots are for $B^+ \to \psi' K^*(892)^+$ decay mode, middle one are for $B^+ \to \psi'(K^+\pi^0)_{NR}$ and bottom plots are for $B^+ \to \psi' {K_2}^*(1430)^+$ decay mode.

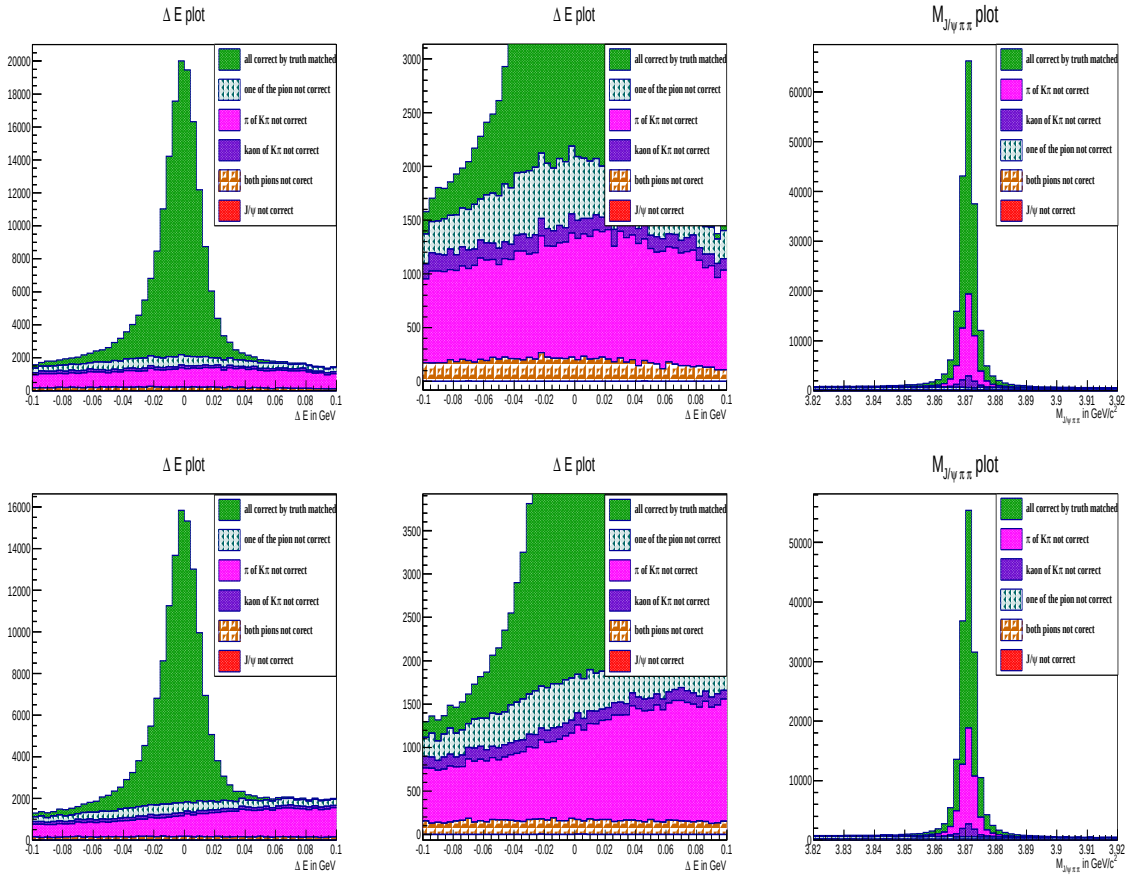

Figure 6.17: Correctly reconstructed (CR) and self cross feed (SCF) signal events plots for signal MC sample in ΔE and $M_{J/\psi\pi\pi}$ (middle plots are zoomed plots for ΔE dimension) for $B^+ \to X(3872)K^+\pi^0$ decay mode. Top plots are for $B^+ \to X(3872)(K^+\pi^0)_{NR}$ decay mode and bottom plots are for $B^+ \to X(3872)K^*(892)^+$ decay mode.

respectively for ψ' and $X(3872)$ mass regions. Fitting strategy is same as described earlier in previous analyses. Reconstruction efficiencies based upon above fitting for signal MC are given in Table 6.8.

6.6.2 Background Study

For the $B^+ \to \psi'(K^+\pi^0)$ decay, signal and background in ΔE region and $M_{J/\psi\pi\pi}$ region are shown in Figure 6.20. In this Figure, $B^+ \to \psi' K^*(892)^+$ (green color) is

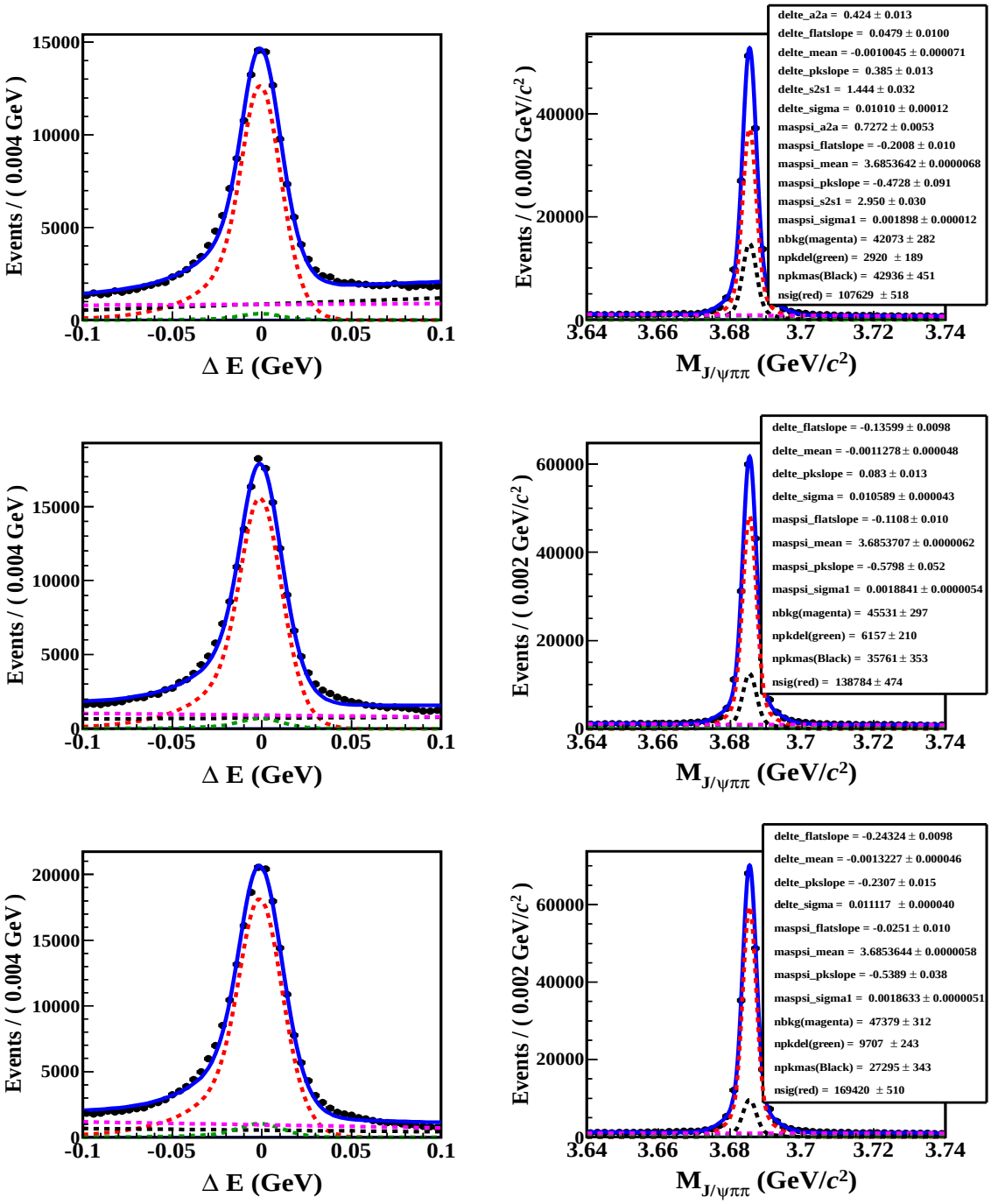

Figure 6.18: 2D extended UML fit to signal MC events for $B^+ \to \psi' K^*(892)^+$ (top), $B^+ \to \psi'(K^+\pi^0)_{NR}$ (middle), $B^+ \to \psi' K_2^*(1430)^+$ (bottom) decay mode, where signal is plotted with red dotted curve, black curve shows peaking SCF in $M_{J/\psi\pi\pi}$ dimension (flat in ΔE) and vice-versa for green curve, while magenta curve shows combinatorial background in both dimensions and blue solid for total fit.

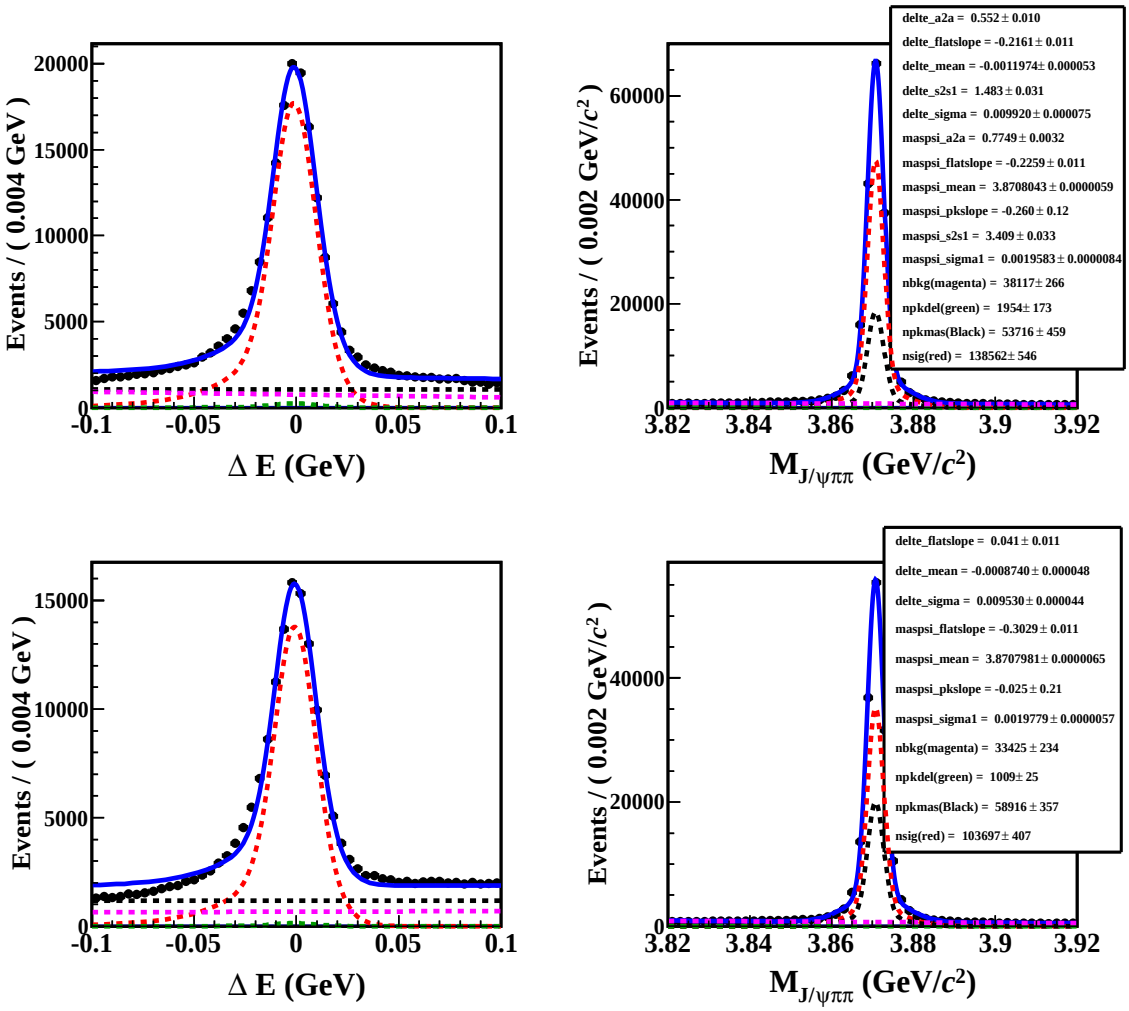

Figure 6.19: 2D extended UML fit to signal MC events for $B^+ \to X(3872)(K^+\pi^0)_{NR}$ (top), $B^+ \to X(3872)K^*(892)^+$ (bottom) decay mode, where signal is plotted with red dotted curve, black curve shows peaking SCF in $M_{J/\psi\pi\pi}$ dimension (flat in ΔE) and vice-versa for green curve, while magenta curve shows combinatorial background in both dimensions and blue solid for total fit.

Table 6.8: Reconstruction efficiencies of different signal MC samples estimated from 2D extended UML fit study.

Decay Channel	Reconstruction Efficiency in %
$B^+ \to \psi' K^*(892)^+$	(5.49 ± 0.03)
$B^+ \to \psi'(K^+\pi^0)_{NR}$	(7.14 ± 0.02)
$B^+ \to \psi' K_2{}^*(1430)^+$	(8.47 ± 0.03)
$B^+ \to X(3872)(K^+\pi^0)_{NR}$	(6.93 ± 0.03)
$B^+ \to X(3872)K^*(892)^+$	(5.18 ± 0.02)

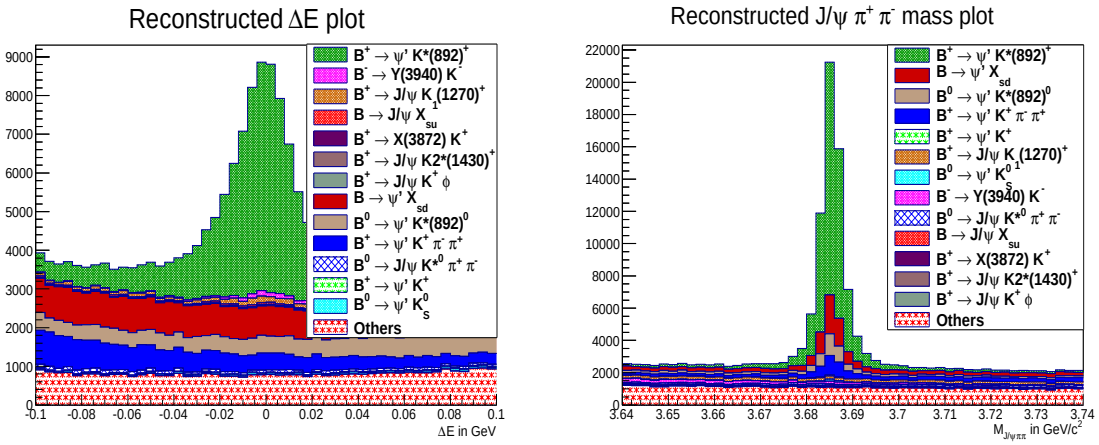

Figure 6.20: Background estimation for $B^+ \to \psi' K^+\pi^0$ decay mode using J/ψ inclusive MC ($\sim 100\times$ experimental data) for ΔE (left) and $M_{J/\psi\pi\pi}$ (right) dimensions.

our signal (peaking in both dimensions). In the $M_{J/\psi\pi\pi}$ region, the peaking background is coming from $B \to \psi' X_{sd}$ (red color), $B^0 \to \psi' K^*(892)^0$ (light brown color), $B^+ \to \psi' K^+\pi^+\pi^-$ (blue color), $B^+ \to \psi' K^+$ (dotted green color) and $B^+ \to \psi' K_S^0$ (cyan color) decay modes, but they are not peaking in the ΔE dimension. In ΔE dimension, there are few peaking backgrounds (flat in $M_{J/\psi\pi\pi}$) like $B^- \to Y(3940)K^-$, $B^+ \to J/\psi K_1(1270)^+$, $B \to J/\psi X_{su}$, $B^+ \to X(3872)K^+$, $B^+ \to J/\psi K_2^*(1430)^+$ and $B^+ \to J/\psi K^+\phi$. Rest of the background comprises of combinatorial events in both distributions (ΔE and $M_{J/\psi\pi\pi}$) and has no peaking structure.

For $B^+ \to X(3872)K^+\pi^0$ decay mode, the various backgrounds contribution in the ΔE and $M_{J/\psi\pi\pi}$ dimensions are shown in Figure 6.21. All backgrounds are flat

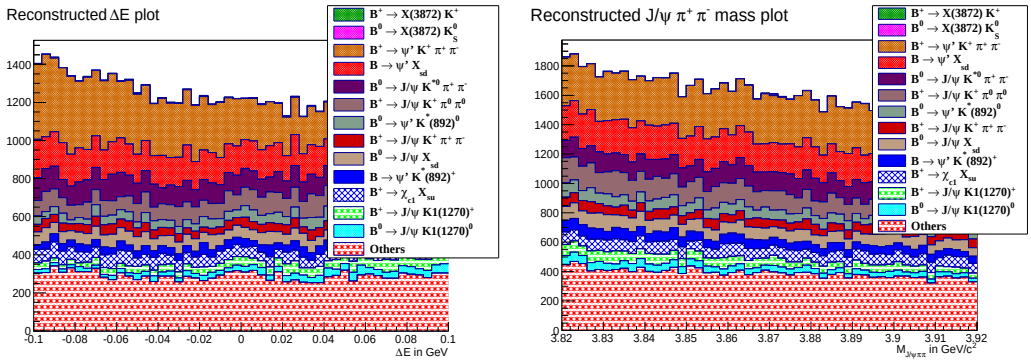

Figure 6.21: Background estimation for $B^+ \to X(3872)K^+\pi^0$ decay mode using J/ψ inclusive MC ($\sim$ 100$\times$ experimental data) for ΔE (left) and $M_{J/\psi\pi\pi}$ (right) dimensions.

in both $M_{J/\psi\pi\pi}$ and ΔE distributions and there is no peaking background.

6.6.3 Extraction of Signal Yield from Experimental Data and Results

Based upon above signal MC sample study, a 2D extended UML fit is performed to the experimental data using the same strategy. The fit to the experimental data for $B^+ \to \psi' K^+\pi^0$ decay modes in signal and background enhanced regions is shown in Figure 6.22. The branching fractions (B.F) obtained from the 2D fitting of experimental data comes out to be $(3.56 \pm 0.24(\text{stat.})) \times 10^{-4}$ after using weighted efficiency.

Fitting of the experimental data for $B^+ \to X(3872)(K^+\pi^0)$ decay mode in signal and background enhanced regions is shown in Figure 6.23. From the fit, obtained signal yield is (39 ± 17) events with no clear peak with present statistics of the Belle experimental data. Therefore we are able to set only the 90% confidence level (C.L.) upper limit (U.L.) on the product of branching fractions $\mathcal{B}(B^+ \to X(3872)K^+\pi^0) \times \mathcal{B}(X(3872) \to J/\psi\pi^+\pi^-) < 11.2 \times 10^{-6}$ after considering weighted efficiency (shown in Figure 6.24). To set this U.L., frequentist method is used which is based on an ensemble of pseudo-experiments.

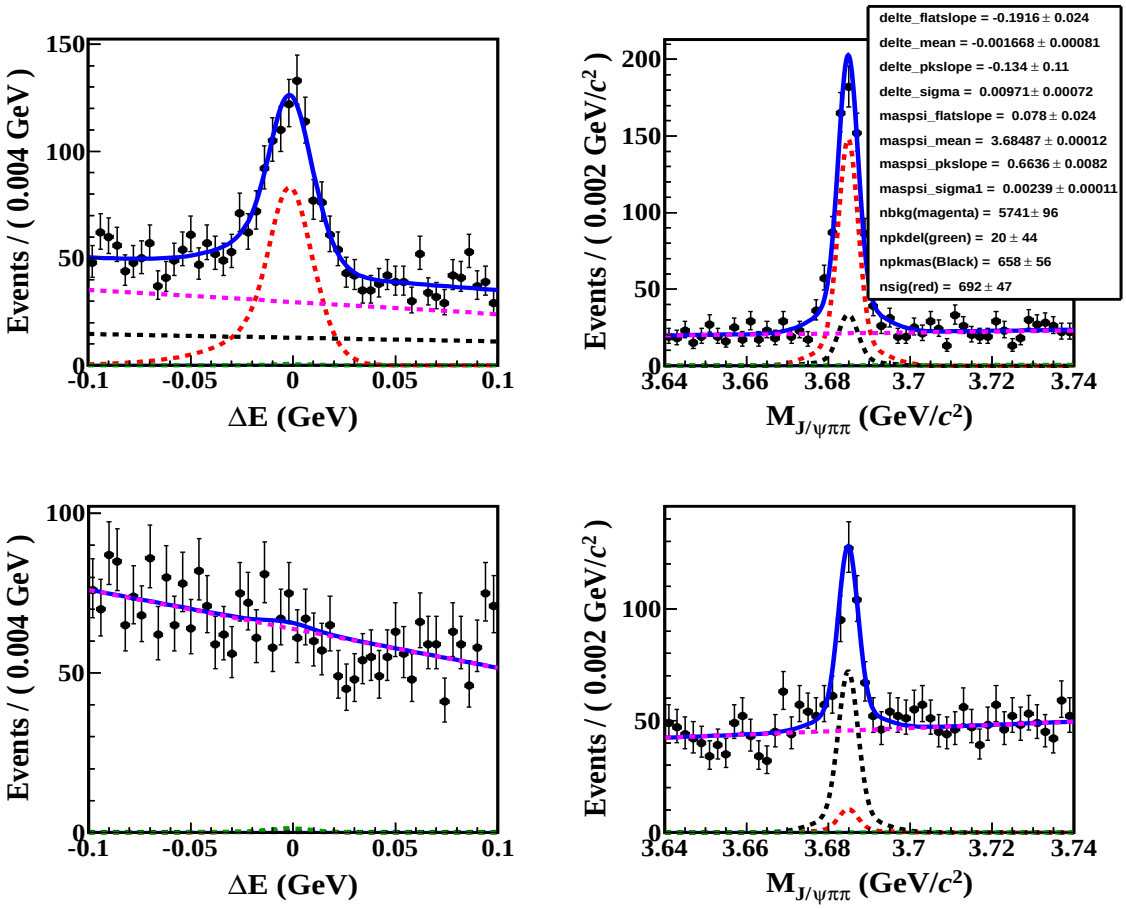

Figure 6.22: Top: Signal region projections of experimental data for $B^+ \to \psi' K^+ \pi^0$ decay mode. Left plot is the projection for $M_{J/\psi\pi\pi}$ signal region and right plot is the projection for ΔE signal region. Bottom: Projection plots in background enhanced regions of ΔE and $M_{J/\psi\pi\pi}$. Left (right) is for $M_{J/\psi\pi\pi}$ (ΔE) sidebands in ψ' mass region. Red color represents signal in both dimensions, black color represent peaking background in $M_{J/\psi\pi\pi}$ dimension which is flat in ΔE dimension, green color represent peaking background in ΔE which is flat in $M_{J/\psi\pi\pi}$, magenta color represents combinatorial backgrounds in both dimensions and blue solid for total fit.

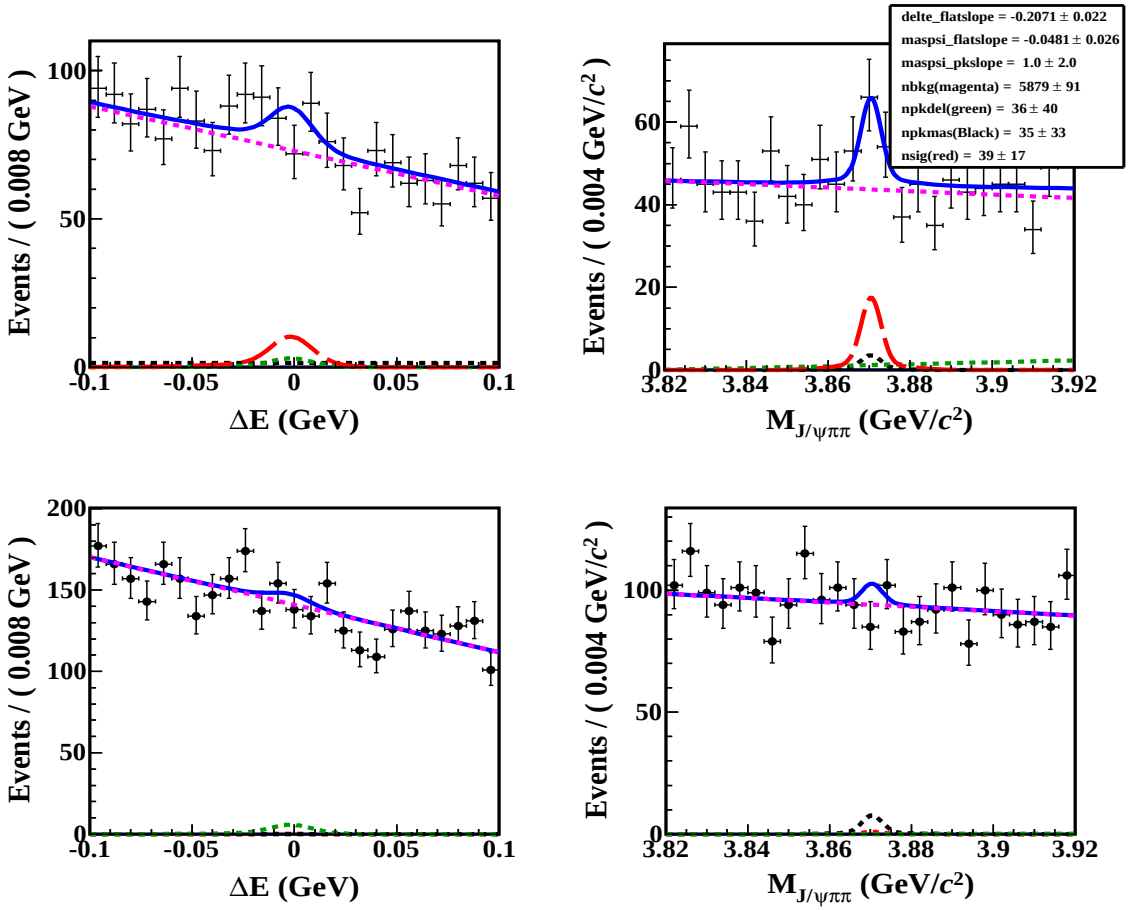

Figure 6.23: Top: Signal region projections of experimental data for $B^+ \to X(3872)K^+\pi^0$ decay mode. Left plot is the projection for $M_{J/\psi\pi\pi}$ signal region and right plot is the projection for ΔE signal region. Bottom: Projection plots in background enhanced regions of ΔE and $M_{J/\psi\pi\pi}$. Left (right) is for $M_{J/\psi\pi\pi}$ (ΔE) sidebands in ψ' mass region. Red color represents signal in both dimensions, black color represent peaking background in $M_{J/\psi\pi\pi}$ dimension which is flat in ΔE dimension, green color represent peaking background in ΔE which is flat in $M_{J/\psi\pi\pi}$, magenta color represents combinatorial backgrounds in both dimensions and blue solid for total fit.

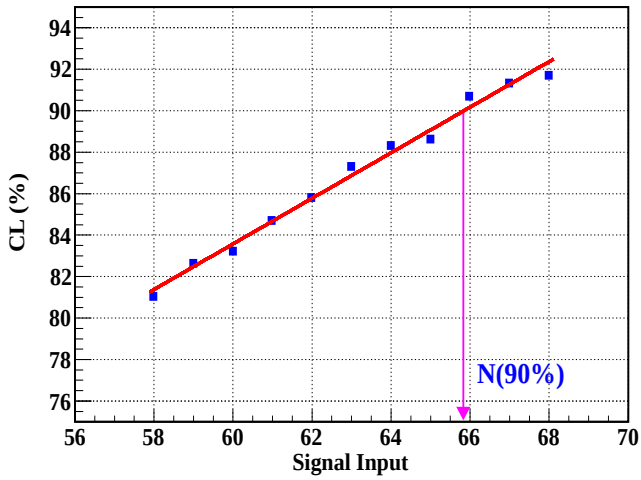

Figure 6.24: Relationship between input value of signal for Toy MC yield and confidence level for $B^+ \to X(3872)K^+\pi^0$ decay mode.

6.7 Chapter in Compact

In this Chapter, a detail study of charged B meson decay mode $B^+ \to \psi' K^0_S \pi^+$ and $B^+ \to X(3872)K^0_S\pi^+$ has been presented. The branching fractions for the calibration decay mode $B^+ \to \psi' K^0 \pi^+$ has been obtained as $(6.00 \pm 0.28(\text{stat.}) \pm 0.35(\text{syst.})) \times 10^{-4}$. This calibration decay mode result is consistent with the world average value $(5.88 \pm 0.34) \times 10^{-4}$. First evidence of $B^+ \to X(3872)K^0_S\pi^+$ decay mode has been found with a statistical significance of 3.7σ and the product of branching fractions measured is $\mathcal{B}(B^+ \to X(3872)K^0\pi^+) \times \mathcal{B}(X(3872) \to J/\psi\pi^+\pi^-) = (10.64 \pm 3.04(\text{stat.})^{+0.81}_{-0.86}(\text{syst.})) \times 10^{-6}$. Search has also been performed for $B^+ \to X(3872)K^+\pi^0$ decay mode. The branching fraction for the calibration decay mode $\mathcal{B}(B^+ \to \psi' K^+\pi^0)$ has been measured as $(3.56 \pm 0.24(\text{stat.})) \times 10^{-4}$ and upper limit (@ 90%) on the product of branching fractions $\mathcal{B}(B^+ \to X(3872)K^+\pi^0) \times \mathcal{B}(X(3872) \to J/\psi\pi\pi) < 11.2 \times 10^{-6}$ has been assigned. The existing Belle data statistics is not sufficient to establish the evidence/observation of this decay mode. However, One can access this decay mode easily with coming Belle II, which is expected to have 50 times more data than Belle I.

7

Summary of Results and Conclusions

The investigation carried out in this thesis is based on 711 fb^{-1} of Belle data containing 771.6 Million $B\bar{B}$ events collected with the Belle detector at the KEKB e^+e^- asymmetric-energy collider, situated at Tsukuba, Japan. This data sample was collected by operating collider at the $\Upsilon(4S)$ resonance, which is at threshold of $B\bar{B}$ mass. As soon as $\Upsilon(4S)$ resonance is produced in e^+e^- collision, it decays to pair of B-meson (B-meson pair is produced at rest). In this Chapter, we summarize and discuss the results which are obtained from the study of $B \to X(3872)K\pi$ decay modes undertaken in this work. The $X(3872)$ is electrically neutral particle, which is discovered by the Belle Collaboration in 2003 and rapidly confirmed by other experiments, still its nature has remained unsettled. Being neutral, it is challenging to distinguish the $X(3872)$ from an ordinary charmonium resonances. In this investigation, production of $X(3872)$ and ψ' in three body decay of B-meson, namely $B^0 \to X(3872)K^+\pi^-$, $B^0 \to \psi' K^+\pi^-$, $B^+ \to X(3872)K^0_S\pi^+$, $B^+ \to \psi' K^0_S\pi^+$, $B^+ \to X(3872)K^+\pi^0$ and $B^+ \to \psi' K^+\pi^0$, have been studied. This is the first time the decay of B-mesons to three body decay having $X(3872)$ has been studied in such detail and results have been published [130]. We could only perform preliminary study for $B^+ \to \psi' K^+\pi^0$ and $B^+ \to X(3872)K^+\pi^0$ decay modes, because of high background and low sensitivity to signal with the current statistics.

Decays of B mesons to three body final states having charmonium in final states

(ψ') are expected to occur predominantly via the color-suppressed spectator diagrams and are also Cabibbo-favored ones at tree level. With the analysis of full Belle experimental data, we have performed a search for $X(3872)$ in the three body decay of B-mesons and present the first observation of $B^0 \to X(3872)K^+\pi^-$ decay, first evidence for $B^+ \to X(3872)K^0_S\pi^+$ decay. However no observation/evidence for $B^+ \to X(3872)K^+\pi^0$ decay mode has been found. In addition to the above study, we have also searched for any new resonant structures in the observed decay mode $B^0 \to X(3872)K^+\pi^-$ by studying background subtracted mass distributions of $M_{X(3872)K}$, $M_{X(3872)\pi}$ and $M_{K\pi}$.

7.1 Search for $B^0 \to X(3872)K^+\pi^-$ and $B^+ \to X(3872)K^0_S\pi^+$ Decay Modes

The procedure carried out for the search of $B^0 \to X(3872)K^+\pi^-$ and $B^+ \to X(3872)K^0_S\pi^+$ decay modes can be summarized as follows:

- Monte Carlo Study: A Monte Carlo simulation study is performed to estimate reconstruction efficiency for branching fraction calculations using 2 Million signal events for each decay mode. Using this MC study, it is found that we can extract signal yield by using two dimensional extended unbinned maximum likelihood fitting of ΔE and $M_{J/\psi\pi\pi}$ variables.

- Background Study: To understand nature of backgrounds and types of backgrounds, officially generated J/ψ inclusive MC sample (all decay modes of type $B \to J/\psi X$, where X can be any particle) has been used. This sample is two order magnitude higher than the luminosity of final data set accumulated by Belle detector. Based upon this study, we found that due to mis-reconstruction and cross-feed from few decay modes (having similar kinematics) some events (not coming from signal) can peak in the signal region of one dimension, while being flat in the other dimension. We identify those decay modes and parametrize them in our signal extraction procedure. Rest of the backgrounds have no

structure and hence are flat in both dimensions. Non-J/ψ backgrounds are also checked using J/ψ mass sidebands distributions and no peaking structure is seen in the signal region.

- Verification of Signal Extraction strategy: Based upon background study, we perform fit modeling using 2D extended UML fitting and verify branching fractions of known decay modes based upon signal yield and efficiency from MC. It has been found to be consistent with the generated branching fractions.

- Calibration Decay Mode Study: In order to calibrate the detector resolution and to verify our background understanding in the experimental data for our search decay modes, we use $B^0 \to \psi' K^+\pi^-$ and $B^+ \to \psi' K^0_S\pi^+$ decay modes as our calibration decay modes, as these modes have been well studied. This study provides confidence and reliability to our signal extraction procedure.

- Fudge Factor Estimation: The difference between Monte Carlo simulation and experimental data is called Fudge Factors which is estimated using calibration decay mode. Difference due to different decay dynamics and kinematics of $\psi' \to J/\psi\pi^+\pi^-$ and $X(3872) \to J/\psi\rho^0(\to \pi^+\pi^-)$ is also taken into account.

- Background Modeling and Fit Validation: The 2D fitter is used to extract signal yield. Fit bias in extraction of signal yield is verified using toy MC study and GSIM study. We did not observe any significant bias, hence it provides confidence in our fitter and technique of analysis. However, as a conservative, we added the insignificant bias to our source of systematics uncertainty.

- Signal Extraction Method: After validating our reconstruction procedure, selections and fitter, same strategy is adopted to extract signal events from experimental data. We find statistical significance of 7σ and 3.7σ for extracted signal yield for the $B^0 \to X(3872)K^+\pi^-$ and $B^+ \to X(3872)K^0\pi^+$ decay modes respectively. These are used to estimate product of branching fractions $\mathcal{B}(B^0 \to X(3872)K^+\pi^-) \times \mathcal{B}(X(3872) \to J/\psi\pi^+\pi^-)$ and $\mathcal{B}(B^+ \to X(3872)K^0\pi^+) \times \mathcal{B}(X(3872) \to J/\psi\pi^+\pi^-)$.

- Efficiency Correction and Systematic Uncertainty Study: As we know the method used to estimate reconstruction efficiency and procedure used to extract signal yield has some limitation due to uncontrollable factors, so these uncertainties are estimated in order to provide the most correct and best measurement as one can think of. So we correct the reconstruction efficiency (which is estimated from signal MC) because of small difference in the signal detection efficiency between signal MC events and experimental data. This is due to lepton, kaon and pion identification differences and also because of difference in charged tracks identification e.g. kaon, pion, leptons etc. In our case, we try to include all major sources of systematic uncertainties which can affect our signal yield and hence branching fraction measurements.

  To be conservative in our announcement of observation/evidence, we include systematic uncertainty in our estimation of statistical significance (only those systematic uncertainties are included which affects signal yield).

7.2 Preliminary Study of $B^+ \to X(3872)K^+\pi^0$ Decay Mode

The very preliminary study of $B^+ \to X(3872)K^+\pi^0$ decay mode is also performed in the present investigation. Because of large multiple B candidates during reconstruction of events, more self cross feed, wide range of ΔE and $M_{J/\psi\pi\pi}$, it becomes difficult to handle backgrounds in this decay mode at the same footing as that of previous decay modes. Because of this we could not get statistically significant yield to claim any evidence or observation for this decay mode and could set only upper limit at 90% C.L. The $B^+ \to \psi' K^+\pi^0$ decay mode is used as calibration decay mode for above study and is analysed with the full experimental data of Belle.

7.3 Results for $B^0 \to X(3872)K^+\pi^-$, $B^+ \to X(3872)K^0_S\pi^+$ and $B^+ \to X(3872)K^+\pi^0$ Decay Modes

The $B \to \psi' K\pi$ decay modes are Cabibbo-favored and color-suppressed one at tree level. The branching fraction for this decay mode $\mathcal{B}(B^0 \to \psi' K^+\pi^-)$ is measured to be $(5.79 \pm 0.14(\text{stat.}) \pm 0.31(\text{syst.})) \times 10^{-4}$, which agrees well with the world average value, $(5.8 \pm 0.4) \times 10^{-4}$ [1]. We have observed $B^0 \to X(3872)K^+\pi^-$ decay mode for the first time in world with a statistical significance of 7σ. The product of branching fractions $\mathcal{B}(B^0 \to X(3872)K^+\pi^-) \times \mathcal{B}(X(3872) \to J/\psi\pi^+\pi^-)$ is estimated to be $(7.91 \pm 1.29(\text{stat.})^{+0.43}_{-0.42}(\text{syst.})) \times 10^{-6}$.

Branching fractions for $B^+ \to \psi' K^0\pi^+$ decay mode is measured as $(6.00 \pm 0.28(\text{stat.}) \pm 0.35(\text{syst.})) \times 10^{-4}$, which is also consistent with the PDG value as $(5.88 \pm 0.34) \times 10^{-4}$. With the present study, we find first evidence of $B^+ \to X(3872)K^0\pi^+$ decay mode with statistical significance of 3.7σ. The product of branching fractions $\mathcal{B}(B^+ \to X(3872)K^0\pi^+) \times \mathcal{B}(X(3872) \to J/\psi\pi^+\pi^-)$ is estimated as $(10.64 \pm 3.04(\text{stat.})^{+0.81}_{-0.86}(\text{syst.})) \times 10^{-6}$.

The branching fraction $\mathcal{B}(B^+ \to \psi' K^+\pi^0)$ obtained from the 2D fitting of experimental data comes out to be $(3.56 \pm 0.24(\text{stat.})) \times 10^{-4}$. Upper limit (@ 90% C.L) for the product of branching fractions is $\mathcal{B}(B^+ \to X(3872)K^+\pi^0) \times \mathcal{B}(X(3872) \to J/\psi\pi^+\pi^-) < 11.2 \times 10^{-6}$.

The results for the decay modes studied in this investigation can be summarized in Table 7.1 and Table 7.2.

7.4 Search for Resonances/New Particles in Background Subtracted Mass Distributions

In order to understand the production mechanism of three body decay $B^0 \to X(3872)K^+\pi^-$, the background subtracted $M_{X(3872)K}$, $M_{X(3872)\pi}$ and $M_{K\pi}$ distributions are investigated for $B^0 \to X(3872)K^+\pi^-$ decay mode. Also one can investigate the pro-

Table 7.1: Signal yield (Y) from the fit, weighted efficiency (ϵ) after PID correction and measured branching fractions for $B^0 \to \psi' K^+\pi^-$, $B^+ \to \psi' K^0_S\pi^+$ and $B^+ \to \psi' K^+\pi^0$ decay modes. The first (second) uncertainty represents a statistical (systematic) contribution.

Decay Mode	Yield (Y)	ϵ (%)	$\mathcal{B}(B \to \psi' K\pi)$
$B^0 \to \psi' K^+\pi^-$	2599 ± 61	14.14	$(5.79 \pm 0.14 \pm 0.31) \times 10^{-4}$
$B^+ \to \psi' K^0_S\pi^+$	629 ± 30	9.55	$(6.00 \pm 0.28 \pm 0.35) \times 10^{-4}$
$^\dagger B^+ \to \psi' K^+\pi^0$	692 ± 47	6.13	$(3.56 \pm 0.24(\text{stat.})) \times 10^{-4}$

† It is to be noted that for $B^+ \to \psi' K^+\pi^0$ decay mode, results are without any PID correction and without any systematic uncertainty study. These results are only preliminary one.

Table 7.2: Signal yield (Y) from the fit, weighted efficiency (ϵ) after PID correction, significance (Σ) and measured branching fractions for $B^0 \to X(3872)K^+\pi^-$, $B^+ \to X(3872)K^0_S\pi^+$ and $B^+ \to X(3872)K^+\pi^0$ decay modes. The first (second) uncertainty represents a statistical (systematic) contribution.

Decay Mode	Yield (Y)	ϵ (%)	Σ (σ)	$\mathcal{B}(B \to X(3872)K\pi)\times$ $\mathcal{B}(X(3872) \to J/\psi\pi^+\pi^-)$
$B^0 \to X(3872)K^+\pi^-$	116 ± 19	15.99	7.0	$(7.91 \pm 1.29^{+0.43}_{-0.42}) \times 10^{-6}$
$B^+ \to X(3872)K^0_S\pi^+$	35 ± 10	10.31	3.7	$(10.64 \pm 3.04^{+0.81}_{-0.86}) \times 10^{-6}$
$^\ddagger B^+ \to X(3872)K^+\pi^0$	39 ± 17	6.38	–	$< 11.2 \times 10^{-6}$ (@90% C.L.)

‡ It is to be noted that for $B^+ \to X(3872)K^+\pi^0$ decay mode, results are without any PID correction and without any systematic uncertainty study. These results are only preliminary one.

duction of new particle/resonance with these distributions. This study is motivated from the fact that Belle Collaboration found a clear peak in mass distribution of $M_{\psi'\pi^{\pm}}$ [131], which they named it as $Z(4430)^{\pm}$. Almost 7 years later, LHCb reports a more detailed measurement of the $Z(4430)^{\pm}$ that confirms that it is unambiguously a particle, and a long-sought exotic hadron [132]. And also to check the production mechanism of $(K\pi)$ in $B^0 \to X(3872)K^+\pi^-$ decay mode, because it was found that for ordinary charmonium states like ψ' and χ_{c1} [133] mass regions, resonant $(K^*(892)^0 \to K^+\pi^-)$ contribution is more as compared to non-resonant $((K\pi)_{NR})$ one. To get background subtracted mass distributions for $M_{X(3872)K}$, $M_{X(3872)\pi}$ and $M_{K\pi}$, the 2D extended UML fitting is performed in each bin of $M_{X(3872)K}$, $M_{X(3872)\pi}$ and $M_{K\pi}$, respectively to the ΔE and $M_{J/\psi\pi\pi}$ variables. This will return us signal yield and custom error for each distribution of $M_{X(3872)K}$, $M_{X(3872)\pi}$ and $M_{K\pi}$. These distributions are without any backgrounds and hence called background subtracted distribution. We didn't observe any obvious pattern in $M_{X(3872)K}$ and $M_{X(3872)\pi}$ background subtracted distributions as shown in Figure 5.4. However a clear peak is observed in background subtracted $M_{K\pi}$ distribution. Further to get different components of $(K\pi)$ system, it is necessary to perform the fitting of $M_{K\pi}$ background subtracted distribution. So binned minimum χ^2 fitting is performed to extract the $(K\pi)$ resonant and non-resonant contributions. This total procedure is called background subtracted binned fit study. This study can be summarized as follows:

- Monte Carlo Study: A Monte Carlo study is performed to get reconstruction efficiency. We perform 2D extended UML fitting in each bin of $M_{K\pi}$ mass for each generated signal MC sample and get only signal $M_{K\pi}$ distribution for each signal MC sample. From this signal yield, we estimate the reconstruction efficiency for different $K\pi$ components.

- Background Study and Verification of Strategy: Official generated J/ψ inclusive MC sample includes $B^0 \to \psi' K^*(892)^0$ decay mode, but there is no $B^0 \to X(3872)K^+\pi^-$ decay mode included. So we embed signal events for both ψ' and $X(3872)$ mass regions to do background subtracted binned fit study.

Furthermore, the whole J/ψ inclusive MC sample is divided into 100 parts (equivalent to the luminosity we have for our experimental data) and embedded signal events into each part. After that we perform fitting of background subtracted $M_{K\pi}$ distribution using binned minimum χ^2 method and study its pull distribution. From pull distribution no significant bias has been observed, so this provides us confidence in the fitter as well as in the strategy adopted for $K\pi$ component study. Insignificant bias has been added to systematic uncertainty study.

- Calibration Decay Mode Study: Further verification is done with the calibrated $B^0 \to \psi' K^+\pi^-$ decay mode. For this decay mode, we assume $K^*(892)^0$, $K_2^*(1430)^0$ and non-resonant $(K^+\pi^-)$ as major contribution in whole $(K\pi)$ system. From the fitting of background subtracted $M_{K\pi}$ distribution, we get ratio of $K^*(892)^0$ to the whole $(K\pi)$ system contribution. This ratio is found to be consistent with PDG value [128]. For concerned decay mode $B^0 \to X(3872)K^+\pi^-$, the decay mode $B^0 \to X(3872)K_2^*(1430)^0$ is kinematically suppressed. So, we consider here rest two components of $(K\pi)$ system.

- Fudge Factor Estimation: The Fudge Factors, differences between Monte Carlo and experimental data for mean and width parameters (which is fixed in each bin) are estimated using calibration decay mode.

- Modeling and Fit Validation: We have used binned minimum χ^2 fit for signal extraction. Fit bias in the extraction of signal yield is estimated from toy MC study and from GSIM study. No significant bias has been observed, which gives us surety about our fitter and signal extraction procedure.

- Signal Extraction Method: After validating our reconstruction procedure with signal MC and calibration decay mode, we apply same strategy to extract signal events for concerned decay mode with full experimental data set.

- Efficiency Correction and Systematic Uncertainty Study: As explained in previous decay modes, it is required to correct efficiency obtained from signal MC.

This is also called particle identification (PID) correction. The estimated systematic uncertainty is calculated with the knowledge of all sources of systematic uncertainties.

Another important conclusion from the above study is about ratios of branching fractions. We obtain the ratio of branching fractions for ψ' mass region given below:

$$\frac{\mathcal{B}(B^0 \to \psi' K^*(892)^0) \times \mathcal{B}(K^*(892)^0 \to K^+\pi^-)}{\mathcal{B}(B^0 \to \psi' K^+\pi^-)} = 0.68 \pm 0.01(\text{stat.}) \pm 0.01(\text{syst.}). \quad (7.1)$$

while this ratio in case of $X(3872)$ mass region is:

$$\frac{\mathcal{B}(B^0 \to X(3872) K^*(892)^0) \times \mathcal{B}(K^*(892)^0 \to K^+\pi^-)}{\mathcal{B}(B^0 \to X(3872) K^+\pi^-)} = 0.34 \pm 0.09(\text{stat.}) \pm 0.02(\text{syst.}). \quad (7.2)$$

From above two ratios, we observe that in the ψ' mass region, the contribution $B^0 \to \psi' K^*(892)^0$ decay mode dominates as compared to $B^0 \to \psi'(K^+\pi^-)_{NR}$ one. However, for $X(3872)$ mass region, the $B^0 \to X(3872)K^*(892)^0$ is not dominating which is in contrast with other charmonium states like ψ' mass region. This result also didn't match with χ_{c1} charmonium state [133], which has same J^{PC} as that of $X(3872)$ i.e. 1^{++}. But with more knowledge about quark content of $X(3872)$, one may clearly observe this difference.

7.5 Results from Resonance Study

For $B^0 \to X(3872)K^+\pi^-$ decay mode, we search for any resonant structure from background subtracted distributions of $M_{X(3872)K}$, $M_{X(3872)\pi}$ and $M_{K\pi}$. It has been observed that there is no clear peak in $M_{X(3872)K}$ and $M_{X(3872)\pi}$ distributions. But peak is observed at background subtracted $M_{K\pi}$ distribution. Further binned minimum χ^2 fit is performed to get different $(K\pi)$ components. From this study, it was found that for $X(3872)$ mass region, ratio of branching fractions i.e. $\frac{\mathcal{B}(B^0 \to X(3872)K^*(892)^0) \times \mathcal{B}(K^*(892)^0 \to K^+\pi^-)}{\mathcal{B}(B^0 \to X(3872)K^+\pi^-)}$ is $0.34 \pm 0.09(\text{stat.}) \pm 0.02(\text{syst.})$, which is in contrast with the same ratio for ordinary charmonium states like ψ' mass region (where

this ratio is $0.68 \pm 0.01(\text{stat.}) \pm 0.01(\text{syst.})$). This property indicates that $X(3872)$ is not behaving like ordinary charmonium state. These ratios of branching fractions are summarized in Table 7.3.

Table 7.3: Ratio of Branching fractions and its estimated value. The first (second) uncertainty represents a statistical (systematic) contribution.

Ratio of Branching fractions	Estimated Value
$\frac{\mathcal{B}(B^0 \to \psi' K^*(892)^0) \times \mathcal{B}(K^*(892)^0 \to K^+\pi^-)}{\mathcal{B}(B^0 \to \psi' K^+\pi^-)}$	$0.68 \pm 0.01(\text{stat.}) \pm 0.01(\text{syst.})$
$\frac{\mathcal{B}(B^0 \to X(3872) K^*(892)^0) \times \mathcal{B}(K^*(892)^0 \to K^+\pi^-)}{\mathcal{B}(B^0 \to X(3872) K^+\pi^-)}$	$0.34 \pm 0.09(\text{stat.}) \pm 0.02(\text{syst.})$

Branching fractions for $B^0 \to \psi' K^*(892)^0$ decay mode is measured to be $(5.88 \pm 0.18(\text{stat.}) \pm 0.31(\text{syst.})) \times 10^{-4}$, which is also consistent with PDG value which is $(6.0 \pm 0.4) \times 10^{-4}$. The product of branching fractions $\mathcal{B}(B^0 \to X(3872) K^*(892)^0) \times (X(3872) \to J/\psi\pi^+\pi^-)$ is found to be $(3.99 \pm 1.48(\text{stat.}) \pm 0.28(\text{syst.})) \times 10^{-6}$. This signal yield has statistical significance of 3σ. Results for above described decay modes are summarized in Table 7.4.

Table 7.4: Signal yield (Y) from the fit, efficiency (ϵ) after PID correction, significance (Σ) and measured branching fractions for $B^0 \to \psi' K^*(892)^0$ and $B^0 \to X(3872) K^*(892)^0$ decay modes. The first (second) uncertainty represents a statistical (systematic) contribution.

Decay Mode	Yield (Y)	ϵ (%)	Σ (σ)	$\mathcal{B}$
$\mathcal{B}(B^0 \to \psi' K^*(892)^0)$	1708 ± 52	13.74	>30	$(5.88 \pm 0.18 \pm 0.31) \times 10^{-4}$
$\mathcal{B}(B^0 \to X(3872) K^*(892)^0) \times \mathcal{B}(X(3872) \to J/\psi\pi^+\pi^-)$	38 ± 14	15.38	3.0	$(3.99 \pm 1.48 \pm 0.28) \times 10^{-6}$

7.6 Discussions and Future Scenario

In the present investigation, we have observed $B^0 \to X(3872)K^+\pi^-$ decay mode with full Belle data set collected with Belle detector at e^+e^- asymmetric collider (KEK B-factory). The product of branching fractions for this decay mode has also been measured.

Investigation has also been performed with the background subtracted mass distributions of $(X(3872)K)$, $(X(3872)\pi)$ and $(K\pi)$ systems for the search of any resonance/new particle. We didn't observe any new resonance/new particle in $(X(3872)K)$ and $(X(3872)\pi)$ mass distributions. However in $(K\pi)$ mass distribution, we found that resonant $K^*(892)^0$ component is small as compared to non-resonant $((K\pi)_{NR})$ component, which doesn't match with the normal charmonium states property (where $K^*(892)^0$ is dominating).

The first evidence for the decay mode $B^+ \to X(3872)K^0_S\pi^+$ is also seen and measurement on its product of branching fractions is performed. However, the significance of $B^+ \to X(3872)K^+\pi^0$ is not sufficient enough for any clear evidence and hence only upper limit is set. Search for $X(3872)$ in the decay mode $B^+ \to X(3872)K^+\pi^0$ decay mode is constrained due to procedure adopted and due to limited statistics. We can access this decay mode with more precision in future with more experimental data available from Belle II at super-KEKB Factory.

With the present analysis of Belle data and latest results from other experiments, the $X(3872)$ has come out to be more interesting and wonderful state. One can clearly see that there is a difference in the production of the normal charmonium state $B \to \psi' K\pi$ and "exotic" state $B \to X(3872)K\pi$. This different behaviour of $X(3872)$ is also seen if we compare this state with other charmonium states like ψ', χ_{c1}. This suggests that $X(3872)$ does not have normal charmonium content and it might be a molecular state of $D^0\bar{D}^{0*}$ with an admixture of $c\bar{c}$. This hypothesis is seen to be consistent with other searches such as $X(3872)$ or $\chi_{c1}(2P)$ in $B \to \chi_{c1}\pi^+\pi^-K$

decay [133] and results from the study of radiative decay of $X(3872)$. However, coming to this conclusion is still not very comfortable and one needs more statistics to really pinpoint the structure of $X(3872)$. But one thing is sure, $X(3872)$ is really a special state and this may be inherited by it due to its proximity to the $D^0\bar{D}^{0*}$ mass.

A

Weighted Efficiency

The weighted efficiency is used for the estimation of branching fractions, this is because the signal yield extracted from 2D extended UML fit returns total yield. The fractions of each component is known from $M_{K\pi}$ fit study as shown in Figure 5.8 and Figure 5.9. So weighted efficiency is calculated using different $(K\pi)$ components with the following formulae:

For ψ' mass region and for both neutral and charged B-meson decay modes

$$\epsilon_{\text{weighted}} = \frac{(Y_{\psi' K^*(892)^0} \times \epsilon_{\psi' K^*(892)} + Y_{\psi' K_2^*(1430)^0} \times \epsilon_{\psi' K_2^*(1430)} + Y_{\psi'(K^+\pi^-)NR} \times \epsilon_{\psi'(K\pi)NR})}{(Y_{\psi' K^*(892)^0} + Y_{\psi'(K^+\pi^-)NR} + Y_{\psi' K_2^*(1430)^0})}. \quad \text{(A.1)}$$

For $X(3872)$ mass region and for both neutral and charged B-meson decay modes

$$\epsilon_{\text{weighted}} = \frac{(Y_{X(3872)K^*(892)^0} \times \epsilon_{X(3872)K^*(892)} + Y_{X(3872)(K^+\pi^-)NR} \times \epsilon_{X(3872)(K\pi)NR})}{(Y_{X(3872)K^*(892)^0} + Y_{X(3872)(K^+\pi^-)NR})}. \quad \text{(A.2)}$$

Since it is known that each $(K\pi)$ yield has some statistical error on it, so weighted efficiency has also some uncertainty on it. This uncertainty on weighted efficiency is also included as source of systematic uncertainty (systematic uncertainty due to limited knowledge to generate MC events).

B

Significance (Including Systematic)

Systematic uncertainties (which affects only signal yield) are included in signal significance using marginalization technique [134]. Systematics due to PDF modeling and fit bias are included in significance estimation, as these are the only uncertainties which can potentially affect the signal yield [134, 135]. First maximum likelihood curve is obtained by fixing the signal yield zero to the nominal value and the negative log-likelihood minimization curve was obtained with the statistical uncertainties. This likelihood is then smeared with the probability distribution ($p_y\mathcal{B}$),

$$p_y(\mathcal{B}) = \int_0^\infty exp^{-\mathcal{B}S} \frac{1}{\sqrt{2\pi\sigma_S^2}} exp^{-(S-\hat{S})^2/2\sigma_S^2} \, dS \tag{B.1}$$

Where, σ_S is the systematic uncertainty on yield (y) and branching fraction ($\mathcal{B}$) is given by $\mathcal{B} = y\hat{S}$ and S is the true value of sensitivity (combination of beam flux, detector acceptance etc.).

Bibliography

[1] K.A. Olive *et al.* (Particle Data Group), Chin. Phys. C, **38**, 090001 (2014).

[2] W. Marciano and H. Pagels, Phys. Rep. **C36**, 137 (1978).

[3] S.L. Glashow, Nucl. Phys. **22**, 579 (1961); S. Weinberg, Phys. Rev. Lett. **19**, 1264 (1967);
A. Salam, "Elementary Particle Theory: Relativistic Groups and Analyticity (Nobel Symposium No. 8)", edited by N. Svartholm, p. 367 (1968).

[4] J. Goldstone, A. Salam and S. Weinberg, Phys. Rev. **127**, 965 (1962).

[5] P.W. Higgs, Phys. Rev. Lett. **12**, 132 (1964); Phys. Rev. Lett. **13**, 508 (1964).

[6] S. Chatrchyan *et al.* (CMS Collaboration), Phys. Lett. **B716**, 30-61 (2012)

[7] S. Chatrchyan *et al.* (CMS Collaboration), JHEP **1306**, 081 (2013).

[8] G. Aad *et al.* (ATLAS Collaboration), Phys. Lett. **B716**, 1-29 (2012).

[9] P. Langacker, Phys. Rep. **72**, 185 (1981).

[10] C.S. Wu *et al.*, Phys. Rev. **105**, 1413 (1957).

[11] J.H. Christenson, J.W. Cronin, V.L. Fitch, and R. Turlay, Phys. Rev. Lett. **13**, 138 (1964).

[12] J.J. Aubert *et al.*, Phys. Rev. Lett. **33**, 1404 (1974);
J.E. Augustin *et al.*, Phys. Rev. Lett. **33**, 1406 (1974).

[13] G.S. Abrams *et al.*, Phys. Rev. Lett. **33**, 1453 (1974).

[14] S.L. Glashow, J. Iliopoulos and L. Maiani, Phys. Rev. D. **2**, 1985 (1970).

[15] E. Eichten *et al.* Phys. Rev. Lett. **34**, 369 (1975);
E. Eichten, K. Gottfried, T. Kinoshita, K.D. Lane and T.M. Yan, Phys. Rev. D **17**, 3090 (1978); **21**, 313(E) (1980); **21**, 203 (1980).

[16] T. Barnes, S. Godfrey and E.S. Swanson, Phys. Rev. D **72**, 054026 (2005).

[17] S. Godfrey and N. Isgur, Phys. Rev. D. **32**, 189 (1985).

[18] A. Buijs, Nucl. Phys. B (Proc. Suppl.) **82**, 300 (2000).

[19] K. Abe *et al.* (Belle Collaboration), Phys. Rev. Lett. **98**, 082001 (2007).

[20] P. Pakhlov *et al.* (Belle Collaboration), Phys. Rev. D **79**, 071101 (R) (2009).

[21] S. Godfrey and S. Olsen, Annu. Rev. Nucl. Part. Sci. **58** , 51-73 (2008).

[22] A. Zhang, T. Huang, T.G. Steele, Phys. Rev. D **76**, 036004 (2007).

[23] B. Aubert *et al.* (BaBar Collaboration), Phys. Rev. Lett. **90**, 242001 (2003).

[24] D. Besson *et al.* (CLEO Collaboration), Phys. Rev. D **68**, 032002 (2003).

[25] T. Nakano *et al.* (LEPS Collaboration), Phys. Rev. Lett. **91**, 012002 (2003).

[26] S. Stepanyan *et al.* (CLAS Collaboration), Phys. Rev. Lett. **91**, 252001 (2003).

[27] B. McKinnon *et al.* (CLAS Collaboration), Phys. Rev. Lett. **96**, 212001 (2006).

[28] J. Hicks, J. Phys.: Conf. Ser. **9**, 183 (2005).

[29] D. Horn and J. Mandula, Phys. Rev. D **17**, 898 (1978).

[30] T.Barnes, F.E. Close and E.S. Swanson, Phys. Rev. D **52**, 5242 (1995).

[31] P. Guo, A.P. Szczepaniak, G. Galata, A. Vassallo and E. Santopinto, Phys. Rev. D **78**, 056003 (2008).

[32] L. Liu *et al.* [Hadron Spectrum Collaboration], JHEP **1207**, 126 (2012).

[33] S. Perantonis *et al.*, Nucl. Phys. **B347**, 854 (1990).

[34] K.J. Juge, J. Kuti and C.J. Morningstar, Phys. Rev. Lett. **82**, 4400 (1999).

[35] Y. Liu and X.Q. Luo, Phys. Rev. D **73**, 054510 (2006).

[36] X.Q. Luo and Y. Liu, Phys. Rev. D **74**, 034502 (2006) [Erratum-ibid. D **74**, 039902 (2006)].

[37] L. Liu, S.M. Ryan, M. Peardon, G. Moir and P. Vilaseca, arXiv:hep-lat/1112.1358 (2011).

[38] F. Close, Proceedings, 12th International Conference on Hadron Spectroscopy, arXiv:hep-ph/0801.2646 (2008).

[39] M.B. Voloshin, Flavor Physics and CP Violation Conference (2006), arXiv:hep-ph/0602233 (2006).

[40] J. Sexton, A. Vaccarino, D. Weingarten, Phys. Rev. Lett. **75**, 4563 (1995).

[41] S.K. Choi *et al.* (Belle Collaboration), Phys. Rev. Lett. **91**, 262001 (2003).

[42] D. Acosta *et al.* (CDF II Collaboration), Phys. Rev. Lett. **93**, 072001 (2004); T. Aaltonen *et al.* (CDF II Collaboration), Phys. Rev. Lett. **103**, 152001 (2009).

[43] V.M. Abazov *et al.* (D0 Collaboration), Phys. Rev. Lett. **93**, 162002 (2004).

[44] B. Aubert *et al.* (BaBar Collaboration), Phys. Rev. D **71**, 071103 (2005), Phys. Rev. D **77**, 111101(R) (2008).

[45] R. Aaij *et al.* (LHCb Collaboration), Eur. Phys. J **C72**, 1972 (2012).

[46] V. Chiochia *et al.* (CMS collaboration), arXiv:hep-ex/1201.6677 (2012).

[47] A. Abulencia *et al.* (CDF Collaboration), Phys. Rev. Lett. **98**, 132002 (2007).

[48] V. Bhardwaj *et al.* (Belle Collaboration), Phys. Rev. Lett. **107**, 091803 (2011).

[49] B. Aubert *et al.* (BaBar Collaboration), Phys. Rev. D **74** , 071101 (2006).

[50] R. Aaij *et al.* (LHCb Collaboration), Nucl .Phys. **B886**, 665 (2014) [arXiv:hep-ex/1404.0275 (2014)].

[51] K. Abe *et al.* (Belle Collaboration), BELLE-CONF-0540 [arXiv:hep-ex/0505037 (2005)].

[52] P. del Amo Sanchez *et al.* (BaBar Collaboration), Phys. Rev. D **82**, 011101(R) (2010).

[53] G. Gokhroo *et al.* (Belle Collaboration), Phys. Rev. Lett. **97**, 162002 (2006).

[54] B. Aubert *et al.* (BaBar Collaboration), Phys. Rev. D **77**, 011102(R) (2008).

[55] T. Aushev *et al.* (Belle Collaboration), Phys. Rev. D **81**, 031103(R) (2010).

[56] S.-K. Choi *et al.* (Belle Collaboration), Phys. Rev. D **84**, 052004 (2011) [arXiv:hep-ex/1107.0163 (2011)].

[57] A. Abulencia *et al.* (CDF II Collaboration), Phys. Rev. Lett. **96**, 102002 (2006).

[58] T. Barnes, S. Godfrey, Phys. Rev. D **69**, 054008 (2004).

[59] K. Abe *et al.* (Belle collaboration), arXiv:hep-ex/0408116v2 (2004).

[60] N. Brambilla *et al.*, "Heavy Quarkonium Physics" [arXiv:hep-ph/0412158 (2004)].

[61] R. Aaij *et al.* (LHCb Collaboration), Phys. Rev. Lett. **110**, 222001 (2013).

[62] L. Maiani *et al.*, Phys. Rev. D **71**, 014028 (2005) [arXiv:hep-ph/0412098 (2004)].

[63] B. Aubert *et al.* (BaBar Collaboration), Phys. Rev. D **71**, 031501 (2005).

[64] T. Aaltonen *et al.* (CDF II Collaboration), Phys. Rev. Lett. **103**, 152001 (2009).

[65] T. Iwashita *et al.* (Belle Collaboration), Prog. Theor. Exp. Phys. **2014**, 043C01 (2014).

[66] V. Bhardwaj *et al.* (Belle Collaboration), Phys. Rev. Lett. **111**, 032001 (2013).

[67] E.S. Swanson, Phys. Lett. **B598**, 197 (2004);
E.S. Swanson, Phys. Rep. **429**, 243 (2006);

[68] M. Suzuki, Phys. Rev. D **72**, 114013 (2005).

[69] B. Aubert *et al.* (BaBar Collaboration), Phys. Rev. Lett. **102**, 132001 (2009).

[70] J. Bian, arXiv: hep-ex/1411.4343 (2014).

[71] E.S. Swanson, Phys. Lett. **B588**, 189 (2004) [arXiv:hep-ph/0410284 (2004)].

[72] Y. Dong, A. Faessler, T. Gutsche and V.E. Lyubovitskij, J. Phys. G **38**, 015001 (2011) [arXiv:hep-ph/0909.0380 (2010)].

[73] N. Brambilla *et al.*, Eur. Phys. J. C **71**, 1534 (2011) [arXiv:hep-ph/1010.5827 (2011)].

[74] M. Kobayashi and T. Maskawa, Prog. Theor. Phys. **49**, 652 (1973).

[75] J.-E. Augustin *et al.*, Phys. Rev. Lett. **33**, 1406 (1974).

[76] J.J. Aubert *et al.*, Phys. Rev. Lett. **33**, 1404 (1974).

[77] S.W. Herb *et al.*, Phys. Rev. Lett. **39**, 252 (1977).

[78] H. Sagawa *et al.* (AMY Collaboration), Phys. Rev. Lett. **63**, 2341 (1989);
K. Nagai *et al.* (TOPAZ Collaboration), Phys. Lett. **B278**, 506 (1992);
M. Shirakata *et al.* (VENUS Collaboration), Phys. Lett. **B278**, 499 (1992).

[79] A. Carter and A.I. Sanda, Phys. Rev. Lett. **45**, 952 (1980).

[80] E. Fernandez *et al.* (MAC), Phy. Rev. Lett. **51**, 1022 (1983);
N.S. Lockyer *et al.* (Mark II), Phy. Rev. Lett. **51**, 1316 (1983).

[81] S. Kurokawa *et al.* (B-Factory Accelerator Task Force), *Accelerator design of the KEK B-factory*, KEK Report 90-24 (1991).

[82] N. Toge *et al.*, *KEKB B-factory design report* KEK Report 95-7 (1995).

[83] M.T. Cheng *et al.* (Belle Collaboration), *Letter of Intent for a study of CP violation in B meson decays*, KEK Report 94-2 (1994).

[84] M.T. Cheng *et al.* (Belle Collaboration), *A study of CP violation in B meson decays: Technical design report*, KEK Report 95-1 (1995).

[85] A. Abashian *et al.* (Belle Collaboration), Nucl. Instrum. Methods Phys. Res., Sect, **A 479**, 117 (2002).

[86] http://www.lns.cornell.edu/public/CLEO/.

[87] http://www.slac.stanford.edu/BFROOT/.

[88] http://belle.kek.jp/.

[89] http://www-hera-b.desy.de/.

[90] http://lhcb.web.cern.ch/lhcb/.

[91] J.P. Alexander *et al.* (CLEO Collaboration), Phys. Rev. Lett. **86**, 2737 (2001).

[92] K. Akai *et al.* (Belle Collaboration), Nucl. Instrum. Methods Phys. Res., Sect, A **499**, 45 (2003).

[93] G. Alimonti *et al.* (Belle Collaboration), Nucl. Instrum. Methods Phys. Res., Sect, A **453**, 71 (2000).

[94] H. Hirano *et al.* (Belle Collaboration), Nucl. Instrum. Methods Phys. Res., Sect, A **455**, 294 (2000).

[95] T. Iijima *et al.* (Belle Collaboration), Nucl. Instrum. Methods Phys. Res., Sect, A **453**, 321 (2000).

[96] H. Kichimi *et al.* (Belle Collaboration), Nucl. Instrum. Methods Phys. Res., Sect, A **453**, 315 (2000).

[97] O. Toker *et al.* (Belle Collaboration), Nucl. Instrum. Methods Phys. Res., Sect, A **340**, 572 (1994).

[98] Y. Ushiroda (Belle Collaboration), Nucl. Instrum. Methods Phys. Res., Sect, A **511**, 6 (2003);
Z. Natkaniec *et al.* (Belle SVD2 Group), Nucl. Instrum. Methods Phys. Res., Sect. A 560, 1 (2006).

[99] S. Uno *et al.* (Belle Collaboration), Nucl. Instrum. Methods Phys. Res., Sect, A **330**, 55 (1993).

[100] MQT300 Fabrication Package, Le-Croy Research System, (1995).

[101] R. Fruwirth (Belle Collaboration), Nucl. Instrum. Methods Phys. Res., Sect, A **262**, 444 (1987);
R. Harr, IEEE Trans. Nucl. Sci. **42**, 134 (1995).

[102] I. Adachi *et al.* (Belle Collaboration), Nucl. Instrum. Methods Phys. Res., Sect, A **335**, 390 (1995).

[103] R. Suda *et al.* (Belle Collaboration), Nucl. Instrum. Methods Phys. Res., Sect, A **406**, 213 (1998).

[104] H. Ikeda *et al.* (Belle Collaboration), Nucl. Instrum. Methods Phys. Res., Sect, A **441**, 401 (2000).

[105] K. Hanagaki *et al.* (Belle Collaboration), Nucl. Instrum. Methods Phys. Res., Sect, A **485**, 490 (2002).

[106] V. Zhilich, "Online luminosity measurements with CsI calorimeter at the Belle detector", Internal Belle Note 465 (2001).

[107] A. Abashian *et al.* (Belle Collaboration), Nucl. Instrum. Methods Phys. Res., Sect, A **449**, 112 (2000).

[108] M.Z. Wang *et al.* (Belle Collaboration), Nucl. Instrum. Methods Phys. Res., Sect, A **455**, 319 (2000).

[109] Y. Ushiroda *et al.* (Belle Collaboration), Nucl. Instrum. Methods Phys. Res., Sect, A **438**, 460 (1999).

[110] M. Nakao *et al.*, IEEE Trans. Nucl. Sci. **47**, 61 (2000).

[111] S. Nagayama, "PANTHER-User's Manual, Reference Manual and Primer", Internal Belle Note 130, 131 and 132 (1996).

[112] H. Ozaki, "Mini-DST Tables V0.0", Internal Belle Note 146 (1996).

[113] T. Nozaki, "Event selection of $B \to J/\psi K_S$", Internal Belle Note 318 (2000); B. Casey, "HadronB", Internal Belle Note 390 (2001).

[114] R. Itoh, "BASF User's Manual", Internal Belle Note 161 (1996).

[115] D.J. Lange, Nucl. Instrum. Methods Phys. Res., Sect. A **462**, 152 (2001).

[116] R. Brun *et al.*, GEANT3.21, CERN Report No. DD/EE/84-1 (1984).

[117] E. Barberio and Z. Wąs, Comput. Phys. Commun. **79**, 291 (1994); P. Golonka and Z. Wąs, Eur. Phys. J. C **45**, 97 (2006); **50**, 53 (2007).

[118] F. Fang, "A study of $K_S \to \pi^+\pi^-$ selection", Internal Belle Note 323 (2000).

[119] S.K.Choi, S.L. Olsen, "Determination of the J^{PC} quantum numbers of the $X(3872)$", Internal Belle Note 800 (2005).

[120] H. Albrecht *et al.* (ARGUS Collaboration), Phys. Lett **B241**, 278 (1990).

[121] T. Skwarnicki, Ph.D Thesis, Institute for Nuclear Physics, Krakow 1986; DESY Internal Report, DESY F31-86-02 (1986).

[122] G. Fox and S. Wolfram, Phys. Rev. Lett., **41** 1581 (1978).

[123] S. Nishida, "Study of kaon and pion identification using Inclusive D* sample", Internal Belle Note 779 (2005).

[124] B. Bhuyan, "High p_T tracking efficiency using partially reconstructed D^* decays", Internal Belle Note 1165 (2010).

[125] L. Hinz, "Lepton ID efficiency correction and systematic error", Internal Belle Note 954 (2006).

[126] E. White, "Determination of K_S Systematic Uncertainty and Efficiency", Internal Belle Note 1207 (2011).

[127] K.-F. Chen *et al.* (Belle Collaboration), Phys. Rev. D **72**, 012004 (2005).

[128] K. Chilikin *et al.* (Belle Collaboration), Phys. Rev. D **88**, 074026 (2013) [arXiv:hep-ex/1306.4894 (2013)].

[129] Karim Trabelsi, "Study of $B \to X(3872)(\to J/\psi\pi^+\pi^-)K$ and $B \to X(3872)(\to J/\psi\pi^+\pi^-)K^+\pi^-$ decays", Internal Belle Note 999 (2009).

[130] A. Bala *et al.* (Belle Collaboration), Phys. Rev. D **91**, 051101(R) (2015).

[131] S. Choi *et al.* (Belle Collaboration), Phys. Rev. Lett. **100**, 142001 (2008);
R. Mizuk *et al.* (Belle Collaboration), Phys. Rev. D **80**, 031104 (2009);
K. Chilikin *et al.* (Belle Collaboration), Phys. Rev. D **88**, 074026 (2013).

[132] R. Aaij *et al.* (LHCb Collaboration), Phys. Rev. Lett. **112**, 222002 (2014).

[133] V. Bhardwaj, "Study of inclusive and multi-body B decays into χ_{c1} and χ_{c2}", Internal Belle Note 1288 (2015).

[134] N.J. Joshi, "Measurement of $\mathcal{BR}(B^0 \to D_S^* h)$", Internal Belle Note 995 (2009).

[135] R.D. Cousins and V.L. Highland, Nucl. Instrum. Meth. A **320**, 331 (1992).

Publications/Conferences

Publication

Publication as a first author:

1. Observation of $X(3872)$ in $B \to X(3872)K\pi$ meson decays.
   A. Bala *et al.* (Belle Collaboration), Phys. Rev. D. **91**, 051101(R) (2015).

2. Search for $B \to X(3872)K\pi$ decays.
   A. Bala *et al.* (Belle Collaboration), "Search for $B \to X(3872)K\pi$ decays", in the proceedings of "XV International Conference on Hadron Spectroscopy" PoS(Hadron 2013)058 (2013).

List of publications as a member of Belle Collaboration:

1. Search for CP violation in the $D^0 \to \pi^0\pi^0$ decay.
   N.K. Nisar *et al.* (Belle Collaboration) Phys. Rev. Lett. **112**, 211601 (2014).

2. Updated cross section measurement of $e^+e^- \to K^+K^-J/\psi$ and $K^0_SK^0_SJ/\psi$ via initial-state-radiation at Belle.
   C.P. Shen *et al.* (Belle Collaboration) Phys. Rev. D. **89**, 072015 (2014).

3. Measurements of the masses and widths of the $\Sigma_c(2455)^{0/++}$ and $\Sigma_c(2520)^{0/++}$ baryons.
   S.-H. Lee *et al.* (Belle Collaboration) Phys. Rev. D. **89**, 091102(R) (2014).

4. Search for the $B^+ \to e^+\nu_e$ and $B^+ \to \mu^+\nu_\mu$ decays using hadronic tagging method.
   Y. Yook *et al.* (Belle Collaboration), Phys. Rev. D. **91**, 052016(R) (2015).

5. Amplitude analysis of $e^+e^- \to \Upsilon(nS)\pi^+\pi^-$ at $\sqrt{s} = 10.865$ GeV.
   A. Bondar *et al.* (Belle Collaboration), Phys. Rev. D. **91**, 072003(R) (2015).

6. Observation of $D^0 - \bar{D}^0$ mixing in e^+e^- collisions.
   B.R. Ko *et al.* (Belle Collaboration), Phys. Rev. Lett. **112**, 111801 (2014).

7. Measurement of $\mathcal{B}(\Lambda_C^+ \to pK^-\pi^+)$.
   A. Zupanc *et al.* (Belle Collaboration), Phys. Rev. Lett. **113**, 042002 (2014).

8. Measurement of $D^0\bar{D}^0$ mixing and search for indirect CP violation using $D^0 \to K_S^0\pi^+\pi^-$ decays.
   T. Peng *et al.* (Belle Collaboration), Phys. Rev. D **89**, 091103(R) (2014).

9. Search for doubly charmed baryons and study of charmed strange baryons at Belle.
   Y. Kato *et al.* (Belle Collaboration), Phys. Rev. D **89**, 052003 (2014).

10. Measurement of branching fractions and CP violation parameters in $B \to \omega K$ decays and first evidence of CP violation in $B^0 \to \omega K_S^0$.
    V. Chobanova *et al.* (Belle Collaboration), Phys. Rev. D **90**, 012002 (2014).

11. Measurement of the τ-lepton lifetime at Belle.
    K. Belous *et al.* (Belle Collaboration), Phys. Rev. Lett. **112**, 031801 (2014).

12. Measurement of the lepton forward-backward asymmetry in inclusive $B \to X_S\ell^+\ell^-$ decays.
    Y. Sato *et al.* (Belle Collaboration), arXiv:hep-ex/1402.7134(2014).

13. Evidence for the suppressed decay $B^- \to DK^-$, $D \to K^+\pi^-\pi^0$.
    M. Nayak *et al.* (Belle Collaboration), Phys. Rev. D **88**, 091104(R) (2013).

14. Measurement of branching fractions of τ lepton decays containing one or more K_S^0.
    S. Ryu *et al.* (Belle Collaboration), Phys. Rev. D **89**, 072009 (2014).

15. Measurement of $e^+e^- \to \omega\pi^0$, $K^*(892)\bar{K}$ and $K_2^*(1430)\bar{K}$ at $\sqrt{s}$ near 10.6 GeV.
    C.P. Shen *et al.* (Belle Collaboration), Phys. Rev. D **88**, 052019 (2013).

16. Search for $B^0 \to p\bar{\Lambda}\pi^-\gamma$ at Belle.
    Y.-T. Lai *et al.* (Belle Collaboration), Phys. Rev. D **89**, 051103(R) (2014).

17. Measurement of branching fractions for the $B \to J/\psi\eta K$ decays and search for a narrow resonance in the $J/\psi\eta$ final State.
    T. Morii *et al.* (Belle Collaboration), Prog. Theor. Exp. Phys. **2014**, 043C01 (2014).

18. Angular analysis of $B^0 \to \phi K^*$ decays and search for CP violation at Belle.
    M. Prim *et al.* (Belle Collaboration), Phys. Rev. D **88**, 072004 (2013).

19. Measurements of branching fractions of leptonic and hadronic D_S^+ meson decays and extraction of the D_S^+ meson decay constant.
    A. Zupanc *et al.* (Belle Collaboration), Journal of High Energy Physics **09**, 139 (2013).

20. First observation of the $Z_b^0(10610)$ in a Dalitz analysis of $\Upsilon(10860) \to \Upsilon(nS)\pi^0\pi^0$.
    P. Krokovny *et al.* (Belle Collaboration), Phys. Rev. D **88**, 052016 (2013).

21. Search for bottomonium states in exclusive radiative $\Upsilon(2S)$ decays.
    S. Sandilya *et al.* (Belle Collaboration), Phys. Rev. Lett. **111**, 112001 (2013).

22. Measurement of the CP violation parameters in $B^0 \to \pi^+\pi^-$ decays.
    J. Dalseno *et al.* (Belle Collaboration), Phys. Rev. D **88**, 092003 (2013).

23. Experimental constraints on the spin and parity of the $Z(4430)^+$.
    K. Chilikin *et al.* (Belle Collaboration), Phys. Rev. D **88**, 074026 (2013).

24. Study of $B^0 \to \rho^0\rho^0$ decays, implications for the CKM angle ϕ_2 and search for other B^0 decay modes with a four-pion final state.
    P. Vanhoefer *et al.* (Belle Collaboration), Phys. Rev. D **89**, 072008 (2014).

25. Measurement of the wrong-sign decay $D^0 \to K^+\pi^-\pi^+\pi^-$.
    E. White *et al.* (Belle Collaboration), Phys. Rev. D **88**, 051101(R) (2013).

26. Measurement of exclusive $\Upsilon(1S)$ and $\Upsilon(2S)$ decays into vector-pseudoscalar final states.
C.P. Shen *et al.* (Belle Collaboration), Phys. Rev. D **88**, 011102(R) (2013).

27. Study of exclusive $B \to X_u \ell \nu$ decays and extraction of $|V_{ub}|$ using full reconstruction tagging in the Belle experiment.
A. Sibidanov *et al.* (Belle Collaboration), Phys. Rev. D **88**, 032005 (2013).

28. Evidence for semileptonic $B^- \to p\bar{p}\ell^-\bar{\nu}_l$ decays.
K.-J. Tien *et al.* (Belle Collaboration), Phys. Rev. D **89**, 011101(R) (2013).

29. High-statistics study of K^0_S pair production in two-photon collisions.
Y. Watanabe *et al.* (Belle Collaboration), Prog. Theor. Exp. Phys. **2013**, 123C01 (2013).

30. Measurement of the decays $B_S \to J/\psi\phi(1020)$, $B_s \to J/\psi f_2^{'}(1525)$ and $B_S \to J/\psi K^+K^-$ at Belle.
F. Thorne *et al.* (Belle Collaboration), Phys. Rev. D **88**, 114006(R) (2013).

31. Study of $e^+e^- \to \pi^+\pi^- J/\psi$ and observation of a charged charmonium-like state at Belle.
Z.Q. Liu *et al.* (Belle Collaboration), Phys. Rev. Lett. **110**, 252002 (2013).

32. Evidence for the decay $B^0 \to K^+K^-\pi^0$.
V. Gaur *et al.* (Belle Collaboration), Phys. Rev. D **87**, 091101(R) (2013).

33. First observation of Cabibbo-suppressed Ξ_c^0 decays.
R. Chistov *et al.* (Belle Collaboration), Phys. Rev. D **88**, 071103(R) (2013).

34. Search for $e^+e^- \to J/\psi X(1835)$ process at $\sqrt{s} = 10.6$ GeV.
X.H. He *et al.* (Belle Collaboration), Phys. Rev. D **89**, 032003 (2014).

35. Evidence of a narrow resonance decaying to $\chi_{c1}\gamma$ in $B \to \chi_{c1}\gamma K$.
V. Bhardwaj *et al.* (Belle Collaboration), Phys. Rev. Lett. **111**, 032001 (2013).

Thesis results presented in Conferences/Workshops

By Author

1. A. Bala (Panjab), "Search for $B \to X(3872)K\pi$ decays",
   XV International Conference on Hadron Spectroscopy-Hadron 2013.
   (4-8 Nov., 2013, Nara, Japan).

By Collaborators

1. K. Miyabayashi (Nara), "Hadron Physics",
   JPS 70th Annual Meeting (2015).
   (21-24 March, 2015, Waseda University, Tokyo, Japan)

2. K. Miyabayashi (Nara), "Spectroscopy at Belle",
   Hadrons and Hadron Interactions in QCD (HHIQCD).
   (15 February - 15 March, 2015, Kyoto, Japan).

3. P. Krokovny (BINP), "Quarkonium (-like) states at Belle",
   37th International Conference on High Energy Physics (ICHEP 2014).
   (2-9 July, 2014, Valencia, Spain).

4. K. Chilikin (ITEP), "Recent results on quarkonium(-like) states at Belle".
   Moriond QCD 2014.
   (22-27 March, 2014, La Thuile, Italy).

Internal Belle Note

1. Study of $B \to (J/\psi\pi\pi)K\pi$.
   A. Bala, V. Bhardwaj, K. Trabelsi and J.B. Singh, Internal Belle Note 1262 (2013).